9-14-2017

Analysis of Ar($1s_5$) Metastable Populations in High Pressure Argon-Helium Gas Discharges

Daniel J. Emmons II

Analysis of Ar($1s_5$) Metastable Populations in High Pressure Argon-Helium Gas Discharges

DISSERTATION

Daniel J. Emmons II, Maj, USAF

AFIT-ENP-DS-17-S-025

DEPARTMENT OF THE AIR FORCE
AIR UNIVERSITY

AIR FORCE INSTITUTE OF TECHNOLOGY

Wright-Patterson Air Force Base, Ohio

AFIT-ENP-DS-17-S-025

ANALYSIS OF AR($1S_5$) METASTABLE POPULATIONS IN HIGH PRESSURE ARGON-HELIUM GAS DISCHARGES

DISSERTATION

Presented to the Faculty

Graduate School of Engineering and Management

Air Force Institute of Technology

Air University

Air Education and Training Command

in Partial Fulfillment of the Requirements for the

Degree of Doctor of Philosophy in Applied Physics

Daniel J. Emmons II, B.S., M.S.

Maj, USAF

14 September 2017

AFIT-ENP-DS-17-S-025

ANALYSIS OF AR($1S_5$) METASTABLE POPULATIONS IN HIGH PRESSURE ARGON-HELIUM GAS DISCHARGES

DISSERTATION

Daniel J. Emmons II, B.S., M.S.
Maj, USAF

Committee Membership:

Dr. D. E. Weeks
Chairman

Dr. G. P. Perram
Member

Dr. B. F. Akers
Member

Acknowledgements

For Brittany and Danny: Thanks for your love and support over the last few years!

Many thanks to everybody who helped along the way. Dr Akers, thanks for your guidance on numerical modeling and ensuring that our models performed correctly. Dr Perram, thank you for providing the big-picture insight into the research and for your help developing a simple kinetic model for a complex problem. Dr Bailey, thanks for your guidance with all things plasma related and for making sure this project headed in the right direction. Drs Heaven and Han, thanks for letting us model your experiment and for providing keen insight into optically pumped rare gas lasers. Dr Eshel, thanks for keeping us tethered to reality by providing an excellent data set along with many helpful discussions on the nature of gas discharges.

A special thanks goes to Dr Weeks, who helped develop and sharpen my research skills. I've learned that if I can't explain something using the most basic principles, then I don't really understand it. Thanks for your guidance, mentorship, and motivation over the last few years, and thanks for making the research process fun along the way!

Daniel J. Emmons II

Abstract

Simulations of an argon-helium plasma are performed for two high pressure discharge scenarios in an attempt to find a uniform, large-volume plasma with $Ar(1s_5)$ metastable densities on the order of 10^{13} cm^{-3} for use as the ground state in an optically pumped rare gas laser. An analysis of a pulsed direct current discharge is performed for a 7% argon in helium mixture at a pressure of 270 Torr using both zero and one-dimensional models. Kinetics of species relevant to the operation of an optically pumped rare gas laser are analyzed throughout the pulse duration to identify key reaction pathways. Time dependent densities, electron temperatures, current densities, and reduced electric fields in the positive column are analyzed over a single 20 μs pulse, showing temporal agreement between the two models. Through the use of a robust reaction rate package, radiation trapping is determined to play a key role in reducing $Ar(1s_5)$ metastable loss rates through the reaction sequence $Ar(1s_5) + e^- \rightarrow Ar(1s_4) + e^-$ followed by $Ar(1s_4) \rightarrow Ar + \hbar\omega$. Collisions with He are observed to be responsible for $Ar(2p_9)$ mixing, with nearly equal rates to $Ar(2p_{10})$ and $Ar(2p_8)$. Additionally, dissociative recombination of Ar_2^+ is determined to be the dominant electron loss mechanism for the simulated discharge conditions and cavity size.

Simulations are also performed for an α-mode radio frequency dielectric barrier discharge with varying mixtures of argon and helium at pressures ranging from 200-500 Torr using both zero and one-dimensional models. Metastable densities are analyzed as a function of argon fraction and pressure to determine the optimal conditions maximizing metastable density for use in an optically pumped rare gas laser. Argon fractions corresponding to the peak metastable densities are found to be pressure

dependent, shifting from approximately 15% Ar in He at 200 Torr to 10% at 500 Torr. A decrease in metastable density is observed as pressure is increased due to a diminution in the reduced electric field and a quadratic increase in metastable loss rates through Ar_2^* formation. A zero-dimensional effective direct current model of the dielectric barrier discharge is implemented, showing agreement with the trends predicted by the one-dimensional fluid model in the bulk plasma.

Finally, optically pumped rare gas laser performance is analyzed as a function of the $Ar(2p) + M \rightarrow Ar(1s) + M$ branching ratio. Due to the uncertainty in the branching ratio, a sensitivity study is performed to determine the effect on output and absorbed pump laser intensities. The analysis is performed using a radio frequency dielectric barrier discharge as the source of metastable production for a variety of argon in helium mixtures over pressures ranging from 200 to 500 Torr. Peak output laser intensities show a factor of 7 increase as the branching ratio is increased from 25% to 100%. The collection of excited Ar species, Ar^*, in $Ar(1s_4)$ is determined to play the primary role in laser performance as a function of branching ratio as the result of a reduction in the density of species directly involved with laser performance.

Table of Contents

Page

List of Figures

List of Tables

ANALYSIS OF AR($1S_5$) METASTABLE POPULATIONS IN HIGH PRESSURE ARGON-HELIUM GAS DISCHARGES

I. Introduction

A deployable, continuous wave, high energy laser weapon system with excellent beam quality and a renewable power source has been desired for many decades. Chemical lasers of the past required the use of bulky, volatile chemicals, making renewability and portability problematic. The recent development of diode-pumped solid state lasers with powers near 100 kW has sparked interest in renewable, electrically driven lasers, although, the intense heat produced in solid state lasers induces poor beam quality. Applying diode-pumping to a gas phase medium, as demonstrated by the diode-pumped alkali laser (DPAL), takes advantage of the thermal management inherent to gas lasers to produce renewable lasers with excellent beam quality [Krupke et al., 2003]. However, the aggressive nature of the alkali metal vapors creates technical challenges such as photo-induced chemical damage to the cavity windows and "laser snow" due to reactions with the spin-orbit relaxation agent [Pitz et al., 2011].

In an attempt to realize the positive qualities of a DPAL using a medium without a chemically aggressive nature, Han and Heaven [2012] successfully demonstrated a rare gas laser system that utilizes the first excited electronic state, metastable $Rg(1s_5)$ using Paschen notation, as the laser ground state. Optical pumping to the $Rg(2p)$ manifold provides spectral properties similar to DPAL systems while maintaining the inert properties inherent in rare gases. As in the DPAL systems, the atmospheric transmission characteristics of a rare gas system are conducive to operation as a high energy laser weapon.

An optically pumped rare gas laser (OPRGL), as demonstrated by Han et al. [2013], uses a diode laser to pump metastable $Rg(1s_5)$ atoms generated in a gas discharge to the $Rg(2p_9)$ level. At elevated pressures, rapid collisional relaxation from $Rg(2p_9)$ to $Rg(2p_{10})$ allows for a population inversion and subsequent lasing to $Rg(1s_5)$ as displayed in Figure 1. Diode laser absorption, and hence optical gain, are dependent on $Rg(1s_5)$ densities [Rawlins et al., 2015; Demyanov et al., 2013]. Output laser intensities above 100 W/cm^2 may be possible with a uniform volume of metastable densities on the order of 10^{13} cm^{-3} for an active medium length of 1.9 cm [Han et al., 2014]. The broad linewidths of diode lasers require near-atmospheric pressures to broaden the absorption linewidth for efficient pump laser absorption. Additionally, the non-adiabatic transition rate from $Rg(2p_9)$ to $Rg(2p_{10})$, responsible for establishing a population inversion, is enhanced at elevated pressures.

The high pressures required for laser operation mandate a stable gas discharge capable of operating at high pressures. Thermal instabilities are problematic for high pressure gas discharges due to elevated current densities [Raizer, 1997]. These thermal instabilities limit the types of discharges capable of maintaining stability at near-atmospheric gas pressures [Haas, 1973; Fridman et al., 2005]. Pulsed discharges are able to maintain stability at high pressures through a reduction in thermal instabilities caused by the down time in-between pulses [Raizer, 1997]. Additionally, for the same averaged power, the average plasma density of a pulsed system is greater than a steady-state direct current (DC) discharge as a result of a reduction in electron temperature in-between pulses [Ashida et al., 1995; Lieberman and Lichtenberg, 2005]. Similarly, radio frequency dielectric barrier discharges (RF-DBDs) are able to maintain stability at high pressures due to a limited ionization period occurring near the cycle peaks and an increased energy threshold for instability formation [Raizer et al., 1995]. While there are other types of discharges capable of maintaining stability

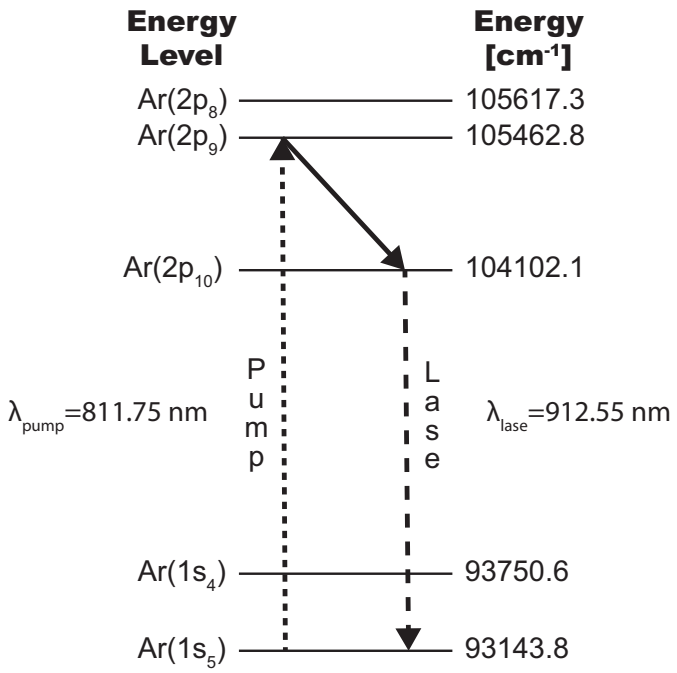

Figure 1. A diagram of energy levels pertinent to an optically pumped rare gas laser with Ar as the rare gas. Optical pumping from $Ar(1s_5)$ to $Ar(2p_9)$ is followed by a non-adiabatic transition to $Ar(2p_{10})$ and subsequent lasing to $Ar(1s_5)$. Lasing to $Ar(1s_4)$ is also possible, and $Ar(2p_8)$ is included due to its proximity to the pumping level $Ar(2p_9)$.

at high pressures, such as microwave driven microplasmas and microhollow cathode discharges, this analysis will focus on pulsed DC discharges and RF-DBDs.

Han et al. [2013] demonstrated the use of a pulsed DC circuit to produce an OPRGL in an Ar-He mixture at atmospheric pressures. Voltages in the range of 1000-2000 V were used for microsecond pulses across a parallel plate geometry. Metastable densities, measured through pump laser absorption, indicated a decay to half the peak value approximately 7 μs after pulse initiation. More recently, Han et al. [2016] performed an Ar-He pulsed DC discharge experiment at a pressure of 270 Torr using a mixture of 7% Ar in He. Pump laser absorption, plasma fluorescence, electrode voltage, and discharge current were measured to provide a complete picture of the discharge conditions for 1000 V pulses with temporal widths of 1, 20, and 35 μs. The kinetics controlling the time-dependent metastable behavior during a pulse are not well understood, and will be analyzed in this document.

Several kinetic studies of OPRGLs have been performed recently [Demyanov et al., 2013; Yang et al., 2015; Rawlins et al., 2015; Han et al., 2014]. One analysis of an Ar-He mixture at atmospheric pressures concluded that a mixture of approximately 1% Ar in He results in the largest total efficiency, defined as the output power divided by the sum of discharge and pump powers [Demyanov et al., 2013]. The study observed that an increase in Ar-fraction increases production of $Ar(1s_5)$, but also results in a larger collision relaxation rate from the $Ar(2p)$ manifold down to the $Ar(1s)$ manifold in addition to an increase in the $Ar(1s_5)$ loss rate through excimer formation. A separate kinetic analysis studied OPRGL performance over a variety of metastable densities, showing the possibility of kilowatt laser powers for an OPRGL system with $Ar(1s_5)$ densities on the order of 10^{13} cm^{-3} and pump laser intensities in the 2-5 kW/cm^2 range [Yang et al., 2015].

An experimental and computational analysis of microwave resonator-driven microplasmas at a variety of Ar-He mixtures and pressures ranging from 100-730 Torr found that an Ar-fraction near 5% at a pressure of 100 Torr produces the largest metastable densities [Hoskinson et al., 2016]. Metastable densities on the order of 10^{13} cm^{-3} were measured for the microplasmas at a pressure of 100 Torr, with a decrease in the $Ar(1s_5)$ density as the pressure increased. A related experiment measured a laser output of 22 mW for an absorbed pump power of $\sim$ 40 mW and an estimated metastable density of 3×10^{12} cm^{-3} [Rawlins et al., 2015]. This measurement provides an optical efficiency of approximately 55%. The gain, G, was found to be linear with respect to metastable density, following $[Ar(1s_5)]/G = 4 \times 10^{12}$ cm^{-2}, measured at 760 Torr for a mixture of 2% Ar in He. Additionally, a computational analysis of the laser kinetics found a better fit to the data when an Arrhenius temperature scaling was applied to the neutral collision transfer rates between the different excited Ar species.

The desired metastable density on the order of 10^{13} cm^{-3} has been achieved using microwave resonator-driven microplasma arrays with cross-sectional areas on the order of 1 mm^2 [Miura and Hopwood, 2011; Rawlins et al., 2015]. Increasing the cross-sectional area of the discharge allows for increased pump laser absorption caused by efficient alignment of the pump laser with the region of high metastable densities. This document outlines approaches to produce uniform metastable densities at high pressures in volumes with cross-sectional areas greater than 1 mm^2.

A zero-dimensional approach to modeling high pressure discharges has been developed and outlined by Eismann [2011]. The creation of the ZDPlasKin model [Pancheshnyi et al., 2008] along with the Boltzmann solver BOLSIG+ [Hagelaar and Pitchford, 2005], allows for a robust method of calculating positive column densities and kinetics. Applying this approach to an RF-DBD, following the procedure outlined in Raizer et al. [1995], allows for a computational inexpensive method for estimating densities in the bulk plasma of an RF-DBD.

Extending the simulations to one-dimension is achieved through the implementation of a fluid model, which has been used for both low and high pressure discharges in many previous analyses [Lymberopoulos and Economou, 1993; Boeuf and Pitchford, 1995; Farouk et al., 2006; Gogolides and Sawin, 1992; Kushner, 2005; Boeuf and Pitchford, 2004]. While some of the intrinsic approximations of fluid models are known to fail for high reduced electric field magnitudes with large spatial gradients, as found in the cathode layer of a DC glow discharge [Raizer, 1997; Hagelaar and Pitchford, 2005], the approach is appropriate for modeling the bulk plasma, which is the region of interest to a gas laser.

Rate coefficients for collisional de-excitation following $Ar(2p) + M \rightarrow Ar(1s) + M$ are well documented [Chang and Setser, 1978; Han and Heaven, 2014]. However, the branching ratios to the specific $Ar(1s)$ levels are uncertain. Additionally, as discussed

in Chang and Setser [1978], the rate coefficients depend strongly on diabatic coupling near crossings of the potential energy surfaces, not just the energy difference between states. Due to the uncertainty in the branching ratios, previous kinetic studies of OPRGL performance have assumed that all $Ar(2p) + M \rightarrow Ar(1s) + M$ collisions channel directly to $Ar(1s_5)$ bypassing the other $Ar(1s)$ levels [Demyanov et al., 2013; Yang et al., 2015; Rawlins et al., 2015; Han et al., 2014]. The effect of the branching ratios on OPRGL performance is investigated in this analysis.

This document is outlined as follows: Chapter II provides the background theory used throughout the remainder of the document. First, the physics of gas discharge simulations are introduced, including the reaction rate package developed for an OPRGL. Then, an overview of pulsed DC discharges and RF-DBDs is provided. Finally, the computational aspects of gas discharge simulation implemented in this analysis are presented.

Chapter III analyzes the pulsed circuit experiment described in Han et al. [2016]. In addition to simulating the measured parameters over time, the zero-dimensional analysis is used to vet the reaction rate package and perform a sensitivity analysis. Simulations are extended to one-dimension, providing the spatial metastable density profile and verifying the positive column predictions of the zero-dimensional approach. Furthermore, EEDF calculations for the one-dimensional model are varied over the pulse duration to test the effectiveness of using a single set of pre-calculated EEDFs.

Chapter IV analyzes the RF-DBD experiments performed by Eshel et al. [2016]. A one-dimensional fluid model is used to calculate metastable density dependence on Ar-fraction, pressure, and applied voltage. The α to γ-mode transition for a 15% Ar in He mixture at a pressure of 200 Torr is simulated as a part the analysis as a function of applied voltage. Additionally, a zero-dimensional effective DC model of the bulk plasma is implemented and compared to the one-dimensional simulations.

A simplified zero-dimensional model is also developed, providing insight into the key kinetics controlling metastable behavior as a function of pressure and Ar-fraction.

Finally, Chapter V analyzes OPRGL performance for a variety of Ar-He mixtures and pressures using an RF-DBD as the discharge. Absorbed pump laser intensities and output laser intensities are calculated as a function of Ar-fraction, pressure, and $Ar(2p) + M \rightarrow Ar(1s) + M$ branching ratio using a time-dependent zero-dimensional discharge model including laser kinetics. Due to the uncertainty in the branching ratio, a sensitivity study of the branching ratio influence on laser intensities is performed. Furthermore, a simplified laser kinetic model is developed and compared to the full discharge laser model.

The overarching goal of this research is to understand the discharge conditions and chemical kinetics of an Ar-He plasma such that an OPRGL system could be developed with a continuous, large volume source of $Ar(1s_5)$ capable of maintaining densities on the order of 10^{13} cm^{-3}. Additionally, we strive to understand the trade-offs between metastable density, pressure, and Ar-fraction with respect to OPRGL performance.

II. Background

This chapter provides the background theory used throughout the remainder of the document. First, the physics of gas discharge simulations are introduced, including the reaction rate package developed for an optically pumped rare gas laser. Then, challenges of high pressure gas discharges are discussed, and an overview of pulsed direct current discharges and radio frequency dielectric barrier discharges is provided. Finally, the computational aspects of gas discharge simulation used throughout this analysis are presented.

2.1 Physics of Gas Discharge Simulation

This section provides an introduction to the physics of gas discharges, focusing on a few key aspects of the discharges analyzed throughout the document: chemical kinetics, ambipolar diffusion, the reduced electric field, and similarity parameters.

Chemical Kinetics.

To properly model the chemical kinetics of an Ar-He plasma, a set of pertinent species must first be selected. Ar has a large variety of excited electronic energy levels, allowing for many possible laser schemes (see Figure 2 for the dipole allowed transitions in the $Ar(1s)$ and $Ar(2p)$ manifolds). However, attempting to model all possible species would be unwieldy and unnecessary for the focus of this study.

A list of the species used to analyze OPRGL kinetics for both the zero and one-dimensional models is displayed in Table 1. Excited Ar species $Ar(1s_5)$, $Ar(2p_{10})$, and $Ar(2p_9)$ are included due to their central role in OPRGL operation. Additionally, $Ar(1s_4)$ and $Ar(2p_8)$ are retained because of their proximity to $Ar(1s_5)$ and $Ar(2p_9)$, respectively. An additional excited species, $Ar(h.l.)$, is used as a macro-species en-

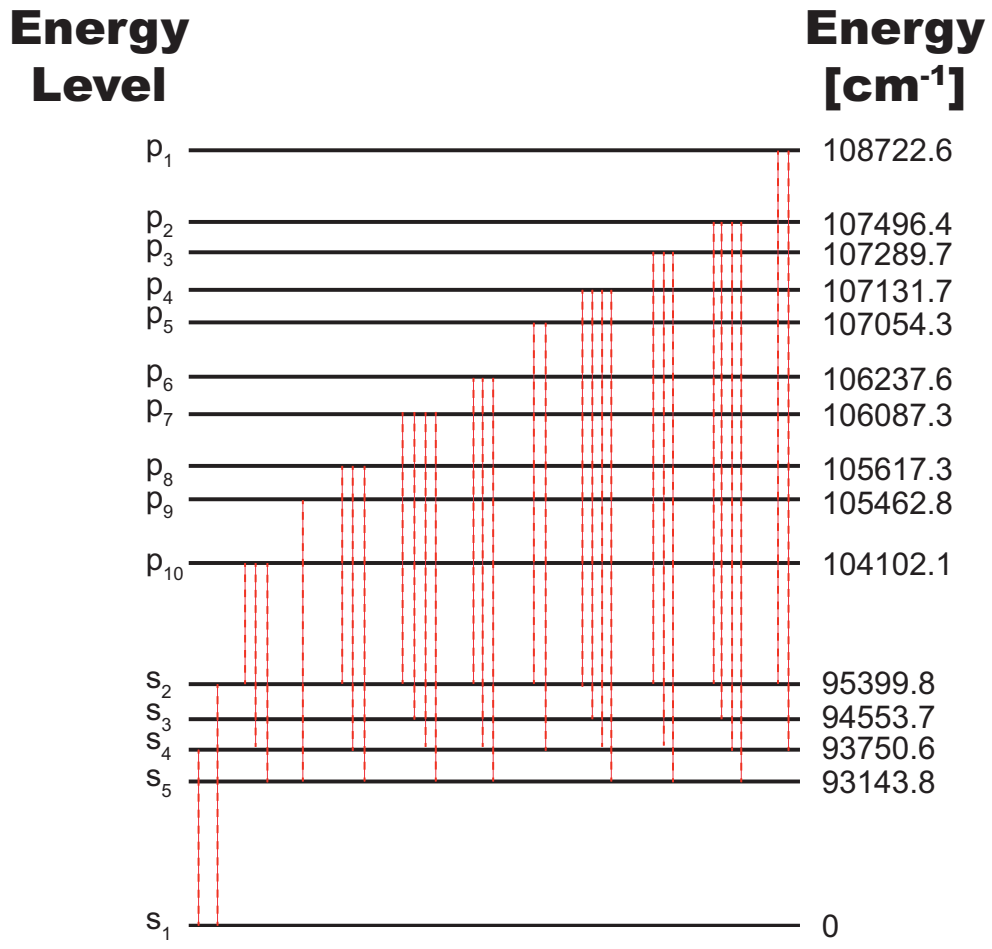

Figure 2. A diagram of the dipole allowed transitions for the $Ar(1s)$ and $Ar(2p)$ manifolds [Eshel et al., 2016].

compassing all higher energy electronic levels of Ar starting with $Ar(3d_{12})$. The remaining $Ar(1s)$ and $Ar(2p)$ species are ignored to limit the reaction rate package complexity.

Excited levels of He are represented by the macro-species He^*. At near-atmospheric pressures, dimers play an important kinetic role requiring the macro-species He_2^* and Ar_2^*, which represent all He and Ar dimer energy levels. Finally, the ion species Ar^+, Ar_2^+, He^+, He_2^+, and $HeAr^+$ are included. The energy used to represent the macro-species is the lowest energy level for the collection of species represented by the macro-species. Dimer energies of 11.06 and 17.97 eV are used for Ar_2^* and He_2^*, respectively [Shon, 1993]. A list of reactions for the species of interest is displayed in Table 2. This reaction rate package includes electron impact, recombination, two-heavy-body, three-heavy-body, and radiative rate coefficients.

Table 1. A list of Ar-He species relevant to the operation of an optically pumped rare gas laser and their corresponding energy levels. Macro-species energies are represented by the lowest energy level for the collection of species represented by the macro-species.

Species	Energy (eV)
Ar_2^*	11.06
$Ar(1s_5)$	11.55
$Ar(1s_4)$	11.62
$Ar(2p_{10})$	12.91
$Ar(2p_9)$	13.08
$Ar(2p_8)$	13.10
$Ar(h.l.)$	13.85
Ar_2^+	14.50
$HeAr^+$	15.74
Ar^+	15.76
He_2^*	17.97
He^*	19.80
He_2^+	22.23
He^+	24.58

Electron impact rate coefficients are calculated using BOLSIG+, which uses a two-term approximation to solve the Boltzmann equation, providing a non-Maxwellian

electron energy distribution function (EEDF) [Hagelaar and Pitchford, 2005]. The main driver of the EEDF is the reduced electric field, E/N, where N is the neutral gas density. Reduced electric fields are calculated over time to provide an updated EEDF for the current discharge conditions. Transport parameters, including electron mobility and diffusion coefficients, are also calculated from the EEDF.

Table 2. A list of reaction rate coefficients used to model high pressure Ar-He gas discharge kinetics for species relevant to the operation of an optically pumped rare gas laser. T_e is in eV and T_{gas} is in K. A discussion of the BOLSIG+ calculated rate coefficients can be found in Hagelaar and Pitchford [2005].

Reaction	Rate Coefficient $\left[\frac{1}{s}, \frac{cm^3}{s}, or \frac{cm^6}{s}\right]$	Reference
Electron Impact		
$Ar + e^- \rightarrow Ar^+ + e^- + e^-$	BOLSIG+	Phelps [2008]
$Ar(1s_5) + e^- \rightarrow Ar^+ + e^- + e^-$	BOLSIG+	Phelps [2008]
$Ar(1s_4) + e^- \rightarrow Ar^+ + e^- + e^-$	BOLSIG+	Phelps [2008][a]
$Ar(2p_{10}) + e^- \rightarrow Ar^+ + e^- + e^-$	BOLSIG+	Phelps [2008][a]
$Ar(2p_9) + e^- \rightarrow Ar^+ + e^- + e^-$	BOLSIG+	Phelps [2008][a]
$Ar(2p_8) + e^- \rightarrow Ar^+ + e^- + e^-$	BOLSIG+	Phelps [2008][a]
$Ar(h.l.) + e^- \rightarrow Ar^+ + e^- + e^-$	BOLSIG+	Phelps [2008][a]
$Ar + e^- \leftrightarrow Ar(1s_5) + e^-$	BOLSIG+	Biagi [2011]
$Ar + e^- \leftrightarrow Ar(1s_4) + e^-$	BOLSIG+	Biagi [2011]
$Ar + e^- \leftrightarrow Ar(2p_{10}) + e^-$	BOLSIG+	Biagi [2011]
$Ar + e^- \leftrightarrow Ar(2p_9) + e^-$	BOLSIG+	Biagi [2011]
$Ar + e^- \leftrightarrow Ar(2p_8) + e^-$	BOLSIG+	Biagi [2011]
$Ar + e^- \leftrightarrow Ar(h.l.) + e^-$	BOLSIG+	Biagi [2011][b]
$Ar(2p_{10}) + e^- \leftrightarrow Ar(2p_9) + e^-$	BOLSIG+	Stauffer [2014]
$Ar(2p_{10}) + e^- \leftrightarrow Ar(2p_8) + e^-$	BOLSIG+	Stauffer [2014]
$Ar(2p_{10}) + e^- \leftrightarrow Ar(h.l.) + e^-$	BOLSIG+	Biagi [2011][c]
$Ar(2p_9) + e^- \leftrightarrow Ar(2p_8) + e^-$	BOLSIG+	Stauffer [2014][d]
$Ar(2p_9) + e^- \leftrightarrow Ar(h.l.) + e^-$	BOLSIG+	Biagi [2011][c]
$Ar(2p_8) + e^- \leftrightarrow Ar(h.l.) + e^-$	BOLSIG+	Biagi [2011][c]
$Ar(1s_4) + e^- \leftrightarrow Ar(2p_{10}) + e^-$	BOLSIG+	Stauffer [2014]
$Ar(1s_4) + e^- \leftrightarrow Ar(2p_9) + e^-$	BOLSIG+	Stauffer [2014]
$Ar(1s_4) + e^- \leftrightarrow Ar(2p_8) + e^-$	BOLSIG+	Stauffer [2014]
$Ar(1s_4) + e^- \leftrightarrow Ar(h.l.) + e^-$	BOLSIG+	Biagi [2011][c]
$Ar(1s_5) + e^- \leftrightarrow Ar(1s_4) + e^-$	BOLSIG+	Stauffer [2014]
$Ar(1s_5) + e^- \leftrightarrow Ar(2p_{10}) + e^-$	BOLSIG+	Stauffer [2014]
$Ar(1s_5) + e^- \leftrightarrow Ar(2p_9) + e^-$	BOLSIG+	Stauffer [2014]
$Ar(1s_5) + e^- \leftrightarrow Ar(2p_8) + e^-$	BOLSIG+	Stauffer [2014]
$Ar(1s_5) + e^- \leftrightarrow Ar(h.l.) + e^-$	BOLSIG+	Biagi [2011][c]
$He + e^- \rightarrow He^+ + e^- + e^-$	BOLSIG+	Phelps [2008], Rapp and Englander-Golden [1965]
$He + e^- \leftrightarrow He^* + e^-$	BOLSIG+	Phelps [2008], Maier-Leibnitz [1935]
$He^* + e^- \rightarrow He^+ + e^- + e^-$	BOLSIG+	Phelps [2008], Maier-Leibnitz [1935]
$Ar_2^* + e^- \rightarrow Ar_2^+ + e^- + e^-$	BOLSIG+	McCann et al. [1979]
$Ar_2^* + e^- \rightarrow Ar + Ar + e^-$	BOLSIG+	Gregório et al. [2012]
$Ar_2^* + e^- \rightarrow Ar(1s_5) + Ar + e^-$	$1.00 \times 10^{-8} \exp(-1.00/T_e)$	Neeser et al. [1997]

Reaction	Rate Coefficient $\left[\frac{1}{s},\ \frac{cm^3}{s},\ or\ \frac{cm^6}{s}\right]$	Reference
$Ar_2^+ + e^- \rightarrow Ar^+ + Ar + e^-$	$1.36 \times 10^{-6} \exp(-2.09/T_e)$	Bultel et al. [2002]
$He_2^* + e^- \rightarrow He_2^+ + e^- + e^-$	$9.75 \times 10^{-10} T_e^{0.71} \exp(-3.40/T_e)$	Rauf and Kushner [1999]
$He_2^* + e^- \rightarrow He + He + e^-$	3.80×10^{-9}	Deloche et al. [1976]
$He_2^+ + e^- \rightarrow He^+ + He + e^-$	$1.06 \times 10^{-7} T_e^{-3} \exp(-9.97/T_e)$	Jonkers et al. [2003]
Recombination		
$Ar^+ + e^- + e^- \rightarrow Ar(h.l.) + e^-$	$7.20 \times 10^{-27} T_e^{-4.5}$	Shon and Kushner [1994]
$Ar^+ + e^- + M \rightarrow Ar(h.l.) + M$	$1.10 \times 10^{-30} T_e^{-2.5}$	Bekefi [1976]
$He^+ + e^- + e^- \rightarrow He^* + e^-$	$5.10 \times 10^{-27} T_e^{-4.5}$	Bekefi [1976]
$He^+ + e^- + M \rightarrow He^* + M$	$1.10 \times 10^{-30} T_e^{-2.5}$	Bekefi [1976]
$He_2^+ + e^- \rightarrow He^* + He$	$5.00 \times 10^{-9} T_e^{-0.5}$	Shon and Kushner [1994]
$Ar_2^+ + e^- \rightarrow Ar(h.l.) + Ar$	$7.34 \times 10^{-8} T_e^{-0.67}$	Mehr and Biondi [1968]
$HeAr^+ + e^- \rightarrow Ar(h.l.) + He$	$7.34 \times 10^{-9} T_e^{-0.67}$	Shon and Kushner [1994][e]
Two-Heavy-Body		
$Ar(1s_5) + Ar \rightarrow Ar + Ar$	2.30×10^{-15}	Tachibana [1986]
$Ar(1s_5) + He \rightarrow Ar + He$	1.60×10^{-14}	Han and Heaven [2016]
$Ar(1s_5) + Ar \leftrightarrow Ar(1s_4) + Ar$	2.10×10^{-15}	Demyanov et al. [2013]
$Ar(1s_4) + He \leftrightarrow Ar(1s_5) + He$	1.00×10^{-13}	Han and Heaven [2014][f]
$Ar(2p_{10}) + Ar \leftrightarrow Ar(1s) + Ar$	$1.50 \times 10^{-11} \sqrt{T_{gas}/300}$	Zhu and Pu [2010][g]
$Ar(2p_{10}) + He \leftrightarrow Ar(1s) + He$	$0.50 \times 10^{-13} \sqrt{T_{gas}/300}$	Han and Heaven [2014][g,h]
$Ar(2p_9) + Ar \leftrightarrow Ar(1s) + Ar$	$3.00 \times 10^{-11} \sqrt{T_{gas}/300}$	Zhu and Pu [2010][g]
$Ar(2p_9) + He \leftrightarrow Ar(1s) + He$	$0.20 \times 10^{-11} \sqrt{T_{gas}/300}$	Han and Heaven [2014][g,h]
$Ar(2p_8) + Ar \leftrightarrow Ar(1s) + Ar$	$4.00 \times 10^{-11} \sqrt{T_{gas}/300}$	Zhu and Pu [2010][g]
$Ar(2p_8) + He \leftrightarrow Ar(1s) + He$	$0.10 \times 10^{-11} \sqrt{T_{gas}/300}$	Han and Heaven [2014][g,h]
$Ar(2p_8) + Ar \leftrightarrow Ar(2p_9) + Ar$	1.10×10^{-11}	Han and Heaven [2014]
$Ar(2p_8) + He \leftrightarrow Ar(2p_9) + He$	4.50×10^{-11}	Han and Heaven [2014]
$Ar(2p_8) + Ar \leftrightarrow Ar(2p_{10}) + Ar$	1.10×10^{-11}	Han and Heaven [2014]
$Ar(2p_8) + He \leftrightarrow Ar(2p_{10}) + He$	0.40×10^{-11}	Han and Heaven [2014]
$Ar(2p_9) + Ar \leftrightarrow Ar(2p_{10}) + Ar$	2.60×10^{-11}	Han and Heaven [2014]
$Ar(2p_9) + He \leftrightarrow Ar(2p_{10}) + He$	1.60×10^{-11}	Han and Heaven [2014]
$Ar(h.l.) + M \leftrightarrow Ar(2p) + M$	1.00×10^{-11}	Shon and Kushner [1994][g,i]
$He^* + He^* \rightarrow He^+ + He + e^-$	1.50×10^{-9}	Emmert et al. [1988]
$Ar(1s) + Ar(1s) \rightarrow Ar^+ + Ar + e^-$	$5.00 \times 10^{-10} \sqrt{T_{gas}/300}$	Zhu and Pu [2010]
$Ar(1s) + Ar(2p) \rightarrow Ar^+ + Ar + e^-$	$5.00 \times 10^{-10} \sqrt{T_{gas}/300}$	Zhu and Pu [2010]
$Ar(2p) + Ar(2p) \rightarrow Ar^+ + Ar + e^-$	$5.00 \times 10^{-10} \sqrt{T_{gas}/300}$	Shon and Kushner [1994][h]
$Ar(h.l.) + Ar(1s) \rightarrow Ar^+ + Ar + e^-$	$7.00 \times 10^{-10} \sqrt{T_{gas}/300}$	Zhu and Pu [2010]
$Ar_2^+ + M \rightarrow Ar^+ + Ar + M$	$6.10 \times 10^{-6} T_{gas}^{-1} \exp(-15,130/T_{gas})$	Jonkers et al. [2003][i]
$He_2^+ + M \rightarrow He^+ + He + M$	$1.40 \times 10^{-6} T_{gas}^{-0.67} \exp(-28,090/T_{gas})$	Jonkers et al. [2003][i]
$HeAr^+ + Ar \rightarrow Ar^+ + He + Ar$	$2.94 \times 10^{-11} \sqrt{T_{gas}} \exp(-298/T_{gas})$	estimated[j]
$HeAr^+ + He \rightarrow Ar^+ + He + He$	$1.17 \times 10^{-11} \sqrt{T_{gas}} \exp(-298/T_{gas})$	estimated[j]
$Ar_2^* + Ar_2^* \rightarrow Ar_2^+ + Ar + Ar + e^-$	5.00×10^{-10}	Kannari et al. [1985]
$He_2^* + He_2^* \rightarrow He_2^+ + He + He + e^-$	1.50×10^{-9}	Deloche et al. [1976]
$He^+ + Ar \rightarrow He + Ar^+$	1.00×10^{-13}	Johnsen et al. [1973]
$He^* + Ar \rightarrow Ar^+ + He + e^-$	2.20×10^{-11}	Lindinger et al. [1974][k]
$He^* + Ar \rightarrow HeAr^+ + e^-$	4.90×10^{-11}	Lindinger et al. [1974][k]
$He_2^+ + Ar \rightarrow Ar^+ + He + He$	2.20×10^{-10}	Lee et al. [1976]
$He_2^* + Ar \rightarrow Ar^+ + He + He + e^-$	3.10×10^{-10}	Shon [1993]
Three-Heavy-Body		
$Ar^+ + Ar + Ar \rightarrow Ar_2^+ + Ar$	$2.25 \times 10^{-31} (300/T_{gas})^{0.4}$	Jones et al. [1980]
$Ar^+ + Ar + He \rightarrow Ar_2^+ + He$	$1.13 \times 10^{-31} (300/T_{gas})^{0.4}$	Jones et al. [1980][l]

Reaction	Rate Coefficient $\left[\frac{1}{s},\ \frac{cm^3}{s},\ or\ \frac{cm^6}{s}\right]$	Reference
$He^+ + He + He \rightarrow He_2^+ + He$	$0.83 \times 10^{-31}(300/T_{gas})^{0.6}$	Jones et al. [1980]
$He^+ + He + Ar \rightarrow He_2^+ + Ar$	$1.66 \times 10^{-31}(300/T_{gas})^{0.6}$	Jones et al. [1980][l]
$He^+ + Ar + Ar \rightarrow Ar_2^+ + He$	1.00×10^{-31}	Shon [1993]
$Ar^+ + He + Ar \rightarrow HeAr^+ + Ar$	2.50×10^{-32}	Shon and Kushner [1994]
$Ar^+ + He + He \rightarrow HeAr^+ + He$	1.00×10^{-32}	Shon and Kushner [1994]
$Ar(1s_5) + Ar + Ar \rightarrow Ar_2^* + Ar$	$3.60 \times 10^{-31} T_{gas}^{-0.6}$	Wieme and Lenaerts [1981]
$Ar(1s_5) + Ar + He \rightarrow Ar_2^* + He$	$1.80 \times 10^{-31} T_{gas}^{-0.6}$	Wieme and Lenaerts [1981][l]
$Ar(1s_4) + Ar + Ar \rightarrow Ar_2^* + Ar$	0.95×10^{-32}	Wieme and Lenaerts [1981]
$Ar(1s_4) + Ar + He \rightarrow Ar_2^* + He$	0.48×10^{-32}	Wieme and Lenaerts [1981][l]
$He^* + He + He \rightarrow He_2^* + He$	1.30×10^{-33}	Rauf and Kushner [1999]
$He^* + He + Ar \rightarrow He_2^* + Ar$	2.60×10^{-33}	Rauf and Kushner [1999][l]
Radiative		
$Ar_2^* \rightarrow Ar + Ar$	3.13×10^5	Rolin et al. [2007]
$Ar(2p_8) \rightarrow Ar(1s_4)$	2.20×10^7	Kramida et al. [2015]
$Ar(2p_8) \rightarrow Ar(1s_5)$	9.30×10^6	Kramida et al. [2015]
$Ar(2p_9) \rightarrow Ar(1s_5)$	3.30×10^7	Kramida et al. [2015]
$Ar(2p_{10}) \rightarrow Ar(1s_4)$	5.40×10^6	Kramida et al. [2015]
$Ar(2p_{10}) \rightarrow Ar(1s_5)$	1.90×10^7	Kramida et al. [2015]
$Ar(1s_4) \rightarrow Ar$	1.20×10^8	Kramida et al. [2015][m]
$Ar(h.l.) \rightarrow Ar$	1.00×10^8	Zhu and Pu [2010]
$Ar(h.l.) \rightarrow Ar(2p_{10})$	3.00×10^6	Zhu and Pu [2010]
$Ar(h.l.) \rightarrow Ar(2p_9)$	4.00×10^6	Zhu and Pu [2010]
$Ar(h.l.) \rightarrow Ar(2p_8)$	3.00×10^6	Zhu and Pu [2010]
$Ar(h.l.) \rightarrow Ar(1s_5)$	1.00×10^6	Zhu and Pu [2010][n]
$Ar(h.l.) \rightarrow Ar(1s_4)$	1.00×10^6	Zhu and Pu [2010][n]

[a] Shifted in energy relative to the $Ar(1s_5)$ ionization cross section

[b] The $Ar(3d_{12})$ excitation cross section extracted from PROGRAM MAGBOLTZ is used for $Ar(h.l.)$

[c] Shifted in energy relative to the Ar ground state excitation to $Ar(3d_{12})$ and used for $Ar(h.l.)$

[d] Shifted in energy relative to the $Ar(2p_{10})$ excitation to $Ar(2p_8)$

[e] Following Shon and Kushner [1994], using a value of 1/10 times the dissociative recombination rate for Ar_2^+

[f] Rate coefficient corresponds to room temperature and is larger for temperatures above 300 K [Han and Heaven, 2014]

[g] Assuming equal branching

[h] Assuming $\sqrt{T_{gas}/300}$ temperature dependence following Zhu and Pu [2010]

[i] Assuming rate coefficients for He as the second body are the same as Ar as the second body

[j] Calculated from the forward rate using detailed balance with the $HeAr^+$ parameters provided by Dabrowski et al. [1981]

[k] Branching ratio from Shon [1993]

[l] Assuming three-body rate coefficients with He as the third body are 1/2 the rate coefficient for Ar as the third body

[m] Not including radiation trapping

[n] Assuming equal branching from $Ar(3p)$

Metastable quenching rates due to collisions with neutrals via $Ar(1s_5) + M \rightarrow Ar + M$ play an important role in the decay rates after breakdown. However, these reactions may in part be a proxy for collisions with impurities, allowing the quenching from impurities to be taken into account (see Stefanović et al. [2014] for a discussion on quenching due to impurities). Radiation trapping [Holstein, 1947, 1951] for the

$Ar(1s_4) \rightarrow Ar + \hbar\omega$ transition is taken into account, following the measurements of Han and Heaven [2014] and calculations of Belostotskiy et al. [2011].

With the exception of a few assumptions listed in the footnotes of Table 2 and the $HeAr^+$ neutral dissociation rates, all rate coefficients are taken directly from the literature with no adjustment. Previous kinetic studies of Ar-He discharges have ignored neutral dissociation of $HeAr^+$ and no rate coefficients could be found in the literature. However, due to the low binding energy of approximately 298 K [Dabrowski et al., 1981], neutral dissociation rates should not be ignored, and the rate coefficients have been estimated and included as a part of this analysis.

To estimate the $HeAr^+ + M \rightarrow Ar^+ + He + M$ neutral dissociation rate coefficients, detailed balance is applied to the three-body rate coefficients (k_{3-body} associated with $Ar^+ + He + M \rightarrow HeAr^+ + M$). Following the outline in Smirnov [1981], the steady-state ratio of densities follows

$$\frac{k_{diss}}{k_{3-body}} = \frac{[Ar^+]\,[He]}{[HeAr^+]} = \frac{g_{Ar^+} g_{He}}{g_{HeAr^+}} \left(\frac{\mu k_b T_{gas}}{2\pi\hbar^2}\right)^{3/2} \exp\left(-D/k_b T_{gas}\right), \tag{1}$$

where k_{diss} is the rate coefficient for $HeAr^+$ dissociation, g_{Ar^+} and g_{He} stand for the statistical weights associated with the number of electronic states (assumed to be 2 to account for electron spin degeneracy), g_{HeAr^+} is the mean number of states for the $HeAr^+$ ion, μ is the reduced mass of Ar^+ and He, k_b is the Boltzmann constant, T_{gas} is the neutral gas temperature, $\hbar$ is the reduced Planck constant, and D is the dissociation energy of $HeAr^+$. The dissociation energy is approximately 298 K, which is nearly equal to the room gas temperature [Dabrowski et al., 1981].

To determine g_{HeAr^+}, the average number of rotational and vibration states must be calculated:

$$g_{HeAr^+} = g_e g_{vib} g_{rot}, \tag{2}$$

where $g_e = 2$ is the statistical weight due to the electronic state, g_{vib} is the mean number of vibrational states occupied, and g_{rot} provides the mean number of rotational states occupied. The mean number of occupied vibrational states can be estimated by

$$g_{vib} \approx \sum_n \exp\left(-\epsilon_n / k_b T_{gas}\right) = 1 + \exp\left(-\epsilon_2 / k_b T_{gas}\right) + \exp\left(-\epsilon_3 / k_b T_{gas}\right), \qquad (3)$$

where the lowest vibrational energy state, ϵ_1, is set to zero, and the two additional bounded vibrational states of $HeAr^+$, $\epsilon_2 = 92.9$ cm^{-1} and $\epsilon_3 = 159.1$ cm^{-1}, are the energies relative to ϵ_1 [Dabrowski et al., 1981]. For a gas temperature of 300 K, $g_{vib} \approx 2.11$.

The average rotational occupancy number is calculated by

$$g_{rot} = \int_0^\infty (2J+1) \exp\left(\frac{-BJ\left(J+1\right)}{k_b T_{gas}}\right) = \frac{k_b T_{gas}}{B}, \qquad (4)$$

where J is the rotational quantum number, and $B = 0.6592$ cm^{-1} is the measured rotational constant [Dabrowski et al., 1981].

Using a temperature of 300 K for the mean vibrational occupancy number, the dissociation rate coefficient from Equation 1 provides

$$k_{diss} \approx k_{3-body} \frac{2B}{2.11 k_b T_{gas}} \left(\frac{\mu k_b T_{gas}}{2\pi\hbar^2}\right)^{3/2} \exp\left(-D / k_b T_{gas}\right). \qquad (5)$$

The three-body rate coefficient for $M = Ar$ is 2.50×10^{-32} cm^6/s [Shon and Kushner, 1994], which provides the dissociation rate coefficient of

$$k_{HeAr^+ + Ar \rightarrow Ar^+ + He + Ar} \approx 2.94 \times 10^{-11} \sqrt{T_{gas}} \exp\left(-298 / T_{gas}\right) \text{ cm}^3/\text{s}. \qquad (6)$$

Similarly, for $M = He$, which has a three-body rate coefficient of 1.00×10^{-32} cm^6/s [Shon and Kushner, 1994], the dissociation rate coefficient is

$$k_{HeAr^+ + He \rightarrow Ar^+ + He + He} \approx 1.17 \times 10^{-11} \sqrt{T_{gas}} \exp\left(-298/T_{gas}\right) \text{ cm}^3/\text{s}. \tag{7}$$

Due to the fact that the $HeAr^+$ dissociation energy is approximately equal to the room temperature, the neutral dissociation rates of $HeAr^+$ at room temperature are large. While the three-body formation rates of $HeAr^+$ are elevated at high pressures, the large dissociation rates rapidly convert $HeAr^+$ back to Ar^+, effectively removing $HeAr^+$ from the bulk plasma.

Ambipolar Diffusion.

Ambipolar diffusion may be an important loss mechanism for gas discharges, providing an electron loss pathway which is dependent on cavity size, pressure, and electron temperature. As a result of the difference in electron and ion mobility and diffusion, a space charge is developed pulling the faster electrons back towards the ions and forcing the ions to catch up to the electrons. This effect causes the electrons and ions to diffuse at a combined, ambipolar rate. Following Raizer [1997], the ambipolar diffusion coefficient, D_a, can be approximated by

$$D_a \approx \mu_+ T_e, \tag{8}$$

where μ_+ is the ion mobility and T_e is the electron temperature in eV.

Ion mobility is inversely proportional to the gas density, and can approximated by a constant divided by the gas density, μ_0/N. In a mixture of Ar and He, the ion mobility will depend on the fractional composition due to the difference in mobility between a background He gas compared to an Ar gas. The mobility of Ar^+ in a

mixture of He and Ar can be approximated using Blanc's Law [Blanc, 1908; Biondi and Chanin, 1961]:

$$\frac{1}{\mu_+} = \frac{1}{\mu_{He}} + \frac{1}{\mu_{Ar}}, \tag{9}$$
$$= \frac{N_{He}}{\mu_{0,He}} + \frac{N_{Ar}}{\mu_{0,Ar}},$$
$$\implies \mu_+ = \frac{\mu_{0,Ar}\mu_{0,He}}{\mu_{0,He}N_{Ar} + \mu_{0,Ar}N_{He}}, \tag{10}$$

where $\mu_{He} = \mu_{0,He}/N_{He}$ is the mobility of Ar^+ in He, $\mu_{Ar} = \mu_{0,Ar}/N_{Ar}$ is the mobility of Ar^+ in Ar, and μ_+ is the mobility of Ar^+ in a mixture of He and Ar. Ion mobilities in He are larger than in Ar due to a difference in momentum transfer cross section and mass, as displayed by the values of μ_0 in Table 3. Following measurements by Lindinger and Albritton [1975], the mobilities of Ar_2^+ and $HeAr^+$ are assumed to be equal to the mobility of Ar^+ in He. As a result of the relatively low densities of He^+ and He_2^+ in an Ar-He gas discharge, the change in He ion mobilities with respect to gas mixture are ignored. This representation of the ion mobility allows the ambipolar diffusion coefficient to be a function of the partial pressures of He and Ar.

Table 3. A list of ion mobilities with Ar or He as the background gas.

Ion	μ_0 [$\mathrm{cm^2/V \cdot s}$]	**Source**
Ar^+ in Ar	1.54	Madson and Oskam [1967]
Ar^+ in He	20.5	Lindinger and Albritton [1975]
Ar_2^+ in Ar	1.83	Madson and Oskam [1967]
Ar_2^+ in He	20.5	Assuming equal to Ar^+ in He
He^+ in He	10.7	Oskam and Mittelstadt [1963]
He_2^+ in He	16.2	Oskam and Mittelstadt [1963]
$HeAr^+$ in Ar	1.54	Assuming equal to Ar^+ in Ar
$HeAr^+$ in He	20.5	Assuming equal to Ar^+ in He

The ion mobilities listed in Table 3 are used for the zero-dimensional simulations

where the electric field is assumed to be uniform. An alternative form of ion mobilities used in the one-dimensional simulations is provided by Ward [1962], which includes the E/p dependence, where p is the gas pressure. For Ar^+, the ion mobility follows

$$p\mu_{Ar^+}\left[\text{Torr}\cdot\text{cm}^2/\text{V}\cdot\text{s}\right] = \begin{cases} 10^3\left(1-2.22\times10^{-3}E/p\right), & \text{if } E/p \le 60\,[\text{V/Torr}\cdot\text{cm}] \\ \dfrac{8.25\times10^3}{\sqrt{E/p}}\left(1-\dfrac{86.52}{(E/p)^{3/2}}\right), & \text{if } E/p > 60\,[\text{V/Torr}\cdot\text{cm}]\,. \end{cases} \tag{11}$$

Similarly, the He^+ mobility as a function of E/p is described by

$$p\mu_{He^+}\left[\text{Torr}\cdot\text{cm}^2/\text{V}\cdot\text{s}\right] = \begin{cases} 8\times10^3\left(1-8.0\times10^{-3}E/p\right), & \text{if } E/p \le 25\,[\text{V/Torr}\cdot\text{cm}] \\ \dfrac{4.1\times10^4}{\sqrt{E/p}}\left(1-\dfrac{27.44}{(E/p)^{3/2}}\right), & \text{if } E/p > 25\,[\text{V/Torr}\cdot\text{cm}]\,. \end{cases} \tag{12}$$

As the mobility is inversely proportional to the gas density, N, a temperature factor can be added to the pressure to account for a change in gas temperature. This factor replaces the pressure in Equations 11 and 12 with $p \to p \times (300/T_{gas})$, and assumes that the measurements of Ward [1962] were taken at 300 K.

The electron lifetime, τ_{diff}, due to ambipolar diffusion losses follows

$$\tau_{diff} = \frac{\Lambda^2}{D_a}, \tag{13}$$

where Λ is the characteristic length of the cavity. Characteristic lengths are found by solving the eigenvalue equation for the electron density, n_e, assuming a homogeneous ionization rate and boundary condition of $n_e = 0$ at the cavity walls:

$$D_a\nabla^2 n_e = -\nu_i n_e, \tag{14}$$

where ν_i is the ionization rate [Raizer, 1997]. In steady-state, the electron density

remains constant, forcing the electron loss and production rates to be equal. If recombination is ignored, then the loss rate due to wall diffusion must be equal to the ionization rate. The solution for a cylindrical cavity with length L and radius R is

$$n_e = n_0 \, J_0 \left(\frac{2.4\, r}{R} \right) \cos \left(\frac{\pi z}{L} \right), \tag{15}$$

where n_0 is the electron density at the cavity center. Substituting the solution into Equation 14 provides

$$D_a \left[\left(\frac{2.4}{R} \right)^2 + \left(\frac{\pi}{L} \right)^2 \right] n_e = D_a \left(\frac{1}{\Lambda} \right)^2 n_e = \nu_i n_e, \tag{16}$$

where the terms including the cavity dimensions are combined to calculate a characteristic length, Λ [Raizer, 1997].

The ambipolar diffusion loss rate, R_{D_a}, is given by

$$R_{D_a} = D_a \nabla^2 n_e = -\frac{D_a}{\Lambda^2} n_e, \tag{17}$$

which is equal to the electron density divided by the electron lifetime due to ambipolar diffusion.

The importance of ambipolar diffusion on a gas discharge will depend on the cavity geometry, pressure, and the magnitude of other electron loss mechanisms such as recombination. Diffusion losses can be ignored for large cavities at atmospheric pressures. However, at pressures near 100 Torr and characteristic cavity lengths on the scale of millimeters, ambipolar diffusion plays a key kinetic role (as discussed later in this document).

Reduced Electric Field.

In a gas discharge, electrons gain energy from an applied electric field. The application of a DC electric field will deposit energy into the plasma via Joule heating:

$$P_d = \mathbf{j} \cdot \mathbf{E} = \sigma E^2 = n_e q_e \mu_e E^2, \tag{18}$$

where P_d is the deposited power density, $\mathbf{j}$ is the current density, $\mathbf{E}$ is the electric field, $\sigma = n_e q_e \mu_e$ is the conductivity, and q_e is the electron charge [Cherrington, 2014]. Electron mobility, μ_e, is given by

$$\mu_e = \frac{q_e}{m_e \nu_m}, \tag{19}$$

where m_e is the electron mass, and ν_m is the collision frequency of electrons with neutral atoms. Rewriting the deposited power density in terms of the collision frequency yields

$$P_d = \frac{n_e q_e^2}{m_e \nu_m} E^2. \tag{20}$$

Elastic collisions between electrons and neutrals impart the fractional energy $\delta_\epsilon = 2m_e/M$ from the electrons to the neutrals with mass M. A typical gas discharge is characterized by a non-equilibrium state where, on average, electrons possess much more energy than neutrals. Assuming a Maxwellian distribution, the average electron energy, $\langle \epsilon \rangle$, follows

$$\langle \epsilon \rangle = \frac{3}{2} k_b T_e. \tag{21}$$

Combining this fractional energy loss with the collision frequency, the elastic power loss per unit volume becomes

$$P_{loss} = n_e \, \nu_m \, \delta_\epsilon \, \frac{3}{2} k_b (T_e - T), \tag{22}$$

where $T_e - T$ is the difference between the electron temperature and the neutral gas temperature [Cherrington, 2014].

Combining the power lost and deposited, the change in electron energy density over time becomes

$$\begin{aligned} \frac{d}{dt}\left(\frac{3}{2}n_e k_b T_e\right) &= P_d - P_{loss} \\ &= \frac{n_e q_e^2}{m_e \nu_m} E^2 - n_e\, \nu_m\, \delta_\epsilon\, \frac{3}{2} k_b (T_e - T). \end{aligned} \tag{23}$$

At steady-state, the energy does not change over time, and the electron temperature can be described by

$$T_e = T + \frac{2\, q_e^2\, E^2}{3\, \delta_\epsilon\, k_b\, m_e\, \nu_m^2}. \tag{24}$$

The collision frequency is a function of the neutral gas density:

$$\nu_m = \sigma_m v_r N \tag{25}$$

where σ_m is the momentum transfer cross section between neutrals and electrons, v_r is the relative velocity between electrons and neutrals, and N is the neutral gas density. This shows that the electron temperature is a function of the electric field divided by the neutral gas density, known as the reduced electric field, E/N:

$$T_e\left(\frac{E}{N}\right) = T + \frac{2\, e^2}{3\, \delta_\epsilon\, k_b\, m_e\, \sigma_m^2\, v_r^2}\left(\frac{E}{N}\right)^2. \tag{26}$$

Rate coefficients for electron impact reactions are functions of E/N, and hence T_e. As a result, E/N will be the most important driver of the reaction rates throughout this analysis.

Similarity Parameters.

Discharges are said to be similar if they maintain equal voltages and temperatures at equal currents for discharges in the same gas and electrode material [Von Engel, 1965]. While the geometry of the two discharges may be different, a counterbalance scaling of the gas density (pressure) allows for certain parameters, known as similarity parameters, to be maintained. Following Von Engel [1965] and Mesyats [2006], a change in discharge gap lengths of $d_1 = \xi d_2$ and electrode radii of $r_1 = \xi r_2$ provides the similarity parameters listed in Table 4.

Table 4. A list of similarity parameters for a change in discharge gap lengths of $d_1 = \xi d_2$ and electrode radii of $r_1 = \xi r_2$ [Von Engel, 1965; Mesyats, 2006].

Similarity Parameter	Scaling
Voltage	$V_1 = V_2$
Current	$i_1 = i_2$
Temperature	$T_1 = T_2$
Electrode Surface Area	$S_1 = \xi^2 S_2$
Volume	$\mathrm{Vol}_1 = \xi^3 \mathrm{Vol}_2$
Mean Free Path	$\lambda_1 = \xi \lambda_2$
Gas Density	$N_1 = N_2/\xi$
Gas Pressure	$p_1 = p_2/\xi$
Pressure-Distance Product	$p_1 d_1 = p_2 d_2$
Electric Field	$E_1 = E_2/\xi$
Drift Velocity	$\lambda_1 E_1 = \lambda_2 E_2$
Reduced Electric Field	$E_1/N_1 = E_2/N_2$
Surface Charge Density	$q_1 = q_2/\xi$
Space Charge Density	$\rho_1 = \rho_2/\xi^2$
Current Density	$j_1 = j_2/\xi^2$
Collision Frequency	$\nu_1 = \nu_2/\xi$

Processes maintaining the similarity parameter scaling are allowed, while forbidden processes do not maintain the proper scaling factor (see Mesyats [2006] for a more detailed explanation). Allowed processes include: *ionization at single collisions, electron attachment and detachment, drift and diffusion, secondary processes at the electrodes, charge exchange, recombination at high pressure,* and *penning ioniza-*

tion. Forbidden processes include: *stepwise ionization, photoionization, low pressure recombination, thermal ionization, photoelectric emission, thermionic emission* and *field emission* [Von Engel, 1965; Mesyats, 2006].

Similarity parameters can be used to understand the mechanisms responsible for discharge properties and to allow for scaling due to changes in a parameter while other parameters are held constant. Manifestations of similarity parameters are found in the normal parameters (Equations 29 to 31), where V_C, $(pd)_n$, and j_n/p^2 are constant in a normal glow discharge. To maintain the normal parameters, the sheath thickness follows $d \propto 1/p$ while the normal current density follows $j_n \propto p^2$. This type of relationship allows for scaling due to changes in pressure, and is important in this analysis where pressure is varied in an attempt to maximize metastable density.

While similarity parameters are useful, care must be taken due to the forbidden processes. For example, in a discharge where stepwise ionization is important, the similarity parameters will not hold and should not be used for scaling.

2.2 Challenges at High Pressures

The use of gas discharges in laser development has been widely studied and implemented (see Garscadden et al. [1991] for a detailed summary). Operation of gas discharges at high pressures creates unique challenges due to non-uniform power deposition and discharge instabilities. Excimer lasers, which operate at atmospheric pressures, are often limited by non-uniformity and instability rather than kinetic considerations [Garscadden et al., 1991]. Non-uniformities in gas mixture, electric field, or gas density can initiate an instability which terminates laser operation. Similar to the excimer lasers, OPRGLs operating at high pressure are prone to non-uniformities and instabilities inherent to high pressure gas discharges.

Thermal instabilities are the "most dangerous and wide-spread instability in gas

lasers" [Raizer, 1997]. Other types of instabilities are possible and well documented (see Haas [1973] and Raizer [1997] for more detail), but the discharge characteristics of this analysis are mostly prone to thermal instabilities as a result of the near-atmospheric pressure requirement of an OPRGL system.

Due to an increase in normal current density as pressure is increased, near-atmospheric pressure discharges are particularly prone to thermal instabilities. As the gas temperature is increased via Joule heating ($\mathbf{j} \cdot \mathbf{E}$), the local gas density is decreased. This decrease in gas density increases the local E/N, which in turn elevates the ionization frequency. The elevated ionization frequency creates additional current which heats the local gas even further, rendering the discharge unstable. This instability causes the discharge to contract, transitioning to a filamentary mode [Fridman et al., 2005].

At high pressures, efforts must be taken to reduce the potential of thermal instabilities. One known method is to use pulsed DC discharges, where the down-time between pulses allows for thermal dissipation, increasing the overall stability [Raizer, 1997]. Additionally, due to a reduction in electron temperature in between pulses, the average densities of a pulsed system are greater than a steady-state DC discharge [Lieberman and Lichtenberg, 2005], which is beneficial to maximizing metastable densities in an OPRGL.

A related technique employs a high frequency oscillating voltage, such as in a capacitively coupled plasma (CCP). RF-CCPs are able to maintain stability at high pressures due to a limited ionization period occurring near the cycle peaks and an increased energy threshold for instability formation [Raizer et al., 1995]. Instabilities occur during periods of ionization, and the limited ionization period of RF-CCPs reduces the likelihood of instability formation. The placement of a dielectric barrier across one or both of the electrodes reduces the conduction current magnitude, which

further increases stability [Fridman et al., 2005].

2.3 High Pressure Gas Discharges

This section will introduce the two types of discharges analyzed in this document: pulsed direct current glow discharge and radio frequency capacitively coupled plasma. As a result of the near-atmospheric pressure requirements of an OPRGL, the variety of stable discharges is limited. While there are other forms of discharges capable of maintaining stability at high pressures (for example: microhollow cathode discharges and microwave resonator-driven microplasmas), this analysis will focus on pulsed direct current discharges and radio frequency capacitively coupled plasmas.

Pulsed Direct Current Glow Discharge.

Direct current (DC) glow discharges have a structure of light emission based on electron/ion density and energy (Figure 3). Following Raizer [1997], the qualitative description of the light emission pattern, working left to right, follows: Electrons emitted from the cathode due to secondary emission typically have low energies, which cannot excite or ionize neutral atoms. Maximum secondary electron energies follow

$$\epsilon_{max} = \epsilon_{ion} - 2\epsilon_{\phi}, \tag{27}$$

where ϵ_{max} is the maximum energy of a secondary electron, ϵ_{ion} is the ionization energy of the ion colliding with the surface, and ϵ_{ϕ} is the work function of the surface [Lieberman and Lichtenberg, 2005]. For an Ar ion (15.76 eV) and a typical work function of 5 eV, the maximum energy of a secondary electron is 5.76 eV, which is too low to excite or ionize ground state Ar.

This region near the cathode is known as the *Aston dark space*. Acceleration of the electrons into the *cathode glow* region increase the electron energy to the point where

excitation (and hence light emission) can occur. The electrons continue to accelerate, until they reach energies above the ionization threshold, forming the *cathode dark space*, where the majority of electron impact ionization occurs.

By the end of the cathode layer, the electron flux is large and the electric field becomes relatively small. The electrons have enough energy to excite atoms, and electron densities are high, forming the *negative glow*. Due to the electron energy loss from electron impact excitation in the negative glow, the adjacent region, called the *Faraday dark space*, contains low energy electrons with infrequent excitation. The longitudinal electric field gradually increases in the Faraday dark space, giving rise to the *positive column*. Inside the positive column, the average electron energy is between 1-2 eV, but some energetic electrons are present as well. The energetic electrons excite atoms, creating the light emission associated with the positive column. The length of the positive column depends on the length of the tube, with the positive column growing as the length of the tube increases. This electrically neutral, weakly ionized plasma forms the lasing medium of many lasers [Raizer, 1997].

The behavior of the positive column can be described through a balance of electron production and loss. Without electron attachment, the steady-state electron production and loss rates follow

$$D_a \nabla^2 n_e + \nu_i \left(E/N\right) n_e - \beta n_e^2 = 0, \tag{28}$$

where β is the recombination coefficient [Raizer, 1997]. The ionization frequency's dependence on the reduced electric field controls the behavior of the bulk plasma by adjusting the electron density and electric field until a steady-state is reached.

Near the anode, ions are repelled and electrons attracted, forming an overall negative space charge. The electric field produced by the change in charge density near the anode increases electron energies producing the *anode glow*.

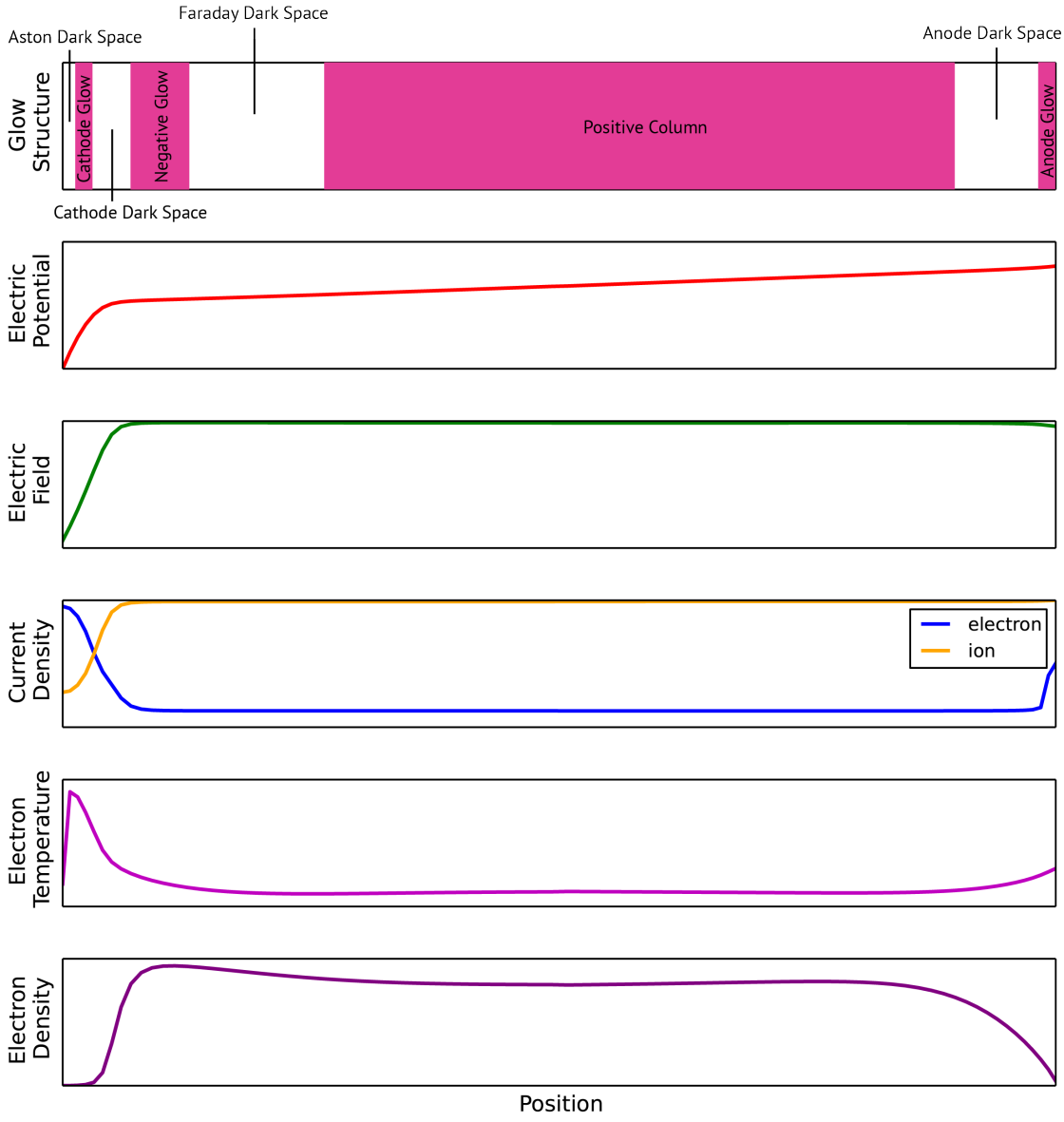

Figure 3. Simulated structure of a DC glow discharge using a one-dimensional fluid model along with a qualitative description of the glow structure [Raizer, 1997]. The cathode is on the left and the anode is on the right.

An elevated concentration of ions and diminished concentration of electrons near the cathode sheath in a glow discharge produces a large voltage drop named *cathode fall*. The cathode fall in a normal glow discharge is characterized by the minimum breakdown voltage in the Paschen curve, V_{min}, taking place over the corresponding pressure-distance product, $(pd)_{min}$, in the sheath near the cathode (Figure 4). This spatial constraint of the breakdown voltage over a short distance sustains the plasma with a relatively small voltage compared to the voltage that would be required if the voltage drop occurred over the entire length of the cavity. Secondary electrons emitted from the cathode provide the seed electrons which are multiplied in the cathode layer, sustaining the glow discharge with a relatively low voltage.

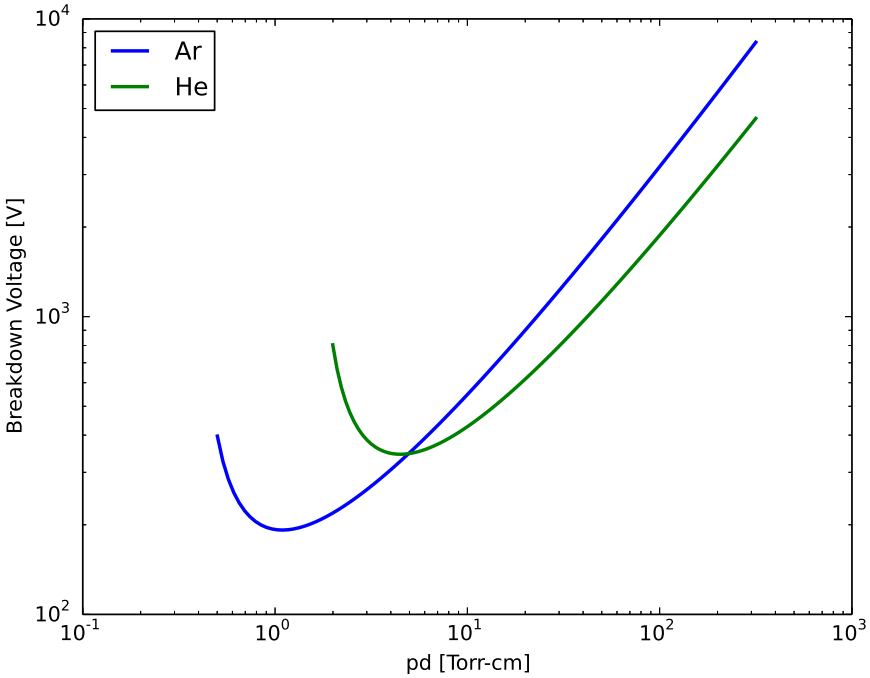

Figure 4. Simulated Paschen curves (breakdown potentials) for He and Ar, using a secondary emission coefficient of 0.01.

The normal parameters (minimum values obtained for a normal discharge) follow

$$V_n = \frac{eB}{A} \ln\left(\frac{1}{\gamma} + 1\right), \tag{29}$$

$$\frac{j_n}{p^2} = \frac{(1+\gamma)4\mu_+\epsilon_0 p V_n^2}{(pd)_n^3}, \tag{30}$$

$$(pd)_n = \frac{e}{A} \ln\left(\frac{1}{\gamma} + 1\right), \tag{31}$$

where V_n is the normal cathode fall, j_n is the normal current density, $(pd)_n$ is the normal thickness-pressure product, $e = 2.718\ldots$, A and B are the Townsend ionization constants, γ is the secondary emission coefficient, μ_+ is the ion mobility, and ϵ_0 is the permittivity of free space [Raizer, 1997]. The factor of 4 in the numerator of Equation 30 is obtained from a linear field distribution in the sheath [Lieberman and Lichtenberg, 2005], where

$$V_n = \int_0^d E_n \left(1 - \frac{x}{d}\right) dx = \frac{E_n\, d}{2}, \tag{32}$$

$$\implies E_n = \frac{2V_n}{d}, \tag{33}$$

and E_n is the electric field in the cathode sheath. Combining the relationship above with the expression for the cathode current found in Raizer [1997], the following relationship is obtained:

$$j_n \approx (1+\gamma)\mu_+\epsilon_0 \frac{E_n^2}{d} \approx (1+\gamma)4\mu_+\epsilon_0 \frac{V_n^2}{d^3}. \tag{34}$$

For argon, $A = 11.5$ 1/cm·Torr and $B = 176.0$ V/cm·Torr [Lieberman and Lichtenberg, 2005]. A secondary emission coefficient of $\gamma = 0.1$ provides a normal cathode fall of $V_n \approx 100$ V, while a secondary emission coefficient of $\gamma = 0.01$ provides a cathode fall of $V_n \approx 190$ V.

Radio Frequency Capacitively Coupled Plasma.

The second type of discharge analyzed in this document is the radio frequency capacitively coupled plasma (RF-CCP), which uses voltages oscillating at radio frequencies to produce a plasma. Due to the time varying potential, dielectrics can be placed over the electrodes while maintaining current flow due to the displacement current. This dielectric barrier discharge (DBD) allows for stable plasma formation at high pressures.

A simple one-dimensional model for an RF-CCP, as described by Raizer [1997], follows

$$\frac{\partial \rho}{\partial t} = -\frac{\partial j_c}{\partial x}, \tag{35}$$

$$\frac{\partial E}{\partial x} = \frac{\rho}{\epsilon_0}, \tag{36}$$

$$j_c = \sigma_e E, \tag{37}$$

$$j_c + \epsilon_0 \frac{\partial E}{\partial t} = j_c + j_{dis} = j\left(t\right), \tag{38}$$

where ρ is the space charge density, j_c is the conduction current density, j_{dis} is the displacement current density, and $j\left(t\right)$ is the total current density, which is independent of position. In the case of an insulated electrode (dielectric barrier) circuit, the equivalent circuit can be thought of as a capacitance of dielectrics, C_d, in series with a parallel plasma resistance, R, and capacitance, C.

As a conduction current is produced in the plasma, charge is carried and attached to the dielectric surface (Figure 5). This collection of charge on the surface effectively reduces the applied voltage from the electrodes. For a *surface charge density*, q, on

the electrode and q_c on the dielectric surface, the electric fields follow

$$E_d = \frac{q}{\epsilon_d}, \tag{39}$$

$$\epsilon_0 E - \epsilon_d E_d = -q_c, \tag{40}$$

where ϵ_d is the dielectric permittivity, E_d is the electric field in the dielectric, and E is the electric field in the plasma. The time rate of change of the surface charges depend on the current:

$$\dot{q}_c = j_c, \tag{41}$$

$$\dot{q} = \frac{i}{S} = j, \tag{42}$$

where i is the current into the electrodes and S is the electrode area.

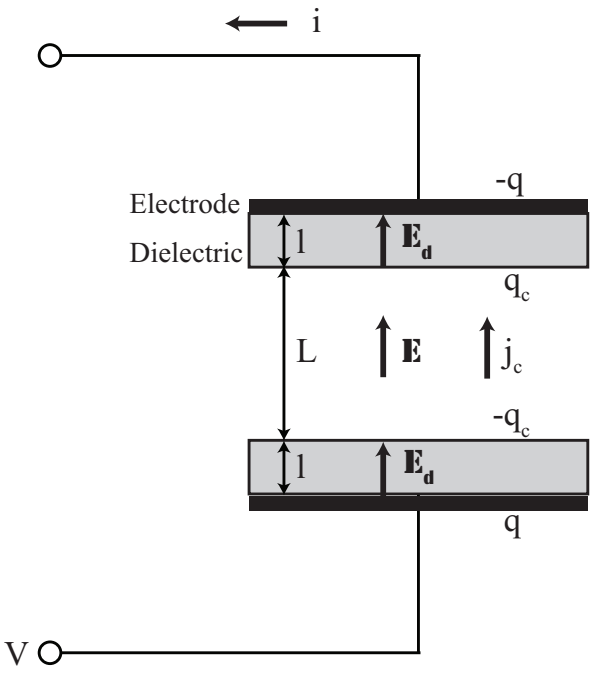

Figure 5. A cross section of the discharge chamber in an insulated electrode (dielectric barrier) RF-CCP [Raizer, 1997].

Ignoring the voltage drops across the sheaths, the total voltage drop across the

electrodes becomes

$$V = 2E_d l + EL, \tag{43}$$

where l is the length of the dielectric, and L is the distance between the dielectrics. Converting the fields to surface charge densities, the voltage and currents become

$$V = \frac{2l}{\epsilon_d} q + \frac{j_c L}{\sigma_e}, \tag{44}$$

$$j_c = \frac{\sigma_e}{\epsilon_0} (q - q_c) . \tag{45}$$

Rewriting the expressions again, using charges $Q = qS$ and $Q_c = q_c S$ along with current $i_c = j_c S$, the more familiar forms of the voltage and currents appear:

$$V = \frac{2Q}{C_d} + i_c R, \tag{46}$$

$$V_b = i_c R = \frac{Q - Q_c}{C}, \tag{47}$$

$$\dot{Q}_c = i_c, \tag{48}$$

$$\dot{Q} = i, \tag{49}$$

where $C_d = \epsilon_d S/l$, $C = \epsilon_0 S/L$, $R = L/\sigma_e S$, and V_b is the voltage across the bulk plasma.

For an applied electrode voltage of $V(t) = V_a \sin \omega t$, Equations 46 to 49 can be integrated to obtain the following expression for the voltage across the bulk plasma as a function of time [Raizer, 1997]:

$$V_b = \frac{V_a \sin(\omega t + \phi)}{1 + 2C/C_d} \frac{\omega\tau}{\sqrt{1 + \omega^2\tau^2}}, \tag{50}$$

$$\tau = R (C_d/2 + C) , \tag{51}$$

$$\phi = \arctan(\omega t) . \tag{52}$$

The conductivity follows

$$\sigma_e = \frac{q_e^2 n_e \nu_m}{m_e \left(\omega^2 + \nu_m^2\right)}, \tag{53}$$

where ν_m is the collision frequency of electrons and neutrals and ω is the voltage driving frequency. As the electron density increases, the conductivity increases, which decreases the plasma resistance, R. This decrease in R decreases the voltage across the bulk plasma.

Sheath behavior gives rise to two distinct modes of operation in an RF-CCP: the α and γ-modes. The α-mode corresponds to a low-current, low-voltage mode of operation, where ionization occurs over the plasma as a whole. Similar to the transition to a glow discharge in a DC scenario, the transition from α to γ-mode occurs when the voltage and sheath thickness are sufficient to cause a breakdown in the sheath. Once this breakdown occurs, the plasma is able to produce large currents without a further increase in voltage. Also comparable to the DC glow discharge, secondary electron emission is required to provide the seed electrons necessary for sustaining ionization in the sheaths of a γ-mode.

Including the drop in voltage due to sheath formation, the voltage across the bulk plasma follows

$$V_b^2 = V_{app}^2 - (V_s + V_d)^2, \tag{54}$$

where V_{app} is the applied voltage, V_s is the potential drop in the sheaths, and V_d is the voltage drop due to charge collection at the dielectrics [Raizer et al., 1995]. The voltage drop due to charge collection on the dielectric surface follows

$$V_d = \frac{2\delta j}{\epsilon_d \omega}, \tag{55}$$

where δ is the thickness of the dielectrics, and j is the current density. In an α-mode,

the sheath voltage follows

$$V_s = \frac{d_\alpha j}{\omega \epsilon_0}, \tag{56}$$

where d_α is the sheath thickness. The sheath thickness can be estimated from the amplitude of sheath oscillation, A, by numerically solving

$$A^2 \left[\left(\omega^2 - \omega_p^2 2A/d_e \right)^2 + \omega^2 \nu_m^2 \right] = \left(\frac{q_e V_{app}}{m_e d_e} \right)^2, \tag{57}$$

where ω_p is the plasma frequency, and ν_m is the electron collision frequency [Raizer et al., 1995]. While the sheath thickness varies over time with the applied voltage, the peak thickness can be estimated as $d_\alpha = 2A$ [Raizer et al., 1995]. The effective distance between electrodes, d_e, accounts for the electric field increase due to the dielectric barrier:

$$d_e = d - 2\delta \left(1 - \frac{\epsilon_0}{\epsilon_d} \right), \tag{58}$$

where d is the actual distance between the electrodes.

2.4 Computational Aspects of Gas Discharge Simulations

In this section, the computational aspects of the models used in the analysis are introduced, beginning with a Boltzmann equation solver, BOLSIG+. BOLSIG+ provides the electronic energy distribution function required to calculate electron impact rate coefficients and electron transport parameters in the kinetic and fluid models. The zero-dimensional plasma kinetics model, ZDPlasKin, provides a method for simulating bulk plasma kinetics over time. One-dimensional spatial profiles are calculated using a fluid model, which is appropriate for modeling the bulk plasma of high pressure gas discharges.

Boltzmann Equation Solver.

A Boltzmann equation solver, BOLSIG+, is used to calculate electron energy distribution functions (EEDFs), electron impact rate coefficients, and electron transport parameters for the zero-dimensional kinetic model and the one-dimensional fluid model. EEDFs are calculated from the Boltzmann Equation,

$$\frac{\partial f}{\partial t} + \mathbf{v} \cdot \nabla f - \frac{q_e}{m_e} \mathbf{E} \cdot \nabla_v f = C[f] \tag{59}$$

using a two-term approximation,

$$f(v, \cos\theta, x, t) = f_0(v, x, t) + f_1(v, x, t) \cos\theta \tag{60}$$

where f is the EEDF, $\mathbf{E}$ is the electric field, $C[f]$ is the rate of change of f due to collisions, and θ is the angle between $\mathbf{v}$ and $\mathbf{E}$ [Hagelaar and Pitchford, 2005]. The collision term, $C[f]$, requires electron impact cross sections, which can be found from the LXcat database (http://nl.lxcat.net/). With the two-term approximation, the separation of energy and space/time, and the assumption of either exponential temporal or spatial growth, a convection-diffusion continuity equation in energy space arises for the EEDF. After discretization of the collision terms, this convection-diffusion equation is solved numerically using a finite volume scheme developed by Scharfetter and Gummel [1969].

Rate coefficients for electron impact collisions are calculated from the EEDF by

$$k_i = \sqrt{\frac{2q_e}{m_e}} \int_0^\infty \epsilon \sigma_i(\epsilon) F(\epsilon)\, d\epsilon, \tag{61}$$

where k_i is the rate coefficient for the i^{th} reaction, ϵ is the electron energy, σ_i is the cross section for the i^{th} reaction as a function of energy, and $F(\epsilon)$ is the energy compo-

nent of the EEDF. The overlap between the EEDF and the cross section provide the rate coefficient, which is graphically displayed in Figure 6. As the E/N increases, the energetic tail of the EEDF becomes more populated, increasing the overlap between the EEDF and cross section, which raises the rate coefficient.

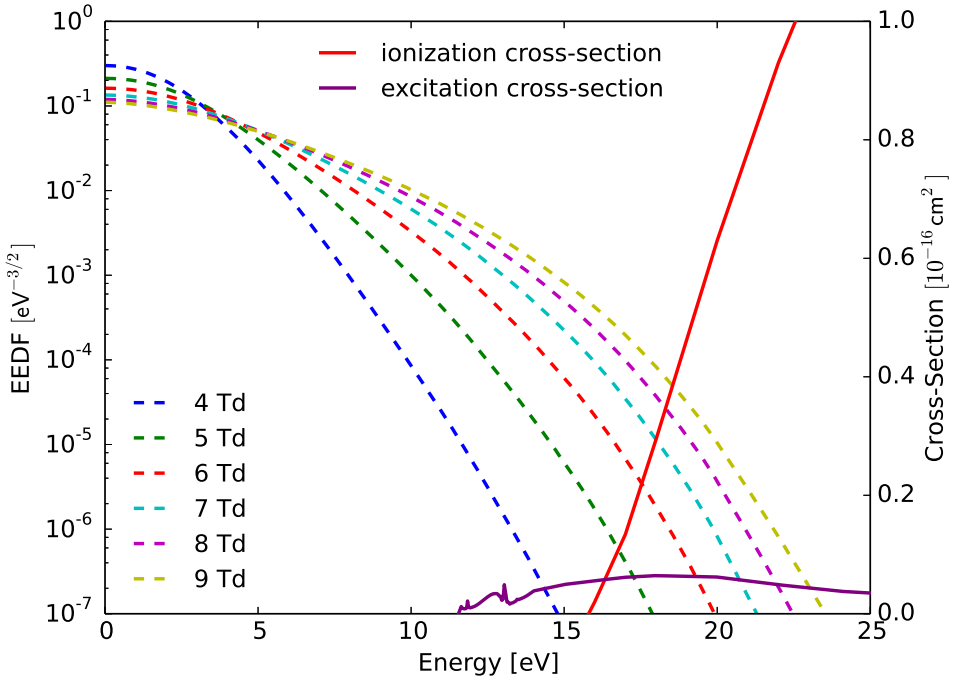

Figure 6. Electron Energy Distribution Function calculated by BOLSIG+ for 3% argon in helium at a variety of E/N magnitudes. The cross sections displayed are for excitation to Ar(1s5) [Biagi, 2011] and ionization [Yamabe et al., 1983] from the ground state.

Calculated EEDFs are also dependent on the gas composition, as displayed in Figure 7. For a given E/N, the EEDF tail population grows as the fraction of He increases (Ar-fraction decreases). The He rich mixtures push the EEDF towards a Maxwellian distribution, thus increasing the ionization and excitation rates for a particular E/N. This dependence on gas composition is due to a difference in excitation/ionization energy thresholds and momentum transfer cross sections. Inelastic collisions in Ar occur for electron energies above 11.55 eV, while He requires a minimum energy of 19.80 eV. The energy loss from inelastic collisions for Ar rich mixtures causes a sharp decline in EEDF population for energies above the 11.55 eV threshold

(Figure 7). This reduction near the Ar excitation energy threshold becomes less severe as more He is added to the mixture due to a diminution in inelastic energy loss to Ar excitation and ionization.

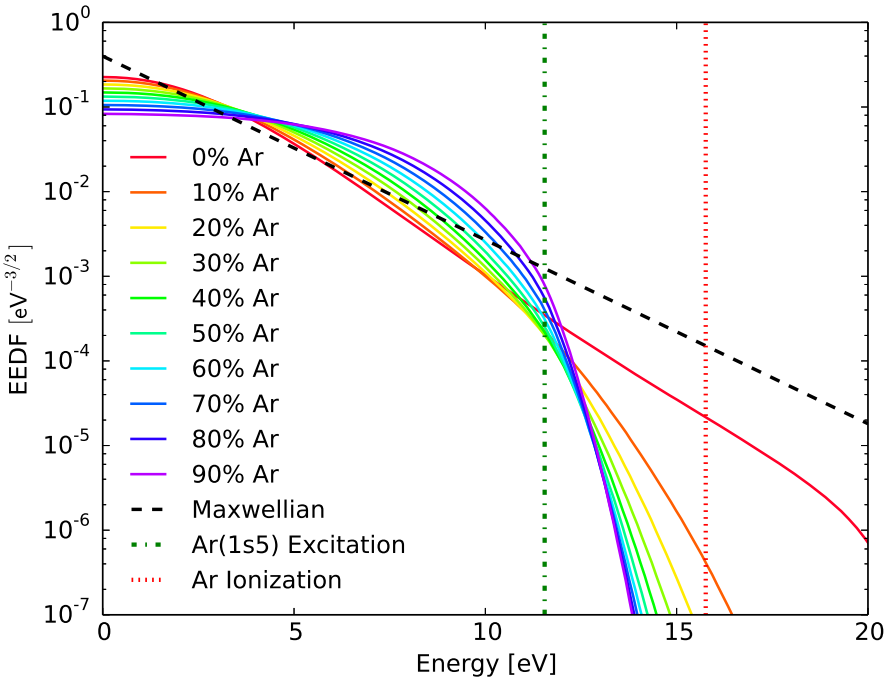

Figure 7. Electron Energy Distribution Functions calculated by BOLSIG+ for a variable composition of Ar in He at an E/N of 5 Td.

In addition to the loss in energetic electrons from inelastic collisions, the He EEDF has a larger population of energetic electrons as a result of a smaller momentum transfer cross section. A reduction in the momentum transfer cross section allows for more acceleration by the electric field. As displayed in Figure 8, Ar has a larger momentum transfer cross section than He for energies above 5 eV, which decreases the population of energetic electrons as the Ar-fraction increases. The Ar momentum transfer cross section shows a strong dependence on energy and is approximately a factor of 3 larger than the cross section for He at 10 eV, near the peak of the momentum transfer cross section in Ar. A static polarizability of 1.6 Å^3 for Ar [Roos et al., 2004] compared to 0.2 Å^3 for He [Łach et al., 2004] may account for the large difference in momentum transfer cross sections. Calculation of the Langevin cross

sections for the two atoms based on the polarizability [Steinfeld et al., 1999] provides a factor of 3 increase in the cross section for Ar relative to He. The factor of 8 increase in polarizability causes a factor of 3 increase in the momentum transfer cross section, matching the ratio of experimental derived cross sections at 10 eV.

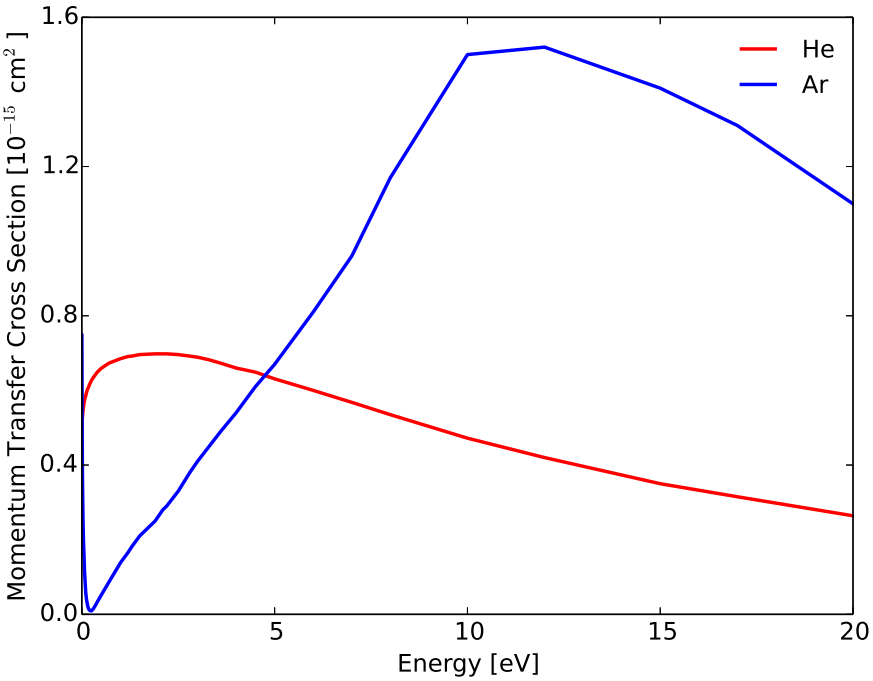

Figure 8. Momentum transfer cross sections for Ar [Yamabe et al., 1983] and He [Crompton et al., 1967] as a function of electron energy.

BOLSIG+ also calculates transport coefficients, elastic/inelastic power loss, and a variety of additional parameters dependent on the EEDF, as outlined in Section 2.4. A comparison of BOLSIG+ calculated parameters to experimental measurements indicate close agreement for a wide range of E/N magnitudes [Pitchford et al., 2013]. Electron mobilities are in agreement for E/N magnitudes up to approximately 100 Td, and ionization/excitation rate coefficients match the measurements up to $\sim$ 500 Td.

Combining BOLSIG+ with a rate equation integrator, such as ZDPlasKin, allows for a zero-dimensional analysis of a plasma discharge. Alternatively, BOLSIG+ can be pre-run for a range of electron temperatures, providing look-up tables of electron

impact rate coefficients and transport parameters to be used in fluid model calculations.

Zero-Dimensional Plasma Kinetics Model.

After electron impact rate coefficients are calculated by BOLSIG+, a system of reaction rate equations can be developed by combining the electron impact reactions with the remaining reactions (radiative, two-heavy-body, etc.), where the rate coefficients are extracted from literature. A zero-dimensional approach to the plasma kinetics is provided by ZDPlasKin (Zero-Dimensional Plasma Kinetics), which models the bulk plasma of a gas discharge by numerically integrating the system of reaction rate equations over time [Pancheshnyi et al., 2008].

For reactions of the form

$$aA + bB \rightarrow a'A + cC\ [+\Delta\epsilon], \tag{62}$$

the system of rate equations integrated over time are described by

$$\begin{aligned} \frac{d[N_l]}{dt} &= \sum_{i=1}^{i_{max}} Q_{li}(t), \\ Q_{Ai} &= (a' - a)R_i, \\ Q_{Bi} &= -bR_i, \\ Q_{Ci} &= cR_i, \\ R_i &= k_i[A]^a[B]^b, \end{aligned} \tag{63}$$

where $[N_l]$ is the concentration of species $l = A, B$, or C, i is the reaction number, a, b, c are the stoichiometric coefficients of the species A, B, C in reaction i, R_i is the reaction rate for reaction i with rate coefficient k_i, Q_{li} is the overall production/loss

rate for species l due to reaction i, and $\Delta\epsilon$ is the energy gained or lost in the reaction [Pancheshnyi et al., 2008].

In addition to the reaction rates, ZDPlasKin can also calculate gas heating based on inelastic and elastic power loss from BOLSIG+:

$$\frac{N_{gas}}{\gamma_c - 1}\frac{dT_{gas}}{dt} = \sum_{i=1}^{i_{max}} \pm\Delta\epsilon_i \cdot R_i + P_{elast} \cdot [n_e], \tag{64}$$

where γ_c is the ratio of specific heats, $\Delta\epsilon_i$ is the inelastic energy loss/gain due to reaction i, and P_{elast} is the elastic power loss due to momentum transfer collisions.

ZDPlasKin uses DVODE to integrate the system of rate equations over time (see Brown et al. 1989 for details). The rate coefficients for each reaction are input, and the electron impact rate coefficients are calculated using BOLSIG+. As the model progresses in time, BOLSIG+ is called to update the electron impact rate coefficients when the densities or E/N change beyond some user defined threshold.

Due to the electron impact rate coefficient dependence on E/N, the bulk plasma E/N must be calculated at each time step to provide an input to BOLSIG+. A simple method for calculating the E/N over time due to a voltage drop across a ballast resistor is described in Eismann [2011], and is used as a basis for this analysis.

Pathway Reduction Method for Plasma Kinetic Models.

An analysis of the reaction rate magnitudes over time, as calculated by ZDPlasKin, is helpful to understand the dominant production and loss rates. However, rates by themselves do not provide information on the pathways (sequences of reactions) creating or destroying species of interest. To analyze the principal pathways, a model such as PumpKin (Pathway redUction Method for Plasma KINetic models) must be employed [Markosyan et al., 2014]. The PumpKin algorithm is based on the algorithm described by Lehmann [2004], which can be summarized by the following steps:

- Each reaction is the starting point for a pathway.
- Branching point (fast species, S_i, with $\tau_i = \bar{c}_i/d_i < \tau_{threshold}$ where τ is the species lifetime defined by the average concentration, $\bar{c}$, divided by the destruction rate, d) is selected as the species with the shortest lifetime relative to the present list of pathways.
- Pathways producing S_i are combined with pathways that consume it.
- Pathways with small rates ($f_k < f_{min}$) are eliminated.
- Process repeated with next branching point until no species with $\tau_i < \tau_{threshold}$ remain.

The use of PumpKin allows the key pathways to be determined, which links together a series of key reactions resulting in a clear picture of the kinetics.

One-Dimensional Fluid Model.

Fluid Equations.

While a zero-dimensional model is helpful to understand chemical kinetics, it is not able to model the spatial profile of densities, voltages, or energies that can be obtained using a one-dimensional model. Understanding the spatial structure of metastable densities is key to this analysis due to the OPRGL requirement of elevated metastable densities over a volume large enough to allow efficient coupling of the pump laser. One common approach to include dimensionality in a gas discharge model is through the use of the fluid approximations to the Boltzmann equation [Lymberopoulos and Economou, 1993; Boeuf and Pitchford, 1995; Farouk et al., 2006; Gogolides and Sawin, 1992; COMSOL, 2016]. The fluid approach allows for high pressure simulations with low computation time compared to particle-in-cell approaches.

The fluid equations are derived from the Boltzmann equation with the assumption that the plasma acts as a conducting fluid instead of individual particles. This approximation is justified when the mean free path is much less than the scale of change of the macroscopic quantities and when the distance between particles is much less than the characteristic distance due to Debye shielding. In other words,

$$N\lambda_D^3 \gg 1, \tag{65}$$

$$\lambda_D = \sqrt{\frac{T_e \epsilon_0}{q_e n_e}}, \tag{66}$$

where λ_D is the Debye length [Cherrington, 2014]. For a 100 Torr discharge with $T_e = 2$ eV and $n_e = 10^{17}$ m^{-3}, the gas density is approximately 3×10^{24} m^{-3} and the Debye length is approximately 3×10^{-5} m, which meets the criteria for using a fluid approximation.

Following the derivation of the drift-diffusion equations found in Hagelaar and Pitchford [2005] and Raizer [1997], the two-term approximation to the Boltzmann equation (Equation 59) using spherical coordinates in velocity while only allowing the EEDF to spatially vary in the direction of the applied electric field provides:

$$\begin{aligned}
&\frac{\partial}{\partial t}\left[f_0(v,x,t) + f_1(v,x,t)\cos\theta\right] + v\cos\theta\frac{\partial}{\partial x}\left[f_0(v,x,t) + f_1(v,x,t)\cos\theta\right] \\
&- \frac{q_e}{m_e}E\left(\cos\theta\frac{\partial}{\partial v}\left[f_0(v,x,t) + f_1(v,x,t)\cos\theta\right] + \frac{\sin^2\theta}{v}\frac{\partial}{\partial\cos\theta}\left[f_0(v,x,t) + f_1(v,x,t)\cos\theta\right]\right) \\
&= C[f_0(v,x,t) + f_1(v,x,t)\cos\theta].
\end{aligned} \tag{67}$$

Averaging over the angular dependence yields

$$\begin{aligned}
&\frac{1}{4\pi}\int \frac{\partial}{\partial t}\left[f_0 + f_1\cos\theta\right]\mathrm{d}\Omega + \frac{1}{4\pi}\int v\cos\theta\frac{\partial}{\partial x}\left[f_0 + f_1\cos\theta\right]\mathrm{d}\Omega \\
&-\frac{1}{4\pi}\int \frac{q_e}{m_e}E\left(\cos\theta\frac{\partial}{\partial v}\left[f_0 + f_1\cos\theta\right] + \frac{\sin^2\theta}{v}f_1\right)\mathrm{d}\Omega = \frac{1}{4\pi}\int C[f_0 + f_1\cos\theta]\,\mathrm{d}\Omega, \\
&\implies \frac{\partial f_0}{\partial t} + \frac{v}{3}\frac{\partial f_1}{\partial x} - \frac{q_e}{3m_e}E\left(\frac{\partial f_1}{\partial v} + \frac{2}{v}f_1\right) = C_0, \\
&\implies \frac{\partial f_0}{\partial t} + \frac{v}{3}\frac{\partial f_1}{\partial x} - \frac{q_e}{3m_e v^2}E\frac{\partial}{\partial v}\left(f_1 v^2\right) = C_0, \qquad (68)
\end{aligned}$$

where $\mathrm{d}\Omega = \sin\theta\,\mathrm{d}\theta\,\mathrm{d}\phi$, and the integral of $C[f]$ has been replaced by C_0. More detail on the specifics of the collision term can be found in Hagelaar and Pitchford [2005]. The velocity dependence can be converted to energy by

$$\begin{aligned}
\frac{1}{2}m_e v^2 = q_e\epsilon \implies m_e v\,\mathrm{d}v = q_e\,\mathrm{d}\epsilon, \qquad (69)\\
\implies \mathrm{d}v = \sqrt{\frac{q_e}{2m_e\epsilon}}\,\mathrm{d}\epsilon,
\end{aligned}$$

where ϵ is the electron energy in eV. Substituting into Equation 68 provides

$$\frac{\partial f_0}{\partial t} + \frac{1}{3}\sqrt{\frac{2q_e\epsilon}{m_e}}\frac{\partial f_1}{\partial x} - \frac{E}{3}\sqrt{\frac{2q_e}{m_e\epsilon}}\frac{\partial}{\partial\epsilon}\left(f_1\epsilon\right) = C_0. \qquad (70)$$

Following a similar procedure of multiplying Equation 67 by $\cos\theta$ and averaging over the angular dependence produces the complementary equation

$$\frac{\partial f_1}{\partial t} + \sqrt{\frac{2q_e\epsilon}{m_e}}\frac{\partial f_0}{\partial x} - E\sqrt{\frac{2q_e\epsilon}{m_e}}\frac{\partial f_0}{\partial\epsilon} = -N\sigma_m\sqrt{\frac{2q_e\epsilon}{m_e}}f_1, \qquad (71)$$

where the term on the right hand side is due to the angular integral of the collision term (see Raizer [1997] for a detailed derivation).

The electron continuity equation is obtained by multiplying Equation 70 by $\sqrt{\epsilon}$

and integrating over energy:

$$\int_0^\infty \frac{\partial f_0}{\partial t}\sqrt{\epsilon}\,\mathrm{d}\epsilon + \frac{1}{3}\sqrt{\frac{2q_e}{m_e}}\int_0^\infty \epsilon\frac{\partial f_1}{\partial x}\,\mathrm{d}\epsilon - \frac{E}{3}\sqrt{\frac{2q_e}{m_e}}\int_0^\infty \frac{\partial}{\partial \epsilon}\left(f_1\epsilon\right)\mathrm{d}\epsilon = \int_0^\infty C_0\sqrt{\epsilon}\,\mathrm{d}\epsilon. \tag{72}$$

Using the normalization condition

$$\int_0^\infty f_0\sqrt{\epsilon}\,\mathrm{d}\epsilon = \frac{1}{2\pi}\left(\frac{m_e}{2q_e}\right)^{3/2} n_e, \tag{73}$$

along with the fact that $f_1\epsilon$ goes to zero as ϵ goes to zero or infinity, provides the electron continuity equation:

$$\frac{\partial n_e}{\partial t} + \frac{\partial \Gamma_e}{\partial x} = R_e. \tag{74}$$

The electron source term, R_e, is the total electron production/loss rate. The flux term, Γ_e, is described by

$$\Gamma_e = \frac{2\pi}{3}\left(\frac{2q_e}{m_e}\right)^2 \int_0^\infty \epsilon f_1\,\mathrm{d}\epsilon. \tag{75}$$

Solving for f_1 in Equation 71 yields

$$-f_1\left(\sigma_m + \frac{\bar{\nu}_i}{N}\sqrt{\frac{m_e}{2q_e\epsilon}}\right) = \frac{1}{N}\frac{\partial f_0}{\partial x} - \frac{E}{N}\frac{\partial f_0}{\partial \epsilon}, \tag{76}$$

where the time derivative of f_1 is replaced by the net ionization frequency, $\bar{\nu}_i$, times f_1:

$$\frac{\partial f_1}{\partial t} = f_1\bar{\nu}_i. \tag{77}$$

Defining the effective momentum transfer cross section, $\tilde{\sigma}_m$, as

$$\tilde{\sigma}_m = \sigma_m + \frac{\bar{\nu}_i}{N}\sqrt{\frac{m_e}{2q_e\epsilon}}, \tag{78}$$

provides

$$f_1 = -\frac{1}{N\tilde{\sigma}_m}\frac{\partial f_0}{\partial x} + \frac{E}{N\tilde{\sigma}_m}\frac{\partial f_0}{\partial \epsilon}. \tag{79}$$

Substituting f_1 into Equation 75 produces

$$\Gamma_e = -\frac{2\pi}{3N}\left(\frac{2q_e}{m_e}\right)^2 \frac{\partial}{\partial x}\int_0^\infty \frac{\epsilon}{\tilde{\sigma}_m} f_0 \,\mathrm{d}\epsilon + \frac{2\pi E}{3N}\left(\frac{2q_e}{m_e}\right)^2 \int_0^\infty \frac{\epsilon}{\tilde{\sigma}_m}\frac{\partial f_0}{\partial \epsilon}\,\mathrm{d}\epsilon. \tag{80}$$

Defining the electron mobility, μ_e, and electron diffusion coefficient, D_e, as

$$D_e n_e = \frac{2\pi}{3N}\left(\frac{2q_e}{m_e}\right)^2 \int_0^\infty \frac{\epsilon}{\tilde{\sigma}_m} f_0 \,\mathrm{d}\epsilon, \tag{81}$$

$$\mu_e n_e = -\frac{2\pi}{3N}\left(\frac{2q_e}{m_e}\right)^2 \int_0^\infty \frac{\epsilon}{\tilde{\sigma}_m}\frac{\partial f_0}{\partial \epsilon}\,\mathrm{d}\epsilon, \tag{82}$$

yields the drift-diffusion equation:

$$\Gamma_e = -\frac{\partial\left(D_e n_e\right)}{\partial x} - \mu_e n_e E. \tag{83}$$

A similar derivation provides the energy transport equation, which is obtained by multiplying Equation 70 by $\epsilon^{3/2}$ and integrating over energy:

$$\int_0^\infty \frac{\partial f_0}{\partial t}\epsilon^{3/2}\,\mathrm{d}\epsilon + \frac{1}{3}\sqrt{\frac{2q_e}{m_e}}\int_0^\infty \epsilon^2\frac{\partial f_1}{\partial x}\,\mathrm{d}\epsilon - \frac{E}{3}\int_0^\infty \sqrt{\frac{2q_e}{m_e}}\epsilon\frac{\partial}{\partial \epsilon}\left(f_1\epsilon\right)\mathrm{d}\epsilon = \int_0^\infty C_0\epsilon^{3/2}\,\mathrm{d}\epsilon. \tag{84}$$

Using the normalization condition

$$\int_0^\infty f_0\,\epsilon^{3/2}\,\mathrm{d}\epsilon = \frac{1}{2\pi}\left(\frac{m_e}{2q_e}\right)^{3/2} n_e\langle\epsilon\rangle = \frac{1}{2\pi}\left(\frac{m_e}{2q_e}\right)^{3/2} n_\epsilon, \tag{85}$$

where n_ϵ is the electron energy density and $\langle\epsilon\rangle$ is the mean electron energy in eV,

yields the energy transport equation:

$$\frac{\partial n_\epsilon}{\partial t} + \frac{\partial \Gamma_\epsilon}{\partial x} + E\Gamma_e = R_\epsilon. \tag{86}$$

The electron energy source term, R_ϵ, is the change in energy due to electron collisions. The flux term, Γ_ϵ, is described by

$$\Gamma_\epsilon = \frac{2\pi}{3}\left(\frac{2q_e}{m_e}\right)^2 \int_0^\infty \epsilon^2 f_1 \, \mathrm{d}\epsilon, \tag{87}$$

which can be converted to the drift-diffusion form by defining

$$D_\epsilon n_\epsilon = \frac{2\pi}{3N\langle\epsilon\rangle}\left(\frac{2q_e}{m_e}\right)^2 \int_0^\infty \frac{\epsilon^2}{\tilde{\sigma}_m} f_0 \, \mathrm{d}\epsilon, \tag{88}$$

$$\mu_\epsilon n_\epsilon = -\frac{2\pi}{3N\langle\epsilon\rangle}\left(\frac{2q_e}{m_e}\right)^2 \int_0^\infty \frac{\epsilon^2}{\tilde{\sigma}_m}\frac{\partial f_0}{\partial \epsilon} \, \mathrm{d}\epsilon. \tag{89}$$

The definitions of the electron energy mobility, μ_ϵ, and the electron energy diffusion coefficient, D_ϵ, provide the electron energy flux in the drift-diffusion form:

$$\Gamma_\epsilon = -\frac{\partial\left(D_\epsilon n_\epsilon\right)}{\partial x} - \mu_\epsilon n_\epsilon E. \tag{90}$$

While the two-term approximation assumes a spatially uniform E/N and is known to fail at large E/N magnitudes [Raizer, 1997; Hagelaar and Pitchford, 2005], the approach is appropriate in the bulk plasma (positive column), which is the region of interest for an OPRGL. To properly model sheath behavior, where the E/N is non-uniform and large in magnitude, a hybrid fluid-kinetic approach should be implemented [Fiala et al., 1994; Boeuf and Pitchford, 2004; Derzsi et al., 2009].

Ignoring neutral gas flow, heavy particle transport is calculated by

$$\frac{\partial n_k}{\partial t} + \frac{\partial \Gamma_k}{\partial x} = R_k, \tag{91}$$

$$\frac{\partial n_p}{\partial t} + \frac{\partial \Gamma_p}{\partial x} = R_p, \tag{92}$$

$$\Gamma_k = -D_k \frac{\partial n_k}{\partial x}, \tag{93}$$

$$\Gamma_p = n_p \mu_p E - D_p \frac{\partial n_p}{\partial x}, \tag{94}$$

where n_k is the density of neutral species k, n_p is the density of ion species p, $D_{k,p}$ are the diffusion coefficients (assumed to be independent of position), $R_{k,p}$ are the reaction source terms, and μ_p is the ion mobility. The ion flux Γ_p has a drift term due to migration in the electric field, $E = -\partial V/\partial x$. Electric potentials are calculated from Poisson's equation

$$-\frac{\partial^2 V}{\partial x^2} = \frac{q_e}{\epsilon_0}\left(\sum_{p=1}^{P} n_p - n_e\right), \tag{95}$$

where all ions are assumed to be singly charged with charge q_e.

Near the electrodes, electrons are lost due to thermal motion to the surface, and electrons are created due to secondary emission from ion collisions with the surface, providing the following boundary conditions [Hagelaar et al., 2000]:

$$\mathbf{n} \cdot \mathbf{\Gamma}_e = \frac{1}{2} v_{e,th} n_e - \xi \sum_p \gamma_p \mathbf{\Gamma}_p \cdot \mathbf{n}, \tag{96}$$

$$\mathbf{n} \cdot \mathbf{\Gamma}_\epsilon = \frac{5}{6} v_{e,th} n_\epsilon - \xi \sum_p \epsilon_p \gamma_p \mathbf{\Gamma}_p \cdot \mathbf{n}, \tag{97}$$

$$\xi = \begin{cases} 1, & \text{if } \mathbf{\Gamma}_p \cdot \mathbf{n} > 0 \\ 0, & \text{otherwise} \end{cases}$$

where $\mathbf{n}$ is the outward normal vector to the boundary (electrode), $v_{e,th}$ is the thermal velocity of electrons, ϵ_p is the average energy of the secondary electrons, and γ_p is the secondary emission coefficient for ion species p. Boundary conditions for heavy species follow

$$\mathbf{n} \cdot \mathbf{\Gamma}_k = \frac{1}{2} v_{k,th} n_k, \tag{98}$$

$$\mathbf{n} \cdot \mathbf{\Gamma}_p = \frac{1}{2} v_{p,th} n_p + n_p \mu_p \mathbf{E} \cdot \mathbf{n}, \tag{99}$$

where the sticking coefficient is assumed to be unity, and $v_{k,th}$ and $v_{p,th}$ are the thermal neutral and ion velocities, respectively.

Numerical Approach.

Solutions to the system of partial differential equations may be approximated using the Galerkin finite element method, or through the Scharfetter and Gummel [1969] finite volume scheme. At high pressures, the Scharfetter-Gummel scheme is commonly used to conserve flux between cells [Kushner, 2005; Boeuf and Pitchford, 2004], eliminating instabilities which may arise using the finite element approach.

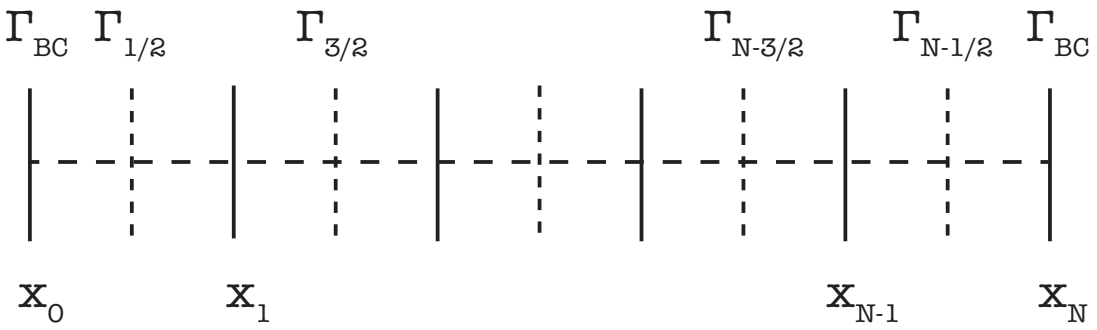

Figure 9. A diagram of the grid and midpoint flux used in the Scharfetter-Gummel finite volume scheme.

This finite volume scheme conserves flux, Γ, between points in space by using an average flux at the midpoints (Figure 9). Assuming the flux is constant over an

interval, but the densities and diffusion coefficients are variable, the midpoint flux can be derived by [Frensley, 2004]

$$\begin{aligned}
\Gamma_{i+1/2} &= -\frac{\partial}{\partial x}\left(D_e n_e\right) - n_e \mu_e E, \\
\implies \Gamma_{i+1/2} \exp\left[\mu_e E(x-x_i)/D_e\right] &= \left(-\frac{\partial}{\partial x}\left(D_e n_e\right) - n_e \mu_e E\right) \exp\left[\mu_e E(x-x_i)/D_e\right], \\
&= -\frac{\partial}{\partial x}\left(D_e n_e \exp\left[\mu_e E(x-x_i)/D_e\right]\right), \qquad (100)
\end{aligned}$$

where i is the spatial index and the temporal index has been ignored to provide a clear derivation of the midpoint flux. Integrating over the length of a cell provides

$$\begin{aligned}
&\int_{x_i}^{x_i+\Delta x_i} \Gamma_{i+1/2} \exp\left[\mu_e E(x-x_i)/D_e\right] dx = \int_{x_i}^{x_i+\Delta x_i} -\frac{\partial}{\partial x}\left(D_e n_e \exp\left[\mu_e E(x-x_i)/D_e\right]\right) dx, \\
&\implies \Gamma_{i+1/2} \int_0^{\Delta x_i} \exp\left[\mu_e E x'/D_e\right] dx' = -\left(D_e n_e \exp\left[\mu_e E(x-x_i)/D_e\right]\right)\Big|_{x_i}^{x_i+\Delta x_i}, \\
&\implies \Gamma_{i+1/2} \left(\frac{D_e}{\mu_e E}\right)_{i+1/2} \left(\exp\left[\left(\mu_e E/D_e\right)_{i+1/2} \Delta x_i\right] - 1\right) \\
&\qquad = \left(D_e n_e\right)_i - \left(D_e n_e\right)_{i+1} \exp\left[\left(\mu_e E/D_e\right)_{i+1/2} \Delta x_i\right]. \qquad (101)
\end{aligned}$$

Solving for the midpoint flux yields

$$\begin{aligned}
\Gamma_{i+1/2} &= \left(\frac{\mu_e E}{D_e}\right)_{i+1/2} \frac{\left(D_e n_e\right)_i - \left(D_e n_e\right)_{i+1} \exp\left[\left(\mu_e E/D_e\right)_{i+1/2} \Delta x_i\right]}{\exp\left[\left(\mu_e E/D_e\right)_{i+1/2} \Delta x_i\right] - 1}, \\
&= \left(\frac{\mu_e E}{D_e}\right)_{i+1/2} \frac{\left(D_e n_e\right)_i \exp\left[\left(-\mu_e E/D_e\right)_{i+1/2} \Delta x_i\right] - \left(D_e n_e\right)_{i+1}}{1 - \exp\left[\left(-\mu_e E/D_e\right)_{i+1/2} \Delta x_i\right]}. \qquad (102)
\end{aligned}$$

Applying the scheme to the electron continuity equation provides

$$\frac{n_{e,i}^{k+1} - n_{e,i}^{k}}{\Delta t} + \frac{\Gamma_{i+1/2}^{k+1} - \Gamma_{i-1/2}^{k+1}}{\Delta x_i} = R_i^k, \quad (103)$$

$$\Gamma_{i+1/2}^{k+1} = \left(\frac{\mu_e E}{D_e}\right)_{i+1/2}^{k} \frac{-D_{e,i+1}^{k} n_{e,i+1}^{k+1} + D_{e,i}^{k} n_{e,i}^{k+1} \exp\left(-\left(\mu_e E/D_e\right)_{i+1/2}^{k} \Delta x_i\right)}{1 - \exp\left[-\left(\mu_e E/D_e\right)_{i+1/2}^{k} \Delta x_i\right]}, \quad (104)$$

$$\Gamma_{i-1/2}^{k+1} = \left(\frac{\mu_e E}{D_e}\right)_{i-1/2}^{k} \frac{-D_{e,i}^{k} n_{e,i}^{k+1} + D_{e,i-1}^{k} n_{e,i-1}^{k+1} \exp\left(-\left(\mu_e E/D_e\right)_{i-1/2}^{k} \Delta x_i\right)}{1 - \exp\left[-\left(\mu_e E/D_e\right)_{i-1/2}^{k} \Delta x_i\right]}, \quad (105)$$

where k is the temporal index [Passchier and Goedheer, 1993; Fiala et al., 1994]. The boundary conditions are described by Equation 96. A forward Euler method is used for the time-stepping, which is a first order explicit scheme in time. Voltages, diffusion coefficients, and mobilities from the previous time step are used to linearize the spatial component. The electron energy continuity equation is solved in the same manner. Following a similar derivation for the neutral species, without the drift term, $\mu_e E$, provides a centered-difference scheme, which is second order in space.

For Dirichlet boundary conditions (DC scenario), a Green's function approach may be used to calculate the voltage:

$$V(x) = \int_0^x \frac{x'}{d}(d-x)\frac{\rho(x')}{\epsilon_0}dx' + \int_x^d x\left(1 - \frac{x'}{d}\right)\frac{\rho(x')}{\epsilon_0}dx' - V(0)\left(\frac{x}{d} - 1\right) + V(d)\frac{x}{d}. \quad (106)$$

Alternatively, for the RF-CCP scenario which provides Neumann boundary conditions at the dielectric interface, a central difference finite difference scheme may be used to solve Poisson's equation.

Electron mobilities, $\mu_{e,\epsilon}$, diffusion coefficients, $D_{e,\epsilon}$, and electron impact rate coefficients are calculated from BOLSIG+, and a look-up table is used to extract the values based on the local T_e. The local electron temperature is mapped to an ef-

fective E/N from BOLSIG+, which is used to extract an EEDF for each point in space. Transport parameters and electron impact rate coefficients are calculated for each point in space from the EEDF corresponding to the local T_e. Reaction source terms are calculated from the plasma chemistry in the same manner as Equation 63, with the addition of an energy term, $\Delta\epsilon_i$, in the energy source term, R_ϵ, to account for the energy gained or lost from reaction i.

III. Pulsed Circuit Direct Current Discharge

An optically pumped rare gas laser (OPRGL), as demonstrated by Han et al. [2013], uses a diode laser to pump metastable $Rg(1s_5)$ atoms generated in a gas discharge to the $Rg(2p_9)$ level. At atmospheric pressures, rapid collisional transfer from $Rg(2p_9)$ to $Rg(2p_{10})$ allows for a population inversion and subsequent lasing to $Rg(1s_5)$, as displayed in Figure 1. Diode laser absorption, and hence optical gain, are dependent on $Rg(1s_5)$ densities [Rawlins et al., 2015; Demyanov et al., 2013]. Output laser intensities above 100 W/cm^2 may be possible with a uniform volume of metastable densities on the order of 10^{13} cm^{-3} [Han et al., 2014]. Due to the broad line widths of diode lasers, near-atmospheric pressures are required to broaden the absorption line width for efficient pump laser absorption. Additionally, the non-adiabatic transition rate from $Rg(2p_9)$ to $Rg(2p_{10})$, responsible for establishing a population inversion, is enhanced at elevated pressures. Pulsed discharges are able to maintain stability at atmospheric pressures due to a reduction in thermal instabilities caused by the down time in-between pulses [Raizer, 1997]. Additionally, for the same averaged power, the average plasma density of a pulsed system is greater than a steady-state direct current (DC) discharge as a result of a reduction in electron temperature in-between pulses [Ashida et al., 1995; Lieberman and Lichtenberg, 2005].

Han et al. [2013] demonstrated the use of a pulsed DC circuit to produce an OPRGL in an Ar-He mixture at atmospheric pressures. Voltages in the range of 1000-2000 V were used for microsecond pulses across a parallel plate geometry. Metastable densities, measured through pump laser absorption, indicated a decay to half the peak value approximately 7 μs after pulse initiation.

Previously, a kinetic study of an OPRGL using a mixture of Ar and He at atmospheric pressures concluded that a mixture of approximately 1% Ar in He results in the largest total efficiency (defined as the output power divided by the sum of dis-

charge and pump powers) [Demyanov et al., 2013]. The kinetic study observed that an increase in Ar-fraction increases production of $Ar(1s_5)$, but also results in a larger collision relaxation rate from the $Ar(2p)$ manifold down to the $Ar(1s)$ manifold in addition to an increase in the $Ar(1s_5)$ loss rate through excimer formation. A separate kinetic analysis studied OPRGL performance over a variety of metastable densities, showing the possibility of kilowatt laser powers for an OPRGL system with $Ar(1s_5)$ densities on the order of 10^{13} cm^{-3} and pump laser intensities in the 2-5 kW/cm^2 range [Yang et al., 2015]. An experimental and computational analysis of microwave resonator-driven microplasmas at a variety of Ar-He mixtures and pressures ranging from 100-730 Torr found that an Ar-fraction near 5% at a pressure of 100 Torr produces the largest metastable densities [Hoskinson et al., 2016]. Metastable densities on the order of 10^{13} cm^{-3} were measured for the microplasmas at a pressure of 100 Torr, with a decrease in $Ar(1s_5)$ density as the pressure increased.

More recently, Han et al. [2016] performed an Ar-He pulsed DC discharge experiment at a pressure of 270 Torr and a mixture of 7% Ar in He, with 2.5 cm $\times$ 2.5 cm stainless steel electrodes separated by 0.5 cm. Metastable $Ar(1s_5)$ densities were measured via transient laser absorption spectroscopy from a custom made diode laser tuned to the $Ar(1s_5) + \hbar\omega \rightarrow Ar(2p_9)$ transition. Plasma fluorescence from the $Ar(2p_{10}) \rightarrow Ar(1s_5) + \hbar\omega$ transition was also measured, providing a proxy for $Ar(2p_{10})$ density over time.

This chapter analyzes the pulsed circuit experiment described in Han et al. [2016]. A zero-dimensional analysis is used to vet the reaction rate package and perform a sensitivity analysis. Simulations are then extended to one-dimension providing spatial metastable density profiles and verifying the positive column predictions of the zero-dimensional approach. Additionally, EEDF calculations for the one-dimensional model are varied over the pulse duration to test the effectiveness of using a single set

of pre-calculated EEDFs.

3.1 Description of Experiment

A recent experiment performed by Han et al. [2016] using a pulsed DC discharge with mixtures of Ar and He at atmospheric pressures has demonstrated the ability to produce high concentrations of $Ar(1s_5)$ over a relatively large volume. A diagram of the experimental design is displayed in Figure 10. Pulsed voltages of approximately 1000 V were applied across stainless steel electrodes with dimensions 2.5 cm $\times$ 2.5 cm, separated by 0.5 cm.

Metastable densities were measured via transient laser absorption spectroscopy from a custom made diode laser tuned to the $Ar(1s_5) + \hbar\omega \rightarrow Ar(2p_9)$ transition (811.754 nm), providing a proxy for the $Ar(1s_5)$ densities over the pulse duration. Plasma fluorescence from the $Ar(2p_{10}) \rightarrow Ar(1s_5) + \hbar\omega$ transition was measured from the side of the cell perpendicular to the diode laser propagation, providing a proxy for the time-dependent $Ar(2p_{10})$ densities.

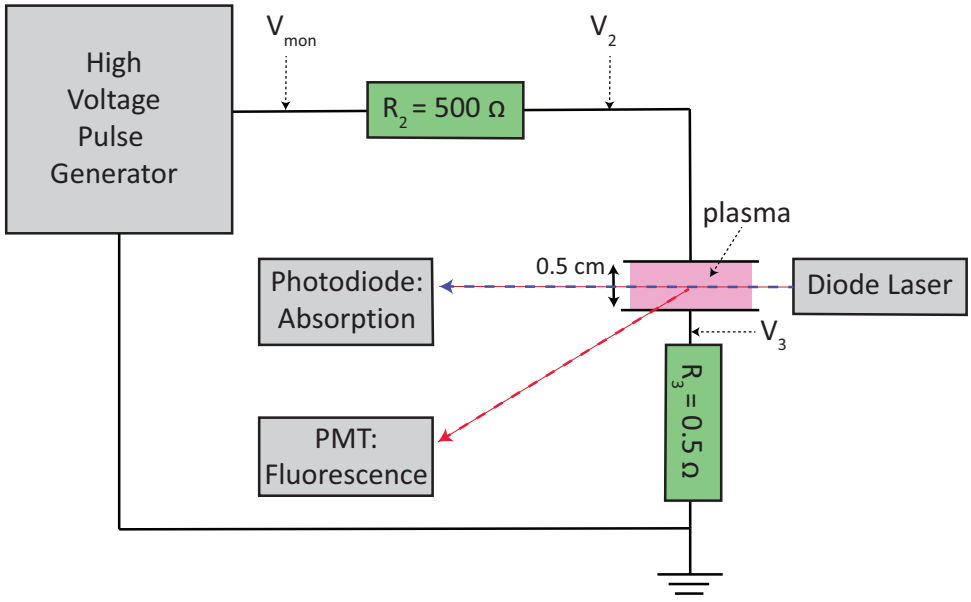

Figure 10. A diagram of the experimental apparatus used for measurement of the pulsed DC discharge [Han et al., 2016].

In addition to the density measurements, several voltages and currents were measured for the pulsed circuit (Figure 10). A high voltage pulse generator was used to produce square wave (single or multiple) pulses amplified to around 1000 V. A 500 Ω ballast resistor (R_2) was used to limit the current, and a 0.5 Ω resistor (R_3) was used to measure the discharge current. Voltages were measured in several locations to provide detailed information about the temporal variations of the circuit, including a measurement of the voltage across the electrodes ($V_2 - V_3 \approx V_2$). A digital oscilloscope was also connected directly to the pulse generator to measure the output voltage, V_{mon}.

The combination of measurements, including voltage across the electrodes, discharge current, metastable absorption, and $Ar(2p_{10})$ fluorescence, provide a detailed picture of the time dependent plasma dynamics during a high voltage pulse.

3.2 Zero-Dimensional Simulations

A zero-dimensional analysis of the pulsed circuit discharge is performed using the rate package in Table 2. While several pressures and Ar-He mixtures were measured experimentally, the simulations focus on the 270 Torr, 7% Ar in He scenario, and investigate various pulse durations. Gas heating is ignored due to the short pulse duration.

Voltages across the positive column are calculated by

$$V_{PC} = V_{mon} - I_D R_2 - V_C, \tag{107}$$

where V_{PC} is the voltage across the positive column, I_D is the discharge current, and V_C is the cathode fall. Measured voltages from the pulse generator, V_{mon}, are smoothed and used as the input voltage for zero-dimensional plasma kinetics model,

ZDPlasKin. ZDPlasKin uses the input voltage to calculate the voltage across the positive column by including the potential drop across the ballast resistor and the cathode fall. The cathode fall is calculated using Equation 29, with the assumption that the discharge is a normal glow. For a secondary emission coefficient of $\gamma = 0.02$ estimated for stainless steel, the calculated normal cathode fall is around 160 V.

The main driver of the EEDF (and hence reaction rates) is the reduced electric field, E/N. The E/N for time $k+1$ is calculated from the current and E/N at time k following the procedure outlined in Eismann [2011]:

$$V_{PC}^{k+1} = V_{mon}^{k+1} - V_C - R_2 I_D^k, \tag{108}$$

$$= V_{mon}^{k+1} - V_C - R_2 A j^k, \tag{109}$$

$$= V_{mon}^{k+1} - V_C - R_2 A n_e^k q_e \mu_e^k N \left(\frac{E}{N}\right)^{k+1}, \tag{110}$$

where the E/N for the current density is selected at time $k+1$ to make the process semi-implicit. Substituting

$$\frac{E}{N} = \frac{V_{PC}}{Nd} \implies V_{PC} = Nd\left(\frac{E}{N}\right), \tag{111}$$

where d is the distance between electrodes, we obtain

$$Nd\left(\frac{E}{N}\right)^{k+1} = V_{mon}^{k+1} - V_C - R_2 A n_e^k q_e \mu_e^k N \left(\frac{E}{N}\right)^{k+1}, \tag{112}$$

$$\implies \left(\frac{E}{N}\right)^{k+1} = \frac{V_{mon}^{k+1} - V_C}{N\left(d + R_2 A n_e^k q_e \mu_e^k\right)}. \tag{113}$$

Using the relationship $n_e q_e \mu_e = j/E$ provides the desired form of E/N at time $k+1$:

$$\left(\frac{E}{N}\right)^{k+1} = \frac{V_{mon}^{k+1} - V_C}{Nd + \dfrac{R_2 I_D^k}{(E/N)^k}}. \tag{114}$$

To compare simulated voltages to measured electrode voltages, the electrode voltage, V_E, is calculated:

$$V_E = V_{PC} + V_C = V_{mon} - I_D R_2. \tag{115}$$

Pulse widths of 1, 20, and 35 μs are analyzed to study the effect of the pulse width on the metastable density. The applied voltages for the three pulses simulated in this analysis are displayed in Figure 11.

Simulated absorption is calculated using the absorption cross section of $\sigma_\alpha = 4.3 \times 10^{-13}$ cm^2 [Demyanov et al., 2013], and the relationship

$$\frac{I}{I_0} = \exp(-\alpha) = \exp\left(-\sigma_\alpha \left[Ar(1s_5)\right] d\right), \tag{116}$$

where I is the measured intensity, I_0 is the initial laser intensity, α is the absorption, and d is the length of the gas traversed by the laser.

Beginning with the 1 μs pulse, the initial simulation results and measurements are displayed in Figure 12. This initial simulation does not account for radiation trapping of the $Ar(1s_4) \rightarrow Ar + \hbar\omega$ transition, causing the metastable density to decay too rapidly after pulse termination. However, the voltage, current, and fluorescence curves match the measurements (accounting for the noise due to the short timescale of the pulse).

Including radiation trapping (see Holstein [1947], Holstein [1951], and Belostotskiy et al. [2011]) by using the radiation rate of 5.6×10^5 s^{-1} measured for the cell geometry by Han and Heaven [2014], drastically decreases the metastable decay rate (Figure 13). The decay rate after the inclusion of radiation trapping qualitatively matches the measured decay rate, highlighting the importance of radiation trapping and the dependence of the metastable density on the $Ar(1s_4)$ loss rate. The rapid transfer

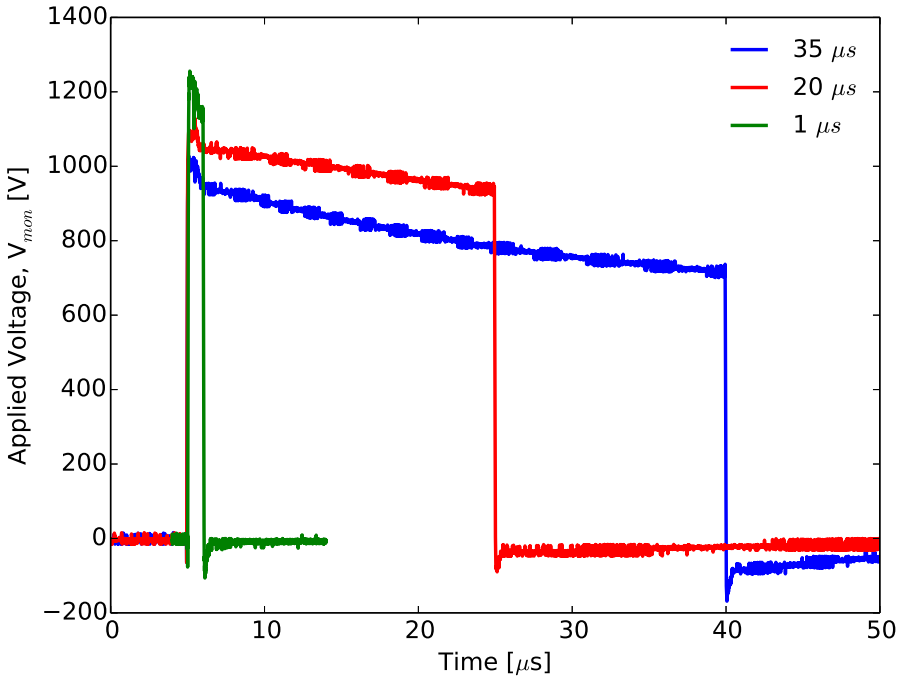

Figure 11. Applied voltages, V_{mon}, for the three pulse widths simulated in this analysis: 1, 20, and 35 μs [Han et al., 2016].

from $Ar(1s_5)$ due to electron impact collisions, $Ar(1s_5) + e \rightarrow Ar(1s_4) + e$, followed by radiative decay, $Ar(1s_4) \rightarrow Ar + \hbar\omega$, is determined to be one of the main loss mechanisms for metastable density.

Discharge characteristics over time become more obvious for the longer pulses. Analyzing the 20 μs scenario, the simulated parameters are found to qualitatively match the measured behavior over time (Figure 14). The computed value of V_E closely follows the observed value beginning with an initial spike associated with breakdown followed by a rapid decrease to a steady-state value. The large spike in V_E during breakdown gives rise to a large value of E/N. Production of $Ar(1s_5)$ is enhanced at higher values of E/N. As a result, the majority of the metastable density is produced within approximately 1 μs after breakdown.

During breakdown, the electron density increases and current begins to flow. As the current flows across the ballast resistor, V_E rapidly decrease by a factor of two to three before reaching a steady-state value. The reduction in V_E combined with

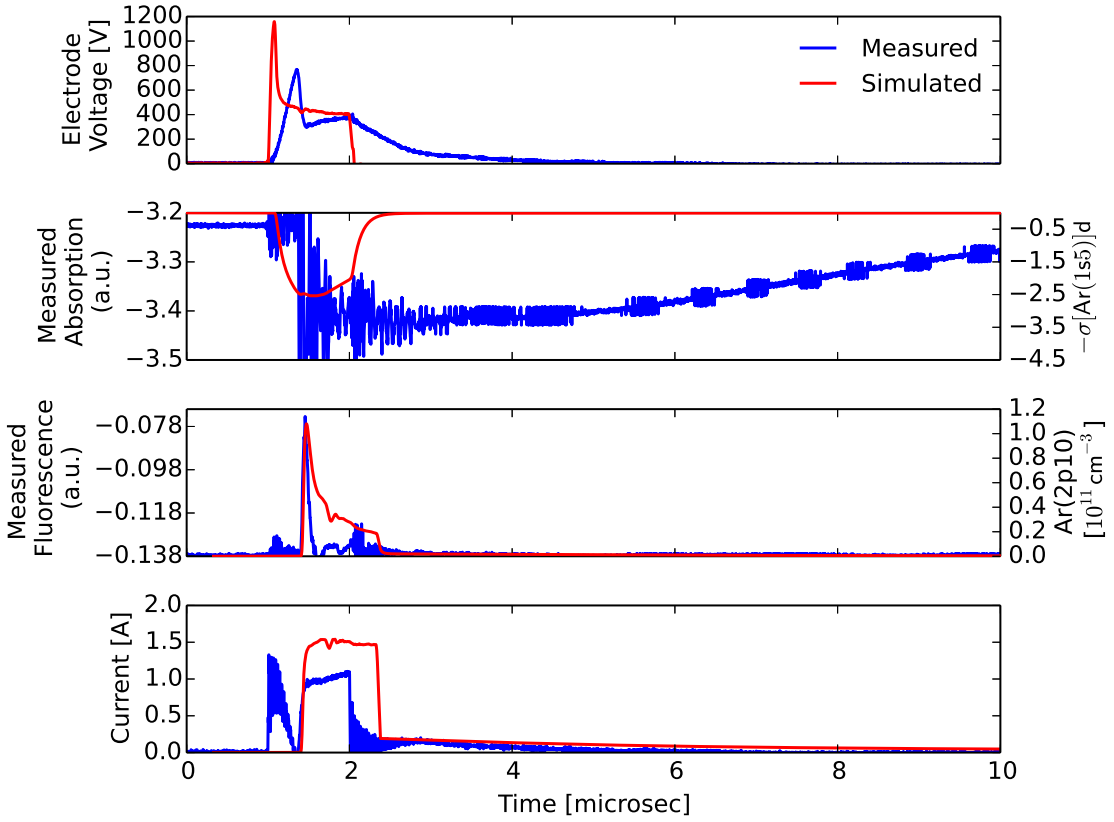

Figure 12. A comparison of the simulated and measured values for electrode voltage, $V_E = V_2 - V_3$ (top), $Ar(1s_5) + \hbar\omega \rightarrow Ar(2p_9)$ absorption (middle top), $Ar(2p_{10}) \rightarrow Ar(1s_5) + \hbar\omega$ fluorescence (middle bottom), and discharge current I_3 (bottom) for a 1 μs pulse. Radiation trapping for the $Ar(1s_4) \rightarrow Ar + \hbar\omega$ transition is not included in this simulation.

the cathode fall caused by sheath formation lowers the positive column E/N by a factor of four to five. At this steady state value of E/N, the metastable production rate is reduced and the metastable density decreases primarily through the reaction sequence $Ar(1s_5) + e \rightarrow Ar(1s_4) + e$ followed by $Ar(1s_4) \rightarrow Ar + \hbar\omega$. The measured $Ar(2p_{10}) \rightarrow Ar(1s_5) + \hbar\omega$ fluorescence and simulated $Ar(2p_{10})$ densities follow the same trend, with a large spike at breakdown, followed by a decrease throughout the remainder of the pulse.

Simulations for the 35 μs scenario follow the same general trend as the 20 μs scenario (Figure 15). However, the simulated current is about 0.5 A lower than the measured current near the end of the pulse, due to a 250 V difference in the electrode

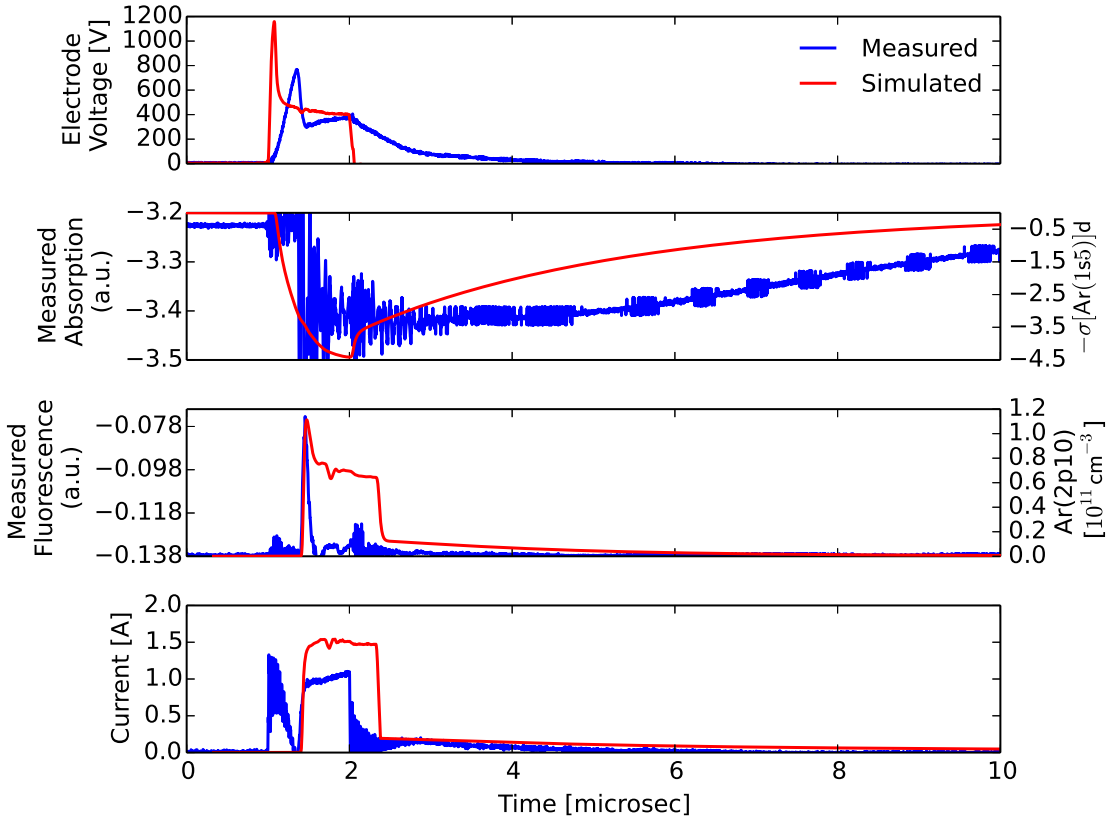

Figure 13. A comparison of the simulated and measured values for electrode voltage, $V_E = V_2 - V_3$ (top), $Ar(1s_5) + \hbar\omega \rightarrow Ar(2p_9)$ absorption (middle top), $Ar(2p_{10}) \rightarrow Ar(1s_5) + \hbar\omega$ fluorescence (middle bottom), and discharge current I_3 (bottom) for a 1 μs pulse. Radiation trapping for the $Ar(1s_4) \rightarrow Ar + \hbar\omega$ transition is included using the value of 5.6×10^5 s^{-1} measured by Han and Heaven [2014].

voltages. Absorption and fluorescence predictions closely follow the measured trends.

The time-dependent $Ar(1s_5)$ densities are displayed in Figure 16 for the different pulse widths. Peak metastable densities range between 3-4$\times 10^{12}$ cm^{-3}, occurring within 1 μs after pulse initiation. The 1 μs pulse experiences the fastest decay caused by the removal of the metastable production mechanism (by removing the applied voltage). However, the longer pulses also experience a rapid decay while the voltage is applied. For example, the 20 μs pulse scenario predicts a decrease in the metastable density from 3.7×10^{12} cm^{-3} to 7.6×10^{11} cm^{-3} over the duration of the pulse. Differences in the metastable decay rates for the 20 and 35 μs pulses are due to

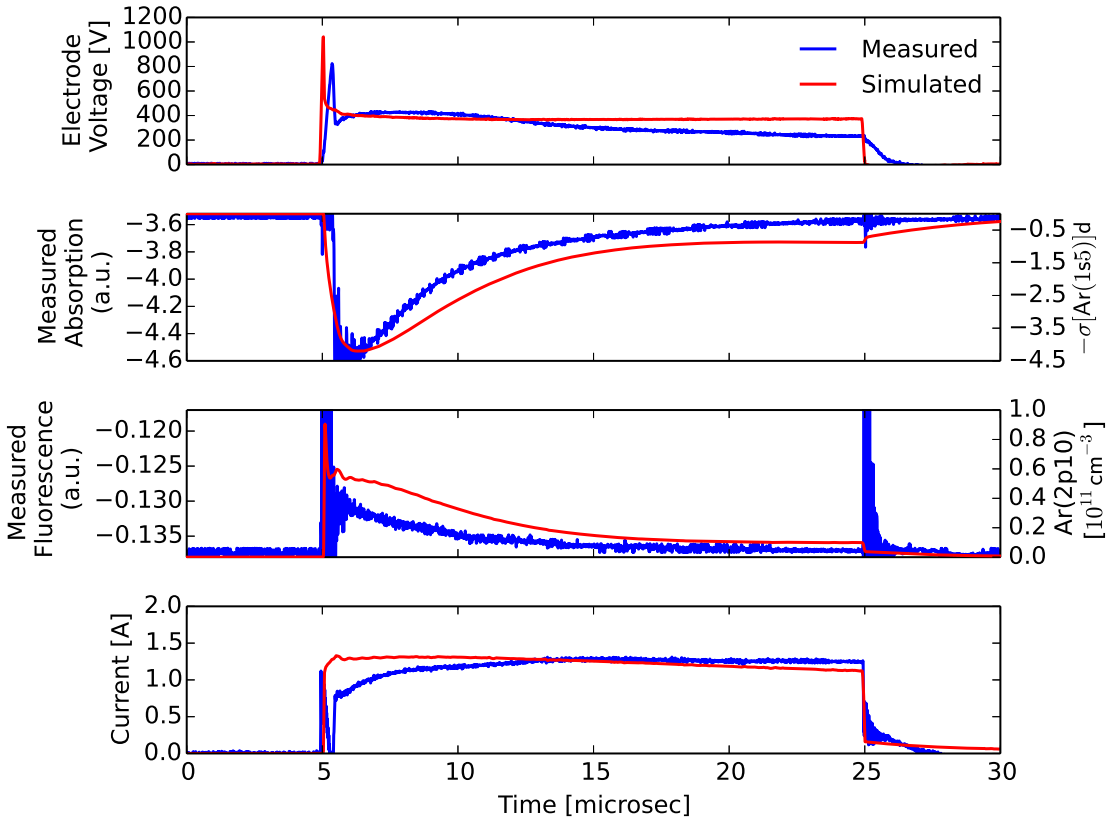

Figure 14. A comparison of the simulated and measured values for electrode voltage, $V_E = V_2 - V_3$ (top), $Ar(1s_5) + \hbar\omega \rightarrow Ar(2p_9)$ absorption (middle top), $Ar(2p_{10}) \rightarrow Ar(1s_5) + \hbar\omega$ fluorescence (middle bottom), and discharge current I_3 (bottom) for a 20 μs pulse.

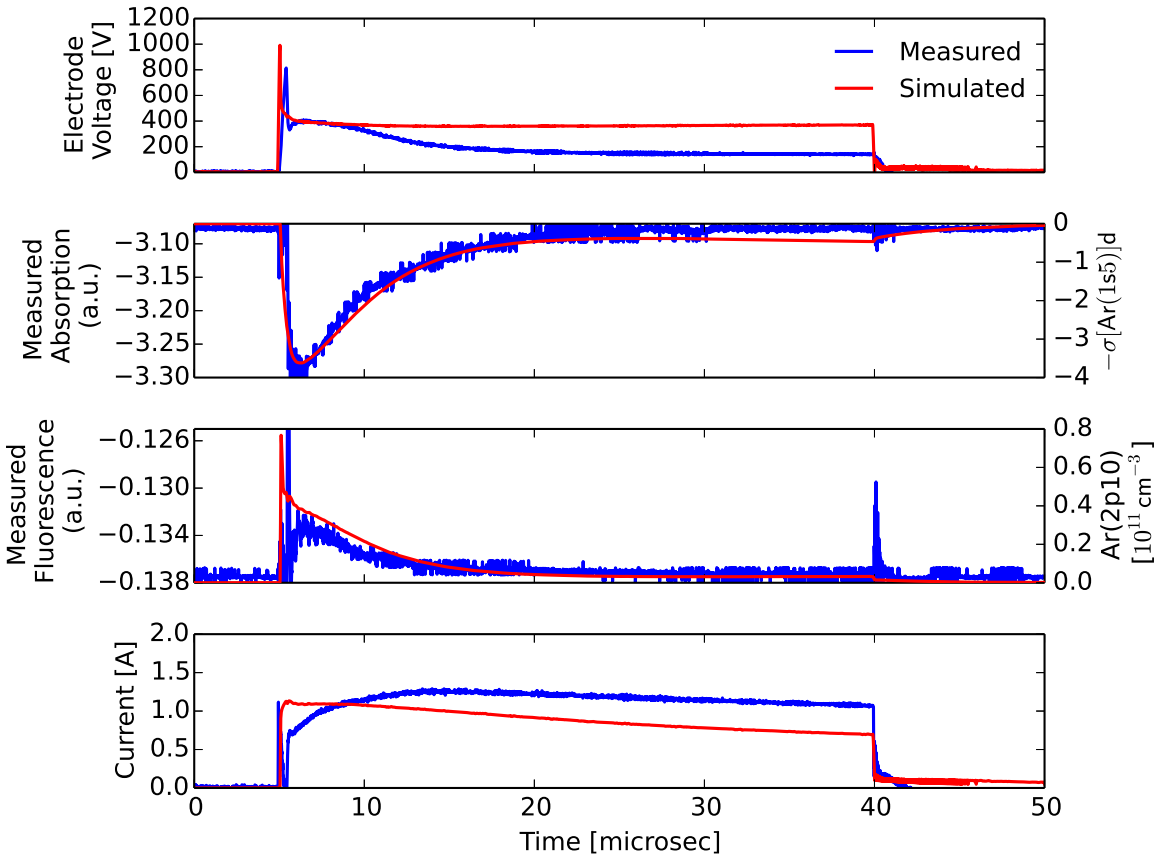

Figure 15. A comparison of the simulated and measured values for electrode voltage, $V_E = V_2 - V_3$ (top), $Ar(1s_5) + \hbar\omega \rightarrow Ar(2p_9)$ absorption (middle top), $Ar(2p_{10}) \rightarrow Ar(1s_5) + \hbar\omega$ fluorescence (middle bottom), and discharge current I_3 (bottom) for a 35 μs pulse.

differences in the applied voltage (Figure 11), with the 35 μs pulse having a lower applied voltage, and consequently, a lower steady-state metastable density.

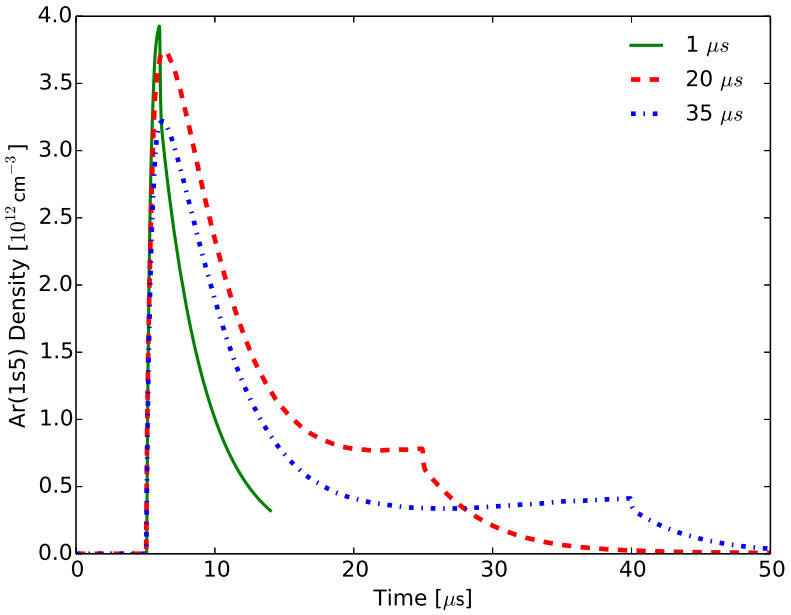

Figure 16. A comparison of the simulated metastable densities for the three pulse widths.

3.3 Kinetics and Sensitivity

To understand the time evolution of the densities, the chemical kinetics are analyzed for the 20 μs pulse scenario, using a simulated 1000 V pulse. In addition to an analysis of the reaction rates, PumpKin is employed to determine the dominant pathways.

Plasma kinetics are analyzed for the zero-dimensional model by investigating production and loss rates over time. The dominant electron production mechanism during breakdown is ionization from the ground state, $Ar + e^- \rightarrow Ar^+ + 2e^-$ (Figure 17). After breakdown, with the reduction in E/N and increase in Ar_2^* density, the dominant production rate becomes excimer ionization: $Ar_2^* + e^- \rightarrow Ar_2^+ + 2e^-$.

Throughout the simulation, dissociative recombination of Ar_2^+ is the dominant electron loss mechanism, followed by ambipolar diffusion. A large change occurs in the loss rates after pulse termination due to the ambipolar diffusion and dissociative recombination dependence on T_e. Once the external voltage is reduced, T_e experiences a large decrease, which decreases the ambipolar diffusion rate and increases the dissociative recombination rate.

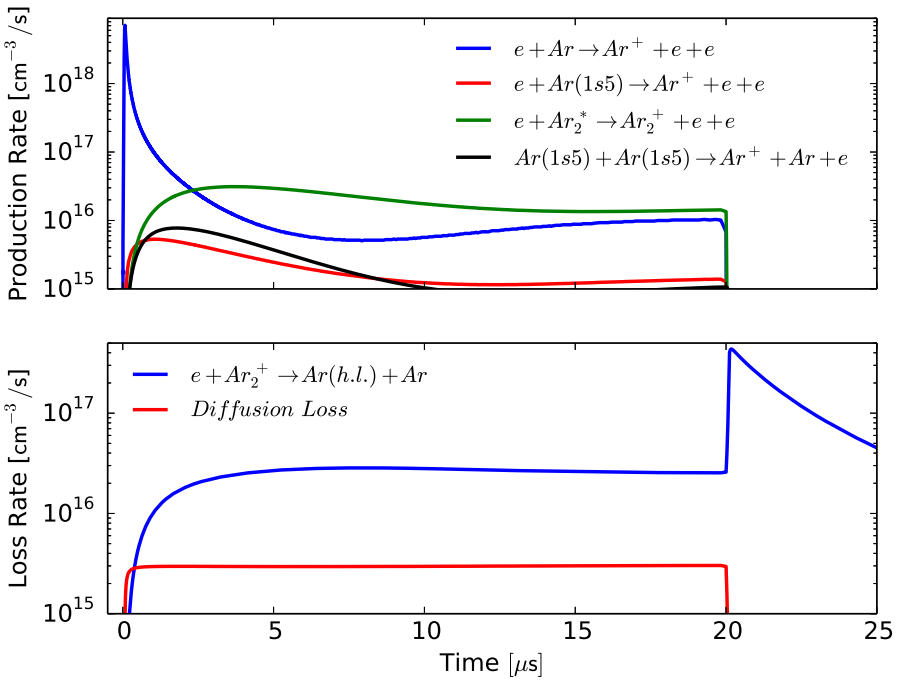

Figure 17. Positive column electron production and loss rates over time. The large increase in the dissociative recombination rate after pulse termination is caused by a large decrease in T_e due to the removal of the applied electric field.

Similar to the electron rates, the dominant $Ar(1s_5)$ production mechanism during breakdown is due to excitation from the ground state, $Ar + e^- \rightarrow Ar(1s_5) + e^-$ (Figure 18). After breakdown, the majority of $Ar(1s_5)$ is produced by electron or neutral de-excitation from $Ar(1s_4)$. The dominant loss rate, over all times, is caused by electron excitation to $Ar(1s_4)$. However, superelastic collisions reduce the overall loss rate of $Ar(1s_5)$. After pulse termination, the large decrease in T_e causes an increase in the $Ar(1s_5) + e^- \leftrightarrow Ar(1s_4) + e^-$ rates due to a collapse in the EEDF

towards lower energies and the relatively small energy difference between the $Ar(1s_5)$ and $Ar(1s_4)$ levels (~ 0.08 eV).

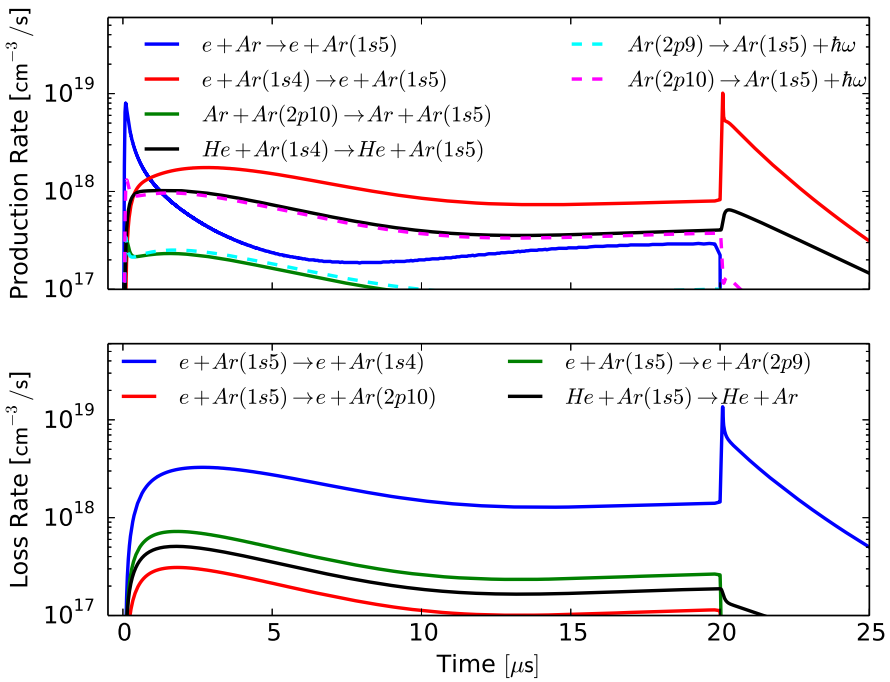

Figure 18. Positive column $Ar(1s_5)$ production and loss rates over time. After pulse termination, the decrease in T_e causes a collapse in the EEDF towards lower energies, which increases $Ar(1s_5) + e^- \leftrightarrow Ar(1s_4) + e^-$ rates.

Electron excitation of ground state Ar to $Ar(2p_9)$ shows a spike during breakdown, when E/N is large, followed by a decrease post breakdown (Figure 19). After breakdown, the majority of $Ar(2p_9)$ is produced through He collisions with $Ar(2p_8)$ and electron excitation from $Ar(1s_5)$. An important mechanism to OPRGL performance is collisional mixing of $Ar(2p)$ levels which is required to transfer pumped $Ar(2p_9)$ densities to $Ar(2p_{10})$. For the 7% Ar in He mixture, collisions with He are the dominant mixing mechanism, with almost equal rates to $Ar(2p_{10})$ and $Ar(2p_8)$. At 300 K, the rate coefficients for $Ar(2p_9) + He \rightarrow Ar(2p_{10}/2p_8) + He$ are in the range of $1.5 - 1.6 \times 10^{-11}$ cm^3/s, with the rate to $Ar(2p_{10})$ slightly larger than the rate to $Ar(2p_8)$. This indicates that a roughly equal number of optically pumped $Ar(2p_9)$ atoms will collisionally transition to the $Ar(2p_{10})$ and $Ar(2p_8)$.

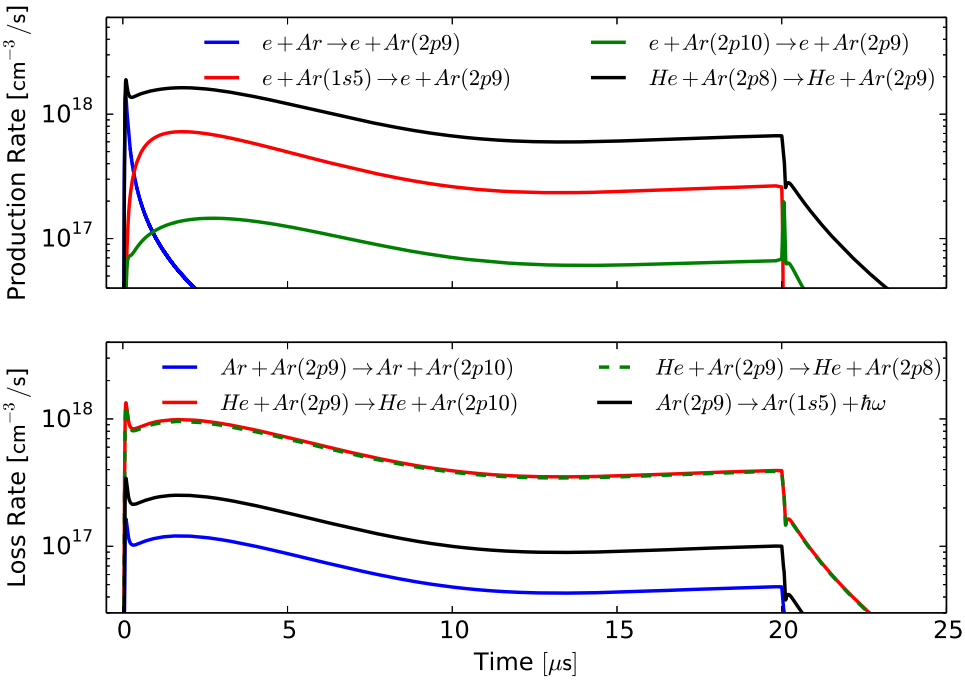

Figure 19. Positive column $Ar(2p_9)$ production and loss rates over time. The post-pulse He mixing rates follow the simulated $Ar(2p)$ densities (using the zero-dimensional model), which show a large decrease at pulse termination followed by a steady decay. After pulse termination, the decrease in T_e causes a collapse in the EEDF towards lower energies, which increases the $Ar(2p_{10}) + e^- \rightarrow Ar(2p_9) + e^-$ rate.

While the rate information by itself is useful, it does not provide enough information to form a complete picture due to the dependence of the rates on intermediate species densities. To analyze the principal pathways, PumpKin (Pathway redUction Method for Plasma KINetic models) is employed [Markosyan et al., 2014]. PumpKin calculates the principal pathways by using an algorithm based on branching at "fast" species. The fast species are calculated as species with a short lifetime relative to the other species. This algorithm determines the sequences of reactions responsible for creating and destroying a species of interest.

Applying PumpKin to the entire pulse period provides pathways matching the dominant rates discussed above, but also presents additional information about the reagents/products involved with the reactions (Table 5). For example, the dominant electron loss pathway is due to dissociative recombination via $Ar_2^+ + e^- \rightarrow Ar(h.l.) +$

Ar followed by radiation to the ground state: $Ar(h.l.) \rightarrow Ar + \hbar\omega$. The dominant electron production pathway early in the pulse is ionization of ground state Ar, which occurs during breakdown. Ionization of Ar_2^* through $Ar_2^* + e^- \rightarrow Ar_2^+ + 2e^-$ is the dominant pathway after breakdown.

Table 5. Electron, $Ar(1s_5)$, and $Ar(2p_9)$ principal pathways calculated by PumpKin over the entire pulse period. The pathways are in order by magnitude (larger rates first), and the arrows, $\Longrightarrow$, link the sequential reactions.

Species	Production or Loss	Principal Pathway
e^-	production	1) $Ar + e^- \rightarrow Ar^+ + 2e^-$
		2) $Ar_2^* + e^- \rightarrow Ar_2^+ + 2e^-$
	loss	1) $Ar_2^+ + e^- \rightarrow Ar(h.l.) + Ar \Longrightarrow Ar(h.l.) \rightarrow Ar + \hbar\omega$
		2) *ambipolar diffusion*
$Ar(1s_5)$	production	1) $Ar + e^- \rightarrow Ar(1s_5) + e^-$
		2) $Ar + e^- \rightarrow Ar(1s_4) + e^- \Longrightarrow Ar(1s_4) + e^- \rightarrow Ar(1s_5) + e^-$
	loss	1) $Ar(1s_5) + e^- \rightarrow Ar(1s_4) + e^- \Longrightarrow Ar(1s_4) \rightarrow Ar + \hbar\omega$
		2) $Ar(1s_5) + He \rightarrow Ar + He$
$Ar(2p_9)$	production	1) $Ar(1s_5) + e^- \rightarrow Ar(2p_9) + e^-$
		2) $Ar(1s_5) + e^- \rightarrow Ar(1s_4) + e^- \Longrightarrow Ar(1s_4) + e^- \rightarrow Ar(2p_8) + e^-$
		$\Longrightarrow Ar(2p_8) + He \rightarrow Ar(2p_9) + He$
	loss	1) $Ar(2p_9) + He \rightarrow Ar(2p_{10}) + He \Longrightarrow Ar(2p_{10}) \rightarrow Ar(1s_5) + \hbar\omega$
		2) $Ar(2p_9) \rightarrow Ar(1s_5) + \hbar\omega$

Concerning metastable production, the dominant pathway is simply electron excitation from the ground state. The second largest production pathway is due to electron excitation to $Ar(1s_4)$ followed by electron de-excitation through $Ar(1s_4) + e^- \rightarrow Ar(1s_5) + e^-$. Loss pathways include electron excitation from $Ar(1s_5)$ to $Ar(1s_4)$ followed by radiation to the ground state: $Ar(1s_4) \rightarrow Ar + \hbar\omega$. Neutral quenching by He, $Ar(1s_5) + He \rightarrow Ar + He$, is the second largest loss pathway. The importance of radiation trapping becomes apparent due to the loss mechanism involving radiation from $Ar(1s_4)$. Radiation from $Ar(1s_4)$ acts as a sink for the metastable density, and a lowered effective radiation rate caused by radiation trapping results in elevated concentrations of $Ar(1s_5)$.

Production pathways for $Ar(2p_9)$ are dominated by electron excitation from the $Ar(1s)$ manifold, either directly from $Ar(1s_5)$ or through $Ar(1s_4)$. Dominant loss pathways for $Ar(2p_9)$ are primarily through collisions with He to $Ar(2p_{10})$ followed

by radiation to $Ar(1s_5)$, or by radiation directly to $Ar(1s_5)$.

A sensitivity analysis is also performed to determine the simulation's dependence on the rate package. Using PumpKin, the principal pathways are calculated for each Ar species at two different time periods: breakdown (time of maximum E/N to 0.5 μs after), and after breakdown. Excited and ionic He species are ignored because of their minor role in the overall kinetics. Two time periods are required due to the difference in the kinetics during and after breakdown. Once the principal pathways are determined, they are filtered by removing pathways with contributions below a certain threshold.

The first reduced rate package is obtained by filtering all pathways contributing less than 10% of the total production or loss rate for each Ar species. Only the pathways contributing over 10% for either time period (breakdown or after breakdown) are added to the reduced package. Ambipolar diffusion is not considered a reaction, and all ambipolar diffusion rates are maintained in the reduced rate packages. This *Above 10%* rate package contains a total of 31 reactions (Table 6), compared to 175 for the *Full* package (Table 2). A second rate package is reduced even further, by only using the reactions associated with the dominant (top) pathway for each species (Table 7). This *Top Rates* package contains only 20 reactions.

A comparison of the simulated electrode voltage, absorption, fluorescence, and current for the three different rate packages (*Full*, *Above 10%*, and *Top Rates*) is displayed in Figure 20. The voltage and current simulations are almost identical for each of the rate packages, but the absorption and fluorescence simulations begin to diverge from the measurements as the number of reactions decrease. However, the difference between the *Full* and *Above 10%* rate packages is small, indicating that 31 reactions capture the majority of the kinetics, and most of the 175 reactions for the *Full* package do not make a large contribution.

Table 6. A list of the reactions forming the pathways that contribute above 10% of the total rate for any Ar species during either breakdown or after breakdown, according to a PumpKin analysis of the principal pathways for the 20 μs pulse scenario.

Reaction Type	Reaction
electron impact	$e^- + Ar \rightarrow e^- + e^- + Ar^+$
	$Ar_2^* + e^- \rightarrow Ar_2^+ + e^- + e^-$
	$e^- + Ar \rightarrow Ar(1s_5) + e^-$
	$e^- + Ar \rightarrow Ar(1s_4) + e^-$
	$e^- + Ar \rightarrow Ar(2p_{10}) + e^-$
	$e^- + Ar \rightarrow Ar(2p_9) + e^-$
	$e^- + Ar \rightarrow Ar(2p_8) + e^-$
	$e^- + Ar \rightarrow Ar(h.l.) + e^-$
	$e^- + Ar(1s_5) \rightarrow Ar(1s_4) + e^-$
	$e^- + Ar(1s_4) \rightarrow Ar(1s_5) + e^-$
	$e^- + Ar(1s_5) \rightarrow Ar(2p_9) + e^-$
	$e^- + Ar(1s_4) \rightarrow Ar(2p_8) + e^-$
	$Ar_2^+ + e^- \rightarrow Ar^+ + Ar + e^-$
	$Ar_2^* + e^- \rightarrow Ar + Ar + e^-$
recombination	$Ar_2^+ + e^- \rightarrow Ar(h.l.) + Ar$
two heavy body	$He + Ar(1s_5) \rightarrow He + Ar$
	$He + Ar(1s_4) \rightarrow Ar(1s_5) + He$
	$Ar + Ar(2p_{10}) \rightarrow Ar(1s_5) + Ar$
	$He + Ar(2p_9) \rightarrow Ar(2p_{10}) + He$
	$He + Ar(2p_8) \rightarrow Ar(2p_9) + He$
	$He + Ar(2p_9) \rightarrow Ar(2p_8) + He$
three heavy body	$Ar^+ + Ar + He \rightarrow Ar_2^+ + He$
	$Ar^+ + Ar + Ar \rightarrow Ar_2^+ + Ar$
	$Ar(1s_5) + Ar + He \rightarrow Ar_2^* + He$
	$Ar(1s_5) + Ar + Ar \rightarrow Ar_2^* + Ar$
	$Ar(1s_4) + Ar + He \rightarrow Ar_2^* + He$
radiative	$Ar(h.l.) \rightarrow Ar$
	$Ar(1s_4) \rightarrow Ar$
	$Ar(2p_{10}) \rightarrow Ar(1s_5)$
	$Ar(2p_9) \rightarrow Ar(1s_5)$
	$Ar_2^* \rightarrow Ar + Ar$

Table 7. A list of the reactions forming the dominant (top) pathway for any Ar species during either breakdown or after breakdown, according to a PumpKin analysis of the principal pathways for the 20 μs pulse scenario.

Reaction Type	Reaction
electron impact	$e^- + Ar \rightarrow e^- + e^- + Ar^+$
	$Ar_2^* + e^- \rightarrow Ar_2^+ + e^- + e^-$
	$e^- + Ar \rightarrow Ar(1s_5) + e^-$
	$e^- + Ar \rightarrow Ar(1s_4) + e^-$
	$e^- + Ar \rightarrow Ar(2p_{10}) + e^-$
	$e^- + Ar \rightarrow Ar(2p_9) + e^-$
	$e^- + Ar \rightarrow Ar(2p_8) + e^-$
	$e^- + Ar \rightarrow Ar(h.l.) + e^-$
	$e^- + Ar(1s_5) \rightarrow Ar(1s_4) + e^-$
	$e^- + Ar(1s_4) \rightarrow Ar(1s_5) + e^-$
	$Ar_2^+ + e^- \rightarrow Ar^+ + Ar + e^-$
recombination	$Ar_2^+ + e^- \rightarrow Ar(h.l.) + Ar$
two heavy body	$He + Ar(2p_9) \rightarrow Ar(2p_{10}) + He$
	$He + Ar(2p_8) \rightarrow Ar(2p_9) + He$
three heavy body	$Ar^+ + Ar + He \rightarrow Ar_2^+ + He$
	$Ar(1s_5) + Ar + He \rightarrow Ar_2^* + He$
radiative	$Ar(h.l.) \rightarrow Ar$
	$Ar(1s_4) \rightarrow Ar$
	$Ar(2p_{10}) \rightarrow Ar(1s_5)$
	$Ar_2^* \rightarrow Ar + Ar$

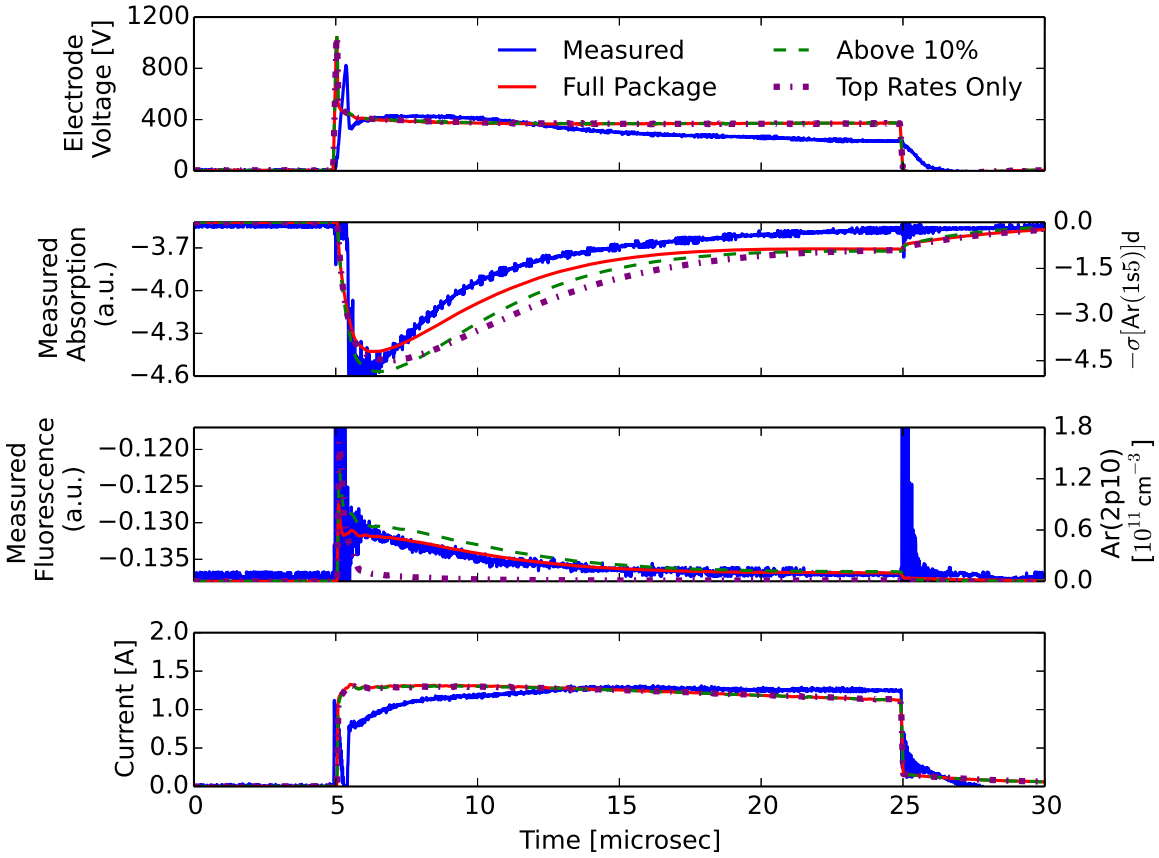

Figure 20. Simulated electrode voltage, absorption, fluorescence, and current for the 20 μs pulse scenario using a variety of reaction rate packages: full rate package, excluding pathways below 10% of the total rate for each species, and only the top pathways for each species.

During the pulse, the metastable densities from the *Above 10%* rate package are within 30% of the densities predicted by the *Full*, as displayed in Figure 21. The *Top Rates* package shows a larger difference of approximately 50% during the pulse. Near the end of the pulse, simulated metastable densities are nearly equal for the three rate packages.

The $Ar(2p_{10})$ densities show a strong dependence on the rate package, with a significant increase in the decay rate for the *Top Rates* versus *Full* packages (Figure 22). Both of the reduced rate packages overestimate the initial $Ar(2p_{10})$ production, with a 120% overestimation for the *Top Rates* package. Similar to the $Ar(1s_5)$ densities, the relative difference between the *Full* and *Above 10%* packages are within approx-

imately 30%. However, the *Top Rates* package shows a large difference, essentially dropping to a zero density shortly after pulse initiation.

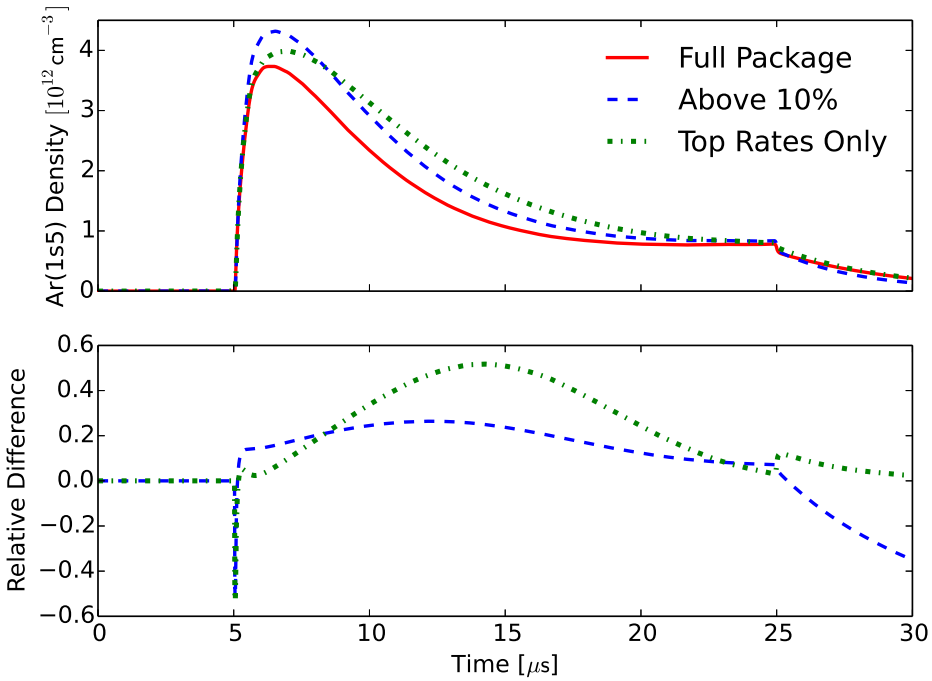

Figure 21. Simulated $Ar(1s_5)$ densities for a 20 μs pulse, using the full reaction rate package and two reduced packages, along with the relative difference between the reduced rate packages compared to the full rate package.

While the *Top Rates* package shows a large difference in the $Ar(2p_{10})$ simulations, the metastable densities are within 50% of the *Full* package simulations. If metastable densities are the focus of a kinetic analysis, then the much reduced *Top Rates* package may suffice. The *Above 10%* rate package closely resembles the *Full* package simulations, indicating that a reduced rate package of only 31 of the key reactions may be sufficient for many modeling efforts.

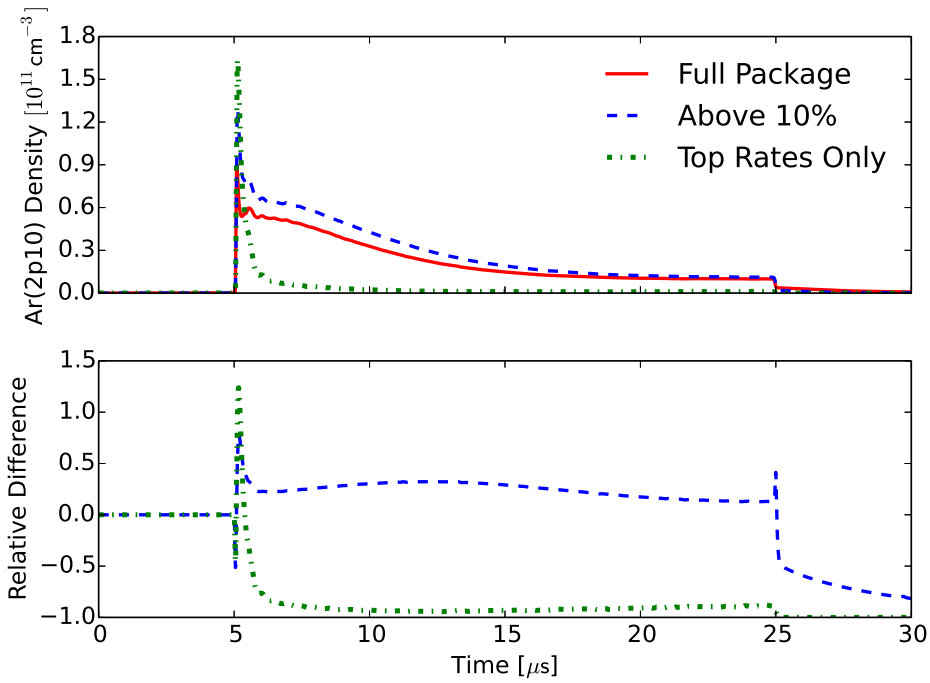

Figure 22. Simulated $Ar(2p_{10})$ densities for a 20 μs pulse, using the full reaction rate package and two reduced packages, along with the relative difference between the reduced rate packages compared to the full rate package.

3.4 Zero and One-Dimensional Model Comparison

Simulations are repeated for the 1000 V, 20 μs pulse using a one-dimensional fluid model. A comparison between the zero and one-dimensional models is performed over time by selecting a representative position in the positive column of the one-dimensional model, here taken to be 3.5 mm from the cathode. Results from the one-dimensional model at the 3.5 mm position are then compared to the zero-dimensional model over time.

Voltages, electron temperatures, reduced electric fields, and current densities simulated by the models show excellent agreement over time in the positive column (Figure 23). During breakdown, the electron density increases and current begins to flow. As the current flows across the ballast resistor the electrode voltage, V_E, is reduced from 1000 V to approximately 400 V. This decrease in V_E in combination with the formation of a cathode fall reduces the positive column E/N from the peak

value of 23 Td during breakdown to 4-5 Td post-breakdown. Similarly, the positive column electron temperature experiences a reduction from approximately 4 eV to 2 eV due to the reduction in E/N. After pulse termination, the electron temperature rapidly approaches the neutral gas temperature.

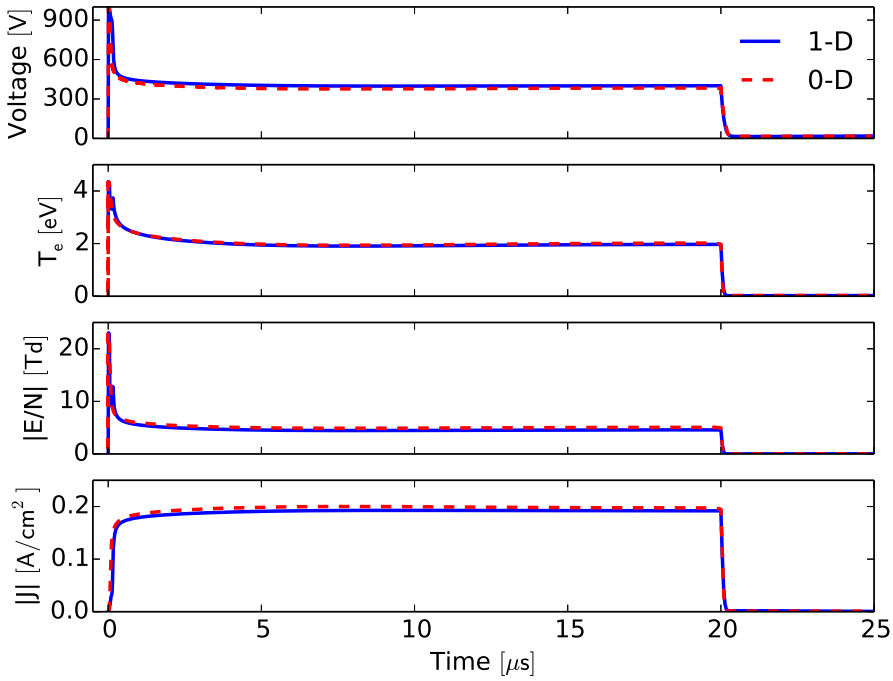

Figure 23. Electrode voltage, positive column T_e, E/N magnitude, and current density magnitude over time for the 20 μs pulse.

Electron densities in the positive column show a rapid increase during breakdown, followed by an almost constant magnitude during the remainder of the pulse, as shown in Figure 24. Initially, Ar^+ is the dominant ion, but three-body collisions at atmospheric pressures convert Ar^+ to $HeAr^+$ and Ar_2^+ throughout the pulse duration. The $\sim$ 0.02 eV binding energy of $HeAr^+$ allows for rapid dissociation by neutral collisions, $HeAr^+ + M \rightarrow Ar^+ + He + M$, and yields a positive column $HeAr^+$ density of approximately 10^9 cm^{-3}. The $\sim$ 1.26 eV binding energy of Ar_2^+ yields dissociation rates due to neutral collisions, $Ar_2^+ + M \rightarrow Ar^+ + Ar + M$, that are insignificant at 300 K. As a result, Ar_2^+ quickly becomes the dominant ion with a positive column density of $\sim 6 \times 10^{11}$ cm^{-3}, which is also displayed in Figure 24.

After pulse termination, electron and ion densities decay rapidly due to the removal of the large voltage required to sustain the glow discharge. The one and zero-dimensional models show reasonable agreement throughout the pulse duration, with slightly lower electron densities predicted by the zero-dimensional model. Both models predict a temporal variation in electron and ion densities before pulse termination, indicating that a steady-state is not reached over the pulse duration.

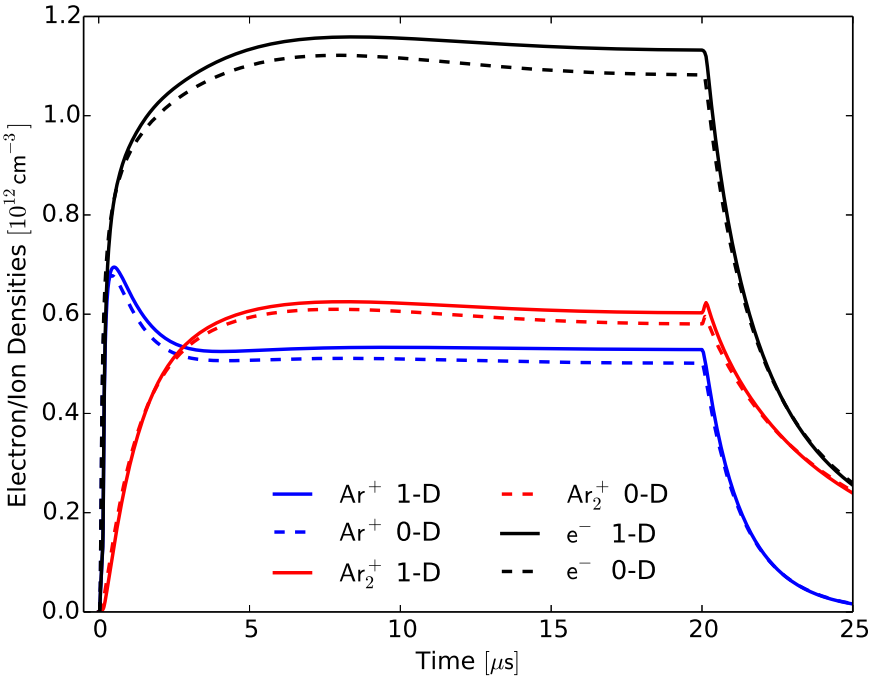

Figure 24. Positive column electron and ion densities over time for the 20 μs pulse.

Excited species densities show peaks during breakdown followed by a decay throughout the remainder of the pulse (Figure 25), qualitatively matching the $Ar(1s_5)$ absorption and $Ar(2p_{10})$ fluorescence measurements by Han et al. [2016]. Densities of the $Ar(1s)$ species show a smooth decay while the $Ar(2p)$ species show a large initial spike. This behavior is due to electron excitation from ground state following $Ar + e^- \rightarrow Ar^* + e^-$, where excitation to the $Ar(1s)$ manifold is maintained at the post-breakdown E/N magnitudes while $Ar(2p)$ manifold excitation is drastically reduced after breakdown. The zero and one-dimensional simulations are in agreement

throughout the pulse and after pulse termination.

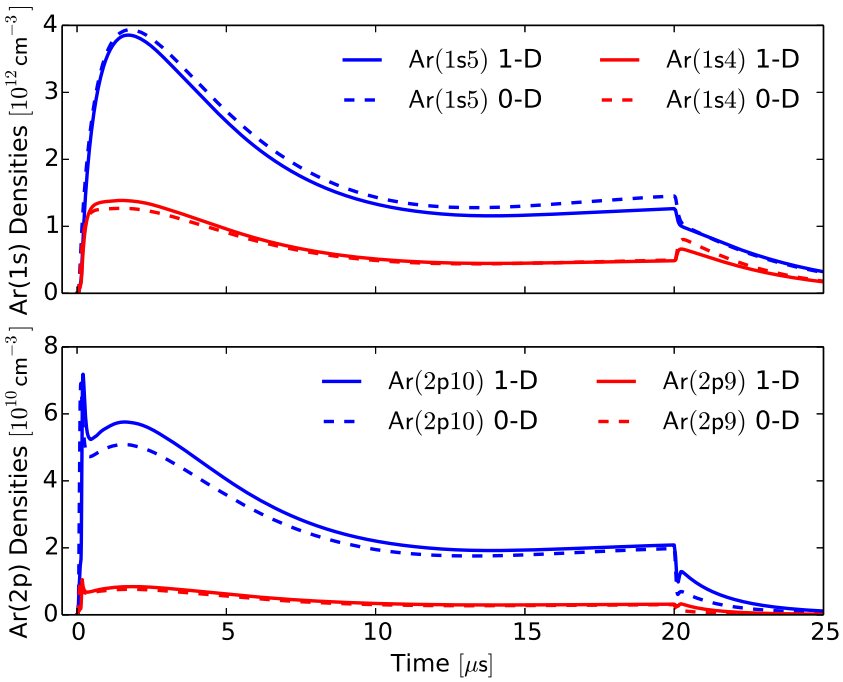

Figure 25. Positive column $Ar(1s)$ and $Ar(2p)$ densities over time for the 20 μs pulse.

One-dimensional spatial distributions are analyzed at the end of the pulse (20 μs), as the discharge approaches a steady-state. In the one-dimensional model, the cathode is located at $x = 0$ mm with the anode at $x = 5$ mm. Voltage, T_e, and E/N show agreement between the zero and one-dimensional models in the positive column (Figure 26). As expected, a large voltage drop of ~ 215 V is observed near the cathode, giving rise to a large E/N magnitude, which in turn elevates the local T_e. An E/N magnitude of approximately 380 Td gives rise to a T_e of 11 eV near the cathode. A positive column E/N magnitude of 4-5 Td produces an electron temperature of approximately 2 eV. Near the anode, a slight increase in E/N magnitude and T_e are observed due to a voltage drop of approximately 3 V occurring over ~ 30 μm.

Figure 27 displays electron and ion densities versus position near the end of the pulse, and shows agreement between the zero and one-dimensional models in the positive column. Peak Ar^+ and electron densities are observed in the cathode layer

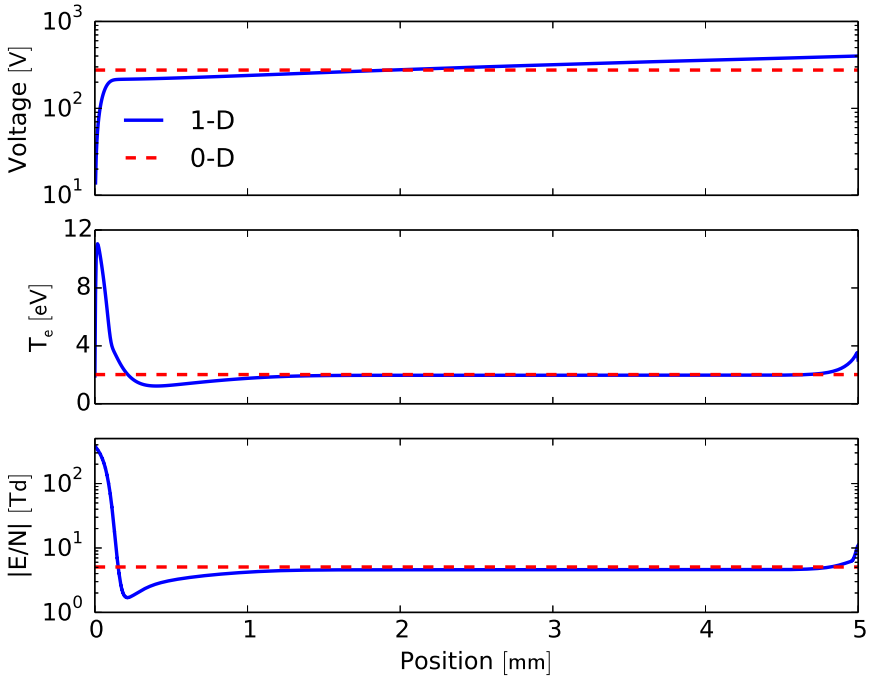

Figure 26. Spatial profile of voltage, T_e, and E/N magnitude at the end of the 20 μs pulse.

due to ionization rate dependence on E/N. In the positive column, Ar_2^+ is the dominant ion with densities $\sim 15\%$ larger than Ar^+. However, Ar^+ is the dominant ion near the electrodes. The low binding energy of $HeAr^+$ together with the reaction $HeAr^+ + M \rightarrow Ar^+ + He + M$ yield $HeAr^+$ densities of $\sim 10^{11}$ cm^{-3} in the cathode layer and $\sim 10^9$ cm^{-3} elsewhere in the cavity.

Similarly, excited species densities simulated by the two models are nearly equal in the positive column (Figure 28). Peak densities are observed in the cathode layer where E/N and T_e are elevated, increasing the excitation rates. Excitation rates are also increased near the anode following the increase in E/N magnitude and T_e. This spatial information is vital to operation of an OPRGL, due to the dependence of laser intensity on the metastable density. The measured distribution of laser intensity was found to follow a similar pattern [Han et al., 2016], with a large peak in intensity near the cathode. However, the measured peak was found to take place approximately 1 mm from the cathode while the simulations show the peak 0.1 mm from the cathode.

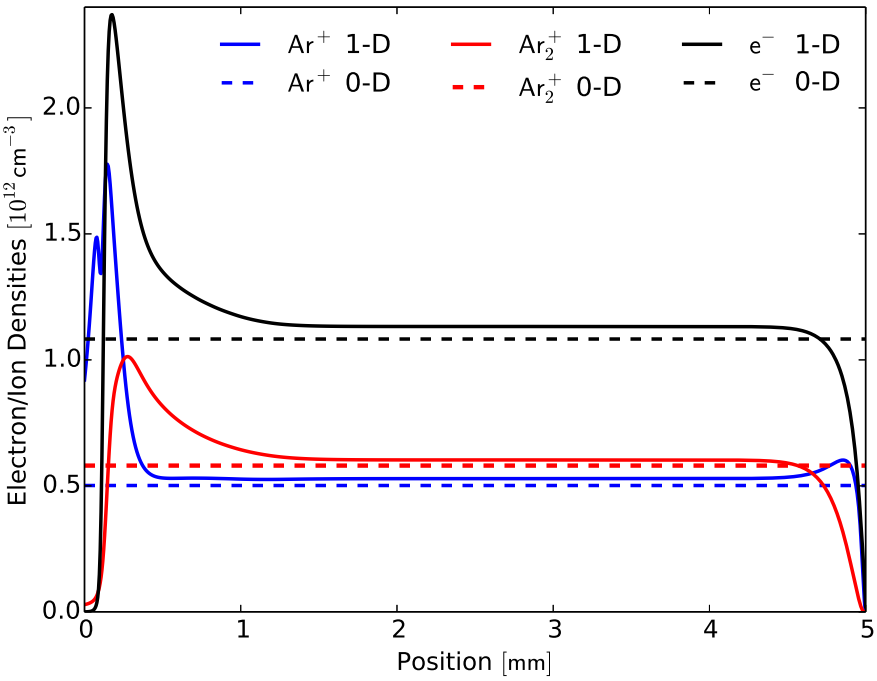

Figure 27. Spatial profile of electron and ion densities at the end of the 20 μs pulse.

This difference is most likely due to the non-local ionization/excitation behavior in the cathode layer and negative glow, which is underestimated using fluid approximations [Fiala et al., 1994; Lymberopoulos and Economou, 1995]. A hybrid kinetic-fluid model would provide more insight into the electron behavior near the electrodes.

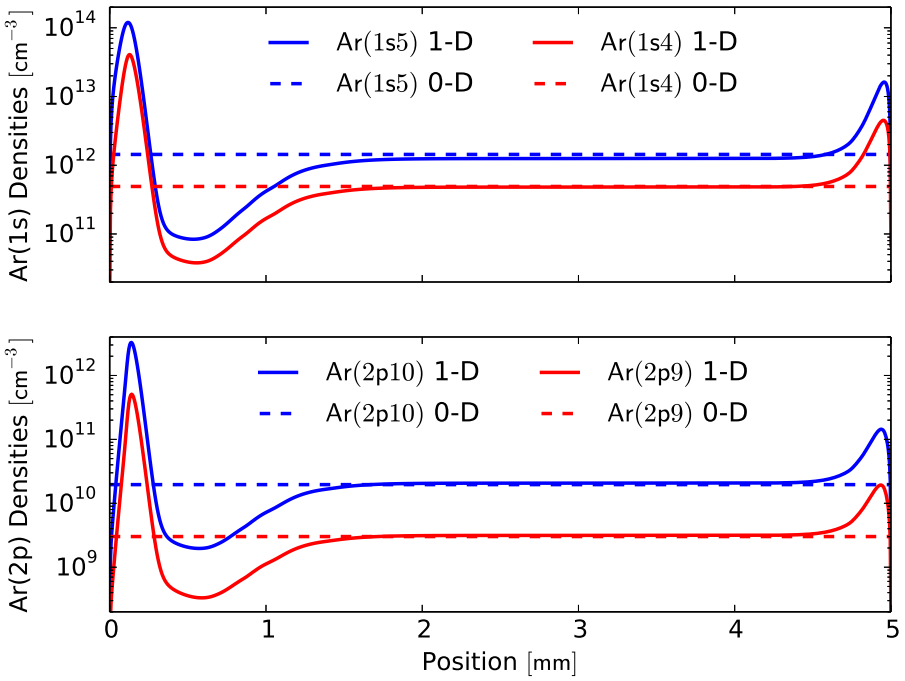

Figure 28. Spatial profile of $Ar(1s)$ and $Ar(2p)$ densities at the end of the 20 μs pulse.

3.5 Variable EEDF Calculations

One-dimensional simulations using rate coefficients extracted from BOLSIG+ require a look-up table of the rate coefficients as a function of T_e to calculate the reaction source terms for the spatial T_e profiles. Following the example provided by COMSOL^{TM}, the rate coefficient look-up tables are calculated before the one-dimensional simulations using estimated densities to calculate the EEDFs. While an initial simulation performed with ZDPlasKin provides a decent estimate of the positive column densities, it is uncertain how this method affects the rate coefficients near the sheaths where the excited species densities are orders of magnitude larger than the positive column densities.

To test the effect of a time varying EEDF calculation on the one-dimensional fluid simulations, results are compared 10 μs after pulse initiation for two methods of calculating the EEDF. The first method uses a pre-run ZDPlasKin simulation of the positive column to estimate densities and provide a constant look-up EEDF table.

The second method uses the densities simulated by the one-dimensional fluid model to update the EEDF look-up table after each simulated microsecond. This variable EEDF calculation uses two sets of EEDFs to provide an EEDF table for each position: one derived from the positive column densities extracted at the 3.5 mm position, and the other from the negative glow where the metastable densities are largest. The two sets of EEDFs are then linearly interpolated at each position, i, based on the current metastable density, $[Ar(1s5)]_i$:

$$EEDF_i = \left(\frac{[Ar(1s5)]_i - [Ar(1s_5)]_{PC}}{[Ar(1s5)]_{peak} - [Ar(1s_5)]_{PC}} \right) EEDF_{peak} + \left(1 - \frac{[Ar(1s5)]_i - [Ar(1s_5)]_{PC}}{[Ar(1s5)]_{peak} - [Ar(1s_5)]_{PC}} \right) EEDF_{PC}, \quad (117)$$

where $EEDF_i$ is the EEDF calculated for position i, $EEDF_{peak}$ is the EEDF calculated for the negative glow with a peak metastable density $[Ar(1s5)]_{peak}$, and $EEDF_{PC}$ is the EEDF calculated for the positive column metastable density $[Ar(1s5)]_{PC}$. In the Faraday dark space, where metastable densities are less than the positive column densities, the EEDF is set to the positive column EEDF. This variable EEDF table updates the EEDFs over time and accounts for differences in the EEDFs due to spatially varying densities.

The calculated electron temperatures for the variable and constant EEDF scenarios 10 μs after pulse initiation are displayed in Figure 29. A peak relative difference of approximately 3% (relative to the constant EEDF) is observed near the minimum T_e, indicating a minor change for the two methods. Electron densities show similar predictions for the two methods, with a maximum relative difference of 4% at the peak electron density (Figure 30). Metastable densities show a slightly larger variation between the two methods with a peak difference of 12% in the transition region between the negative glow and the Faraday dark space (Figure 31). However, the

positive column $Ar(1s_5)$ densities are nearly equal.

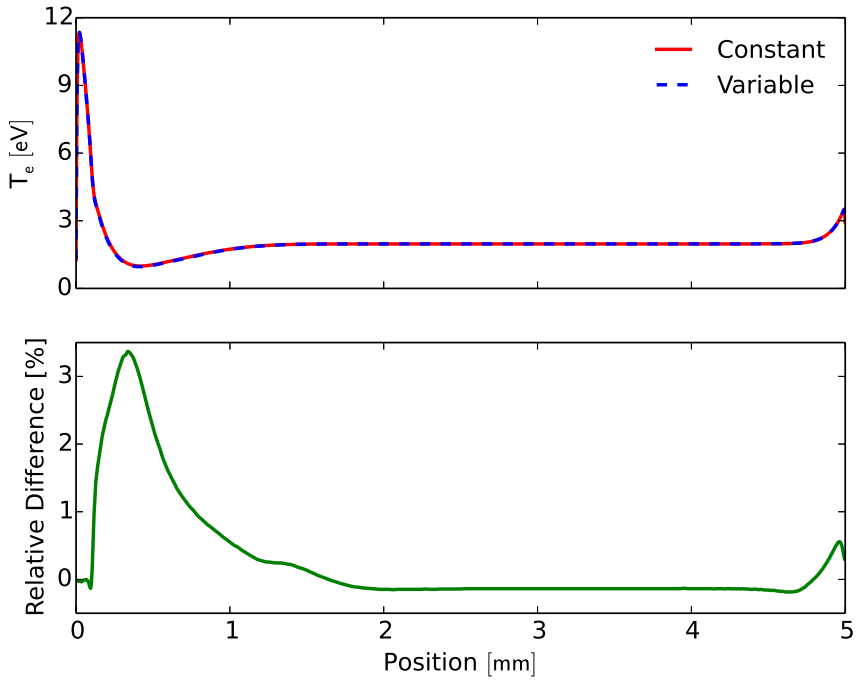

Figure 29. Spatial electron temperature profiles 10 μs after pulse initiation using constant and variable EEDF calculations.

A comparison of the EEDFs calculated using the two methods is displayed in Figure 32. The variable method calculates two sets of EEDFs based on the densities in the positive column and the densities in the negative glow. The constant EEDF method calculates a single set of EEDFs based on the positive column densities estimated by ZDPlasKin. For the peak electron temperature of 11 eV, the EEDFs calculated by the two methods are nearly identical, indicating a minor change in rate coefficients for the large values of T_e. The EEDFs calculated for the positive column electron temperatures of 2 eV show agreement for energies below the $Ar(1s_5)$ excitation threshold, then begin to diverge at higher energies. However, the EEDF values are on the order of 10^{-7} $eV^{-3/2}$ or below when differences above 10% occur, which renders the rate coefficients virtually unchanged as indicated by the agreement in the positive column displayed in Figures 29 to 31.

A comparison of the EEDFs calculated for a variety of electron temperatures is

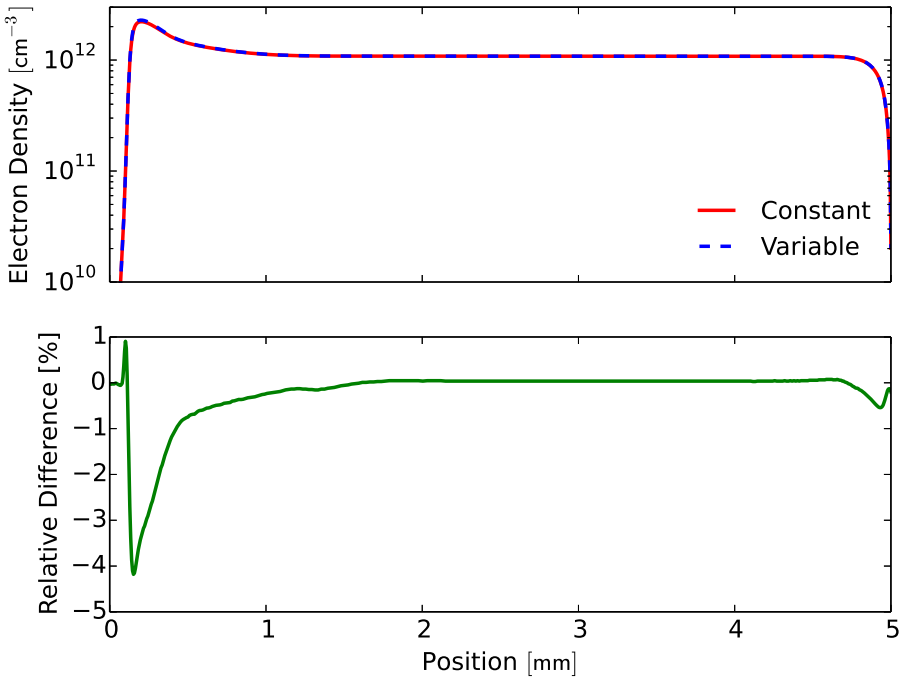

Figure 30. Spatial electron density profiles 10 μs after pulse initiation using constant and variable EEDF calculations.

displayed in Figure 33. The three sets of EEDFs correspond to the densities derived from ZDPlasKin for the constant EEDF and the two sets of densities used in the variable EEDF calculations based on the positive column and negative glow densities from the one-dimensional fluid model. The constant and variable EEDFs calculated using the positive column densities are nearly identical over all electron temperatures. At lower electron temperatures, the variable EEDFs calculated using negative glow densities shows an increase in energetic electrons due to superelastic collisions. As the excited species densities are two orders of magnitude larger than the positive column densities, the contribution of superelastic collisions to the high energy electrons becomes significant. However, at electron temperatures above 8 eV, as observed in the cathode layer, all three sets of EEDFs are nearly identical. This indicates that the contribution of superelastic collisions becomes insignificant at elevated electron temperatures.

Overall, the difference between the two methods is small, indicating that a pre-

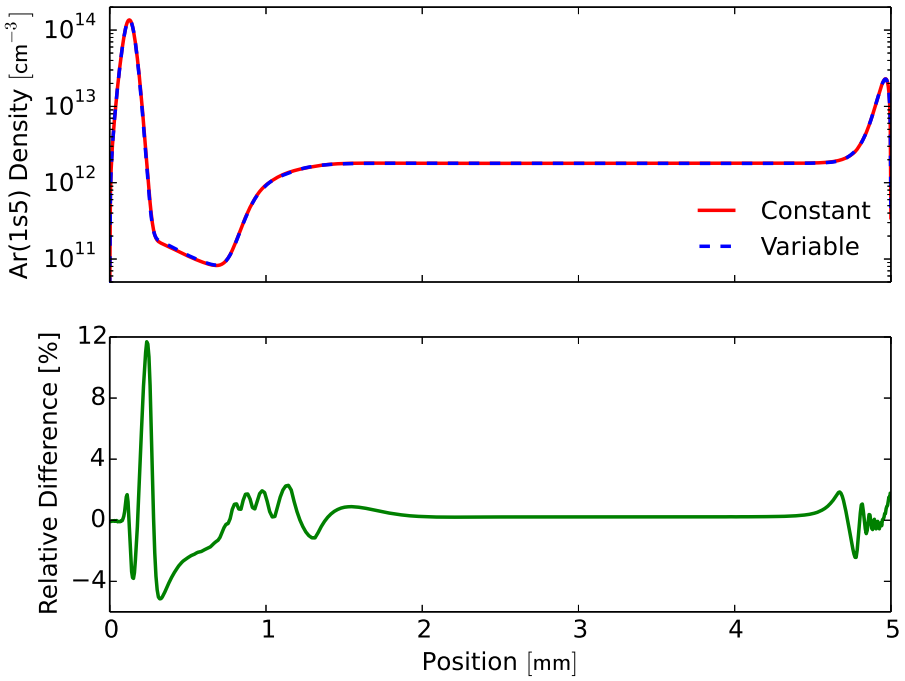

Figure 31. Spatial $Ar(1s_5)$ density profiles 10 μs after pulse initiation using constant and variable EEDF calculations.

run look-up table based on ZDPlasKin simulations of the positive column provides a viable method of obtaining electron impact rate coefficients for one-dimensional fluid simulations. In the positive column, which is the region of interest for an OPRGL, the agreement between the constant and variable EEDF techniques is excellent.

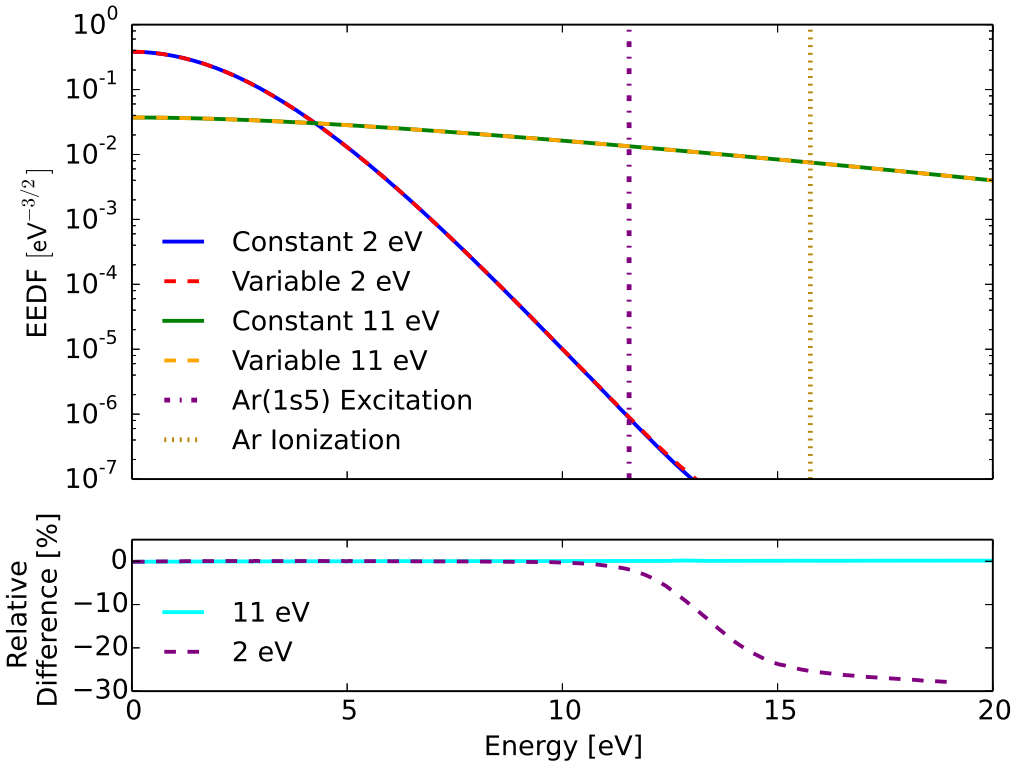

Figure 32. EEDFs calculated using the variable and constant methods for the electron temperatures of 2 and 11 eV corresponding to the positive column and cathode sheath, respectively. The variable EEDF method calculates two EEDFs: one for the positive column densities and one for the negative glow densities.

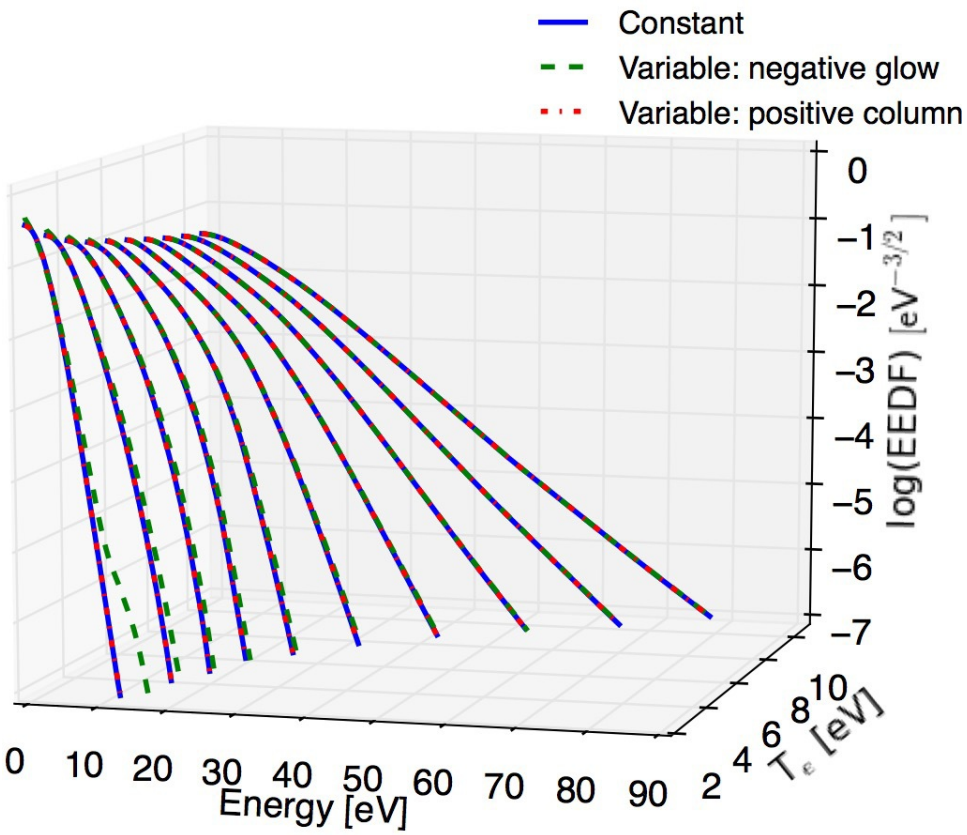

Figure 33. EEDFs calculated for a variety of electron temperatures using the three sets of densities implemented in the constant and variable EEDF calculations. The constant EEDFs are calculated using densities from ZDPlasKin prior to the one-dimensional simulations. The negative glow and positive column EEDFs are calculated using the negative glow and positive column densities from the one-dimensional simulations, which are linearly interpolated to provide a variable EEDF.

3.6 Conclusions

Simulations of a 7% Ar in He pulsed DC discharge at a pressure of 270 Torr are performed for 1000 V pulses with temporal widths of 1, 20, and 35 μs using a zero-dimensional kinetic model. Species relevant to the operation of an optically pumped rare gas laser are analyzed over a single pulse duration to identify key kinetic pathways. Comparisons to the experimental voltage, current, fluorescence, and absorption measurements by Han et al. [2016] show temporal agreement. The inclusion of radiation trapping for the $Ar(1s_4) \rightarrow Ar + \hbar\omega$ transition decreases post-pulse metastable decay rates, matching the measured trends.

One-dimensional fluid simulations are also performed for the 20 μs, 1000 V scenario, providing spatial density profiles. Comparisons of the zero and one-dimensional models show agreement in the positive column, where the zero-dimensional model is appropriate. Both models predict a spike in excitation and ionization rates during breakdown due to elevated voltage, E/N magnitude, and T_e during pulse initiation. After breakdown, the combination of a reduced electrode voltage and cathode fall formation results in a factor of 5 decrease in the positive column E/N. This reduction in E/N drastically decreases Ar excitation and ionization via electron impact, with an order of magnitude reduction in excitation rates and a two order of magnitude reduction in ionization rate within 2 μs after breakdown.

Electron densities steadily approach a constant value while the dominant ion shifts from Ar^+ to Ar_2^+ over the pulse duration due to three-body collisions. For the geometry and simulated discharge conditions, dissociative recombination is found to be the dominant electron loss mechanism. Metastable loss rates rapidly increase post-breakdown, resulting in peak metastable densities near 4×10^{12} cm^{-3}, decreasing by a factor of 3 over the pulse duration. Radiation trapping plays a key role in metastable decay rates through the reaction sequence $Ar(1s_5) + e^- \rightarrow Ar(1s_4) + e^-$

followed by $Ar(1s_4) \rightarrow Ar + \hbar\omega$. The $Ar(2p)$ species display initial spikes followed by an immediate reduction in density after breakdown due to the reduced electron excitation rates from ground state at the post-breakdown E/N. Collisions with He are observed to be responsible for $Ar(2p_9)$ loss, with an almost equal transfer to the $Ar(2p_{10})$ and $Ar(2p_8)$ levels. As expected, excited species densities are largest near the cathode layer, with a two order of magnitude difference between the peak and positive column densities.

A sensitivity analysis of the reaction rate package is also performed, pinpointing the dominant pathways for each species. The number of reactions are reduced by placing a threshold on pathway contributions to the total rate for each species during breakdown and after breakdown. Reducing the number of reactions from 175 to 31 produces a minor change in the simulation results. Further reducing the number of reactions to 20 creates a noticeable difference in the simulations with a factor of 1.5 difference in the metastable densities during the pulse, compared to the full rate package. This sensitivity analysis is performed at a pressure of 270 Torr for a 7% Ar in He mixture, and cannot be extended to all Ar-He discharge scenarios.

An analysis of the one-dimensional fluid model dependence on EEDF calculations is also performed, showing a slight difference between the two methods of calculating the EEDFs. The first method relies on EEDFs calculated from the positive column densities predicted by ZDPlasKin, which is run prior to the fluid model to provide a lookup table of rate coefficients based on the local T_e. The second method calculates a set of EEDFs for the fluid model densities predicted in the negative glow and a separate set of EEDFs for the positive column densities. These two sets of EEDFs are then interpolated to provide an EEDF based on the metastable density at each position. The positive column electron temperatures, electron densities, and metastable densities are nearly equal for the two approaches, verifying the use of pre-calculated

EEDFs for simulations of the positive column.

The metastable $Ar(1s_5)$ densities are highly dependent on the reduced electric field, E/N. Furthermore, laser performance also depends strongly on $Ar(1s_5)$ densities. As a result, efforts to maintain an elevated E/N over large active volumes will be helpful in OPRGL development.

IV. Radio Frequency Dielectric Barrier Discharge

Optically pumped rare gas lasers that employ Ar as the lasing media require sufficient production of $Ar(1s_5)$ to act as the lowest energy species of the laser system [Han et al., 2014]. Diode pumping from $Ar(1s_5)$ to $Ar(2p_9)$ followed by rapid collisional relaxation from $Ar(2p_9)$ to $Ar(2p_{10})$ allows for a population inversion and subsequent lasing to $Ar(1s_5)$. The dependence of diode laser absorption and optical gain on $Ar(1s_5)$ densities [Rawlins et al., 2015; Demyanov et al., 2013] requires metastable densities on the order of 10^{13} cm^{-3} at atmospheric pressures to produce output laser intensities above 100 W/cm^2 for an active medium length of 1.9 cm [Han et al., 2014]. Near-atmospheric pressures help to match the diode laser bandwidth to the $Ar(1s_5) + \hbar\omega \rightarrow Ar(2p_9)$ absorption linewidth and increase the non-adiabatic transition rate from $Ar(2p_9)$ to $Ar(2p_{10})$. Thermal instabilities are problematic at these higher pressures [Haas, 1973; Napartovich, 2001; Fridman et al., 2005], but radio frequency (RF) dielectric barrier discharges (DBDs) are able to maintain stability due to a limited ionization period occurring near the cycle peaks and an increased energy threshold for instability formation [Raizer et al., 1995].

Previous kinetic analyses of Ar-He mixtures in an OPRGL have been performed to find the optimal Ar-fraction and pressure for laser efficiency. One kinetic study analyzed laser efficiency as a function of pressure and Ar-He composition for a non-specific discharge scenario, concluding that a mixture of approximately 1% Ar in He results in the largest total efficiency, defined as the output power divided by the sum of discharge and pump powers [Demyanov et al., 2013]. A separate experimental and computational analysis of microwave resonator-driven microplasmas at a variety of Ar-He mixtures and pressures ranging from 100-730 Torr found that an Ar-fraction near 5% at a pressure of 100 Torr produces the largest metastable densities [Hoskinson et al., 2016]. Additionally, peak metastable densities were found to decrease as the

discharge pressure was increased. The metastable density trends as a function of Ar-He mixture presented in this document for an RF-DBD deviate from the trends observed for microwave resonator-driven microplasmas, most likely due to differences in discharge conditions and cavity size.

This chapter analyzes the $Ar(1s_5)$ metastable density as a function of Ar-fraction, pressure, and voltage for an RF-DBD. A one-dimensional fluid model is used to calculate metastable density dependence on Ar-fraction, pressure, and applied voltage. Simulated fluorescence from the one-dimensional fluid model is compared with experiment in the centerline of the discharge cavity. The α to γ-mode transition for a 15% Ar in He mixture at a pressure of 200 Torr is simulated as a part the analysis as a function of applied voltage. Additionally, a zero-dimensional effective DC model of the bulk plasma is implemented and compared to the one-dimensional simulations. Due to the relatively large computational time required for the one-dimensional RF-DBD simulations, use of the zero-dimensional approach is preferable in the bulk plasma where the model is appropriate. A simplified zero-dimensional model is also developed, providing insight into the key kinetics controlling metastable behavior as a function of pressure and Ar-fraction.

4.1 Models

Electron impact rate coefficients and transport parameters are calculated using BOLSIG+ [Hagelaar and Pitchford, 2005]. Rate coefficients for electron impact collisions are computed from the non-Maxwellian electron energy distribution function along with the reaction cross section. The EEDF is dependent on species densities and the reduced electric field, E/N. A one-to-one mapping of E/N to the electron temperature, $T_e = 2\langle\epsilon\rangle/3$ where $\langle\epsilon\rangle$ is the average electron energy, provides a unique EEDF for a given T_e, allowing T_e to be used as a proxy for E/N during EEDF com-

putation. Additionally, for a driving angular frequency of $\omega = 2\pi \times 13.56$ MHz in the pressure range of 200-500 Torr, the reduced angular frequency ω/N is on the order of 10^{-17} m^3/s, which allows the EEDFs to be calculated using a DC field [Hagelaar and Pitchford, 2005].

The EEDF dependence on Ar-He mixture is displayed in Figure 34 for an electron temperature of 2 eV. As the fraction of He is increased, the population of high-energy (above excitation and ionization thresholds) electrons increases, approaching a Maxwellian distribution. This increase in the population of high-energy electrons increases the Ar excitation and ionization rate coefficients. However, the electron excitation and ionization rates also depend on the Ar density, $[Ar]$, which increases with Ar-fraction. As displayed in Figure 35, the interplay between Ar density and the $Ar + e^- \rightarrow Ar(1s_5) + e^-$ excitation rate coefficient, k_{exc}, controls the excitation frequency, given by the $k_{exc}[Ar]$ (excitation rate divided by the electron density). For the 200 Torr simulations the maximum excitation frequency shifts to larger Ar-fractions for $T_e > 3$ eV. For $T_e < 3$ eV, the lower Ar-fractions have elevated excitation frequencies due to the increased population of high-energy electrons.

The reduced electric field as a function of T_e is displayed in Figure 36 where E/N magnitudes of approximately 5 Td, typical of the bulk plasma at steady-state, correspond to higher values of T_e as the Ar-fraction increases. These larger values of T_e are caused by a reduction in the EEDF for energies below ~ 3 eV as the Ar-fraction becomes larger (Figure 34). The loss in low energy electrons are compensated by increasing the EEDF population at energies just below the excitation threshold, which increases the distribution average. However, the EEDF population at energies above the excitation and ionization thresholds are also decreased as the Ar-fraction is increased. As a result, the increase of T_e with Ar-fraction at $E/N \approx 5$ Td does not correspond to an increase in excitation or ionization.

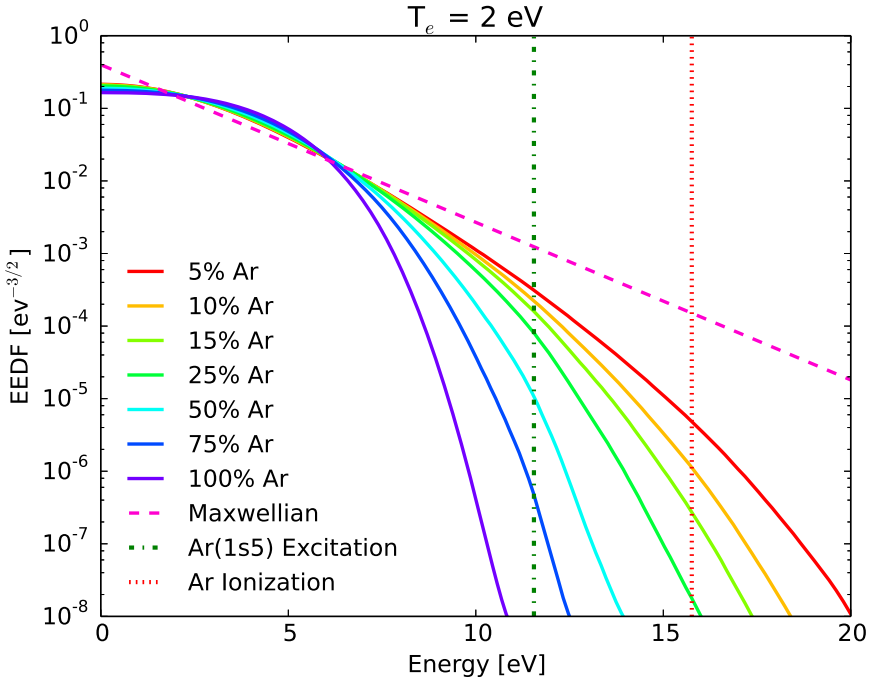

Figure 34. Electron energy distribution functions for varying Ar-He mixtures with an electron temperature of 2 eV, as calculated by BOLSIG+.

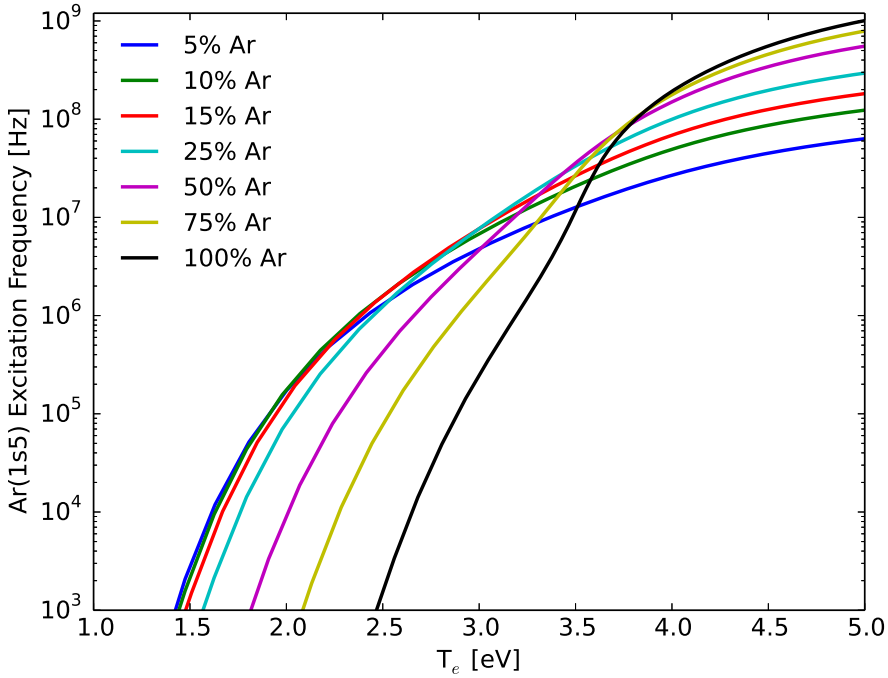

Figure 35. Metastable excitation frequencies, $k_{exc}[Ar]$, at 200 Torr for varying Ar-He mixtures, as calculated by BOLSIG+.

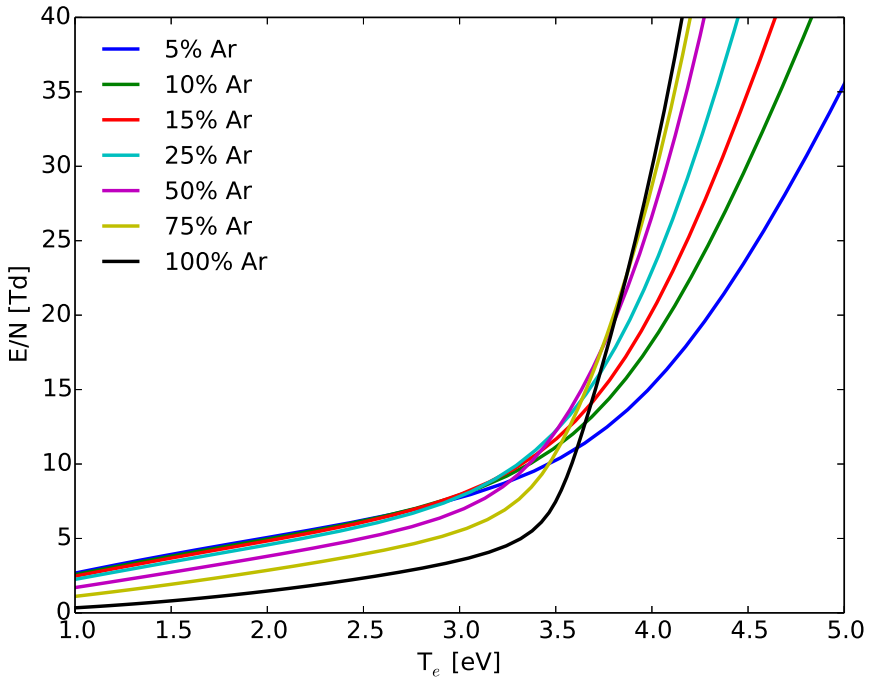

Figure 36. Electron temperatures mapped to reduced electric fields for varying Ar-He mixtures, as calculated by BOLSIG+.

BOLSIG+ calculated electron mobilities and experimentally measured mobilities in pure Ar have been shown to agree in the range of reduced electric fields estimated for this analysis [Pitchford et al., 2013]. Converting the E/N to T_e (Figure 36) and allowing for a variation in Ar-He mixture provides the mobility trends observed in Figure 37. Electron mobilities increase with increasing Ar-fraction for electron temperatures below $\sim$ 2 eV. Above 2 eV, the relationship is reversed, with lower Ar-fractions corresponding to larger electron mobilities. The electron diffusion coefficients follow a similar pattern, but the reversal occurs near 3 eV (Figure 38). Electron energy mobilities and diffusion coefficients (defined in Equations 88 and 89) show similar trends, as displayed in Figures 39 and 40.

A comparison of electron diffusion coefficients calculated by BOLSIG+ to diffusion coefficients calculated from the electron mobility using the Einstein relation, $D_e = \mu_e T_e$, is displayed in Figure 41. For pure Ar, the BOLSIG+ calculated diffusion coefficient is nearly a factor of two larger than the diffusion coefficient calculated

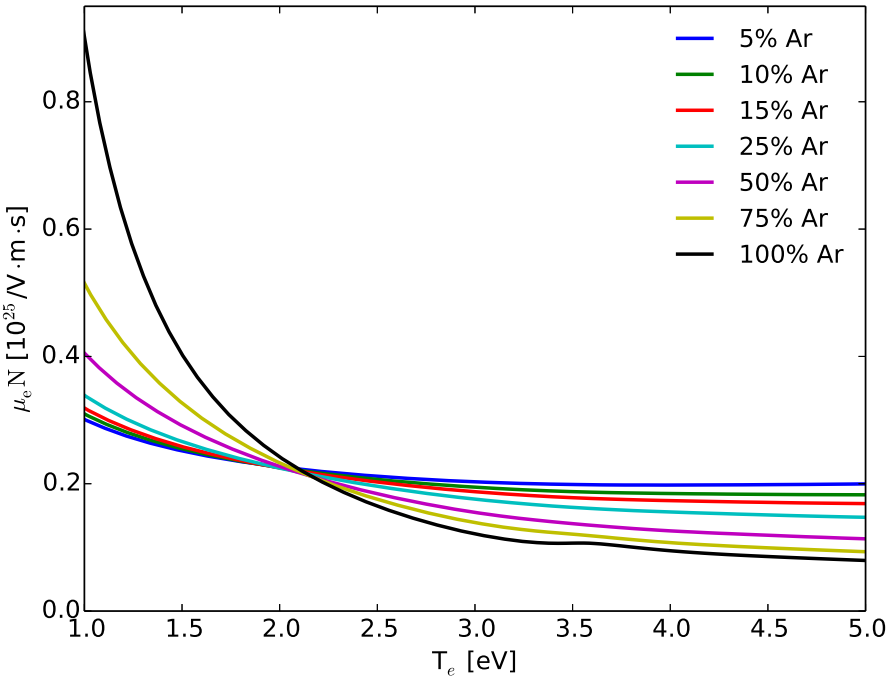

Figure 37. Electron mobilities for varying Ar-He mixtures, as calculated by BOLSIG+.

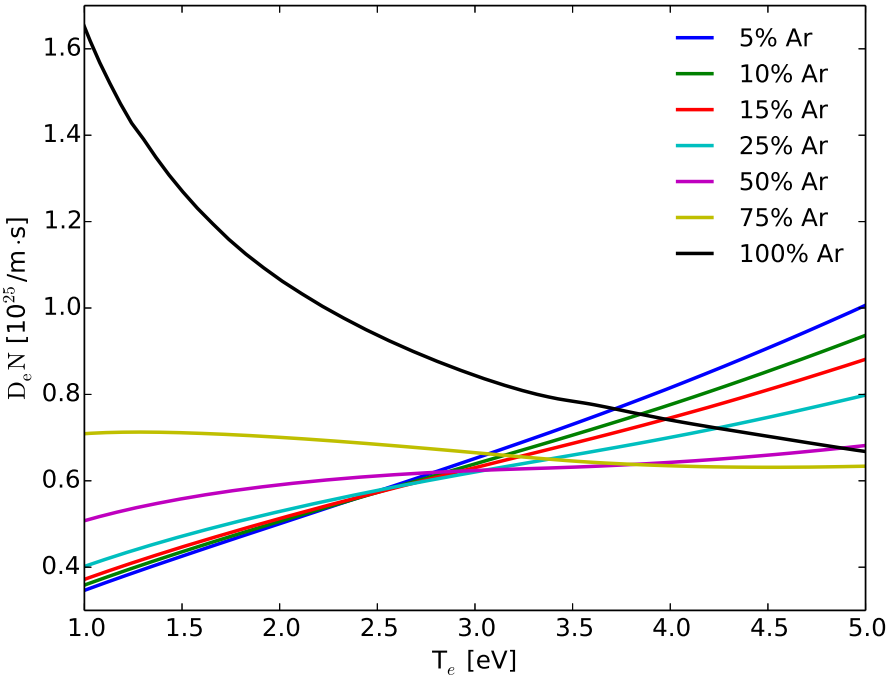

Figure 38. Electron diffusion coefficients for varying Ar-He mixtures, as calculated by BOLSIG+.

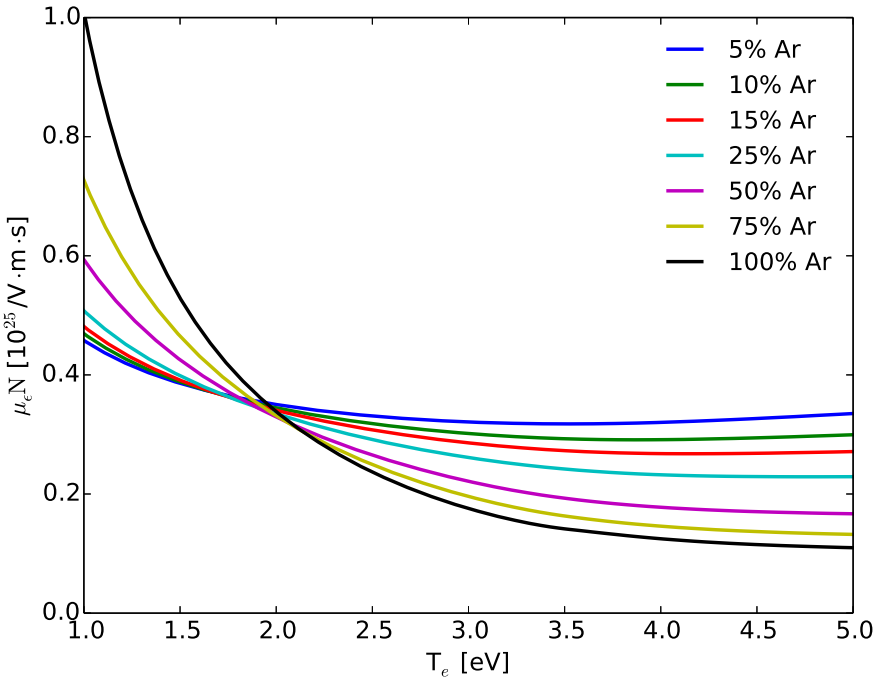

Figure 39. Electron energy mobilities for varying Ar-He mixtures, as calculated by BOLSIG+.

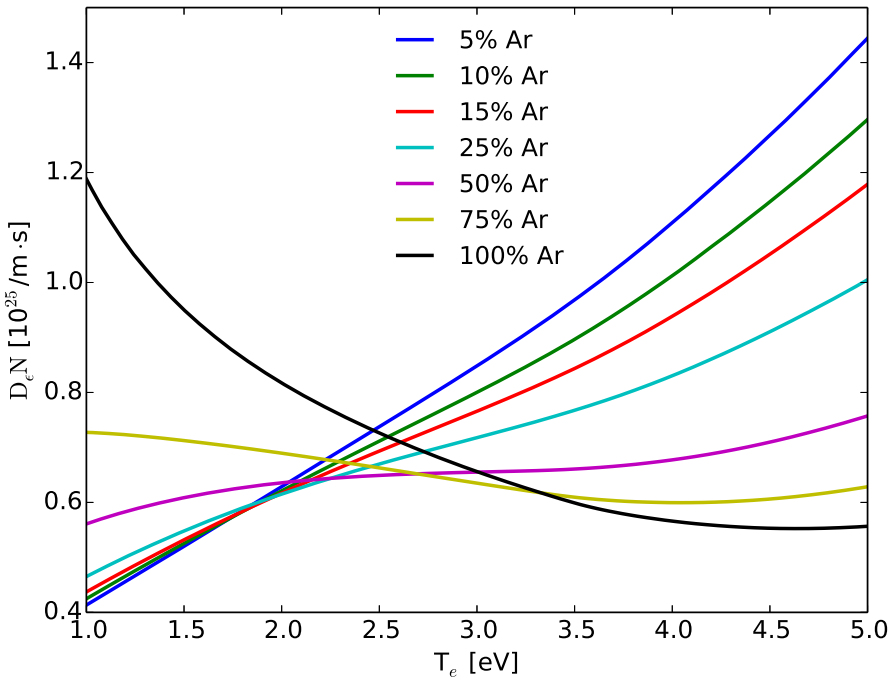

Figure 40. Electron energy diffusion coefficients for varying Ar-He mixtures, as calculated by BOLSIG+.

using the Einstein relation. This is due to the energy dependence of the momentum transfer collision frequency [Hagelaar and Pitchford, 2005]. However, for He rich mixtures, the Einstein relation is satisfied and the diffusion coefficients from the two approaches are nearly equal.

Ion mobilities are taken from Ward [1962] (Equation 11) along with an application of Blanc's Law [Blanc, 1908; Biondi and Chanin, 1961] to determine the mobility in a mixture. Following the measurements of Lindinger and Albritton [1975], all Ar ion species are assumed to have the same mobility as Ar^+, and all He ions are assumed to have the mobility of He^+. To calculate the ion mobilities in a mixture of Ar and He, the mobility of Ar^+ in He is assumed to be equal to the mobility of He^+ in He, and He ion mobilities are held constant over Ar-He mixtures.

A fluid approach [Lymberopoulos and Economou, 1993; Boeuf and Pitchford, 1995; Farouk et al., 2006; Gogolides and Sawin, 1992; COMSOL, 2016] is used to model the discharge in one-dimension, employing the Scharfetter and Gummel [1969] finite volume scheme. The electron density, n_e, and energy density, n_ϵ, are calculated over time via the one-dimensional drift-diffusion equations described in Section 2.4. In the case of a dielectric barrier discharge, Neumann boundary conditions are required for the electric potential, V, at the dielectric boundary:

$$\mathbf{n} \cdot (\epsilon_0 \mathbf{E}_1 - \epsilon_d \mathbf{E}_2) = \sigma_s, \tag{118}$$

$$\frac{d\sigma_s}{dt} = \mathbf{n} \cdot \mathbf{j}_e + \mathbf{n} \cdot \mathbf{j}_p, \tag{119}$$

where $\mathbf{E}_1$ is the electric field at the boundary inside the discharge cavity, $\mathbf{E}_2$ is the electric field in the dielectric, ϵ_d is the dielectric permittivity, σ_s is the surface charge density, $\mathbf{j}_e$ is the electron current density to dielectric surface, $\mathbf{j}_p$ is the ion current density to dielectric surface, and $\mathbf{n}$ is the outward normal vector to the boundary. The electric field inside the left dielectric depends on the applied voltage to the terminal

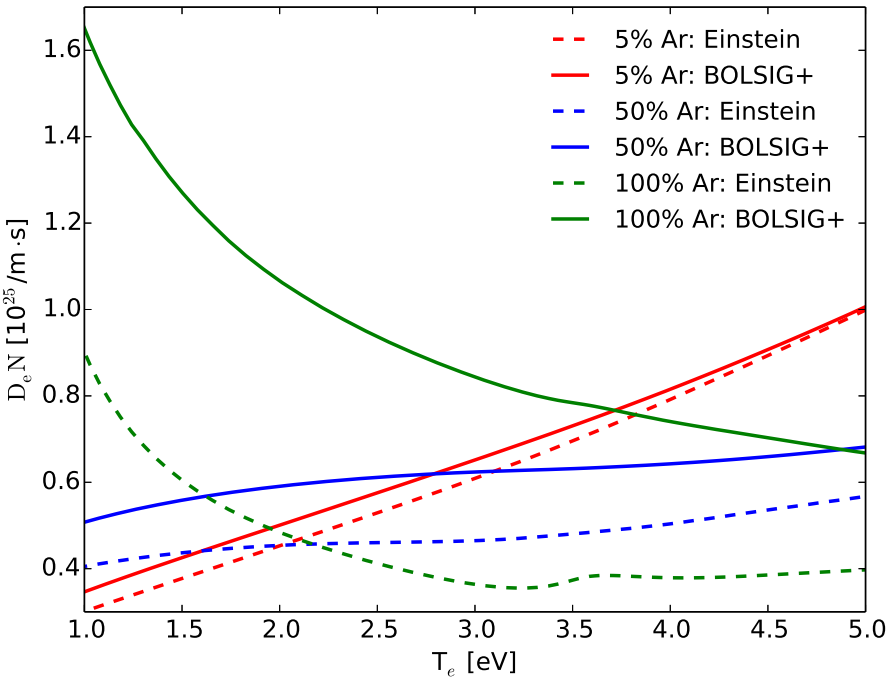

Figure 41. A comparison of electron diffusion coefficients calculated by BOLSIG+ to diffusion coefficients calculated from the electron mobility using the Einstein relation, $D_e = \mu_e T_e$.

and the voltage on the left dielectric boundary: $E_2 = (V_{el} - V_{BC})/\delta$, where V_{el} is the electrode voltage, V_{BC} is the voltage at the dielectric barrier, and δ is the dielectric thickness. Including the electrode voltage, Equation 118 can be rewritten in terms of the Neumann boundary condition for the left boundary in one-dimension:

$$\left.\frac{\partial V}{\partial x}\right|_{BC,left} = -E_{1,left} = \frac{\sigma_{s,left}}{\epsilon_0} + \frac{\epsilon_d \left(V_{BC,left} - V_{el,left}\right)}{\epsilon_0 \delta}. \tag{120}$$

A similar expression is obtained for the right boundary:

$$\left.\frac{\partial V}{\partial x}\right|_{BC,right} = -E_{1,right} = -\frac{\sigma_{s,right}}{\epsilon_0} + \frac{\epsilon_d \left(V_{el,right} - V_{BC,right}\right)}{\epsilon_0 \delta}. \tag{121}$$

In addition to the one-dimensional fluid model, we also develop a simplified zero-dimensional approach to the RF discharge where the root-mean-square (RMS) voltage is treated as an effective DC voltage [Raizer et al., 1995]. This reduces the RF-

DBD discharge to an effective DC discharge, which greatly reduces computation time required for simulation. The zero-dimensional approach is not derived mathematically from the one-dimensional fluid model, but instead provides an alternative approach to modeling an RF-DBD.

If the driving angular frequency, ω, is much greater than the frequency of energy loss by electrons, $(2m_e/M)\,\nu_m$, where M is the mass of the neutral atoms and ν_m is the electron collision frequency, then the ionization frequency, ν_i, in an RF electric field can be approximated by the ionization of a DC electric field with the magnitude reduced by a factor of $\sqrt{2}$ [Raizer et al., 1995]:

$$\nu_{i,RF}\left(E_p\right) \approx \nu_{i,DC}\left(\frac{E_p}{\sqrt{2}}\right) \quad \text{for} \quad \nu_m \gg \omega \gg \left(\frac{2m_e}{M}\right)\nu_m, \tag{122}$$

where E_p is the peak applied electric field for the RF discharge.

For pure Ar at 200 Torr, $\omega \approx 8.5 \times 10^7$ Hz and a collision frequency of $\nu_m \approx 4.6 \times 10^{11}$ Hz calculated by BOLSIG+ for $E/N = 5$ Td provides $(2m_e/M_{Ar})\,\nu_m \approx 1.3 \times 10^7$ Hz, which fulfills the requirements for treating the RF field as a DC field with a reduced magnitude. However, for a 1% Ar in He mixture, a collision frequency of $\nu_m \approx 2.8 \times 10^{11}$ Hz produces an electron energy loss frequency of $(2m_e/M_{He})\,\nu_m \approx 7.7 \times 10^7$ Hz, which does not satisfy the $\omega \gg (2m_e/M)\,\nu_m$ inequality. We note that while the $\omega \gg (2m_e/M)\,\nu_m$ inequality is not satisfied for He rich mixtures in the pressure range of 200-500 Torr, the $\nu_m \gg \omega$ inequality holds over all pressures and mixtures analyzed.

The zero-dimensional effective DC model, implemented through ZDPlasKin, models the bulk plasma of an RF-DBD by numerically integrating the system of reaction rate equations over time. The electron impact rate coefficients and transport parameters are dependent on E/N, which is calculated at each time step to provide an input to BOLSIG+.

Reduced electric fields are calculated from the bulk plasma voltage by

$$\frac{E}{N} = \frac{V_b}{N d_e}, \tag{123}$$

where d_e is the effective distance between electrodes (Equation 58), and V_b is the voltage across the bulk plasma (Equation 54). Bulk plasma voltages are calculated over time following the approach outlined by Eismann [2011], with the sheath and dielectric voltage terms acting as an effective ballast resistor for the RF-DBD. Making the substitution

$$\chi = \frac{d_\alpha}{\omega \epsilon_0} + \frac{2\delta}{\omega \epsilon_d}, \tag{124}$$

$$(V_s + V_d)^2 = j^2 \left(\frac{d_\alpha}{\omega \epsilon_0} + \frac{2\delta}{\omega \epsilon_d} \right)^2 = j^2 \chi^2, \tag{125}$$

the voltage across the bulk plasma can be rewritten as

$$V_b^2 = V_{app}^2 - j^2 \chi^2. \tag{126}$$

For this discharge scenario, the parameter χ acts like the ballast resistor in the DC scenario, limiting the bulk plasma voltage as the current increases.

While the sheath thickness varies over time with the applied voltage, the peak thickness can be estimated as $d_\alpha = 2A$ [Raizer et al., 1995]. At each time step, the amplitude of sheath oscillations, A, is calculated from Equation 57 using the Newton-Raphson method. The electron collision frequency is calculated by BOLSIG+ and the plasma frequency is calculated from the electron density of the previous time-step.

Instead of a time varying applied voltage, the zero-dimensional model uses an RMS voltage for V_{app}, providing an effective DC approach. Bulk plasma E/N magnitudes are calculated over time accounting for changes in V_b due to variations in current

density and sheath thickness [Eismann, 2011]. The time dependent E/N magnitudes provide electron impact rate coefficients used in plasma kinetic calculations, which are performed until the E/N reaches a steady-state value. This zero-dimensional approach requires minutes per simulation on a HP ENVY 750-197c Desktop, which is significantly less than the tens of hours required per simulation using the one-dimensional fluid model. The reduced computation time enables a full exploration of the parameter space.

Convergence Study in Time.

A convergence study in time is performed for our implementation of the Scharfetter and Gummel [1969] finite volume scheme by varying the time step and analyzing the difference in metastable density solutions. One-dimensional simulations of the RF-DBD scenario are performed through 10 cycles using a 15% Ar in He mixture at a pressure of 200 Torr. Each metastable density solution obtained using a time step Δt is compared to the solution obtained using a time step half as large, $\Delta t/2$. Figure 42 displays the relative difference in solutions, $|u_{\Delta t} - u_{\Delta t/2}|/|u_{\Delta t}|$, against the time step, Δt, using a log-log scale.

A forward Euler method is used for time-stepping, which is a first order explicit scheme in time, $\mathcal{O}(\Delta t)$. In a log-log plot, a first order scheme has a slope of one, which is displayed in Figure 42 as $\mathcal{O}(\Delta t)$. The simulated results follow the slope of $\mathcal{O}(\Delta t)$, matching the expected convergence in time for a first order scheme.

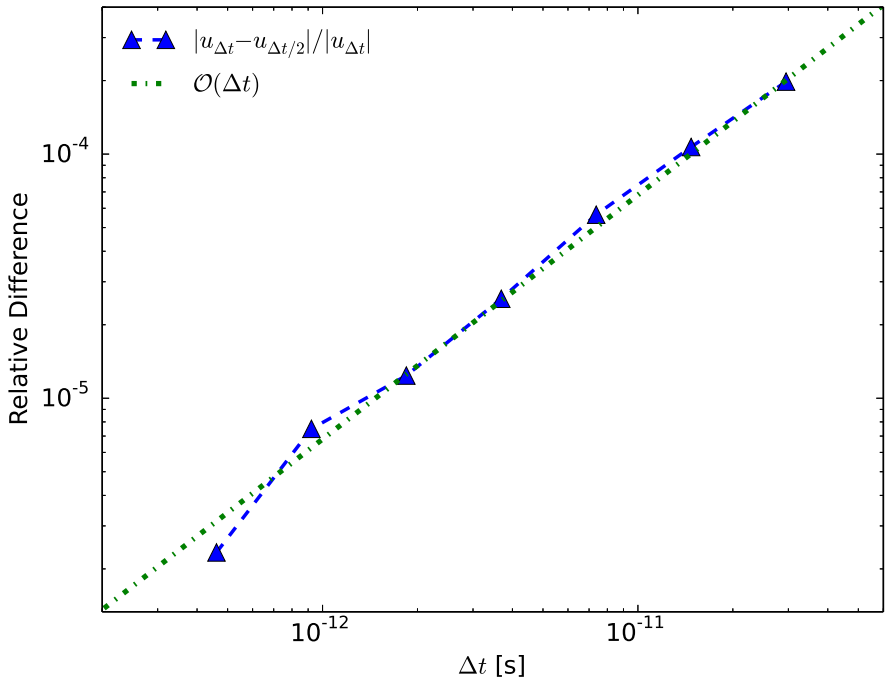

Figure 42. Relative differences in solutions, $|u_{\Delta t} - u_{\Delta t/2}|/|u_{\Delta t}|$, as a function of the time step, Δt. The slope of the solution differences matches the slope of a first order in time method, $\mathcal{O}(\Delta t)$.

4.2 Clam Shell Electrodes Experiment

Description of Experiment.

The clam shell electrodes experiment uses the geometry displayed in Figure 43 with a driving angular frequency of $\omega = 2\pi \times 13.56$ MHz. Ultra-high purity (99.999%) Ar and He gases are filtered through an SAES high-flow rate filter (MC200-904FV) which reduces impurities to 100 parts-per-trillion, 2-3 orders of magnitude lower than the Ar^* density. The Ar-He mixture is varied for an assortment of pressures using a delivered power of 10 W. This configuration consists of a 0.25 inch tube with a 0.15 inch inner diameter in addition to a 2 inch clam shell copper electrode with a 2 mm thickness. Electrodes were machined with an edge gap of 0.13 inch and a maximum gap of 0.25 inch at the center of the tube.

End-on imagery is collected for the RF-DBD. The end-on images are collected

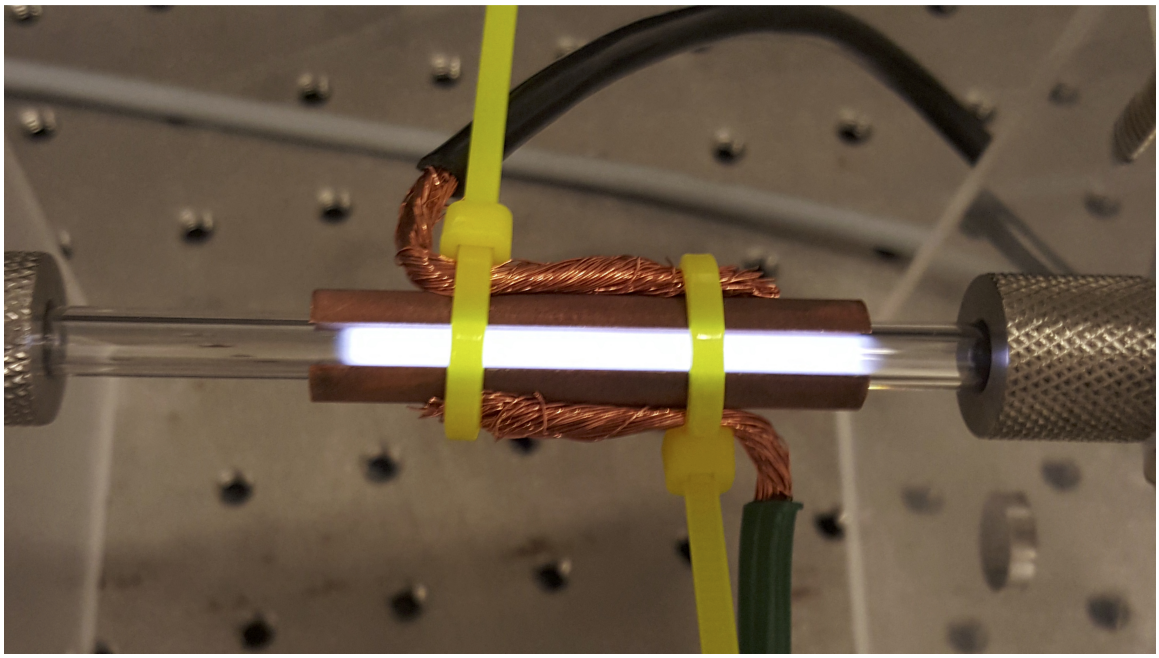

Figure 43. A picture of the clam shell electrode RF-DBD experimental setup during a discharge at a pressure of 800 Torr.

using a Point Grey Grasshopper (GS3-U3-32S4M-C) USB 3.0 camera with 3.45 μm pixel pitch and a 1/1.8″ CMOS detector. The spectra sensitivity of the detector ranges from 300-900 nm. A Computar 50 mm aperture, variable focus, f 1:1.8 lens is used to image the center of the discharge at a distance of 35 cm with an f/# of 16. The optical system results in a resolution of 41 μm per pixel. Figure 44 shows an example of the images collected for a 10% Ar in He mixture at 300 Torr. The yellow rectangle, 90 by 10 pixels or 3.69 by 0.41 mm, outlines the region in which the apparatus is most similar to a parallel plates configuration. These rows are averaged together to facilitate comparison to the simulations. The bright outer region is caused by plasma emission being wave-guided by the Pyrex tube. Doppler widths from the spectra measurements indicated a temperature of 440 ± 20 K, over all pressures and Ar-fractions [Eshel et al., 2016].

While the electric field produced by the clam shell electrodes is different than the electric field for parallel plates, the centerline between electrodes can be approximated

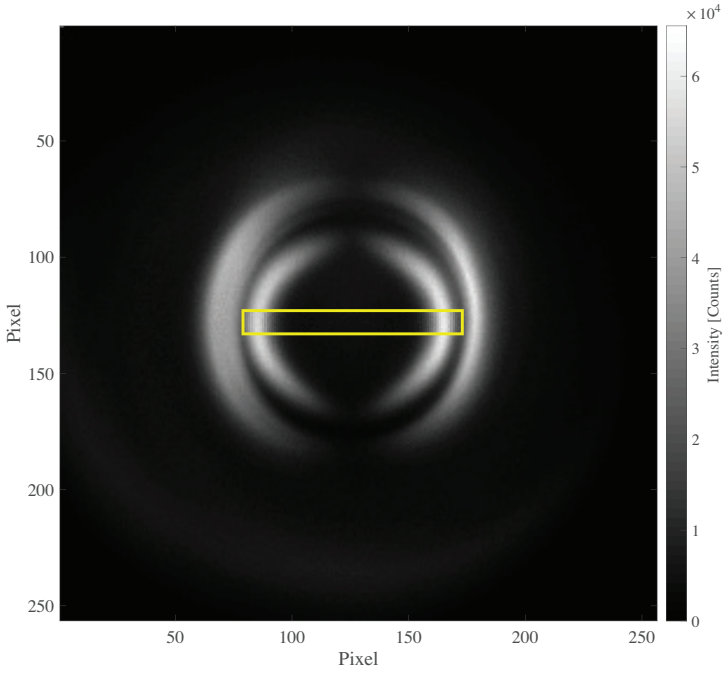

Figure 44. End-on image of an RF-DBD for a 10% Ar in He mixture at 300 Torr with an applied power of 10 W. The outer fluorescence is emission from the sheath that is waveguided down the Pyrex tube.

by parallel plates. The electric potential calculated for the clam shell electrodes is displayed in Figure 45 and the associated electric field is displayed in Figure 46. Near the edge of the electrodes, the electric field is larger due to the shorter distance between electrodes. However, near the center of the electrodes, the electric field is similar to the field produced by parallel plates. A comparison of the electric field magnitude at the center of the tube indicates a roughly 25% increase in the electric field due to the curvature of the electrodes compared to the parallel plates scenario.

Simulations.

Varying Ar-He Mixture.

The discharge chamber used to approximate the centerline of the clam shell geometry consists of parallel-plate electrodes separated by 6.4 mm with both electrodes covered by a 1.3 mm thick dielectric of $\epsilon_d = 5\epsilon_0$ (Figure 47). Including radiation

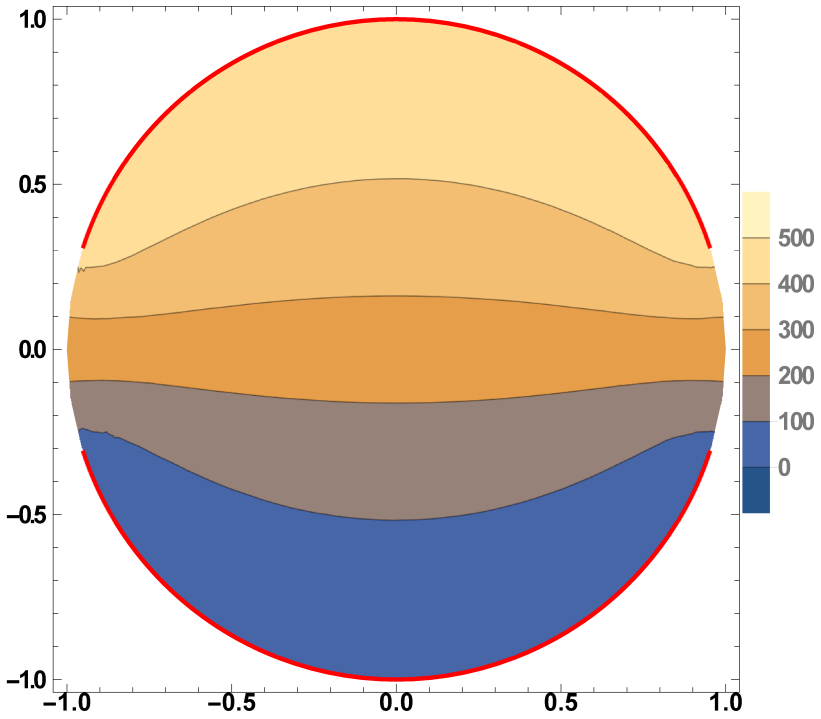

Figure 45. Voltage equipotential curves for clam shell electrodes with 500 V on the top plate and the bottom plate grounded. The red lines are the electrodes.

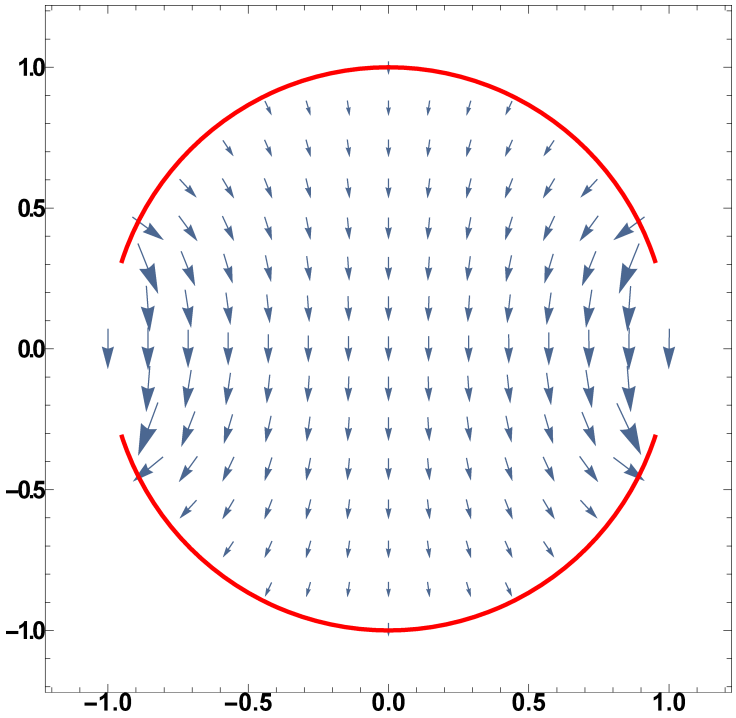

Figure 46. Electric fields for clam shell electrodes with 500 V on the top plate and the bottom plate grounded. The red lines are the electrodes.

trapping, an effective A-coefficient of 1.7×10^5 s^{-1} is used for the $Ar(1s_4) \rightarrow Ar + \hbar\omega$ transition for this discharge geometry [Holstein, 1951]. At near-atmospheric pressures, the magnitude of radiation trapping is assumed to be independent of pressure [Holstein, 1947] and mixture.

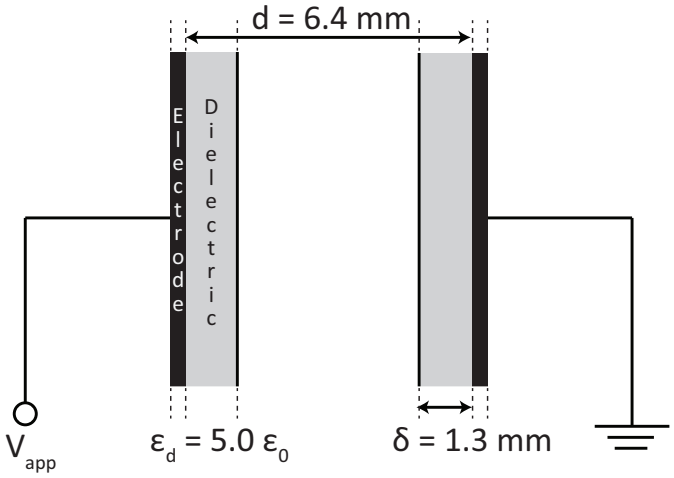

Figure 47. A cross section of the simulated RF-DBD chamber used for the clam shell electrodes. The plates are assumed to be infinite in extent in the calculations.

Simulations are performed for a pressure of 300 Torr and a peak applied voltage of 500 V with a driving angular frequency of $2\pi \times 13.56$ MHz ($V_{app} = 500 \sin[\omega t]$ V). The Ar-He mixture is varied between 1% and 100% to analyze the effect of Ar-fraction on the metastable density. A comparison between the zero and one-dimensional models is performed in the bulk plasma at a point midway between the plates in the steady-state limit. The one-dimensional model requires roughly 2500 cycles to reach a steady-state defined by the convergence criterion outlined in Lymberopoulos and Economou [1993]. Zero-dimensional simulations are performed through 0.3 ms, allowing ample time for all densities and discharge parameters to reach a steady-state. A constant gas temperature of 440 K is used for all simulations, matching the experimentally measured temperatures based on observed Doppler widths [Eshel et al., 2016].

Fluorescence measurements of the discharge scenario indicate an α-mode discharge, as displayed in Figure 48. Simulated fluorescence is estimated by multiplying the Ar^* densities predicted by the one-dimensional fluid model with their respective A-coefficients and averaging over a cycle. The fluorescence trends in the peak and bulk plasma are in agreement, showing a slight decrease as the Ar-fraction is increased from 10 to 25%. Additionally, the simulated and measured trend of sheath fluorescence as a function of Ar-fraction are displayed in Figure 49. While the simulated peak fluorescence is overestimated for the pure Ar scenario, the general trends as a function of Ar-fraction are in agreement. A hybrid fluid-kinetic model would provide a better estimate of sheath behavior, and would likely improve the agreement between measurement and simulation.

Cycled averaged spatial profiles from the one-dimensional simulations are displayed in Figures 50-52. While the electron temperature shows a variation of approximately 0.5-1 eV during an RF cycle, the $Ar(1s_5)$ density is effectively constant throughout the cycle, and the electron density only shows variation in the sheaths. Peak metastable densities on the order of 10^{12} cm^{-3} are observed near the sheaths, with the bulk plasma densities an order of magnitude lower (Figure 50). For the mixtures simulated by the fluid model at 300 Torr, the 25% Ar in He mixture produces the largest metastable densities in the sheaths, with a peak of approximately 5×10^{12} cm^{-3}. In the bulk plasma, the 15% Ar-fraction produces the largest metastable densities, with magnitudes near 4×10^{11} cm^{-3}.

Electron densities are observed to increase with increasing Ar-fraction (Figure 51). Additionally, the peak to bulk plasma ratio increases with Ar-fraction. Electron temperatures in the bulk plasma also display an increase with increasing Ar-fraction (Figure 52), but an opposite trend is observed in the sheaths. Peak sheath voltages, V_s, are observed in the range of 240-250 V, providing peak sheath E/N magnitudes

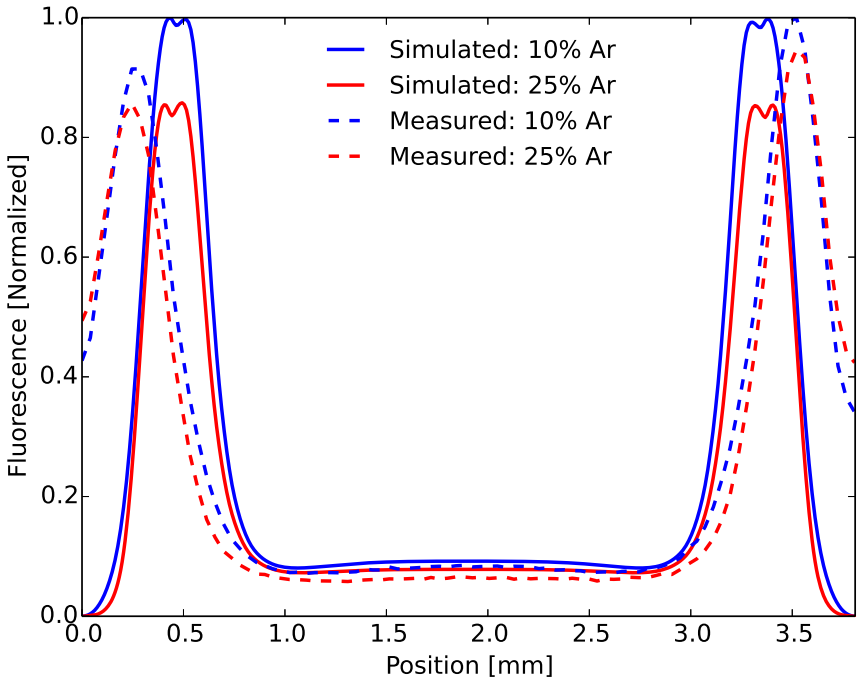

Figure 48. Normalized fluorescence measurements and one-dimensional simulations for 10 and 25% Ar-fractions at 300 Torr. Both the measurements and simulations are indicative of an α-mode discharge.

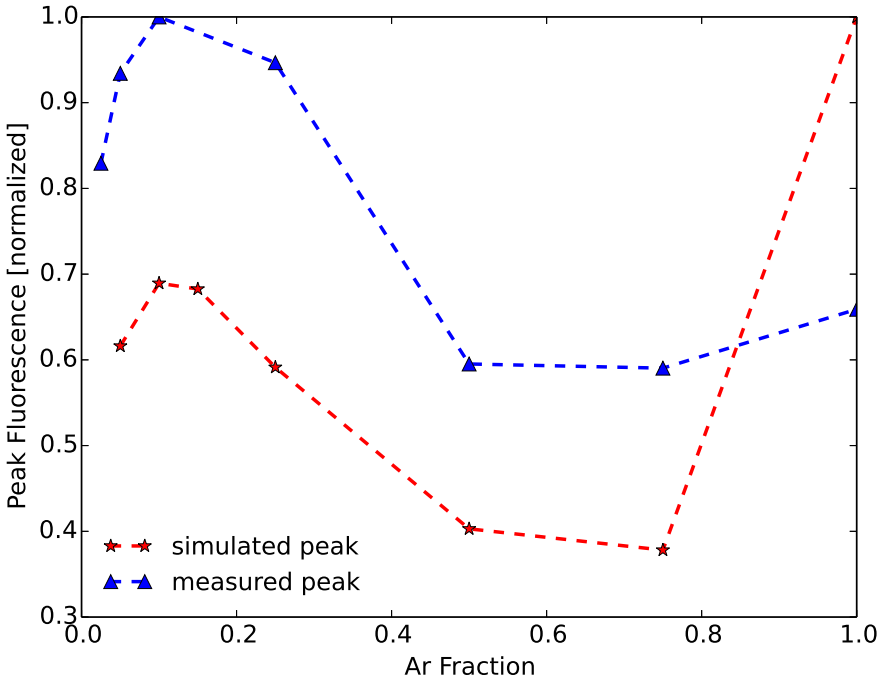

Figure 49. Normalized sheath fluorescence measurements and simulations for a variety of Ar-He mixtures at 300 Torr.

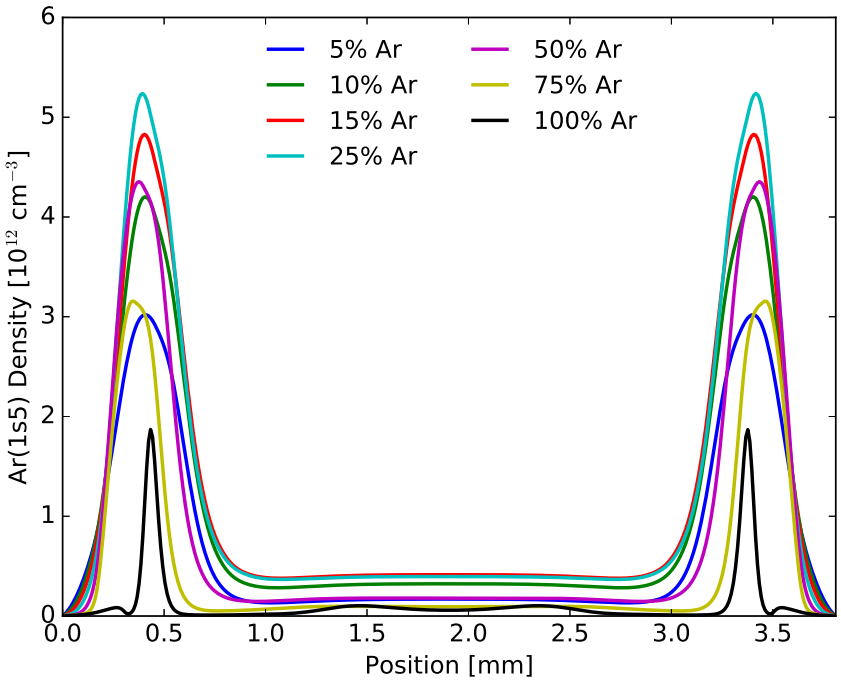

Figure 50. One-dimensional $Ar(1s_5)$ density simulations for varying Ar-He mixtures at 300 Torr.

in the range of 125-155 Td.

A comparison of the bulk plasma electron densities simulated by the zero and one-dimensional models is displayed in Figure 53. Both models predict similar densities and trends, increasing as the partial-pressure of Ar increases for Ar-fractions above $\sim$ 15%. The increase in electron density (and current density) with increasing Ar-fraction corresponds to a decrease in steady-state E/N for the bulk plasma due to an increase in dielectric charging and sheath voltage (Figure 54). As the Ar-fraction increases so does the Ar_2^* density, and the dominant ionization mechanism shifts from $e^- + Ar \rightarrow 2e^- + Ar^+$ to $e^- + Ar_2^* \rightarrow 2e^- + Ar_2^+$. The electron energy required to ionize Ar_2^* is approximately 3.4 eV, compared to the 15.8 eV required to ionize ground state Ar. However, Ar_2^* formation via $Ar(1s_5) + Ar + M \rightarrow Ar_2^* + M$ is dependent on metastable densities, which require electron energies of 11.6 eV for production through $e^- + Ar \rightarrow e^- + Ar(1s_5)$. Therefore, a better comparison of the energies required for the two different ionization mechanisms is between the energy required

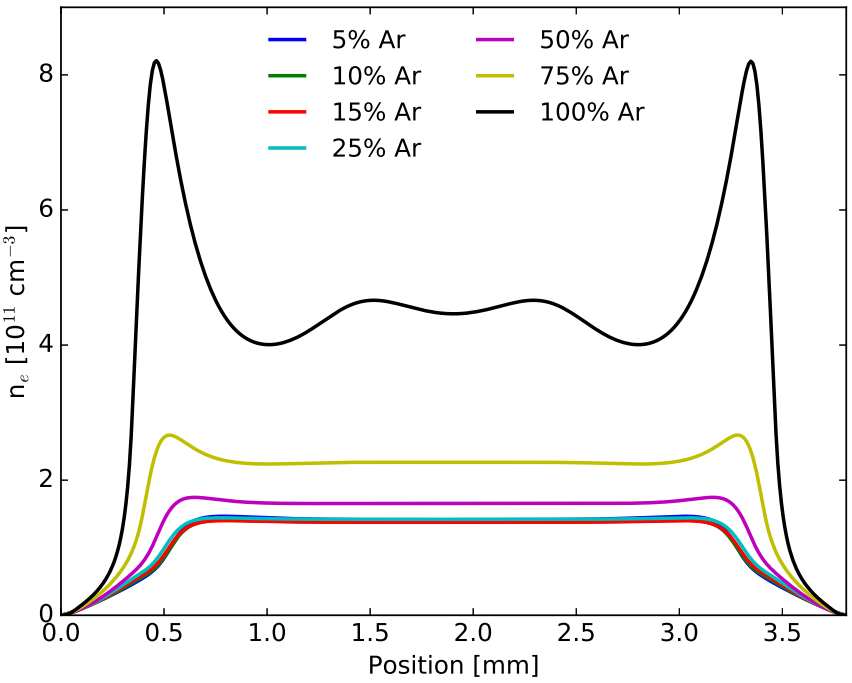

Figure 51. One-dimensional electron density simulations for varying Ar-He mixtures at 300 Torr.

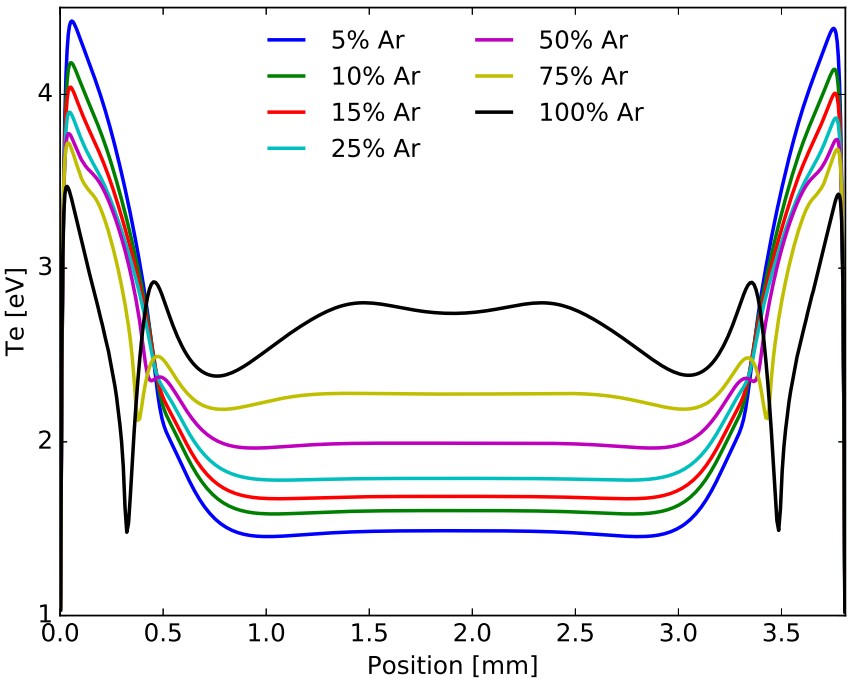

Figure 52. One-dimensional electron temperature simulations for varying Ar-He mixtures at 300 Torr.

for $Ar(1s_5)$ excitation, 11.6 eV, and the energy required for ionization of ground state Ar, 15.8 eV, resulting in a difference of 4.2 eV. The reduction in energy required for ionization via $e^- + Ar_2^* \rightarrow 2e^- + Ar_2^+$ allows for a lower steady-state E/N at larger Ar-fractions, which in turn requires a larger electron density (current density) to reach the steady-state.

The bulk plasma electron temperature increases with increasing Ar-fraction, in contrast to the E/N (Figure 55). This increase in T_e with a reduction of E/N can be described by Figure 36, where the mapping of E/N to T_e is shown to be mixture dependent. For E/N magnitudes below 6 Td, T_e increases as the Ar-fraction increases. The electron temperature (or E/N) predicted using the zero-dimensional DC approach is larger than the average (RMS) values of the one-dimensional RF model, but less than the peaks. While the time-varying electric field in the one-dimensional model allows the electron temperature (E/N) to vary over a cycle, the DC approach maintains a constant electron temperature (E/N) at steady-state.

In the one-dimensional RF model, ionization rates vary over the RF cycle following the change in electron temperature (or E/N). The zero-dimensional effective DC approach maintains a constant ionization rate due to a constant electron temperature (E/N) at steady-state. Ionization rates for the two approaches are displayed in Figure 56, which shows an increase in ionization rates as the Ar-fraction is increased matching the trend in electron density. While the ionization rates for the one-dimensional RF model vary over the cycle, the cycle averaged values are close in magnitude to the constant ionization rates from the zero-dimensional effective DC model. Differences in the ionizations rates correspond to differences in electron loss rates, which are functions of T_e and the electron/ion densities.

The two models predict a similar trend in metastable density, with peaks near 15% Ar in He followed by a reduction in density as Ar-fraction is increased. Metastable

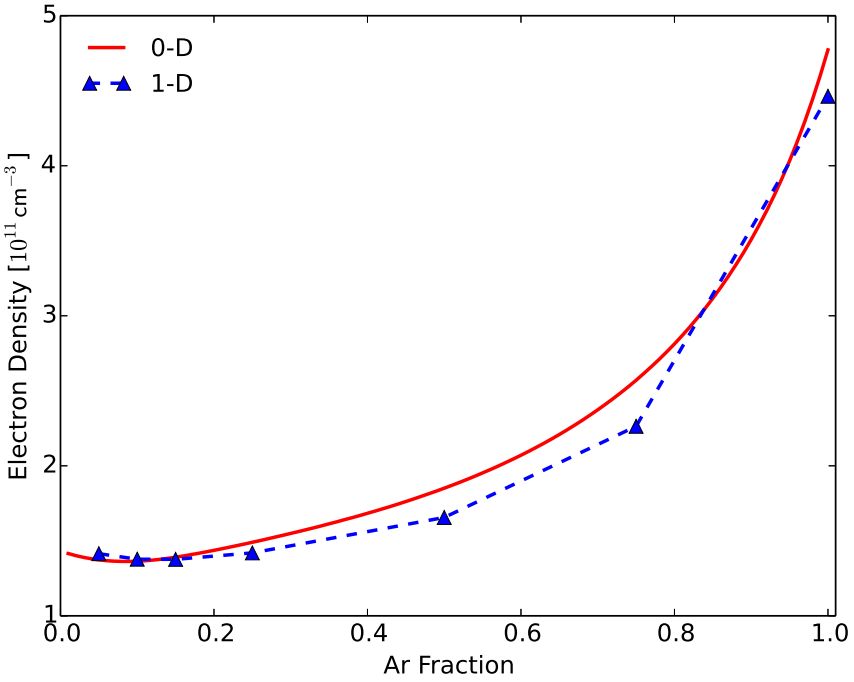

Figure 53. Bulk plasma electron densities for varying Ar-He mixtures at 300 Torr using both the zero and one-dimensional models.

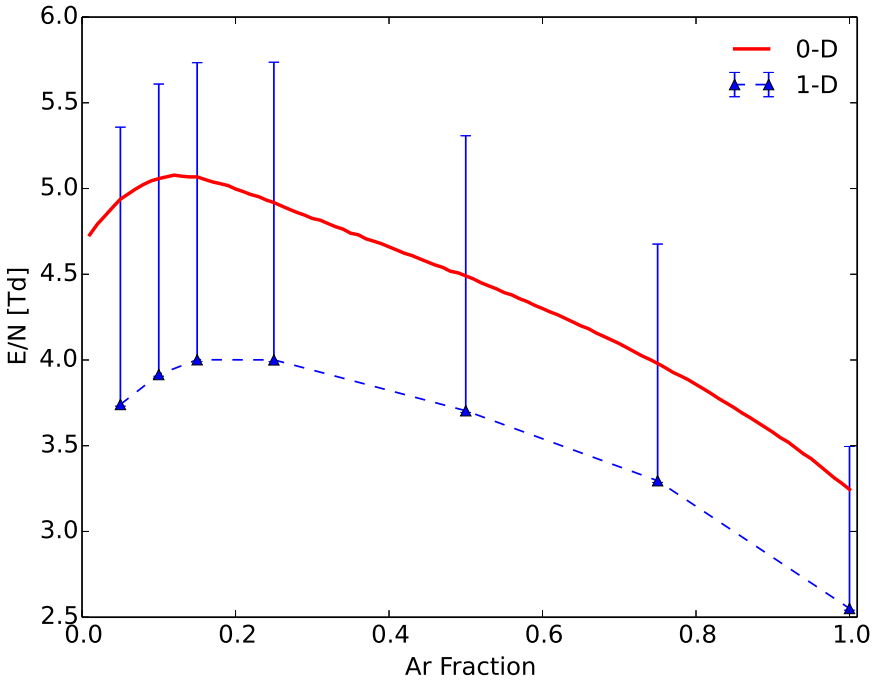

Figure 54. Bulk plasma E/N magnitudes for varying Ar-He mixtures at 300 Torr using both the zero and one-dimensional models. The triangles represent the RMS E/N and the bars represent the maximum E/N attained over a cycle.

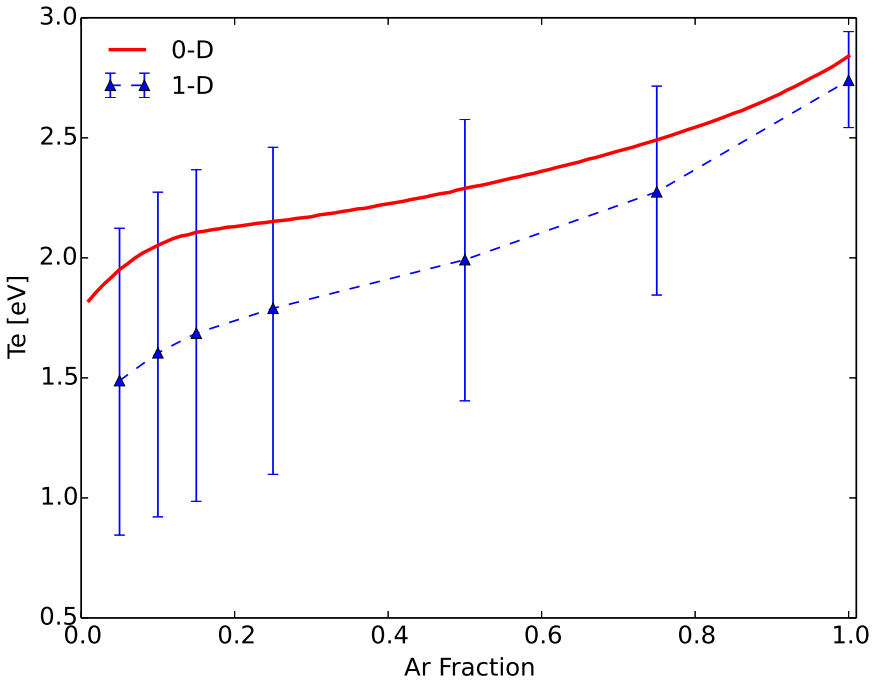

Figure 55. Bulk plasma electron temperatures for varying Ar-He mixtures at 300 Torr using both the zero and one-dimensional models. The triangles represent the cycle-averaged T_e and the bars correspond to the minimum and maximum values obtained over a cycle.

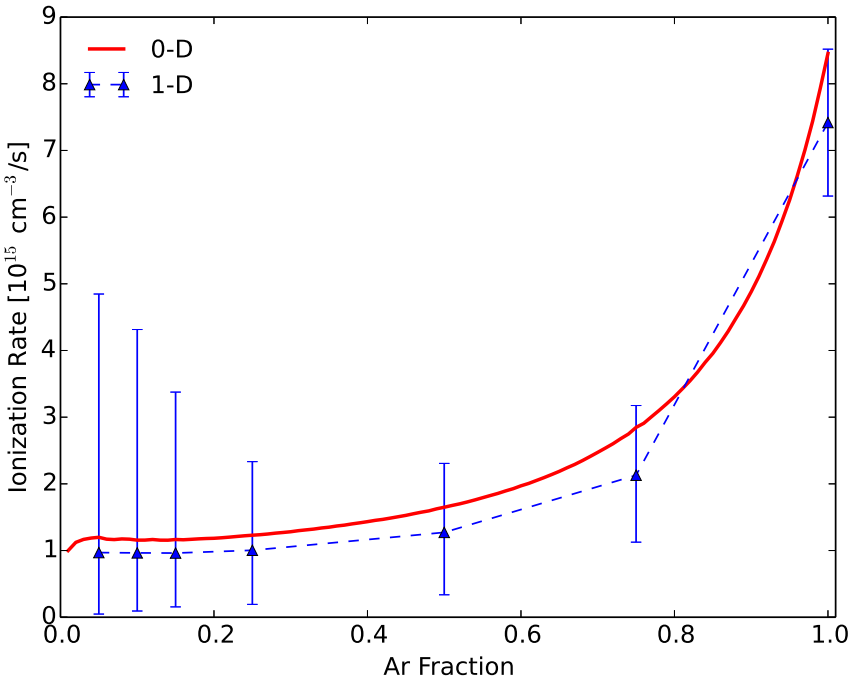

Figure 56. Bulk plasma ionization rates for varying Ar-He mixtures at 300 Torr using both the zero and one-dimensional models. The triangles represent the cycle-averaged ionization rates and the bars correspond to the minimum and maximum values obtained over a cycle.

density trends follow the trends in E/N, which also show peaks near the 15% Ar-fraction. Excitation rate coefficients for metastable production via $Ar + e^- \rightarrow Ar(1s_5) + e^-$ are highly dependent on E/N, which explains the similarity of the E/N and $Ar(1s_5)$ density trends over Ar-fraction.

Varying Pressure.

To analyze the effect of pressure on the metastable density, an Ar-fraction of 15% is simulated for pressures in the range of 200-500 Torr. As pressure is increased, the electron loss rate due to ambipolar diffusion decreases. Additionally, the role of ionization through $e^- + Ar_2^* \rightarrow 2e^- + Ar_2^+$ increases with pressure, accounting for an overall decrease in steady-state T_e and E/N as shown in Figure 58. The electron/current density required to reduce the initial E/N to the steady-state E/N decreases with pressure due to an increased gas density which reduces the initial E/N magnitude (Figure 59). The decrease in electron density and electron temperature combined with an increase in the metastable loss rates, primarily through excimer formation via $Ar(1s_5) + Ar + M \rightarrow Ar_2^* + M$, causes an overall decrease in metastable density with increasing pressure, as displayed in Figure 60. The quadratic dependence of the metastable loss rates on the pressure is larger than the linear increase in Ar density assisting with metastable production rates through $Ar + e^- \rightarrow Ar(1s_5) + e$, which would decrease the steady-state metastable density even if the electron density and temperature were to remain constant.

Bulk plasma electron densities for the zero-dimensional DC model are displayed with the one-dimensional results in Figure 61. Both models predict a nearly constant electron density from 200 to 300 Torr followed by a decrease from 300 to 500 Torr. The electron density is slightly overestimated by the zero-dimensional model at all pressures. A small decrease in E/N and T_e is observed as pressure is increased, with

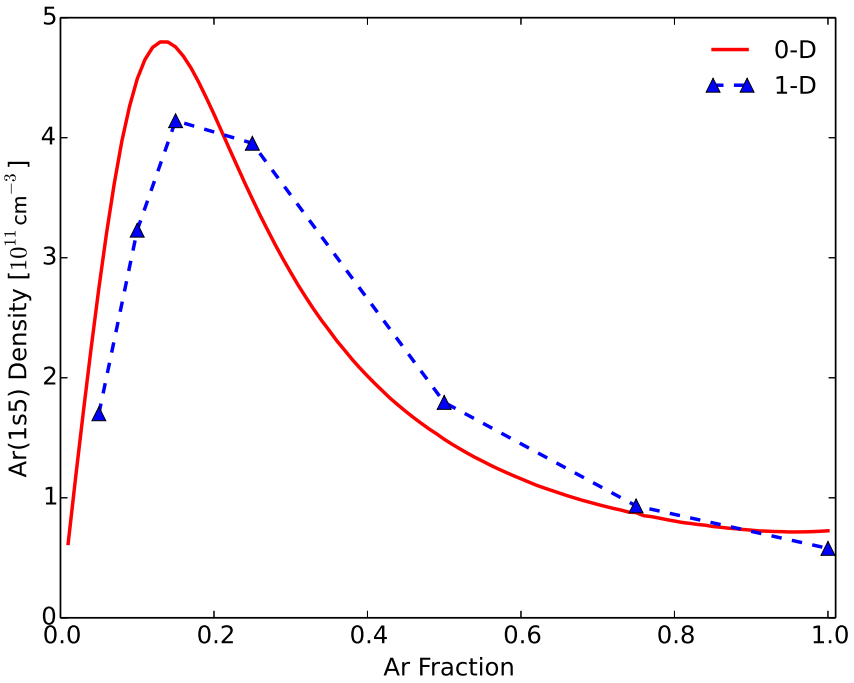

Figure 57. Bulk plasma $Ar(1s_5)$ densities for varying Ar-He mixtures at 300 Torr using both the zero and one-dimensional models.

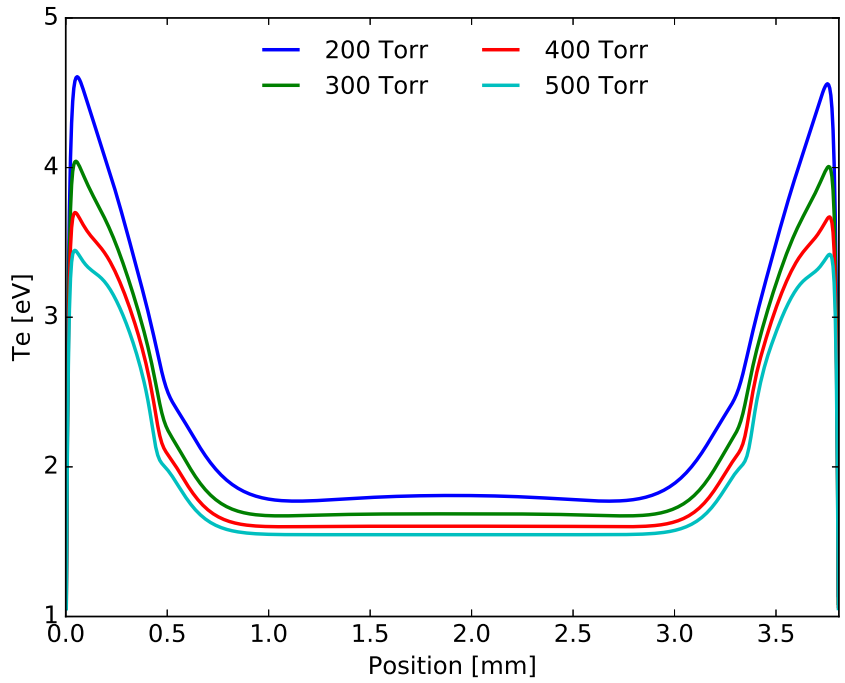

Figure 58. One-dimensional electron temperature simulations for varying pressures in a 15% Ar in He mixture.

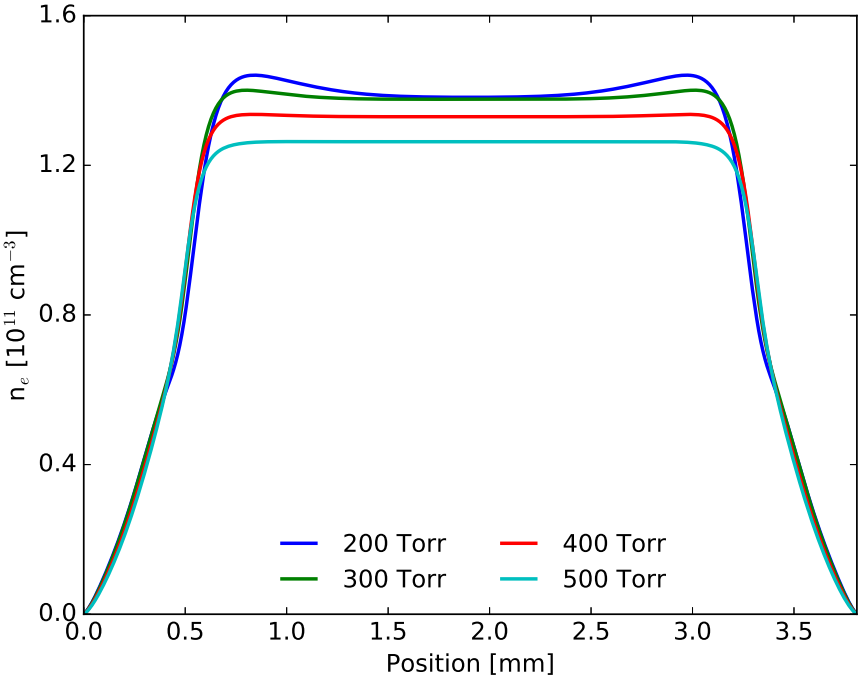

Figure 59. One-dimensional electron density simulations for varying pressures in a 15% Ar in He mixture.

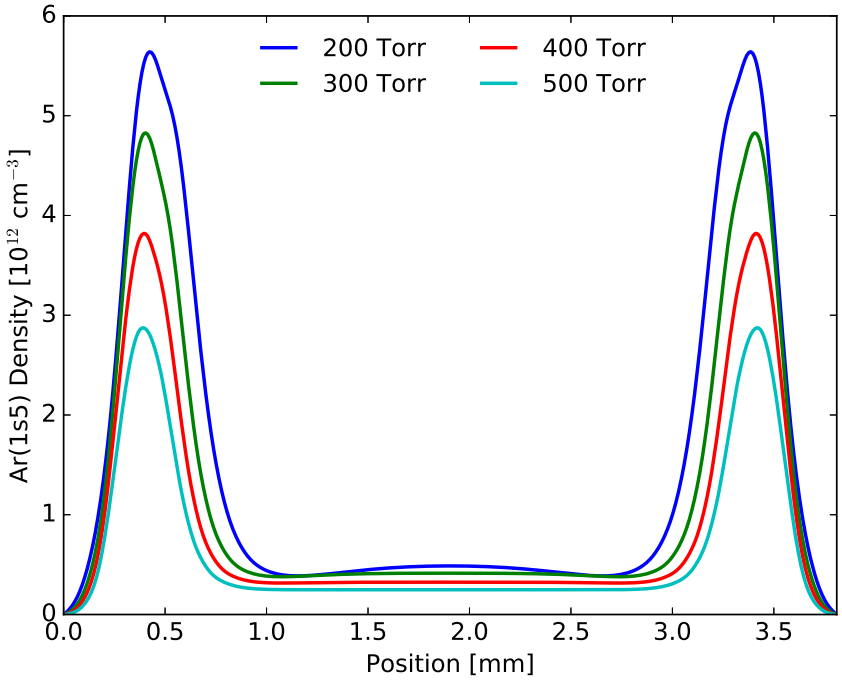

Figure 60. One-dimensional $Ar(1s_5)$ density simulations for varying pressures in a 15% Ar in He mixture.

both models in agreement (Figures 62 and 63). The T_e (or E/N) magnitude for the zero-dimensional DC approach is between the average (RMS) and maximum of the time-varying one-dimensional approach.

The decrease in metastable density with increasing pressure is overestimated by the zero-dimensional DC approach, mainly due to an overestimation at pressures below 400 Torr (Figure 64). While the one-dimensional model predicts a decrease from 4.9×10^{11} to 2.5×10^{11} cm^{-3} as the pressure is increased from 200 to 500 Torr, the zero-dimensional model predicts a factor of 3 decrease from 7.0×10^{11} to 2.2×10^{11} cm^{-3}. However, both models show the same trend with decreasing metastable density as the pressure is increased.

Zero-Dimensional Simulations.

Extending the zero-dimensional simulations to the entire range of Ar-He mixtures and pressures provides the bulk plasma metastable density profile displayed in Figure 65. The trend of $Ar(1s_5)$ as a function of Ar-fraction displayed in Figure 57 can be seen for pressures near 300 Torr in Figure 65. As pressure is increased, three-body collisions via $Ar(1s_5) + Ar + Ar \rightarrow Ar_2^* + Ar$, which is estimated to have twice the rate constant of the $Ar(1s_5) + Ar + He \rightarrow Ar_2^* + He$ analog [Demyanov et al., 2013], causes a drastic decrease in metastable densities for Ar rich mixtures. Increased Ar_2^* production at elevated pressures causes the peak E/N to occur at lower Ar-fractions due to ionization contributions from $Ar_2^* + e^- \rightarrow Ar_2^+ + 2e^-$. This shift in E/N corresponds to a shift in metastable production, causing the peak metastable density to occur at lower Ar-fractions as the pressure is increased. At 200 Torr the peak metastable density occurs near a 15% Ar-fraction, while the peak is shifted to approximately 10% at 500 Torr.

Electron densities follow the trend observed in Figure 53 as a function of Ar-

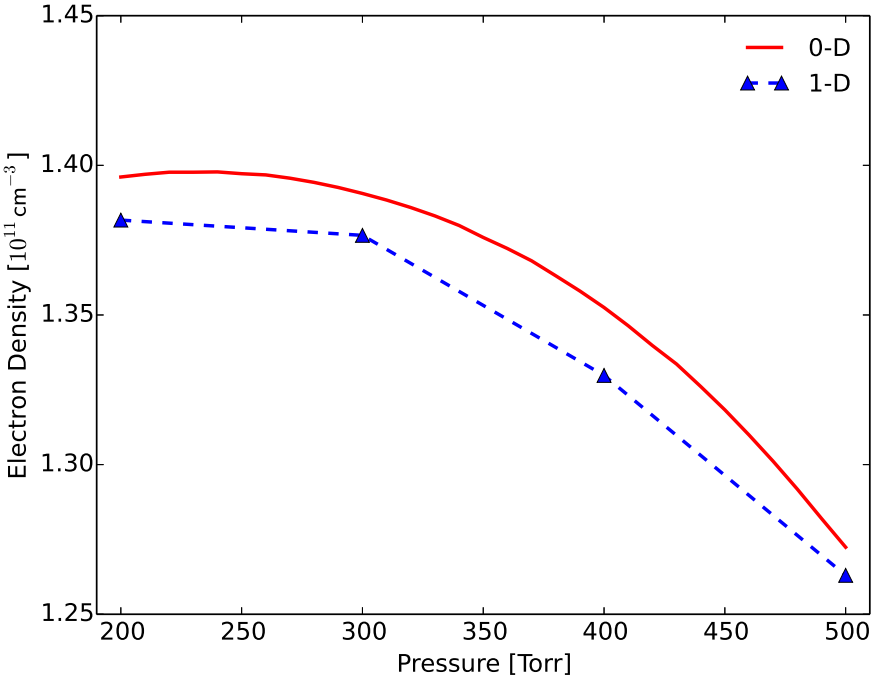

Figure 61. Bulk plasma electron densities for varying pressures in a 15% Ar in He mixture using both the zero and one-dimensional models .

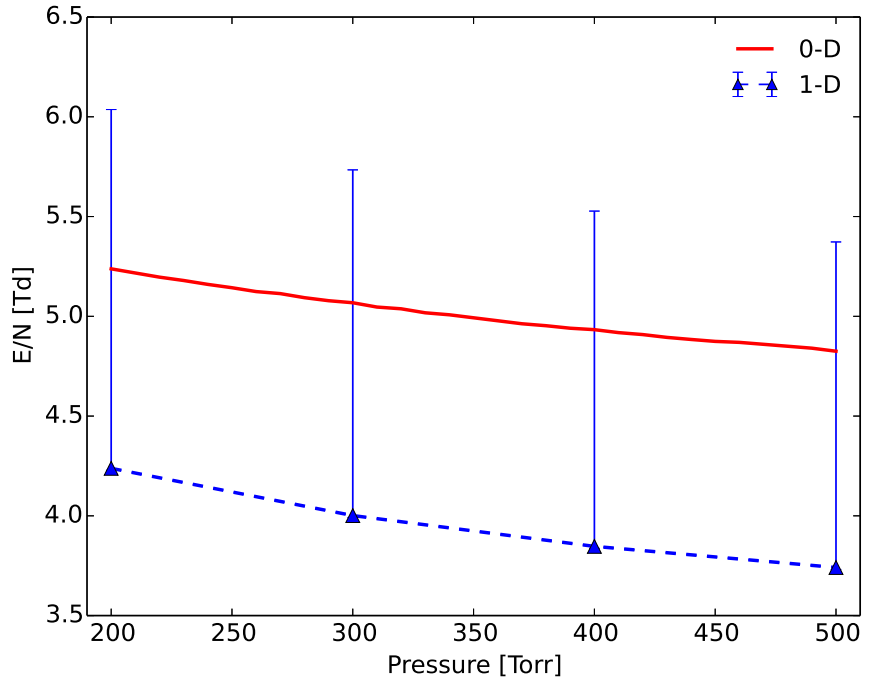

Figure 62. Bulk plasma E/N magnitudes for varying pressures in a 15% Ar in He mixture using both the zero and one-dimensional models. The triangles represent the RMS E/N and the bars represent the maximum E/N attained over a cycle.

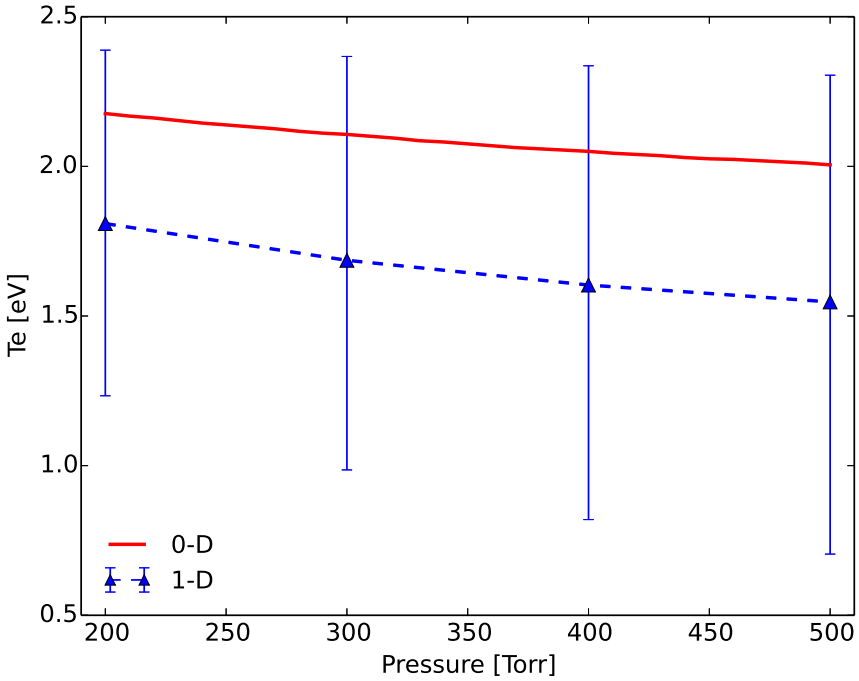

Figure 63. **Bulk plasma electron temperatures for varying pressures in a 15% Ar in He mixture using both the zero and one-dimensional models. The triangles represent the cycle-averaged T_e and the bars correspond to the minimum and maximum values obtained over a cycle.**

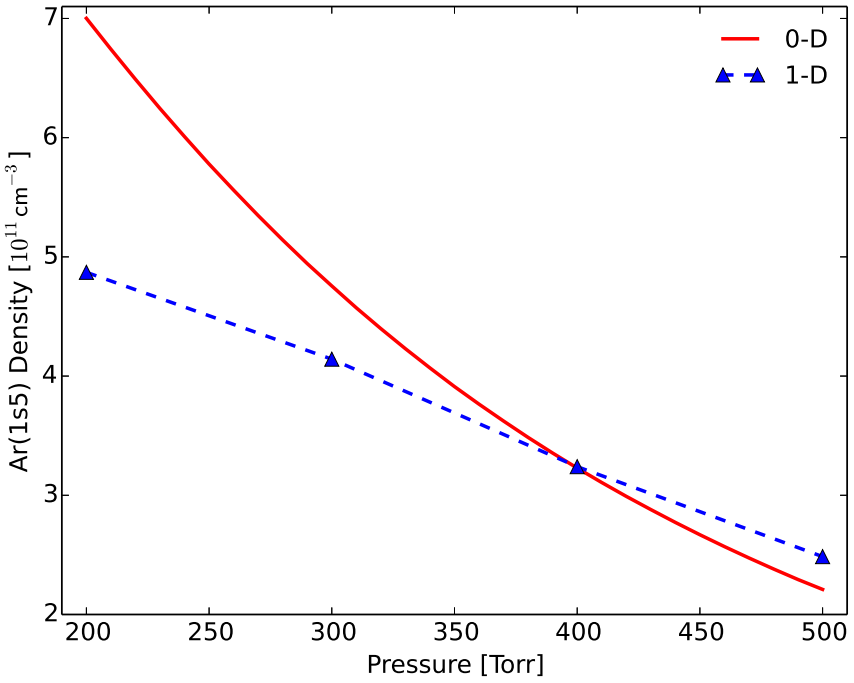

Figure 64. **Bulk plasma $Ar(1s_5)$ densities for varying pressures in a 15% Ar in He mixture using both the zero and one-dimensional models.**

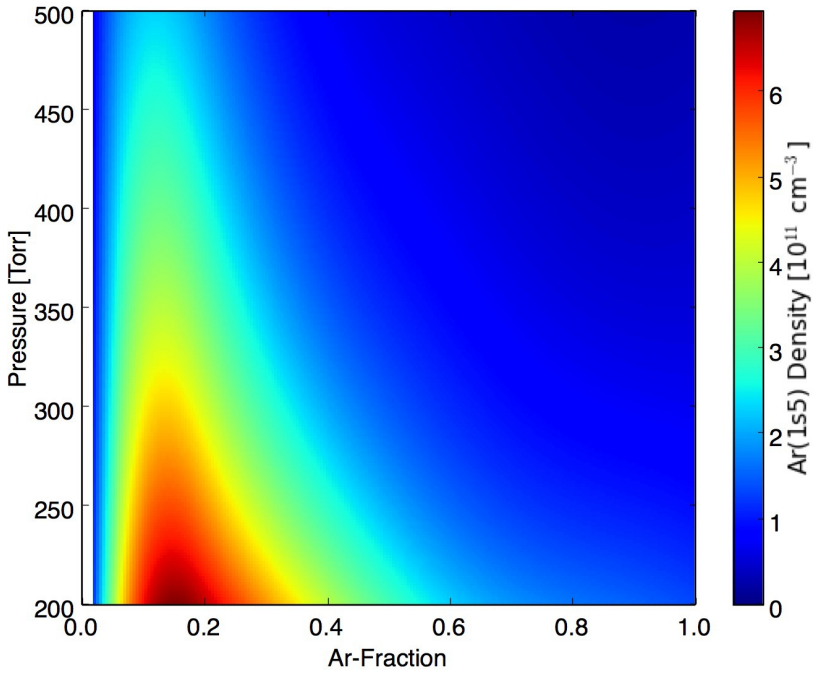

Figure 65. Bulk plasma $Ar(1s_5)$ densities for varying pressures and Ar-fractions using the zero-dimensional effective DC model.

fraction at all pressures (Figure 66). While the electron density shows a slight decrease with increasing pressure at lower Ar-fractions, a small increase with pressure is observed for Ar rich mixtures. Similar to the 15% Ar-fraction scenario, a slight decrease in electron temperature is observed for all Ar-fractions as pressure is increased (Figure 67). The general trend with Ar-fraction is also maintained over all pressures.

Bulk plasma reduced electric fields show a peak near 15% Ar-fraction at 200 Torr with a shift towards lower Ar-fractions as the pressure is increased, as displayed in Figure 68. Additionally, the E/N magnitude is reduced as the pressure is increased. The metastable excitation rates are highly dependent on E/N, which is apparent based on the similarities in the E/N trends (Figure 68) and the $Ar(1s_5)$ density trends (Figure 65)

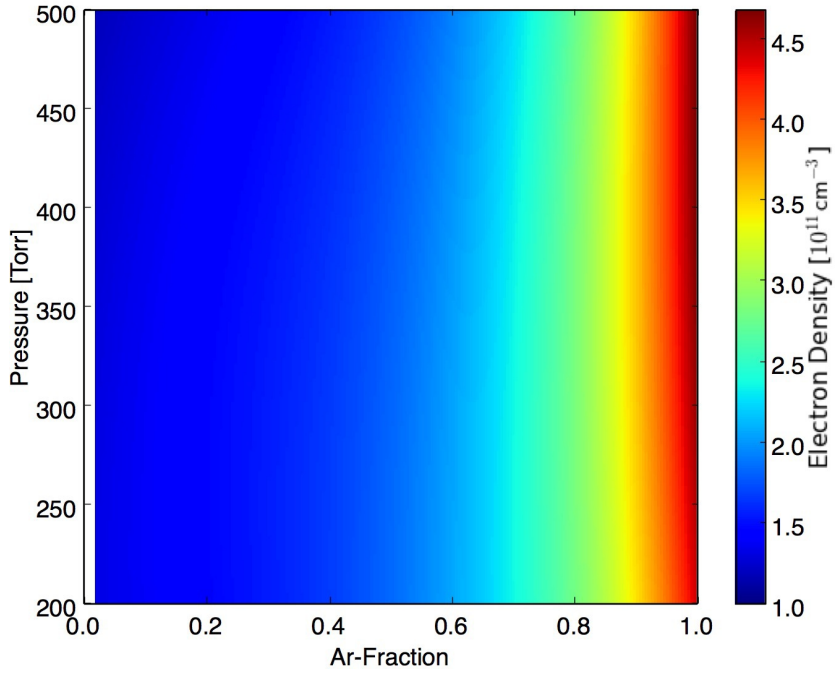

Figure 66. Bulk plasma electron densities for varying pressures and Ar-fractions using the zero-dimensional effective DC model.

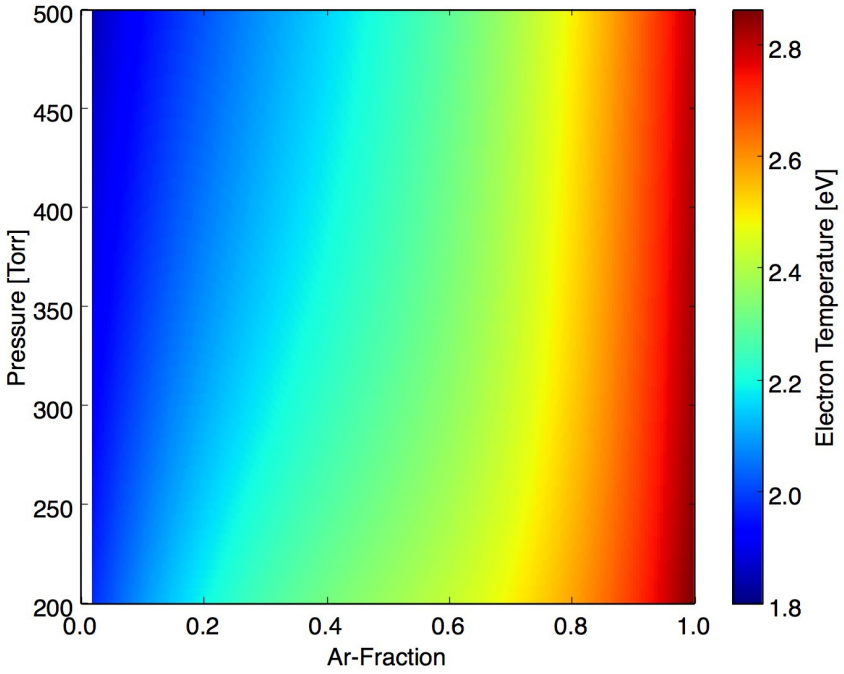

Figure 67. Bulk plasma electron temperatures for varying pressures and Ar-fractions using the zero-dimensional effective DC model.

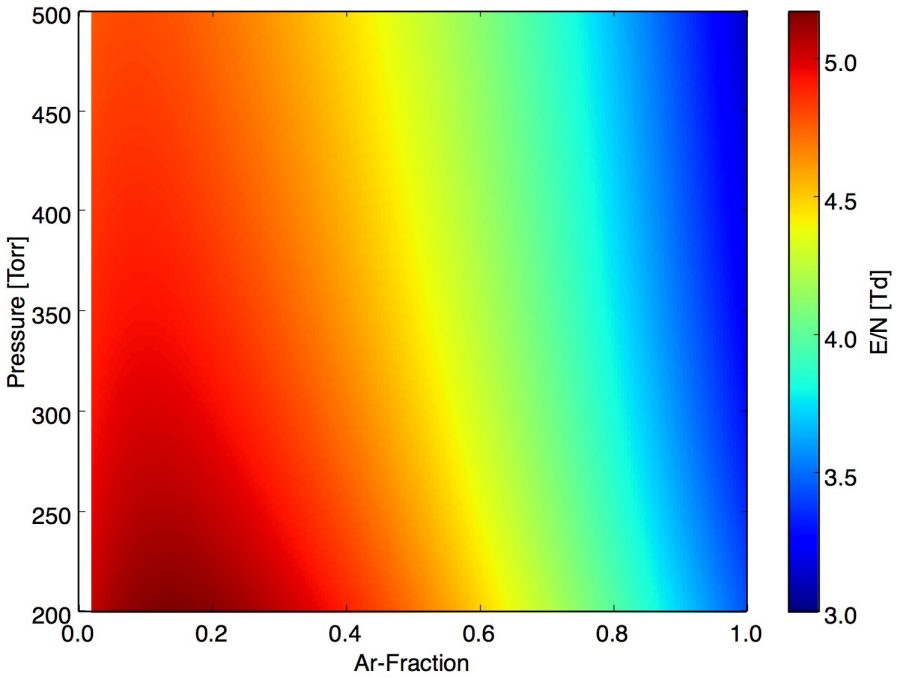

Figure 68. Bulk plasma reduced electric fields for varying pressures and Ar-fractions using the zero-dimensional effective DC model.

Varying Voltage.

To understand the effect of applied voltage on the metastable density profiles, the one-dimensional fluid model is used for a 15% Ar in He mixture at a pressure of 200 Torr for a variety of applied voltages. The peak electrode voltage is increased from 500 to 1750 V in 250 V steps. Gas heating is ignored to simplify the analysis. However, the inclusion of gas heating would provide a more accurate estimation of metastable densities as a function of voltage and should be taken into account during future calculations.

While the previous analyses produced α-mode discharges (based on the measured fluorescence profiles), this increase in voltage will eventually cause a transition to the γ-mode if the electron/current density reaches a critical value. The critical electron density is the electron density which produces a sheath voltage large enough to cause a breakdown in the sheaths (see Raizer et al. [1995] for more detail). Similar to a DC

glow discharge, the breakdown voltage in the sheaths is dependent on the pressure-distance product, as displayed in the Paschen curves (Figure 4). Sheath voltages are dependent on the current density, j, and amplitude of sheath oscillations, A: $V_s = 2Aj/\omega\epsilon_0$. The amplitude of sheath oscillation is also dependent on electron density and applied voltage (Equation 57). From the sheath voltage dependence on the electron density through the current density, the critical electron density is attained when the sheath voltage is equal to the breakdown voltage associated with the sheath thickness:

$$n_{e,critical} = \frac{B_t p \epsilon_0}{q_e A \left(C_t + \ln 2pA\right)}, \tag{127}$$

$$C_t = \ln\left(\frac{A_t}{\ln\left(1 + 1/\gamma\right)}\right), \tag{128}$$

where $B_t = 176.0$ V/cm $\cdot$ Torr is the Townsend B coefficient, $A_t = 11.5$ 1/cm $\cdot$ Torr is the Townsend A coefficient, and γ is the secondary emission coefficient [Raizer et al., 1995].

For the geometry of the clam shell electrode experiment with an applied peak voltage of 500 V, the critical electron density is calculated to be 4.4×10^{11} cm^{-3} at a pressure of 200 Torr for pure Ar. This critical electron density is a function of both pressure and applied voltage. As the pressure is increased, the critical electron density increases due to an increase in the pressure-distance product (Figure 69). The critical electron density increases from approximately 1.1×10^{11} cm^{-3} at 100 Torr to 5.4×10^{12} cm^{-3} at 700 Torr. Additionally, the sheath thickness corresponding to the critical electron density decreases as the pressure is increased (Figure 70).

At a constant pressure, the critical electron density is a function of the effective applied voltage. As the voltage increases, the critical electron density decreases (Figure 71). For a pressure of 200 Torr, the critical electron density decreases from

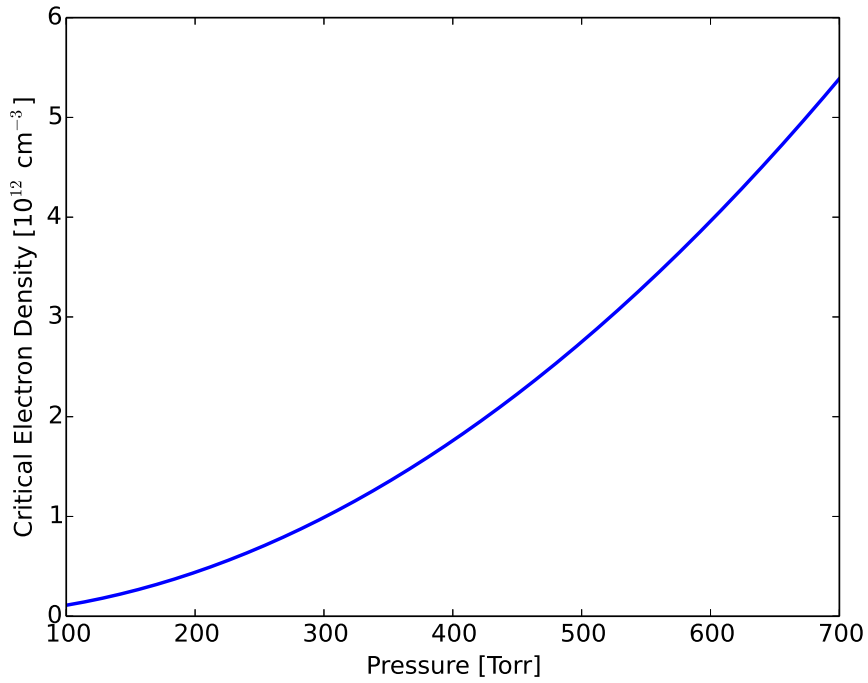

Figure 69. Critical electron density required for an α to γ-mode transition for an applied voltage of 500 V.

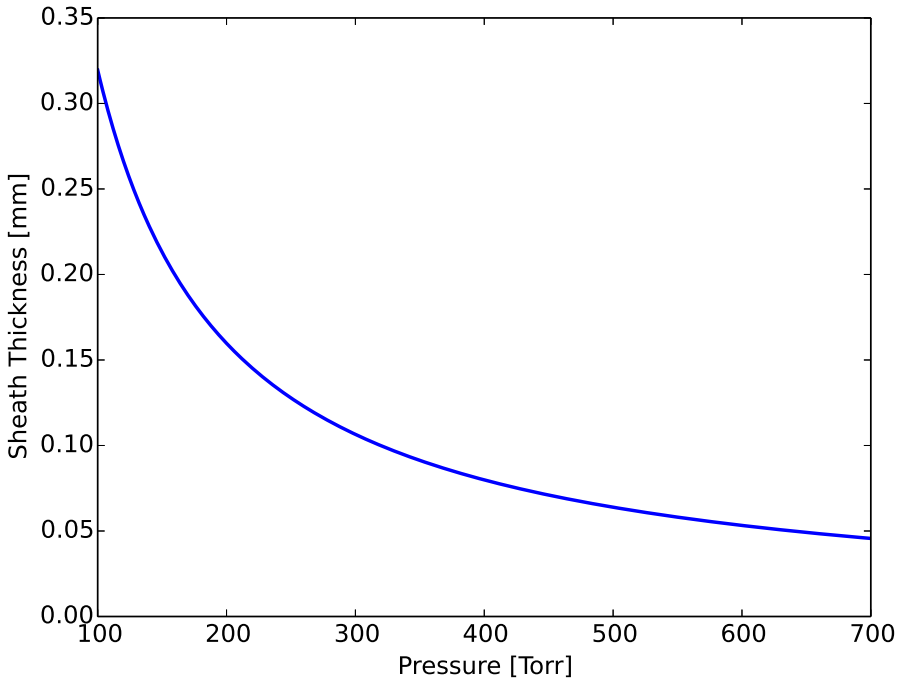

Figure 70. Sheath thickness corresponding to the critical electron density required for an α to γ-mode transition for an applied voltage of 500 V.

5.9×10^{12} cm^{-3} at 200 V to 4.4×10^{11} cm^{-3} at 500 V.

To analyze the α to γ-mode transition, the effective voltage across the plasma, V_p, is defined by:

$$V_p = V_s + V_b = V_{app} - V_d, \tag{129}$$

which provides the voltage applied to the discharge. In this scenario, the voltage drop due to dielectric charging, V_d, acts a ballast resistor by lowering the effective voltage as the current density is increased. Following the example of Balcon et al. [2008], the peak current density is analyzed as a function of V_p. An α-mode is characterized by positive, linear differential conductivity where the current density increases with an increasing V_p. After the transition to a γ-mode, the differential conductivity becomes negative, showing an increase in current for a decrease in V_p.

For a secondary electron emission coefficient of 0.01 estimated for Pyrex tubes the current-voltage characteristic of a 15% Ar-fraction, 200 Torr discharge is displayed in Figure 72. The increase in current is positive and linear, indicating an α-mode discharge at all voltages. The estimated critical electron density for an effective voltage of 420 V, corresponding to V_p for the 1750 V scenario, is approximately 6.1×10^{11} cm^{-3}. A simulated bulk plasma electron density of 9.1×10^{11} cm^{-3} for the 1750 V scenario is larger than the estimated critical electron density, but no α to γ-mode transition has occurred. The peak current density of approximately 200 mA/cm^2 is not large enough to cause a transition for a secondary coefficient of 0.01, according to the simulations.

The average applied power, $\langle P_{app} \rangle$, commonly referred to as the power for an RF circuit, is calculated as the average power delivered over a cycle:

$$\langle P_{app} \rangle = I_{rms} V_{rms} \cos\theta, \tag{130}$$

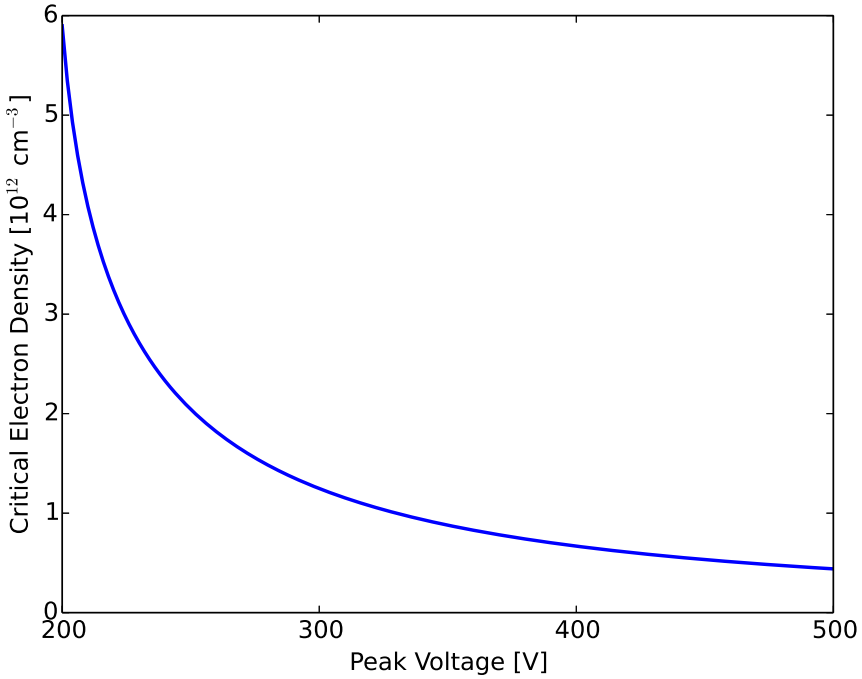

Figure 71. Critical electron density required for an α to γ-mode transition at a pressure of 200 Torr.

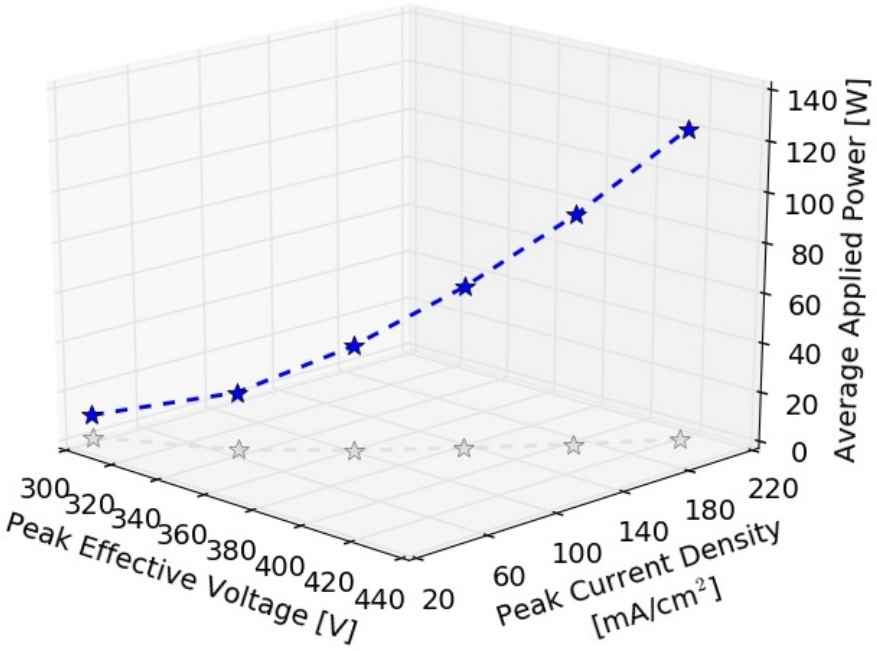

Figure 72. Peak current as a function of the effective voltage across the plasma, V_p, for a secondary emission coefficient of 0.01.

where I_{rms} is the RMS current, V_{rms} is the RMS applied voltage, and θ is the phase difference between the current and voltage. The peak delivered power can be much larger than the average applied power, as displayed in Figure 73. For an applied voltage of 500 V, $\langle P_{app} \rangle$ is approximately 9 W, with a current-voltage phase difference of 73 degrees and a peak delivered power of 40 W. For the 1750 V scenario, an average power of approximately 120 W corresponds to a phase difference of 81 degrees and a peak power of 870 W.

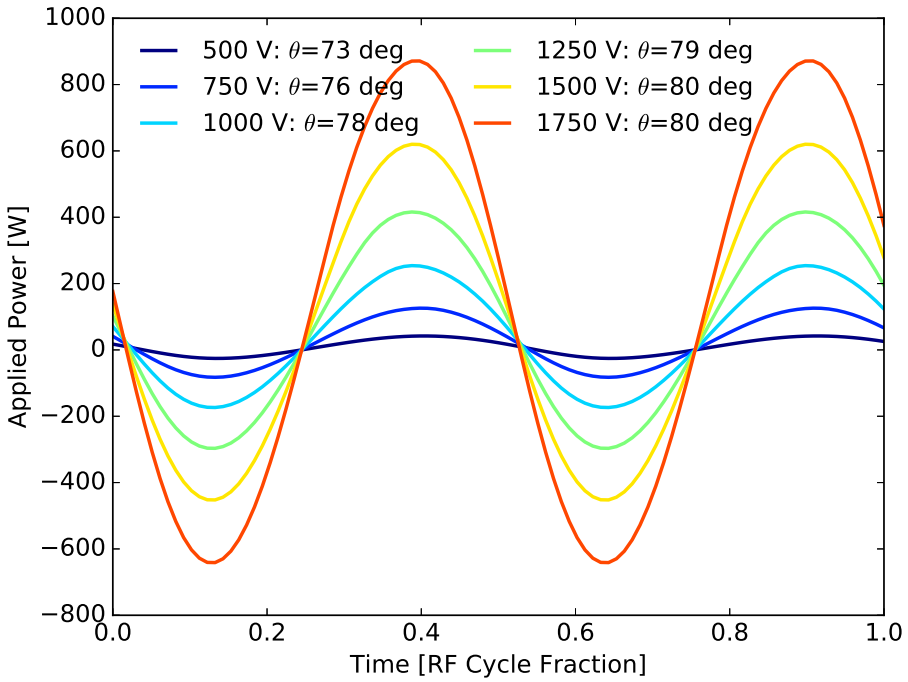

Figure 73. Delivered power over one RF cycle for a secondary emission coefficient of 0.01. The phase difference between the current and applied voltage is represented by θ.

Metastable densities show a large increase as the applied voltage is increased, as displayed in Figure 75. The bulk plasma $Ar(1s_5)$ density increases from approximately 4.9×10^{11} cm^{-3} at 500 V to 2.7×10^{12} cm^{-3} at 1750 V. As the voltage is increased, the bulk plasma metastable density approaches the desired value of 10^{13} cm^{-3}. Peak metastable densities range from 5.6×10^{12} cm^{-3} for the 500 V scenario to 4.1×10^{13} cm^{-3} for the 1750 V scenario. While the increase in metastable density

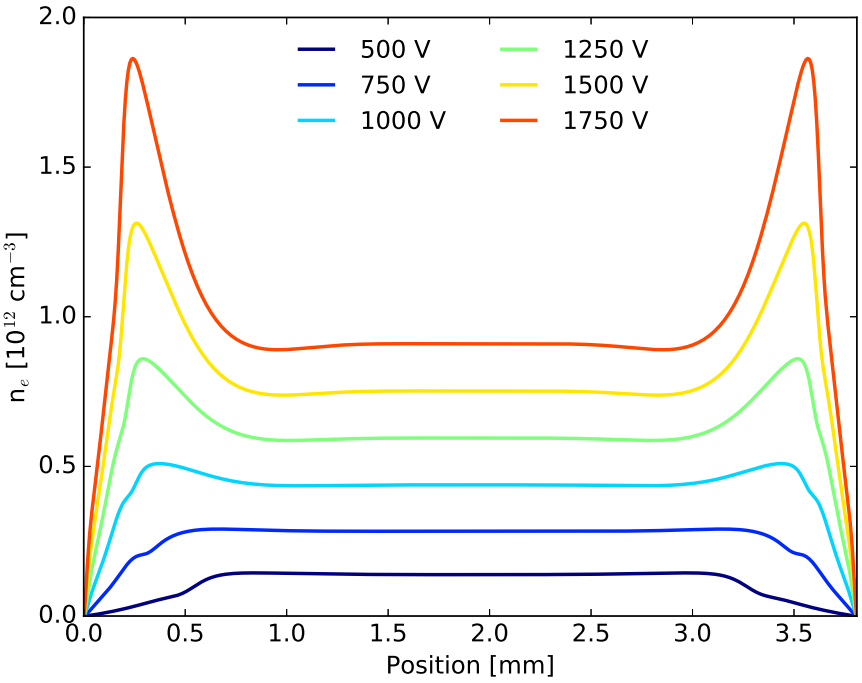

Figure 74. Cycle averaged electron density for a variety of applied voltages at a pressure of 200 Torr and a 15% Ar-fraction using a secondary emission coefficient of 0.01.

with increasing voltage is promising, continuing to increase the voltage will eventually lead to thermal instabilities that terminate laser operation.

Bulk plasma electron temperatures are approximately 1.8 eV for all applied voltages, as displayed in Figure 76. However, the T_e in the sheaths shows a large increase with applied voltage, increasing from 4.6 to 8.6 eV as the applied voltage increases from 500 to 1750 V. The RMS E/N magnitudes show a similar behavior, with bulk plasma values around 4.3 for all applied voltages (Figure 77). Similar to the electron temperature in the sheaths, the RMS E/N increases from a peak of $\sim$ 120 Td for the 500 V scenario to $\sim$ 540 Td for the 1750 V scenario.

To induce an α to γ-mode transition, the analysis as a function of applied voltage is repeated using a secondary electron emission coefficient of 0.1. An increased secondary coefficient allows for an increase in the number of secondary electrons, which are required to maintain a γ-mode discharge. While the secondary coefficient does

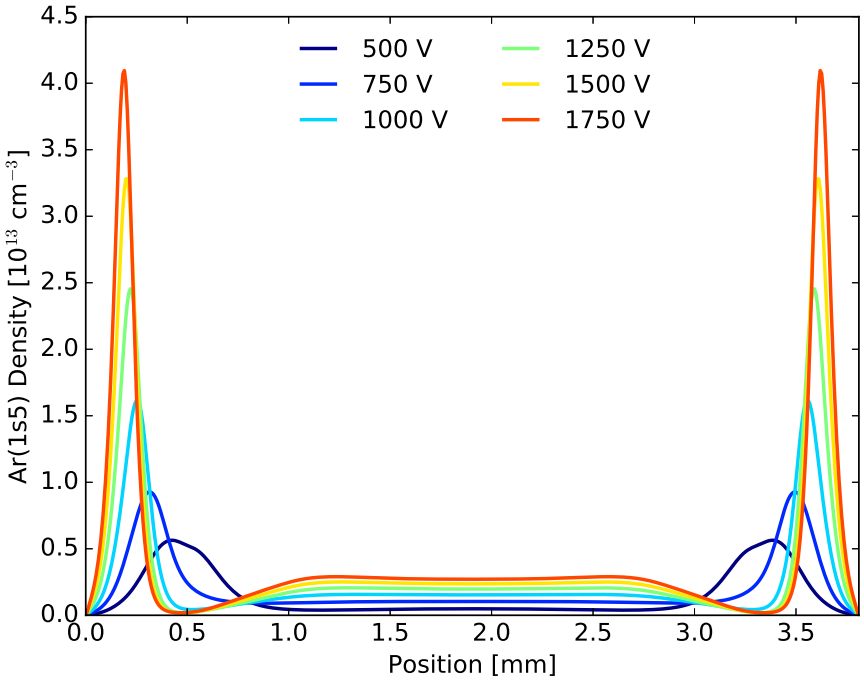

Figure 75. Cycle averaged metastable densities for a variety of applied voltages at a pressure of 200 Torr and a 15% Ar-fraction using a secondary emission coefficient of 0.01.

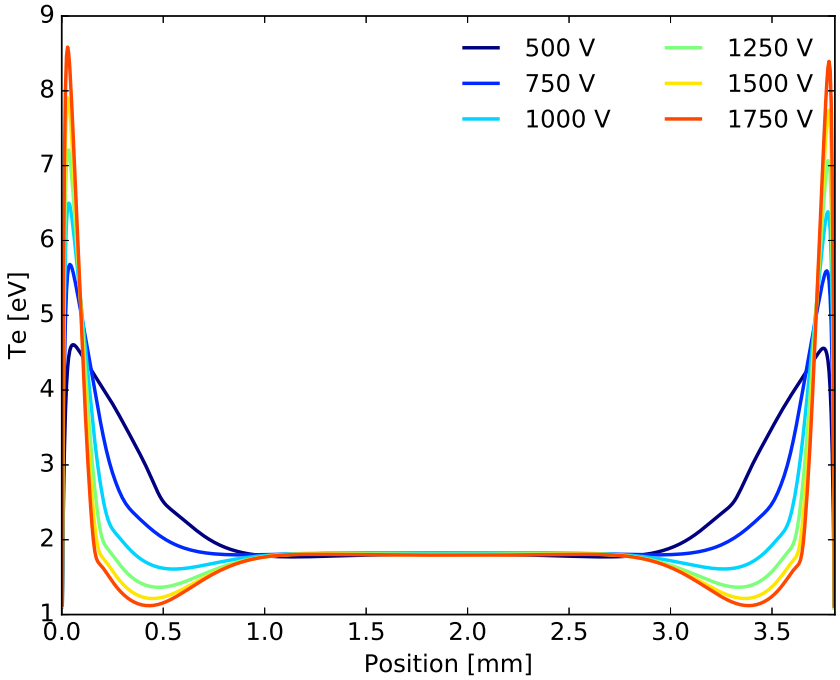

Figure 76. Cycle averaged electron temperature for a variety of applied voltages at a pressure of 200 Torr and a 15% Ar-fraction using a secondary emission coefficient of 0.01.

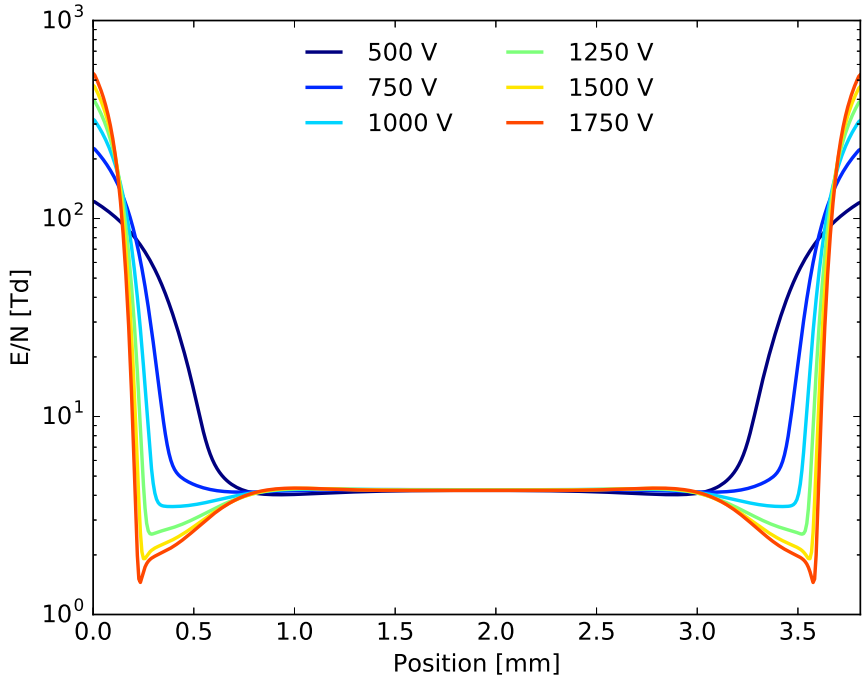

Figure 77. RMS E/N magnitudes for a variety of applied voltages at a pressure of 200 Torr and a 15% Ar-fraction using a 15% Ar-fraction using a secondary emission coefficient of 0.01.

not correspond to the Pyrex tube used in the experiment, it allows for an analysis of a γ-mode in an Ar-He mixture. The current voltage characteristic is displayed in Figure 78, showing an α to γ transition at a current of ~ 175 mA/cm^2, corresponding to the applied voltage of 1400 V. As the applied voltage is increased above this threshold, the effective applied voltage, V_p, decreases while the current increases, providing the negative differential conductivity characteristic of the onset of a γ-mode discharge [Balcon et al., 2008].

The average delivered power, $\langle P_{app} \rangle$, ranges from 14 W for the 500 V scenario to 127 W for the 1750 V scenario (Figure 78). Peak powers range from 60 W to 1000 W as the applied voltage increases from 500 to 1750 V, as displayed in Figure 79. While the peak effective voltage decreases during an α to γ-mode transition, the increase in applied voltage and current causes an increase in the applied power. In the γ-mode, as current density increases drastically for relatively small increases in

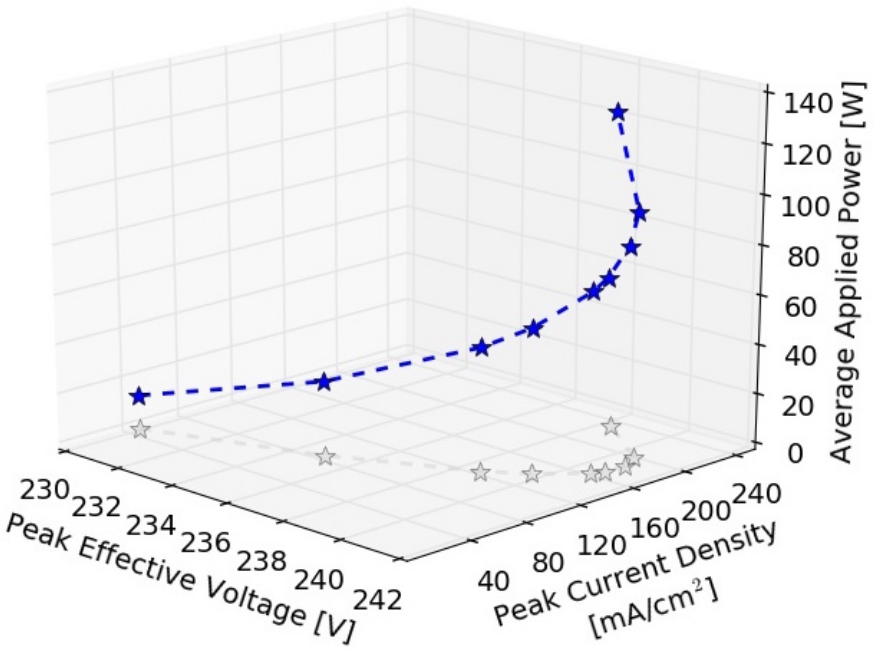

Figure 78. Peak current as a function of the effective voltage across the plasma, V_p, for a secondary emission coefficient of 0.1.

applied voltage, the applied power will increase significantly as the applied voltage is increased.

The estimated critical electron density for an effective voltage of 240 V and a secondary emission coefficient of 0.1 is approximately 9.8×10^{11} cm^{-3}, which is greater than the simulated bulk plasma electron density of 7.9×10^{11} cm^{-3} for the 1400 V applied voltage scenario (Figure 80). However, the electron density near the sheaths is approximately 1.9×10^{12} cm^{-3}, which is greater than the critical electron density. The spatial average of the cycle averaged electron density is approximately 1.0×10^{12} cm^{-3}, which is within 3% of the estimated critical electron density.

Bulk plasma $Ar(1s_5)$ densities range from 7.1×10^{11} cm^{-3} for an applied voltage of 500 V to 2.9×10^{12} cm^{-3} for an applied voltage of 1750 V (Figure 81). The metastable density of the 1750 V γ-mode is slightly larger than the 2.7×10^{12} cm^{-3} bulk plasma density obtained for the 1750 V α-mode calculated using a smaller secondary emission coefficient. Sheath densities range from 6.9×10^{12} cm^{-3} for an applied voltage of 500

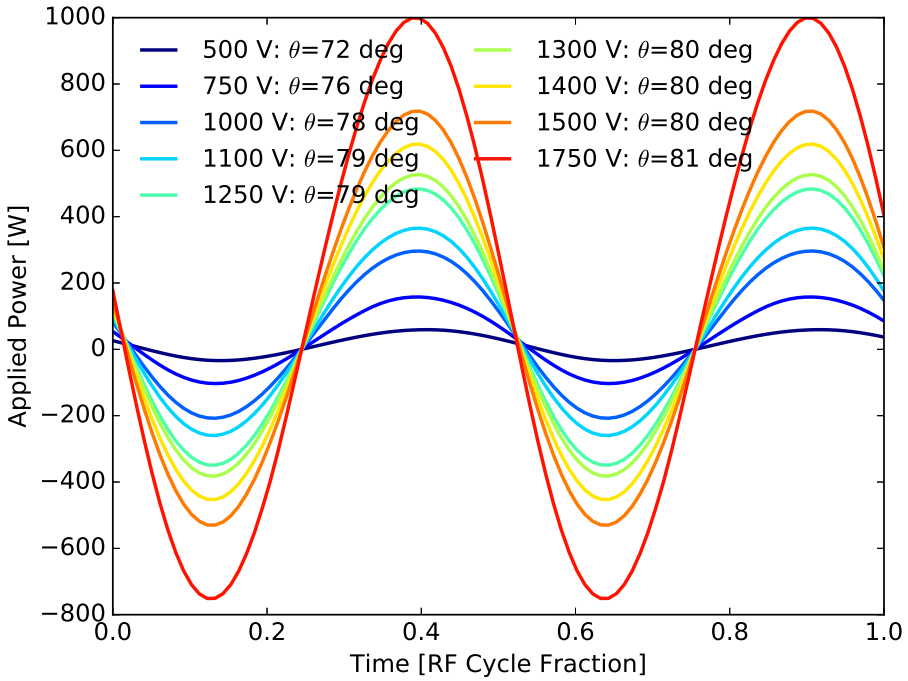

Figure 79. Delivered power over one RF cycle for a secondary emission coefficient of 0.1. The phase difference between the current and applied voltage is represented by θ.

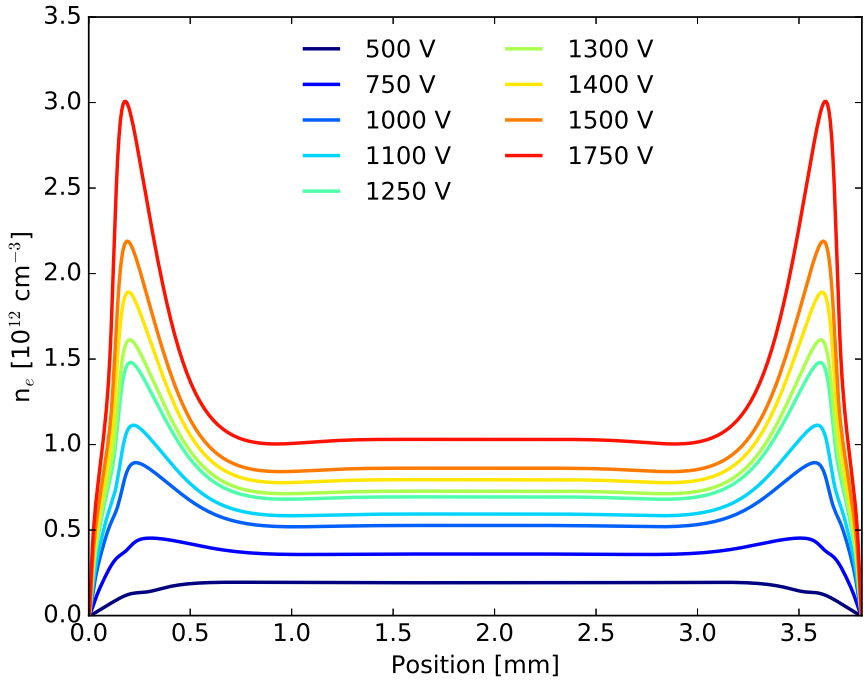

Figure 80. Cycle averaged electron density for a variety of applied voltages at a pressure of 200 Torr and a 15% Ar-fraction using a secondary emission coefficient of 0.1.

V to 5.6×10^{13} cm^{-3} for an applied voltage of 1750 V. The sheath density for the 1750 V γ-mode is about 40% larger than the sheath densities for the 1750 V α-mode. This onset of the γ-mode appears to cause a large increase in sheath densities, with a relatively small increase in bulk plasma densities.

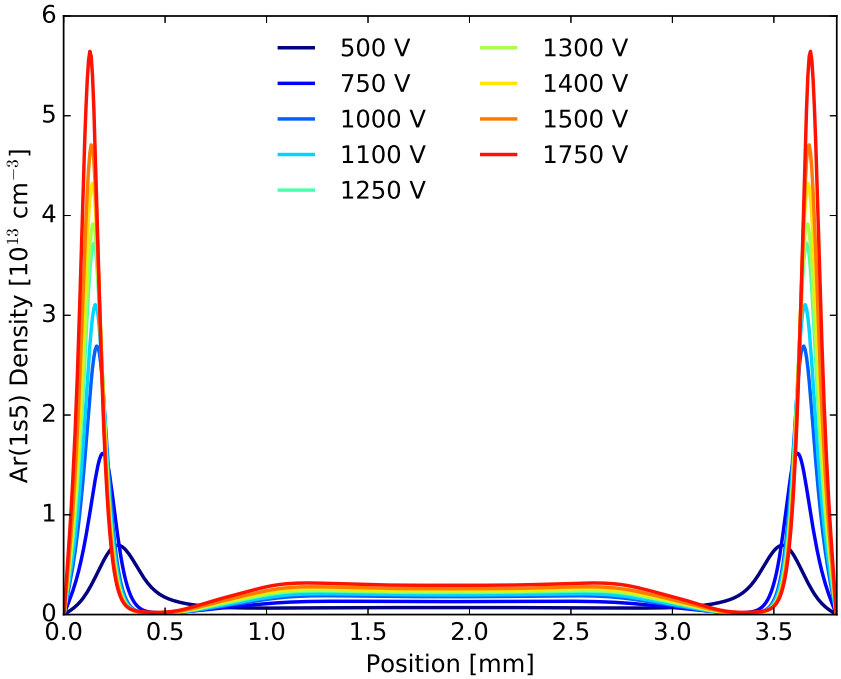

Figure 81. Cycle averaged metastable densities for a variety of applied voltages at a pressure of 200 Torr and a 15% Ar-fraction using a secondary emission coefficient of 0.1.

Similar to the simulations using a secondary emission coefficient of 0.01, the bulk plasma electron temperatures are all approximately 1.8 eV, as displayed in Figure 76. Sheath electron temperatures range from 4.7 eV for the 500 V scenario to 6.9 eV for the 1750 V scenario. No noticeable change in electron temperature profile is visible for the γ-mode scenarios compared to the α-mode profiles. Reduced electric field magnitudes in the bulk plasma are approximately 4.3 Td for all applied voltages. The RMS E/N in the sheaths range from 160 Td for the 500 V scenario to 500 Td for the 1750 V scenario.

Bulk plasma metastable and electron densities as a function of applied voltage for

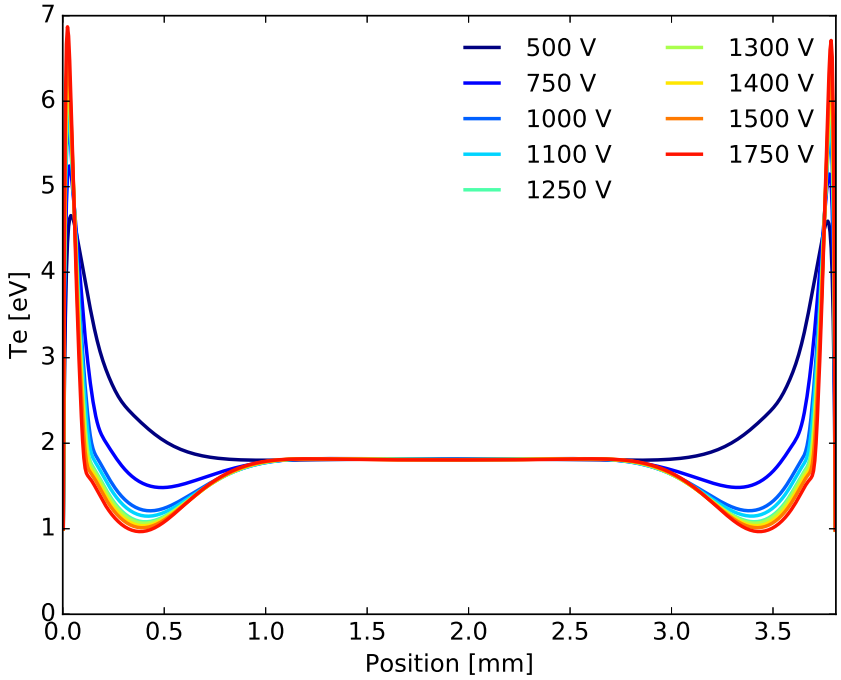

Figure 82. Cycle averaged electron temperature for a variety of applied voltages at a pressure of 200 Torr and a 15% Ar-fraction using a secondary emission coefficient of 0.1.

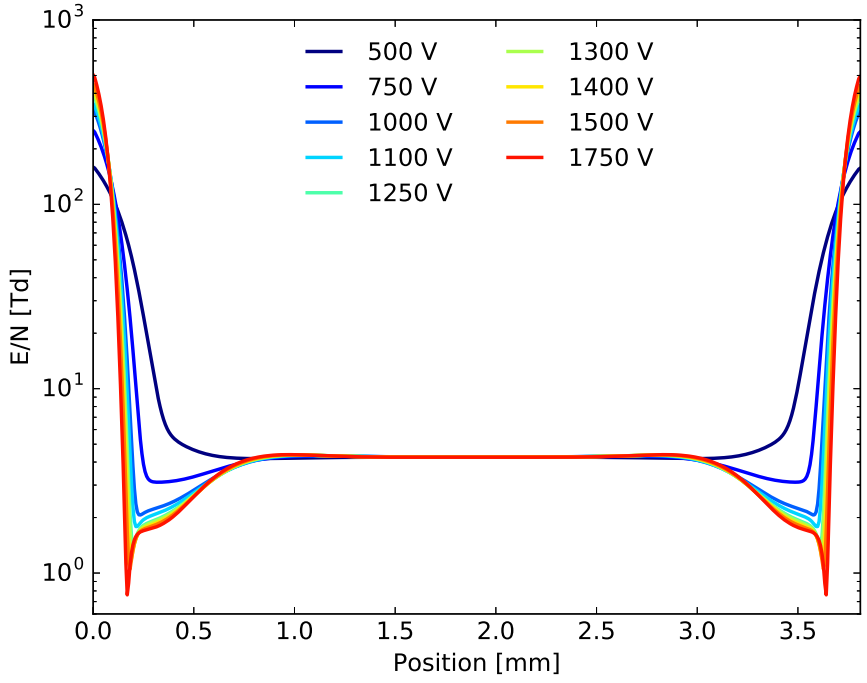

Figure 83. RMS E/N magnitudes for a variety of applied voltages at a pressure of 200 Torr and a 15% Ar-fraction using a secondary emission coefficient of 0.1.

the two secondary electron emission coefficients are displayed in Figures 84 and 85. The densities are slightly larger for the 0.1 secondary coefficient over all applied voltages, and no noticeable change occurs during the γ-mode onset. The dielectric barriers covering the electrodes allows for a subnormal γ-mode where the current densities are lower than bare electrode normal current densities characteristic of the γ-mode due to the dielectric surface charge dependence on the current density [Raizer et al., 1995]. Additionally, a two-dimensional simulation is required to capture the transverse charge diffusion responsible for stabilizing the normal current density [Raizer et al., 1995]. As a result, our simulated one-dimensional subnormal current densities don't show the large increase in electron density expected for the bare electrode γ-mode onset. However, the two-term approximation to the Boltzmann equation fails at the non-uniform, elevated electric fields produced in the sheaths of a γ-mode, which impacts the estimated density profiles.

A hybrid kinetic-fluid model would provide a better estimate of the densities produced in a γ-mode discharge, and should be implemented for further exploration of the γ-mode. Gas heating should also be taken into account due to the increase in current density and associated Joule heating expected as the voltage is increased. This increase in gas heating increases the likelihood of thermal instability formation, which places limitations on the maximum applied voltage. The increase in $Ar(1s_5)$ densities observed with increasing voltage will eventually meet an instability threshold, and continuing to increase the applied voltage will render the discharge unusable as a large volume uniform source of metastable densities in an OPRGL.

Experimental data for the α to γ-mode transition in pure Ar at atmospheric pressures is sparse, which may be due to the likelihood of evolving into a filamentary mode during the α to γ-mode transition [Balcon et al., 2008]. This filamentary mode has been observed for pulsed RF discharges with an applied voltage of 1400 V peak to

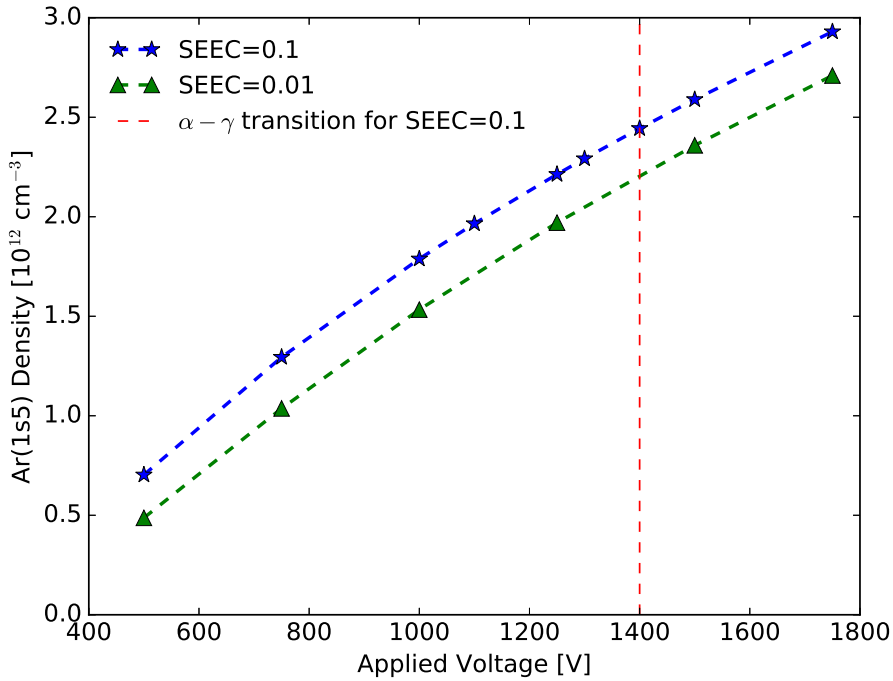

Figure 84. Cycle averaged bulk plasma metastable densities as a function of applied voltage for secondary electron emission coefficients (SEEC) of 0.1 and 0.01. The red dashed vertical line represents the onset of the γ-mode for the secondary coefficient of 0.1.

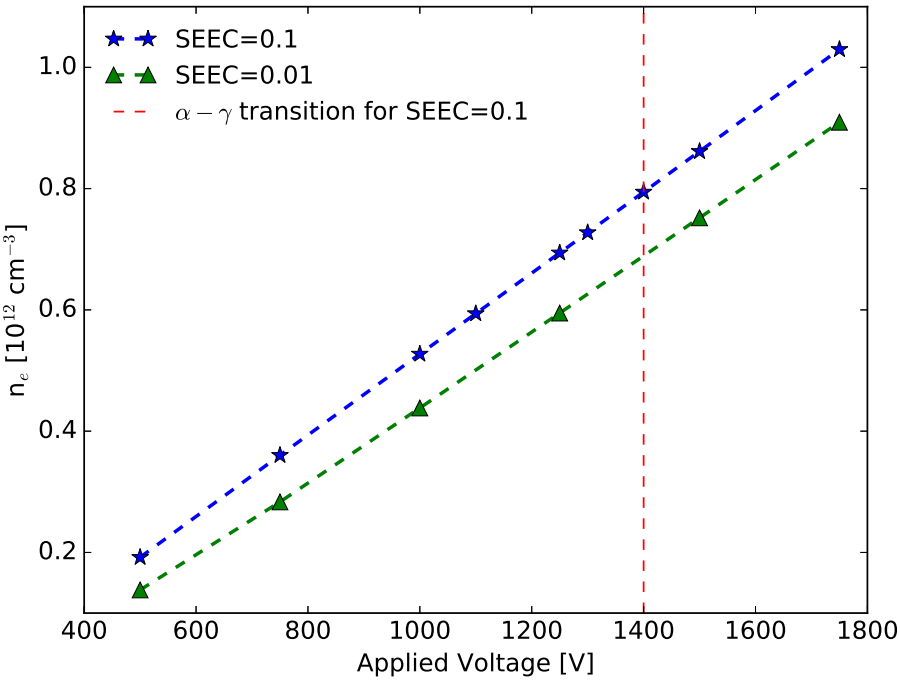

Figure 85. Cycle averaged bulk plasma electron densities as a function of applied voltage for secondary electron emission coefficients (SEEC) of 0.1 and 0.01. The red dashed vertical line represents the onset of the γ-mode for the secondary coefficient of 0.1.

peak and a pressure-distance product of 76 Torr · cm for a single-barrier (one electrode covered with a dielectric) RF-DBD [Balcon et al., 2007]. A separate analysis using a double-barrier (both electrodes covered with a dielectric) RF-DBD with pure Ar and a similar pressure-distance product measured a stable α-mode discharge up to 1400 V peak [Bin et al., 2011]. The inclusion of a dielectric barrier across each electrode increases the voltage threshold due to a reduction in the effective voltage across the plasma caused by dielectric charging. Measurements of the α to γ-mode transition in an Ar-He mixture at high pressures for a double-barrier RF-DBD could not be found in the literature. As a result of the lack of experimental data, a comparison to experiment cannot be performed.

While the normal γ-mode discharge is enticing because of the large electron densities expected, which would increase metastable production rates, care must be taken when using a γ-mode discharge for a gas laser. The excess current and associated Joule heating in the γ-mode increases the likelihood of thermal instabilities and non-uniformity [Garscadden et al., 1991]. The increase of energetic electrons in the γ-mode is known to decrease CO_2 laser efficiency [YATSENKO, 1992], but the dependence of an OPRGL on metastable excitation would benefit from the energetic electrons. However, the current density required to fill the area of an electrode in the γ-mode would increase the power requirements for a large volume discharge. Additionally, the transition to a filamentary mode observed during the γ-mode onset at high pressures is problematic for use as a laser medium and should be analyzed in more detail.

4.3 Ring Electrodes Experiment

In addition to the experiment performed using the clam shell electrodes, a separate RF-DBD experiment was performed using ring electrodes. Zero-dimensional simulations of the bulk plasma are performed for the ring electrode scenario to compare

against measured $Ar(1s_5)$ and $Ar(1s_4)$ densities.

Description of Experiment.

The ring electrode RF-DBD experiment described in Eshel et al. [2016] used the cylindrical geometry and experimental configuration displayed in Figures 86 and 87. A flow rate of 100 sccm and a power of 10 W were used to produce discharges with variable Ar-He mixtures at several pressures. $Ar(1s_5)$ and $Ar(1s_4)$ density measurements were extracted from the absorbance spectra [Eshel et al., 2016]. Doppler widths from the spectra measurements indicated a temperature of 440 ± 20 K, over all pressures and Ar-fractions. In addition to the density and temperature measurements, the total current was measured, providing a detailed analysis of discharge behavior as Ar-fraction and pressure were varied.

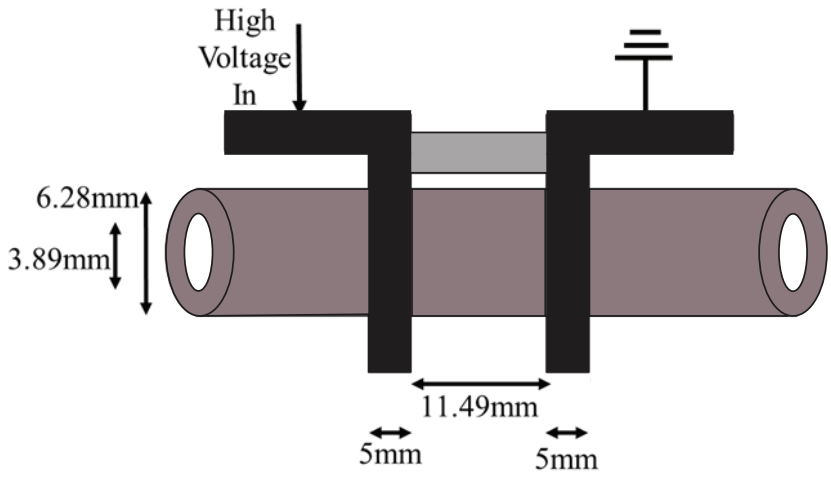

Figure 86. A diagram of the ring electrode RF-DBD discharge tube used for the experimental portion of this analysis.

Zero-Dimensional Simulations.

ZDPlasKin is used to perform zero-dimensional simulations of the ring electrode RF-DBD for a variety of Ar-fractions and pressures ranging from 10 to 160 Torr,

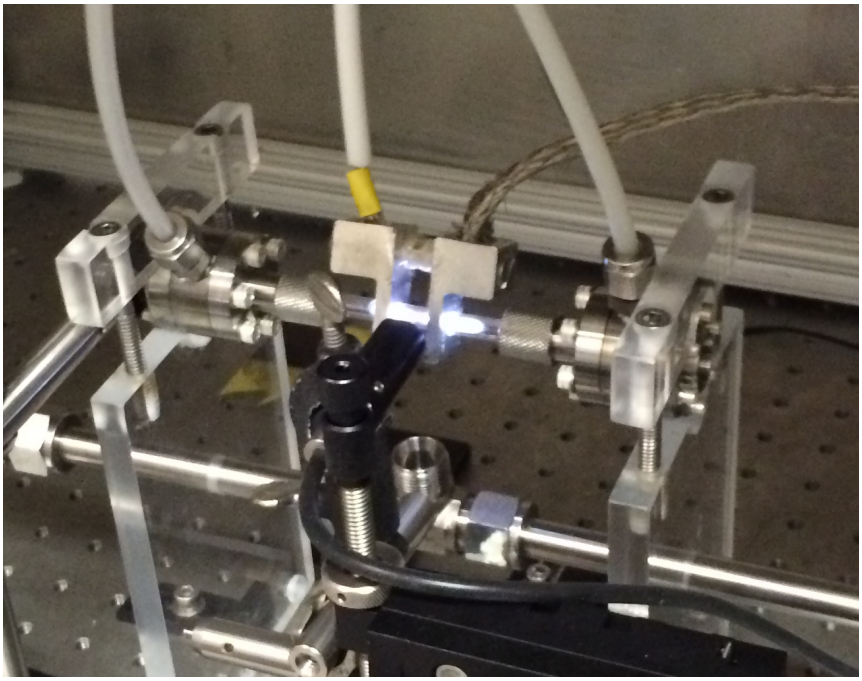

Figure 87. A picture of the ring electrode RF-DBD experimental setup during a discharge.

following the outline in Section 4.1. For the complicated geometry of the RF-DBD, the zero-dimensional model requires multiple assumptions, including the assumption of a parallel plate geometry (which is not accurate). However, the goal of the analysis is to determine the parametric dependence of the $Ar(1s_5)$ and $Ar(1s_4)$ densities on the Ar-fraction and pressure, which can be accomplished by a zero-dimensional model with limited computation expense. An α-mode discharge is assumed for calculation of the sheath voltages. Additionally, a voltage of 400 V peak is used to used for all pressures and Ar-fractions.

Varying Pressure.

Simulated currents show an increase with pressure from 10 to 50 Torr, followed by a decrease as pressure is increased from 50 to 160 Torr (Figure 88). The current for the 25% Ar-fraction is slightly larger than the other Ar-fractions at lower pressures. However, the currents for the different Ar-fractions are within 20% of each other over

all pressures.

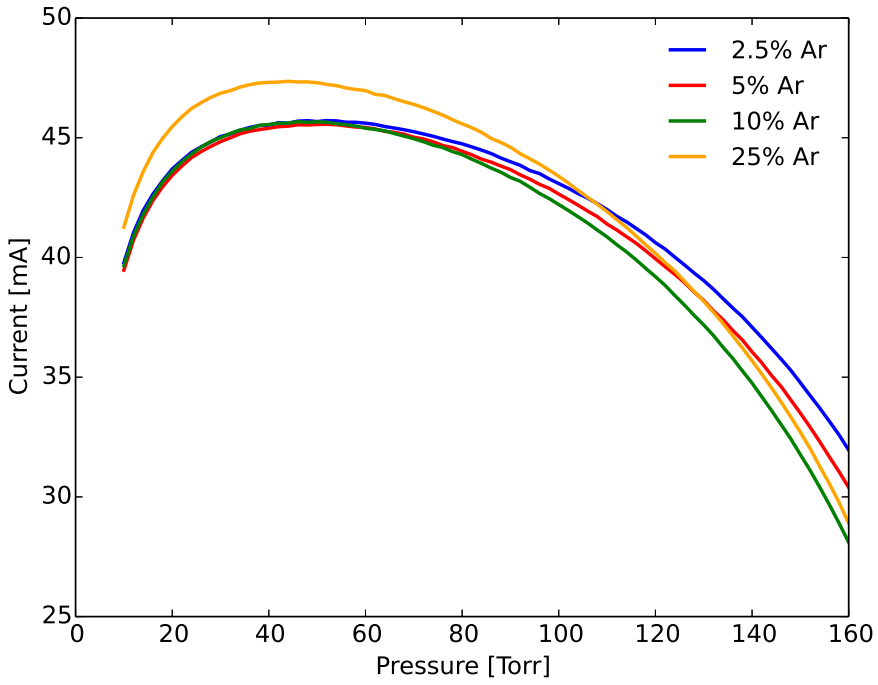

Figure 88. Simulated RMS currents as a function of pressure for the ring electrode RF-DBD.

Current density follows $j = q_e n_e \mu_e E$, and because μ_e is inversely proportional to the neutral gas density, $j \propto n_e \times E/N$. Therefore, the current density versus pressure follows the product of electron density and E/N versus pressure. Simulated electron densities show a large increase from 10 to 50 Torr, remaining nearly constant from 50 to 100 Torr, followed by a large decrease from 100 to 160 Torr (Figure 89). Conversely, simulated E/N values show a large decrease from 10 to 50 Torr, followed by a slight decrease from 50 to 160 Torr (Figure 90). The product of the two provides the simulated current profile over pressure.

To understand the E/N and n_e behavior as a function of pressure, it is helpful to analyze the steady-state electron production and loss rates as a function of pressure. For the relatively small cavity size and pressures studied in the experiment, the dominant loss mechanism for electrons is ambipolar diffusion to the walls. At steady-state, the electron production and loss rates are equal, following Equation 28. Ignoring the

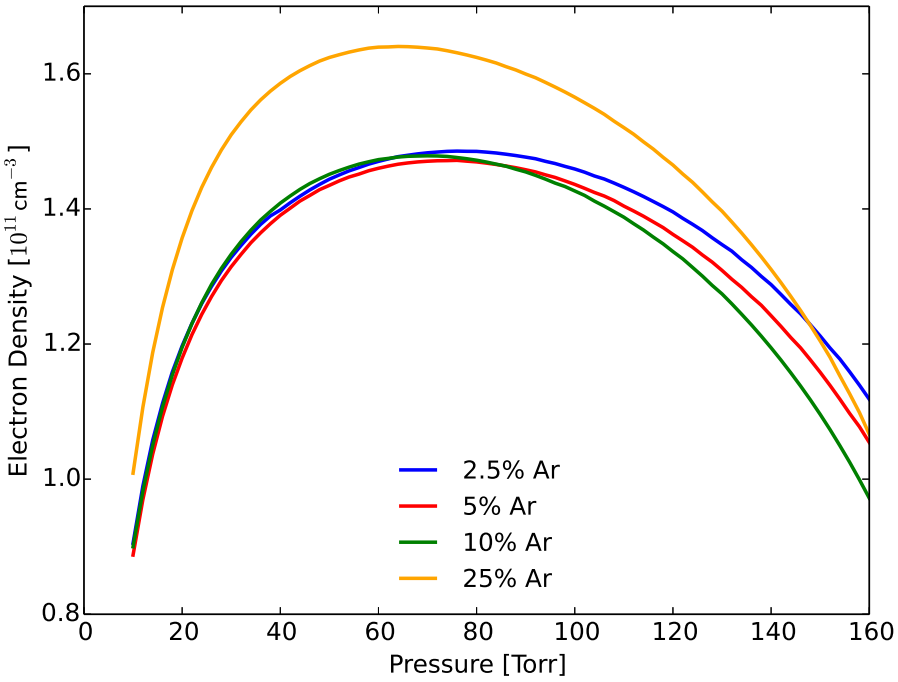

Figure 89. Simulated electron density as a function of pressure for the ring electrode RF-DBD.

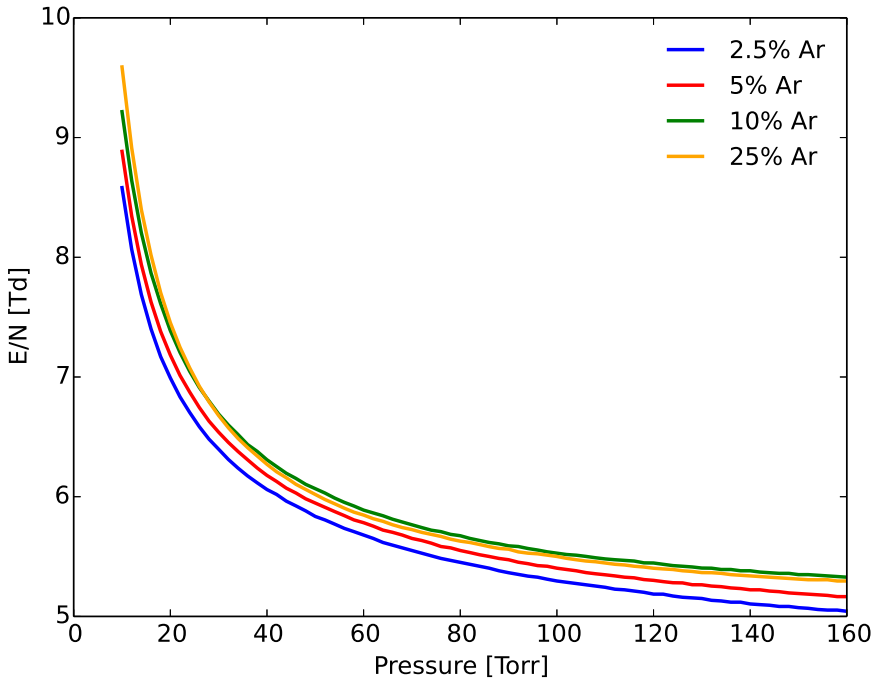

Figure 90. Simulated E/N as a function of pressure for the ring electrode RF-DBD.

recombination rate, we find

$$\nu_i \left(E/N\right) = \frac{D_a}{\Lambda^2}, \tag{131}$$

which is independent of the electron density. The ambipolar diffusion coefficient is inversely proportional to the neutral gas density, indicating a strong decrease with increasing pressure. This decrease in the loss rate allows the ionization rate, and hence E/N, to decrease with increasing pressure, which matches the simulations.

The bulk plasma E/N is related to the electron density through the current density. As the current density increases, more charge is collected on the surface of the dielectrics, and the voltage across the bulk plasma is reduced. Ignoring the potential drop due to the sheaths, the voltage across the bulk plasma follows from Equation 54:

$$\begin{aligned} V_b^2 &= V_{app}^2 - V_d^2, \\ &= V_{app}^2 - \left(\frac{2\delta j}{\epsilon_d \omega}\right)^2, \\ &= V_{app}^2 - \left(\frac{2\delta q_e^2 n_e}{\epsilon_d \omega m_e \sigma_m v_r}\right)^2 \left(\frac{E}{N}\right)_b^2. \end{aligned} \tag{132}$$

Dividing by d^2N^2 and solving for n_e, we obtain

$$n_e = \frac{\epsilon_d \omega m_e \sigma_m v_r N d}{2\delta q_e^2} \sqrt{\frac{\left(E/N\right)_{applied}^2}{\left(E/N\right)_b^2} - 1}, \tag{133}$$

$$\implies n_e \propto p \sqrt{\frac{\left(E/N\right)_{applied}^2}{\left(E/N\right)_b^2} - 1}, \tag{134}$$

where p is the neutral gas pressure, and the terms excluded in Equation 134 are assumed to be constant over pressure. At steady-state, the electron density depends on the product of pressure and the square root of the ratio of the applied E/N, $\left(E/N\right)_{applied}$, to the steady-state E/N in the bulk plasma, $\left(E/N\right)_b$. As determined

above, the steady-state E/N in the bulk plasma depends on the loss rates, which also depend on pressure. This relationship between E/N and n_e provides the simulated trends in Figures 89 and 90.

Measured $Ar(1s_4)$ densities follow the same trend as the simulated E/N, as displayed in Figure 91. While the measured $Ar(1s_4)$ densities show a large decrease with pressure, the simulated densities predict an increase from 10 to 15 Torr, followed by a reduction with pressure that matches the measured decrease. Additionally, the measurements for the 5 and 10% mixtures are close in magnitude over all pressures while the simulation predicts an increase in density for the 10% mixture. Both the measurements and simulations show $Ar(1s_4)$ densities on the order of 10^{11} cm^{-3}.

Metastable simulations follow the measured trend with pressure, decreasing as pressure is increased, similar to the E/N trends (Figure 92). The major difference between the measurements and simulations is the trend from 10 to 25% Ar-fraction: measurements show a decrease in density from 10 to 25% while the simulations show an increase.

Varying Ar-He Mixture.

Repeating the analysis with Ar-fraction as the independent variable, the simulated current shows a minimum in the Ar-fraction range of 10-15% (Figure 93). Current density is responsible for decreasing the bulk plasma voltage through sheath formation and dielectric charging. A larger current corresponds to a lower bulk plasma voltage, which in turn reduces the E/N. This relationship is present in Figure 94, where the peak E/N magnitudes occur at the current minimums.

Qualitatively, the $Ar(1s_4)$ measurements agree with the simulations over the range of measured Ar-fractions (Figure 95), showing an increase in density with increasing Ar-fraction. The simulations show a gradual increase with Ar-fraction, while the

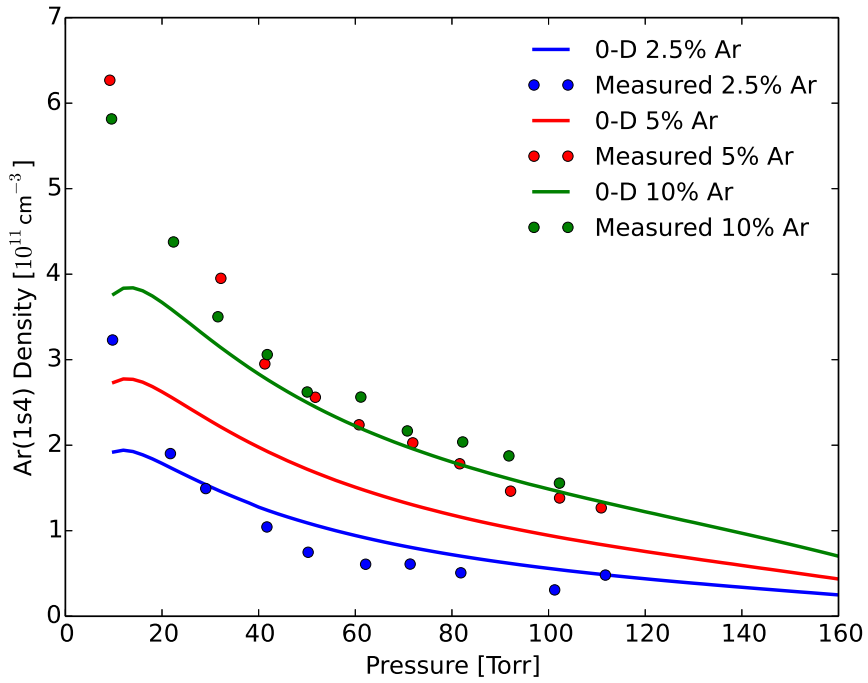

Figure 91. Measured and simulated $Ar(1s_4)$ densities as a function of pressure for the ring electrode RF-DBD.

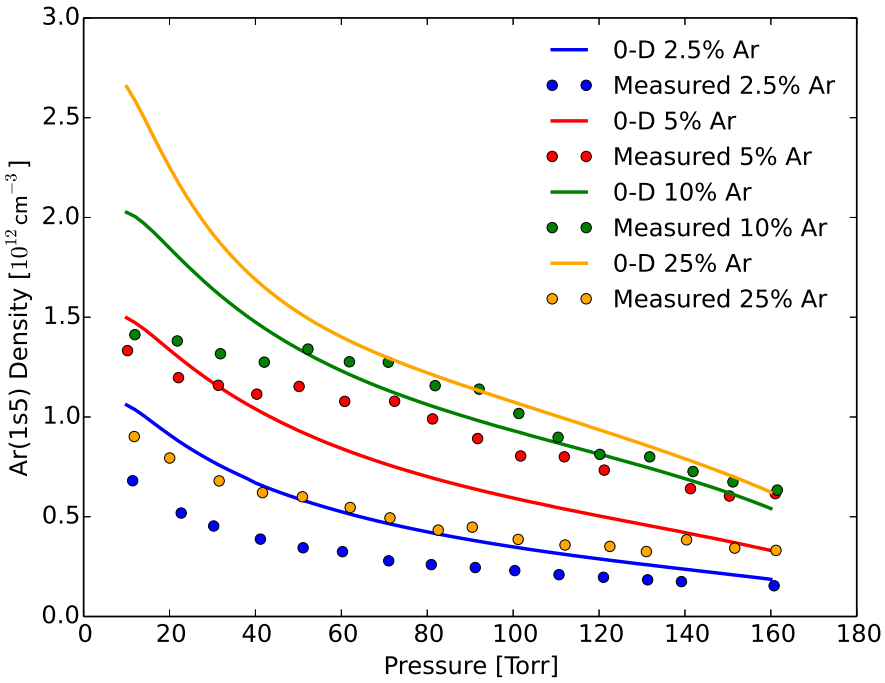

Figure 92. Measured and simulated $Ar(1s_5)$ densities as a function of pressure for the ring electrode RF-DBD.

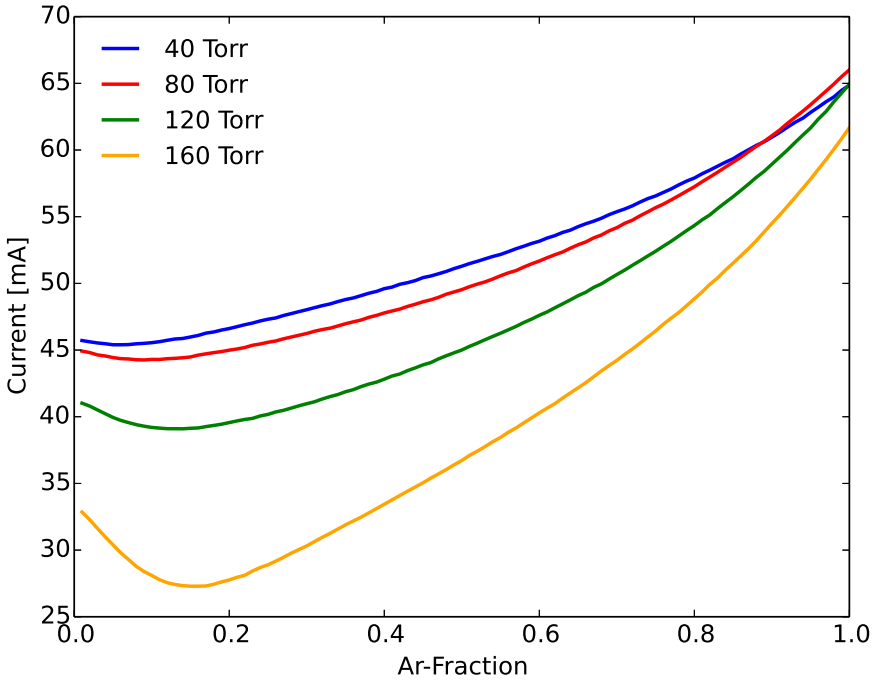

Figure 93. Simulated RMS currents as a function of Ar-fraction for the ring electrode RF-DBD.

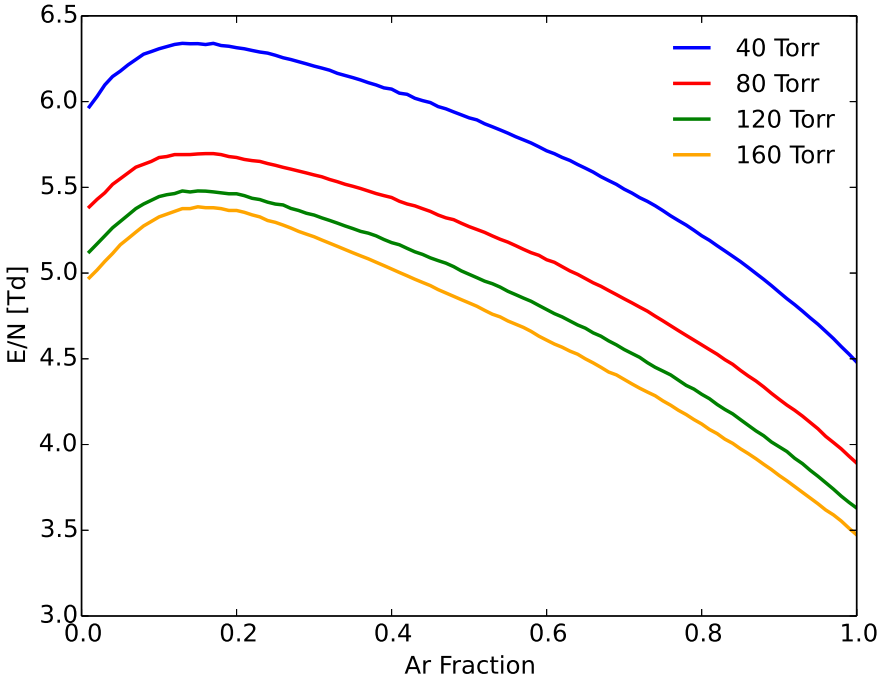

Figure 94. Simulated E/N as a function of Ar-fraction for the ring electrode RF-DBD.

measurements show a large increase from 2.5 to 5% followed by a slight increase to 10%.

Metastable measurements show peaks at 10% Ar-fraction for all pressures followed by a large decrease as the Ar-fraction is increased to 25% (Figure 96). The simulated metastable density does not predict the peak at 10%, but instead predicts peaks near 20% Ar-fraction. The largest difference between measurement and simulation is the sharp drop in metastable densities measured from 10 to 25% Ar-fraction, which is not observed in the simulations.

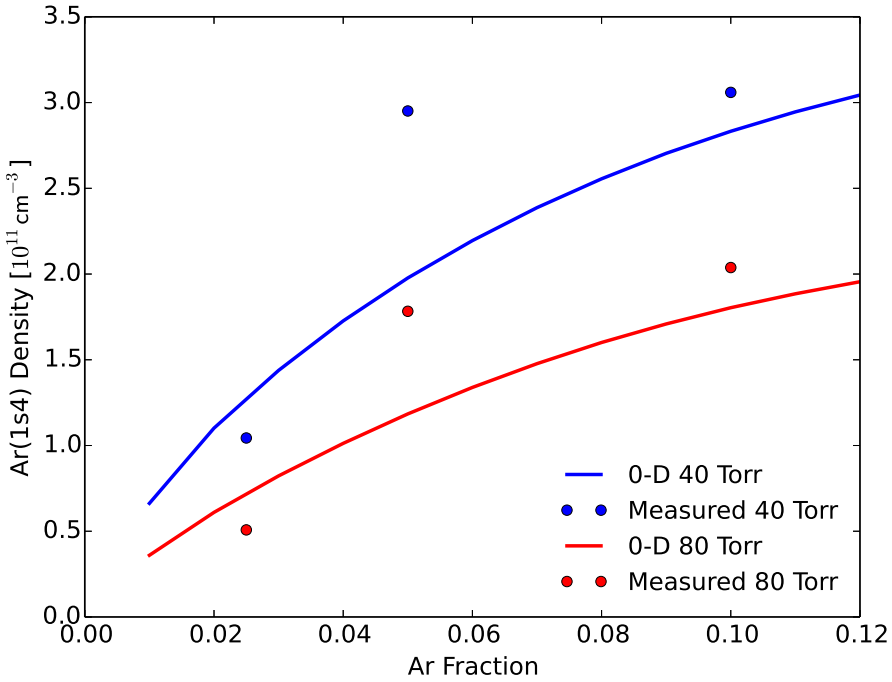

Figure 95. Measured and simulated $Ar(1s_4)$ densities as a function of Ar-fraction for the ring electrode RF-DBD.

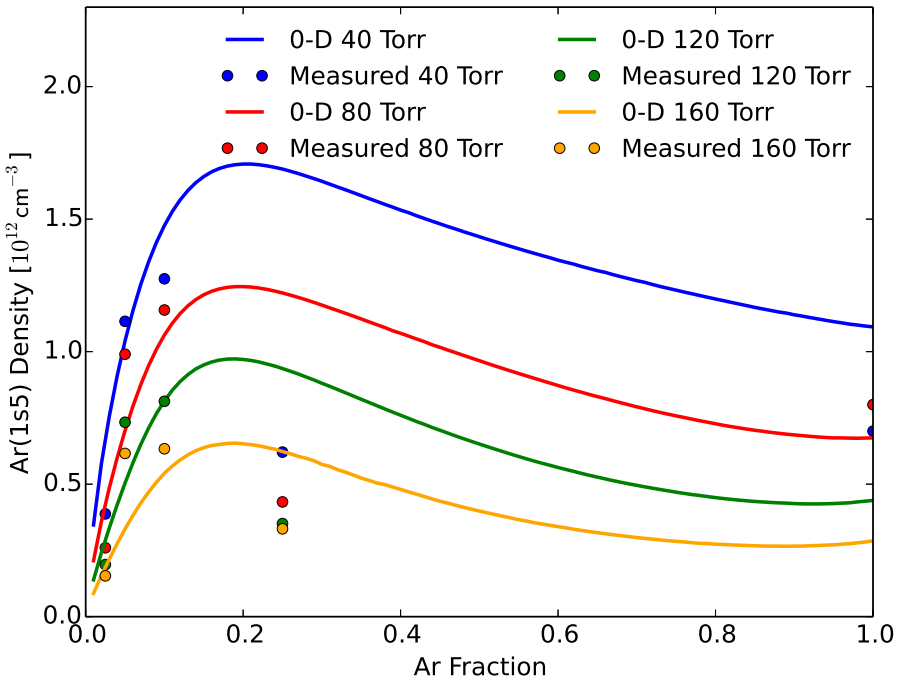

Figure 96. Measured and simulated $Ar(1s_5)$ densities as a function of Ar-fraction for the ring electrode RF-DBD.

4.4 Simplified Model

Model Description.

To investigate the key kinetics controlling metastable density as a function of Ar-fraction and pressure, a simplified model of the bulk plasma in an RF-DBD is developed. Instead of using the time dependent approach employed by the previous models in this analysis, a steady-state approach is implemented using a limited set of species and reactions. Only the key reactions and species pertinent to the metastable density are maintained, providing a simplified kinetic model which maintains the trends predicted by the full zero-dimensional model implemented through ZDPlasKin. The set of excited/ion species used in the simple model are: $Ar(1s_5)$, Ar_2^*, Ar_2^+, and Ar^+. A list of the reactions is displayed in Table 8. Additionally, ambipolar diffusion

is taken into account, following

$$\nu_{diff} = \frac{\mu_+ T_e}{\Lambda^2}, \tag{135}$$

where ν_{diff} is the diffusion loss frequency, μ_+ is the ion mobility calculated using Blanc's Law, T_e is the electron temperature in eV, and $\Lambda = 0.38/\pi \approx 0.12$ cm is the characteristic length of the cavity for the clam shell electrode experiment assuming a parallel plates discharge with a gap length of 0.38 cm.

Table 8. A list of the reactions and rate coefficient labels used in the simple RF-DBD model.

Rate Coefficient Label	Reaction
k_1	$Ar + e^- \rightarrow Ar^+ + e^- + e^-$
k_2	$Ar(1s_5) + e^- \rightarrow Ar^+ + e^- + e^-$
k_3	$Ar_2^* + e^- \rightarrow Ar_2^+ + e^- + e^-$
k_4	$Ar(1s_5) + Ar(1s_5) \rightarrow Ar^+ + Ar + e^-$
k_5	$Ar_2^+ + e^- \rightarrow Ar + Ar$
k_6	$Ar + e^- \rightarrow Ar(1s_5) + e^-$
k_7	$Ar(1s_5) + He \rightarrow Ar + He$
k_8	$Ar(1s_5) + Ar \rightarrow Ar + Ar$
k_9	$Ar(1s_5) + Ar + He \rightarrow Ar_2^* + He$
k_{10}	$Ar(1s_5) + Ar + Ar \rightarrow Ar_2^* + Ar$
k_{11}	$Ar_2^* + e^- \rightarrow Ar + Ar + e^-$
k_{12}	$Ar_2^* \rightarrow Ar + Ar + \hbar\omega$
k_{13}	$Ar^+ + Ar + He \rightarrow Ar_2^+ + He$
k_{14}	$Ar^+ + Ar + Ar \rightarrow Ar_2^+ + Ar$
k_{15}	$Ar_2^+ + e^- \rightarrow Ar^+ + Ar + e^-$

At steady-state, there is no variation in the species densities, providing the fol-

lowing coupled non-linear equations:

$$k_1[Ar]n_e + k_2[Ar(1s_5)]n_e + k_3[Ar_2^*]n_e + k_4[Ar(1s_5)][Ar(1s_5)] = \frac{\mu_+ T_e}{\Lambda^2} n_e + k_5[Ar_2^+]n_e,$$

$$k_6[Ar]n_e = k_7[Ar(1s_5)][He] + k_8[Ar(1s_5)][Ar] + k_9[Ar(1s_5)][Ar][He] + k_{10}[Ar(1s_5)][Ar][Ar],$$
$$+ k_2[Ar(1s_5)]n_e + k_4[Ar(1s_5)][Ar(1s_5)],$$

$$k_9[Ar(1s_5)][Ar][He] + k_{10}[Ar(1s_5)][Ar][Ar] = (k_3 + k_{11})[Ar_2^*]n_e + k_{12}[Ar_2^*],$$

$$k_{13}[Ar^+][Ar][He] + k_{14}[Ar^+][Ar][Ar] + k_3[Ar_2^*]n_e = (k_5 + k_{15})[Ar_2^+]n_e + \frac{\mu_+ T_e}{\Lambda^2}[Ar_2^+],$$

$$[Ar^+] + [Ar_2^+] = n_e, \tag{136}$$

where the final equation is based on the assumption of an electrically neutral bulk plasma. The electron density, n_e, is coupled to bulk plasma E/N through the following equations:

$$\left(\frac{q_e n_e \mu_e}{\omega d_e}\right)^2 \left(\frac{2A}{\epsilon_0} + \frac{2\delta}{\epsilon_d}\right)^2 + 1 = \frac{(E/N)^2_{applied}}{(E/N)^2_b} \tag{137}$$

$$A^2 \left[\left(\omega^2 - \frac{2An_e q_e^2}{m_e \epsilon_0 d_e}\right)^2 + \omega^2 \nu_m^2\right] = \left(\frac{q_e V_{app}}{m_e d_e}\right)^2, \tag{138}$$

where $(E/N)_{applied}$ is the applied E/N and $(E/N)_b$ is the bulk plasma E/N. These equations are obtained by expressing the current density and plasma frequency in Equations 54-57 in terms of the electron density and dividing Equation 54 by $d_e^2 N^2$ to convert the voltage to E/N. The solution to these coupled equations provides the electron density required to produce an $(E/N)_b$ for a given $(E/N)_{applied}$. At steady-state, $(E/N)_b$ is the magnitude required to maintain bulk plasma ionization rates equal to the electron loss rates and is a function of pressure and Ar-fraction.

To include the ambipolar diffusion loss rate, T_e is required and can be calculated from $(E/N)_b$. The conversion is dependent on the Ar-fraction due to the change in the EEDF observed with changes in mixture. To calculate the conversion, BOLSIG+

is run for Ar-fractions from 1 to 100% for a variety of electron temperatures, providing the E/N profile displayed in Figure 97. This one-to-one mapping between E/N and T_e for a given Ar-fraction allows the model to solve for T_e as a proxy for $(E/N)_b$.

In addition to the relationship between E/N, T_e, and Ar-fraction, the electron impact rate coefficients and electron mobility are also dependent on T_e (or E/N) and Ar-fraction. Electron impact rate coefficients are required for the electron impact reactions in Equation 136, and electron mobilities are required to solve Equation 137. BOLSIG+ is used to calculate the rate coefficients and mobilities, providing results as a function of T_e and Ar-fraction, which are used in the steady-state calculations.

The BOLSIG+ calculated rate coefficients, mobilities, and E/N to T_e conversions are used as inputs to the model in addition to an applied voltage, Ar-fraction, and pressure. For a user defined voltage, Ar-fraction and pressure, solutions to T_e, n_e, $[Ar(1s_5)]$, $[Ar_2^*]$, $[Ar^+]$, and $\left[Ar_2^+\right]$ in Equations 136 to 138 are calculated using a numerical root-finding technique implemented in Mathematica. Initial estimates of T_e, $[Ar(1s_5)]$, $[Ar_2^*]$, $[Ar^+]$, and $\left[Ar_2^+\right]$ are input to the model, and n_e is determined from Equations 137 and 138 based on the steady-state T_e.

Before analyzing the results of the simple model, it is helpful to understand the behavior of the input electron impact rate coefficients calculated using BOLSIG+. Ionization rate coefficients as a function of T_e and Ar-fraction are displayed in Figures 98 to 100. For electron temperatures near 2.5 eV (expected in the bulk plasma), electron impact ionization rate coefficients for $Ar + e^- \rightarrow Ar^+ + 2e^-$ range from 4.7×10^{-12} cm^3/s at lower Ar-fractions to 1.4×10^{-17} cm^3/s for Ar rich mixtures. Rate coefficients for ionization of $Ar(1s_5)$ via $Ar(1s_5) + e^- \rightarrow Ar^+ + 2e^-$ show much less of a decrease with Ar-fraction, ranging from 2.1×10^{-9} cm^3/s at lower Ar-fractions to 1.3×10^{-9} cm^3/s near pure Ar. An opposite trend is observed for ionization of Ar_2^* via $Ar_2^* + e^- \rightarrow Ar_2^+ + 2e^-$, which shows a slight increase with increasing Ar-fraction,

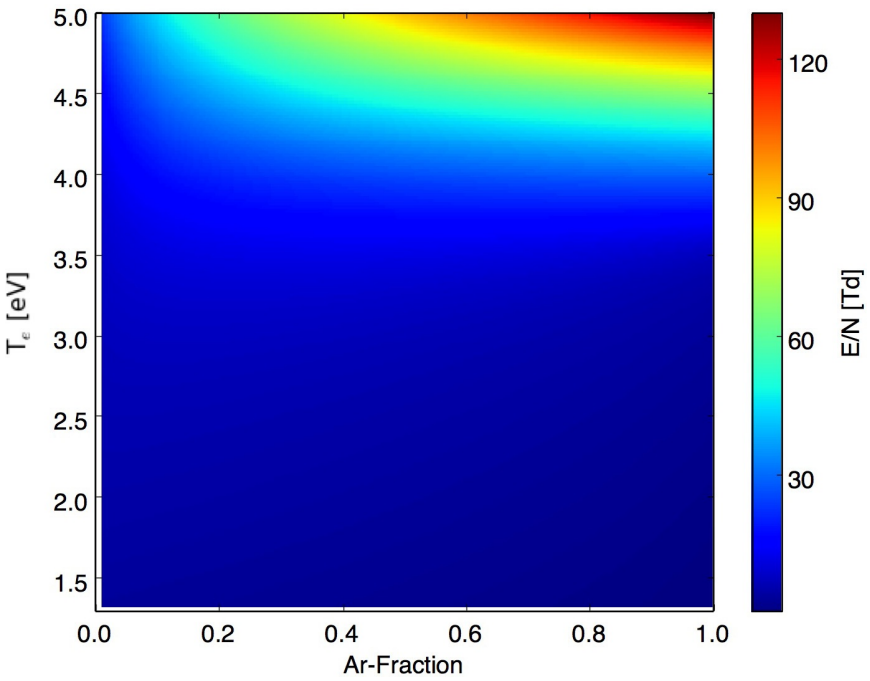

Figure 97. Reduced electric field as a function of Ar-fraction and electron temperature, calculated by BOLSIG+.

possessing rate coefficients near 1.3×10^{-7} cm^3/s over all Ar-fractions for $T_e = 2.5$ eV. In the bulk plasma, where the electron temperatures are relatively low, the electron impact rate coefficients for ionization of Ar_2^* are orders of magnitude larger than the rate coefficients for ionization of $Ar(1s_5)$ or ground state Ar.

Metastable excitation rate coefficients for $e^- + Ar \rightarrow e^- + Ar(1s_5)$ are displayed in Figure 101 as a function of T_e and Ar-fraction. Similar to the ionization rate from ground state Ar, the metastable excitation rate coefficients show a large variation with Ar-fraction at typical bulk plasma electron temperatures. At 2.5 eV, the excitation rate coefficient varies from 7.8×10^{-12} cm^3/s for an Ar-fraction of 1% to 4.1×10^{-15} cm^3/s in pure Ar.

The electron impact rate coefficient for Ar_2^* dissociation is displayed in Figure 102. A relatively small increase in the rate coefficient is observed as the electron temperature increases. Additionally, a slight increase is observed as Ar-fraction is increased.

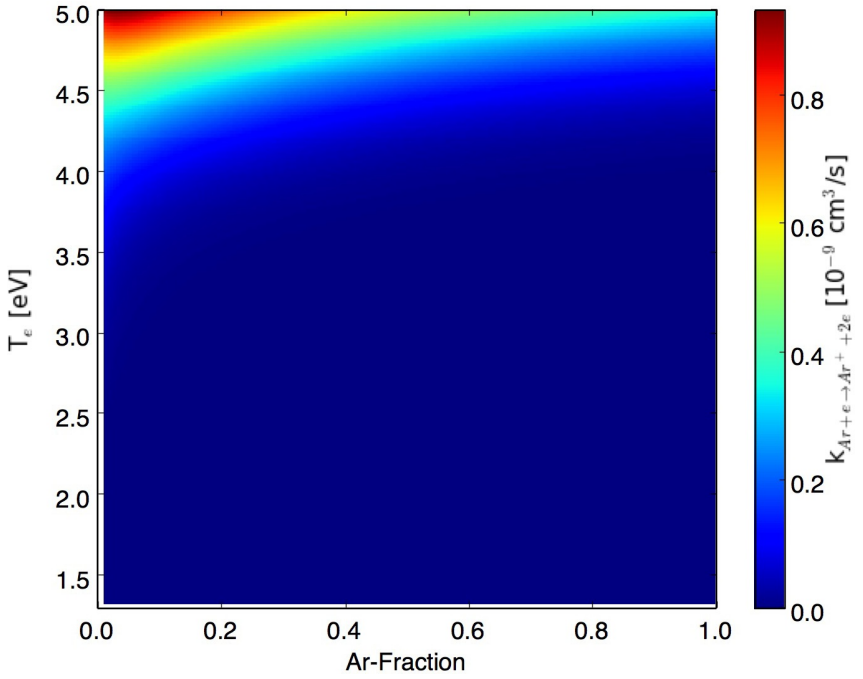

Figure 98. Rate coefficient for ionization of ground state Ar as a function of Ar-fraction and electron temperature, calculated by BOLSIG+.

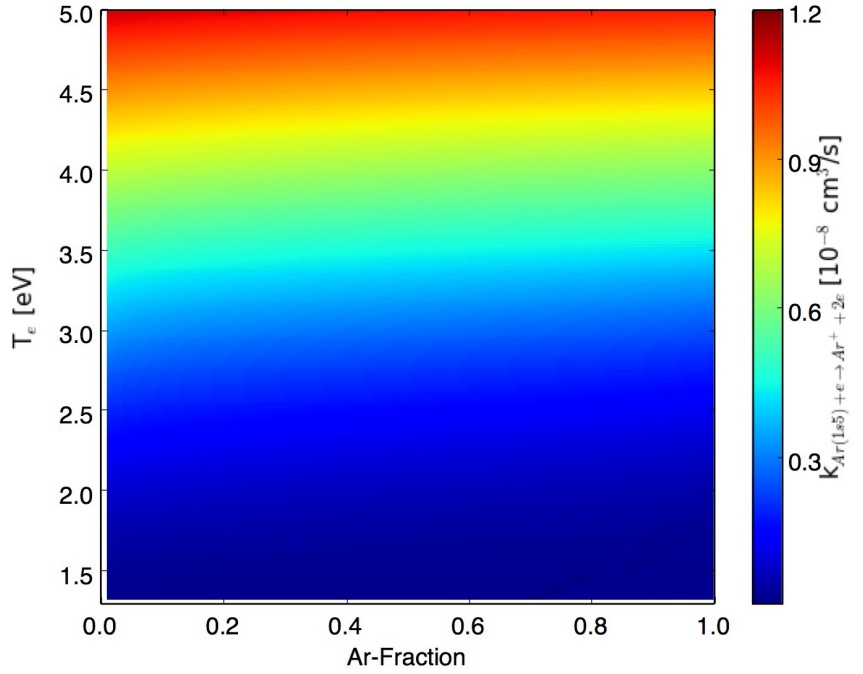

Figure 99. Rate coefficient for ionization of $Ar(1s_5)$ as a function of Ar-fraction and electron temperature, calculated by BOLSIG+.

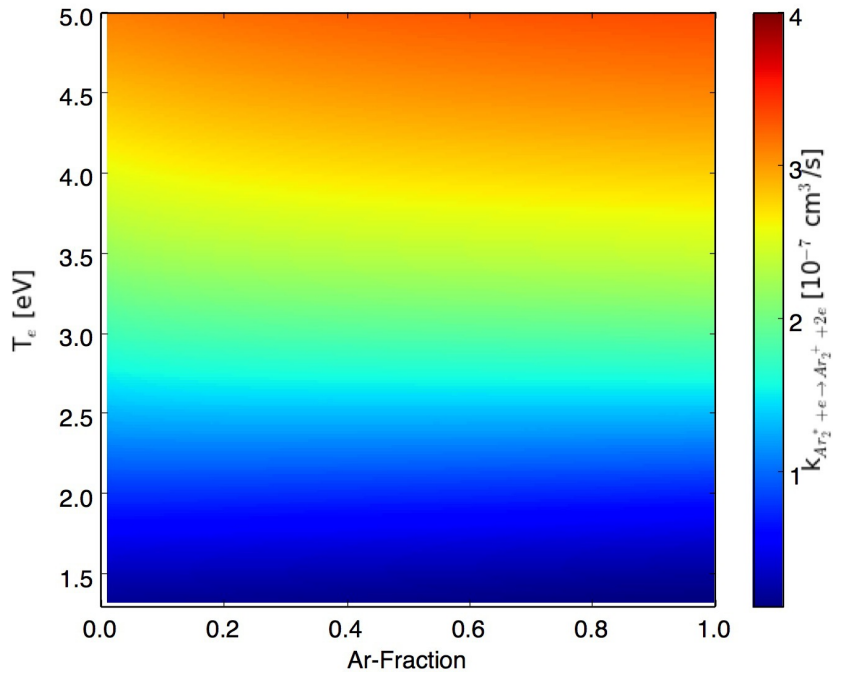

Figure 100. Rate coefficient for ionization of Ar_2^* as a function of Ar-fraction and electron temperature, calculated by BOLSIG+.

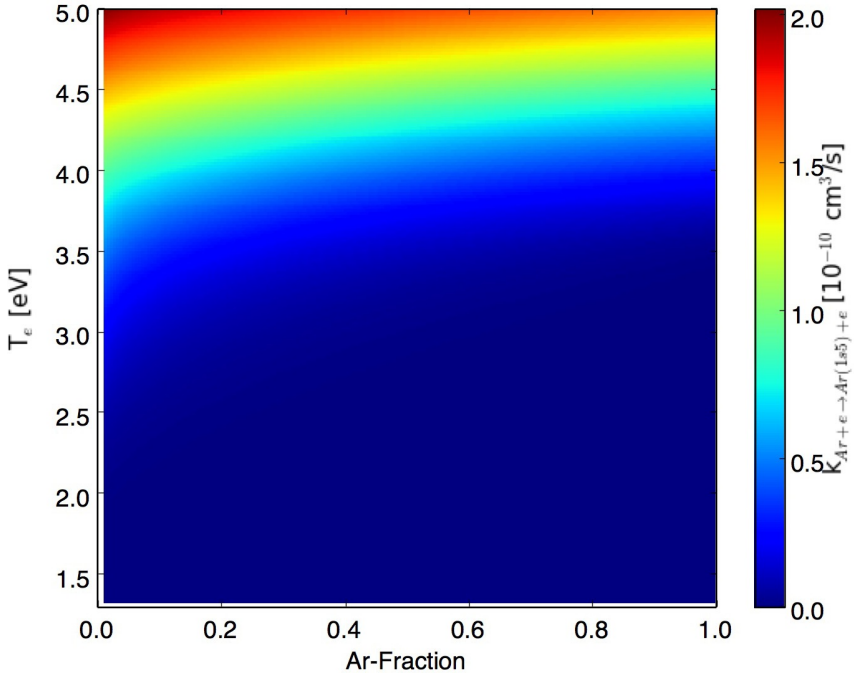

Figure 101. Rate coefficient for metastable excitation from the ground state as a function of Ar-fraction and electron temperature, calculated by BOLSIG+.

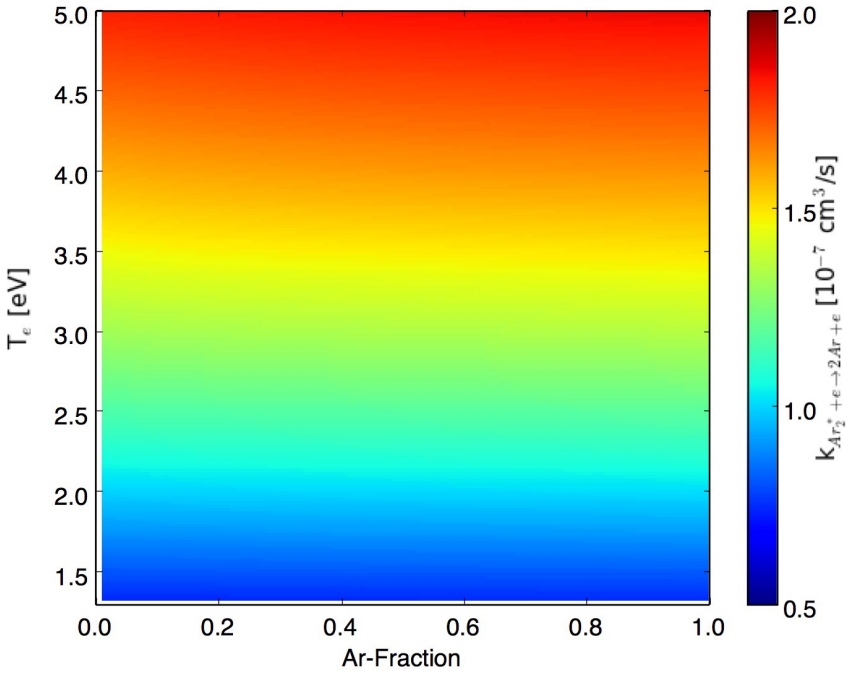

Figure 102. Rate coefficient for Ar_2^* dissociation due to electron impact as a function of Ar-fraction and electron temperature, calculated by BOLSIG+.

Results.

Following the zero-dimensional effective DC simulations of Section 4.2, simulations are performed for Ar-fractions ranging from 1 to 100% in the pressure range of 200 to 500 Torr using an applied voltage of $500/\sqrt{2}$ V and a gas temperature of 440 K. The metastable density dependence on Ar-fraction and pressure is analyzed over this parameter space using the simple model to gain insight into the kinetics controlling metastable behavior.

To understand the metastable dependence on Ar-fraction and pressure, it is helpful to analyze the steady-state E/N as a function of Ar-fraction and pressure due to the strong relationship between the $Ar(1s_5)$ excitation rate coefficient and E/N. In the bulk plasma at steady-state, the ionization rate is equal to the electron loss rate. Both the electron loss and ionization frequencies are functions of Ar-fraction and pressure. Analyzing the electron loss frequencies for a constant pressure of 200 Torr, as displayed

in Figure 103, provides insight into the behavior as a function of Ar-fraction. For Ar-fractions below 20%, ambipolar diffusion is the dominant loss mechanism. Above 20% Ar-fraction, dissociative recombination of Ar_2^+ provides the dominant electron loss rate while recombination of Ar^+ is extremely small, playing an insignificant role in the kinetics. Extending the simulations to entire range of pressures indicates that the loss frequencies show little variation with pressure due to the dominant role of Ar_2^+ recombination (Figure 104). However, above 200 Torr, the role of ambipolar diffusion is reduced due to a decrease in ion mobility, which reduces the loss rates for the lower Ar-fractions.

To counter the electron loss rates, the total ionization rate as a function of Ar-fraction must equal the combined loss rate. The ionization mechanisms as a function of Ar-fraction at 200 Torr are displayed in Figure 105. At Ar-fractions below approximately 15%, ionization of ground state Ar dominates electron production. Above 15%, ionization of Ar_2^* is the dominant ionization mechanism. This shift in the ionization mechanism is key to the metastable behavior over Ar-fraction due to the energy required for the two mechanisms. Ionization of ground state Ar requires electron energies of 15.8 eV to overcome the ionization barrier. However, Ar_2^* only requires electron energies of 3.4 eV. The key role of Ar_2^* in the kinetics of a high pressure Ar-He discharge is exposed when analyzing the ionization mechanisms.

Ionization rates via $e^- + Ar_2^* \rightarrow 2e^- + Ar_2^+$ are also dependent on the Ar_2^* densities, which are a function of Ar-fraction and pressure. Three body collisions through $Ar(1s_5) + Ar + M \rightarrow Ar_2^* + M$ increase quadratically with pressure. Additionally, the rate for $M = Ar$ is estimated to have twice the rate coefficient as $M = He$ [Demyanov et al., 2013]. This combined effect produces the Ar_2^* profile displayed in Figure 106, which shows an increase in density as the pressure is increased.

The contributions due to each ionization mechanisms over the entire range of Ar-

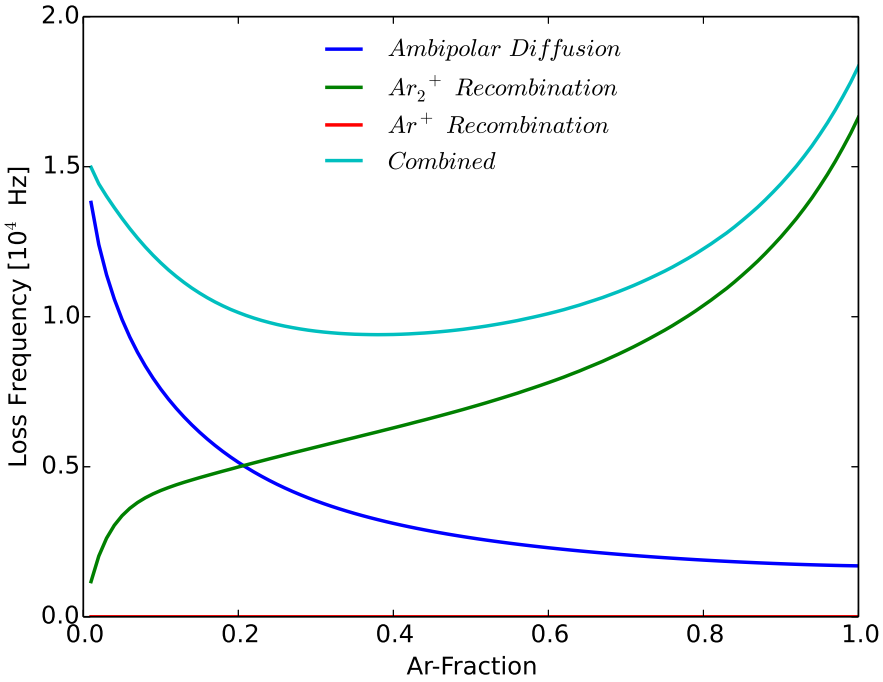

Figure 103. Electron loss frequencies as a function of Ar-fraction at a pressure of 200 Torr.

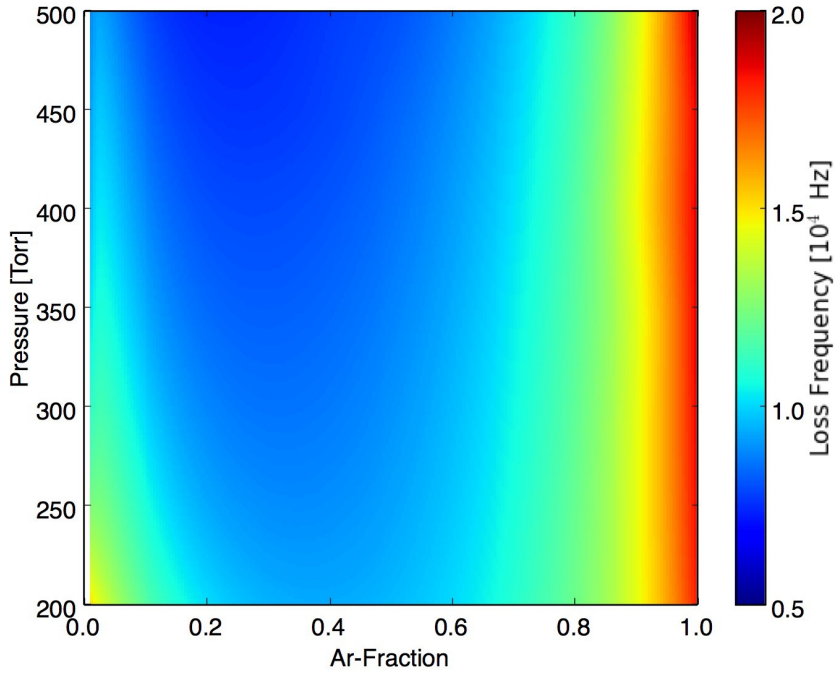

Figure 104. Electron loss frequencies as a function of Ar-fraction and pressure.

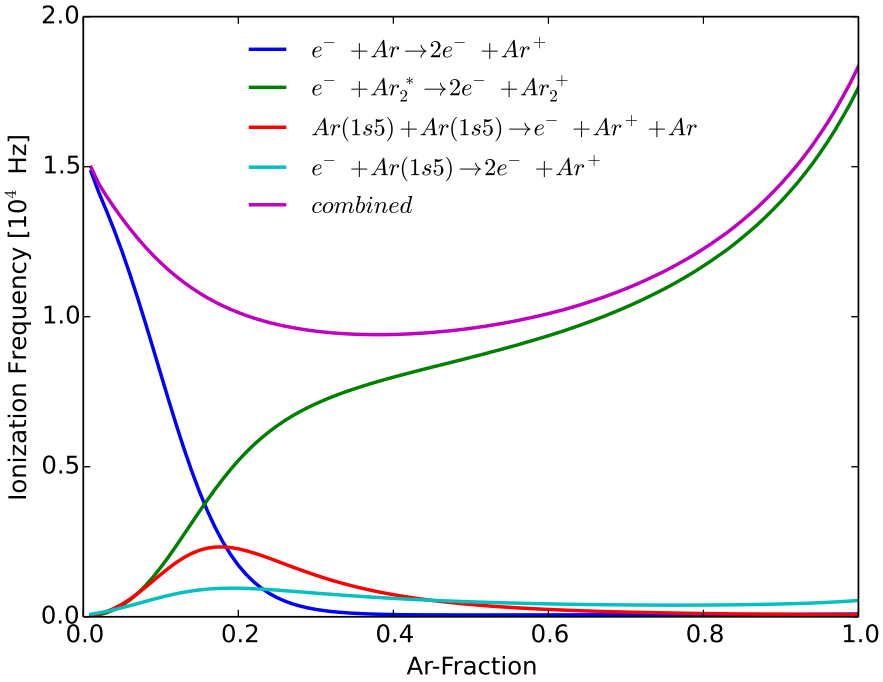

Figure 105. Ionization frequencies as a function of Ar-fraction at a pressure of 200 Torr.

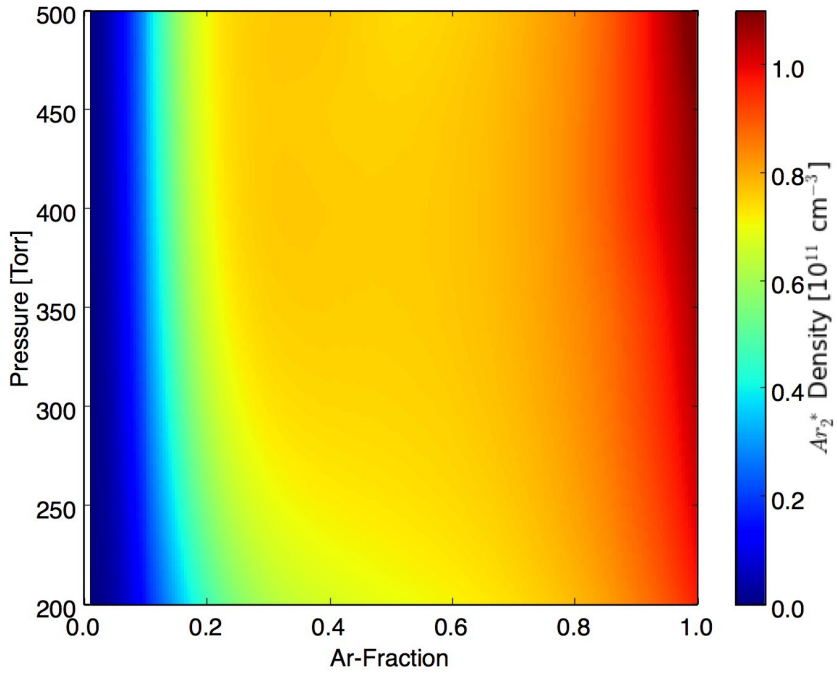

Figure 106. Ar_2^* densities as a function of Ar-fraction and pressure.

fractions and pressures are displayed in Figures 107 to 110. Similar to Figure 105, the dominant ionization mechanism at lower Ar-fractions for all pressures is due to ionization from the ground state (Figure 107). As the Ar_2^* density increases, ionization via $Ar_2^* + e^- \rightarrow Ar_2^+ + e^-$ dominates, following the Ar_2* density profile (Figure 108). The relative contributions of stepwise and metastable-metastable ionization are minor, as displayed in Figures 109 and 110.

As the ionization mechanism shifts from ionization of ground state Ar to ionization of Ar_2^*, the E/N required to maintain ionization is lowered due to a reduction in the electron energy required for ionization, as displayed in Figure 111. At 200 Torr, a peak E/N is observed near an Ar-fraction of 15%, where the transition in ionization mechanisms occurs. As the pressure is increased, a decrease in steady-state E/N is predicted, and the E/N contours are shifted towards lower Ar-fractions. Near 500 Torr, the peak E/N occurs at an Ar-fraction of 10%. The general E/N trend as a function of pressure and Ar-fraction (Figure 111) matches the trends predicted by ZDPlasKin (Figure 68).

Reduced electric fields as a function of Ar-fraction and pressure (Figure 111) combined with the Ar density dependence on Ar-fraction and pressure can be used to understand the metastable excitation frequencies displayed in Figure 112. The trend follows the E/N trend with peaks in the range of 10-15% Ar in He, shifting to lower Ar-fractions as the pressure is increased. Additionally, due to the increase in Ar density as pressure is increased, a slight increase in the excitation frequency is observed with increasing pressure.

The final contribution required to understand the metastable density profile as a function of pressure and Ar-fraction are the metastable loss rates. At 200 Torr, the metastable loss frequencies are displayed in Figure 113. Loss frequencies at lower Ar-fractions are dominated by quenching due to He, which may be a proxy for impurities

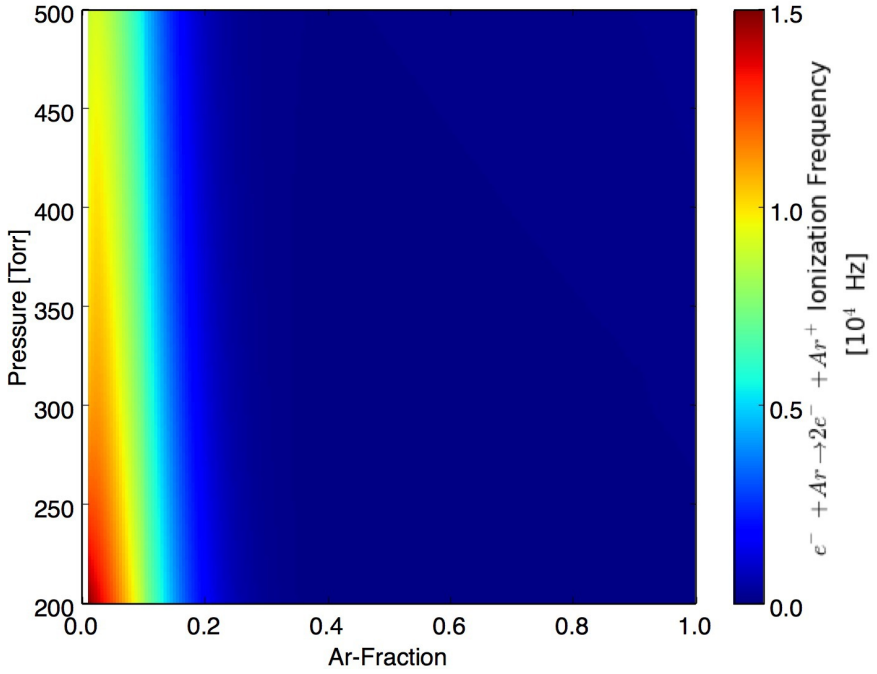

Figure 107. Ionization frequency of $Ar + e^- \rightarrow Ar^+ + 2e^-$ as a function of Ar-fraction and pressure.

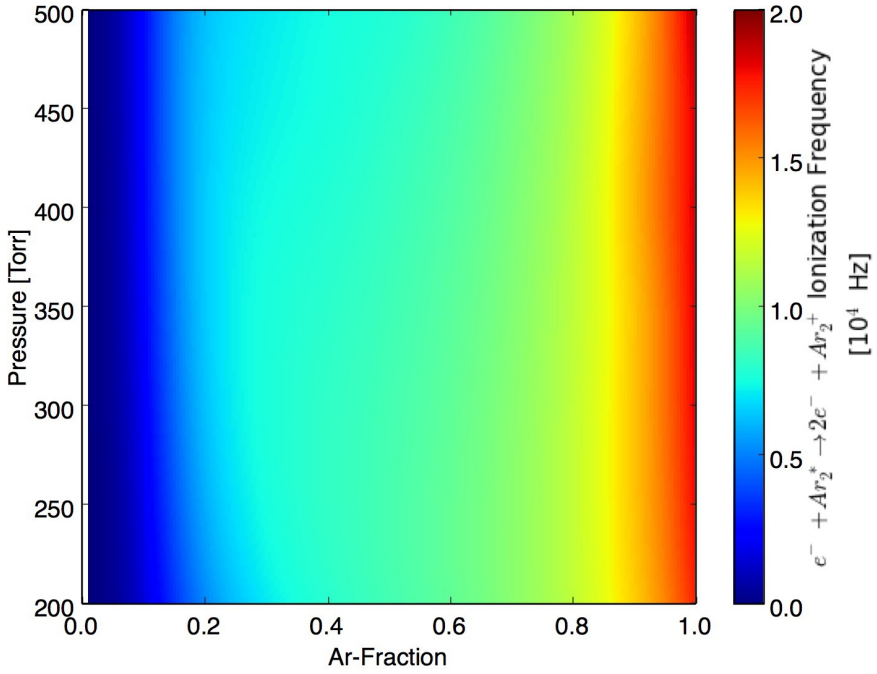

Figure 108. Ionization frequency of $Ar_2^* + e^- \rightarrow Ar_2^+ + 2e^-$ as a function of Ar-fraction and pressure.

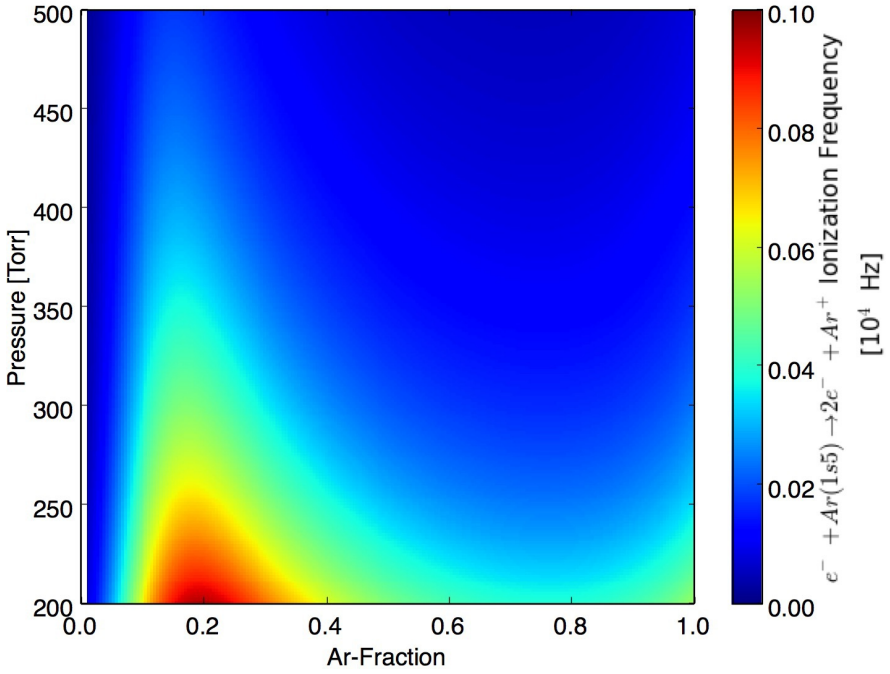

Figure 109. Ionization frequency of $Ar(1s_5)+e^- \rightarrow Ar^+ + 2e^-$ as a function of Ar-fraction and pressure.

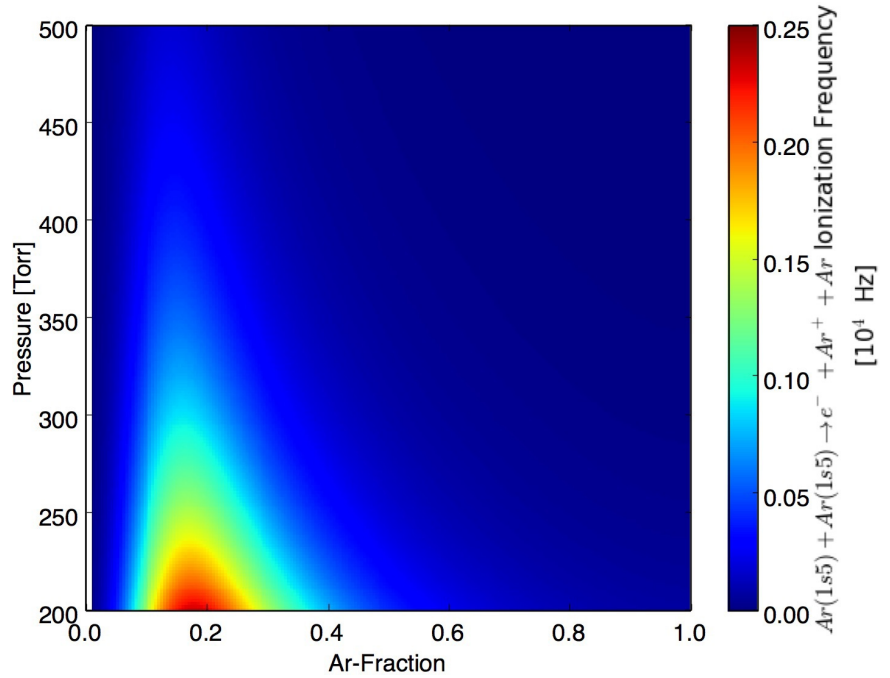

Figure 110. Ionization frequency of $Ar(1s_5) + Ar(1s_5) \rightarrow Ar^+ + Ar + e^-$ as a function of Ar-fraction and pressure.

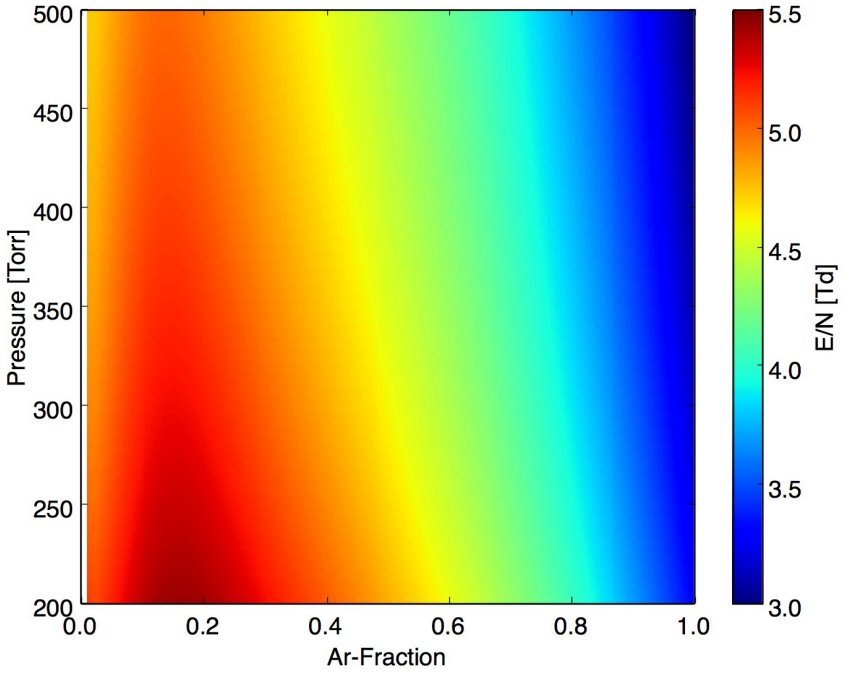

Figure 111. Reduced electric field as a function of Ar-fraction and pressure. Note the similarity to the ZDPlasKin simulated reduced electric fields displayed in Figure 68.

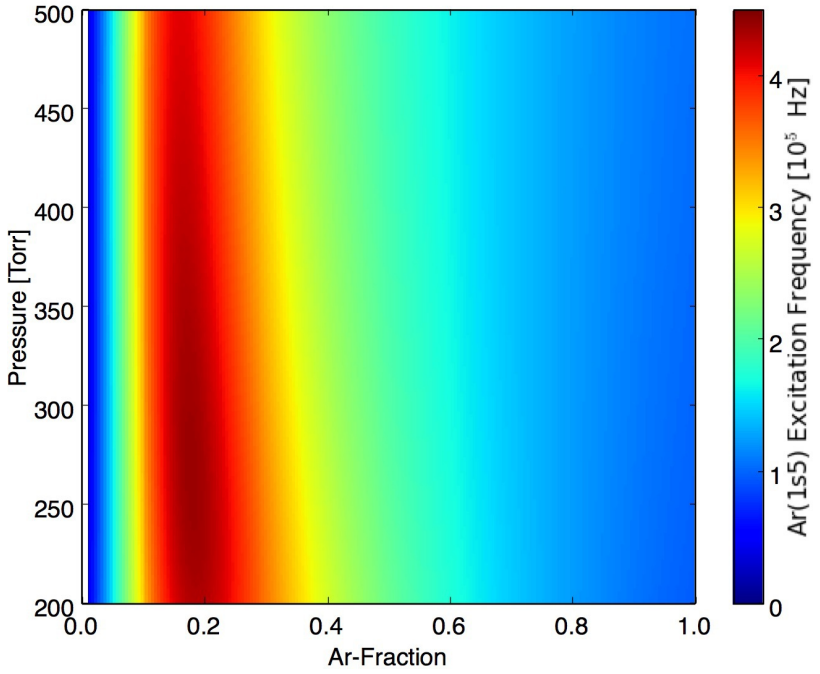

Figure 112. Metastable excitation frequency via $e^- + Ar \rightarrow e^- + Ar(1s_5)$ as a function of Ar-fraction and pressure.

(see Stefanović et al. [2014] for a discussion on quenching due to impurities). Above approximately 50% Ar-fraction, the three-body loss mechanism of $Ar(1s_5) + Ar + Ar \rightarrow Ar_2^* + Ar$ dominates as a result of the quadratic increase in the rate with Ar density. As the pressure is increased, the loss rates due to He quenching increase linearly while the three-body loss rates increase quadratically. This quadratic increase in loss rates due to excimer formation dominates the metastable loss mechanisms as the pressure is increased, causing the loss rates for Ar-rich mixtures at high pressures to become large (Figure 114).

Combining the metastable excitation frequencies (Figure 112) with the loss frequencies (Figure 114) explains the overall metastable density profile displayed in Figure 115. Due to the large increase in loss rates as the pressure in increased, the metastable density shows a large decrease with pressure. The behavior versus Ar-fraction follows the E/N trends, peaking near 15% Ar-fraction at 200 Torr and shifting to 10% at 500 Torr.

A comparison of the simple model results with the zero-dimensional time dependent simulations through ZDPlasKin is presented in Figure 116 for a pressure of 200 Torr. Overall, the predicted densities are nearly equal for both models. The slight increase in metastable densities for the simple model are due to the removal of the loss mechanism through $Ar(1s_5)+e^- \rightarrow Ar(1s_4)+e^-$ followed by $Ar(1s_4) \rightarrow Ar+\hbar\omega$. However, the large $He + Ar(1s_4) \rightarrow He + Ar(1s_5)$ rate at 440 K reduces the effect of the radiation loss mechanism from $Ar(1s_4)$. The results of the simple model as a function of Ar-fraction and pressure (Figure 115) closely follow the trends predicted by ZDPlasKin (Figure 65).

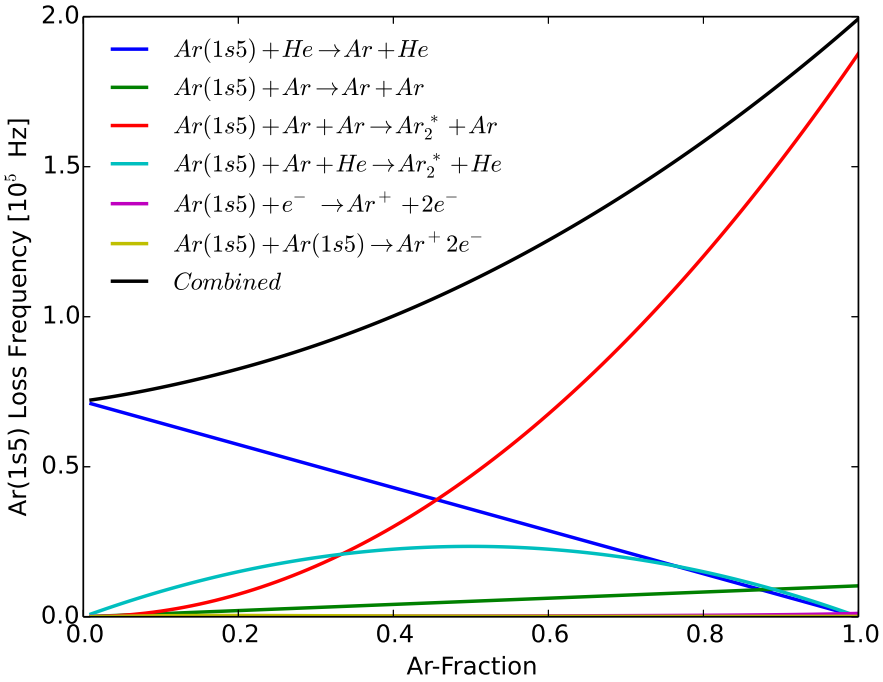

Figure 113. Metastable loss frequencies as a function of Ar-fraction at a pressure of 200 Torr.

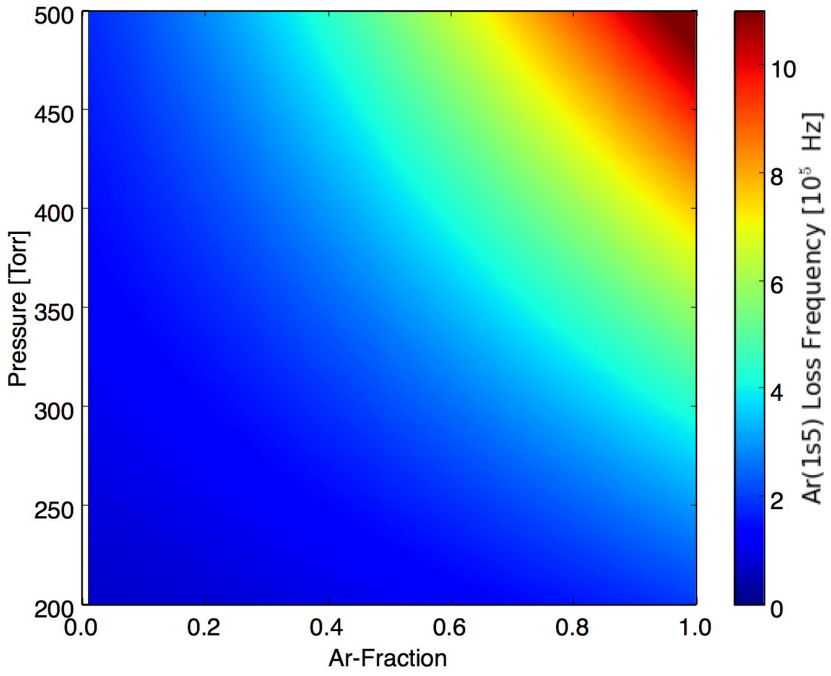

Figure 114. Metastable loss frequencies as a function of Ar-fraction and pressure.

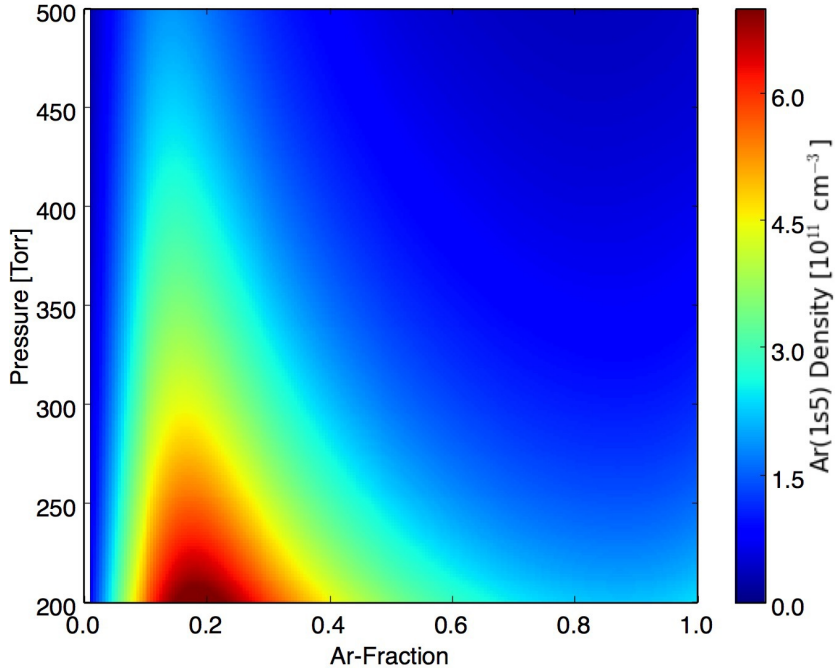

Figure 115. Metastable density as a function of Ar-fraction and pressure using the simplified RF-DBD model. Note the similarity to the ZDPlasKin simulated metastable densities displayed in Figure 65.

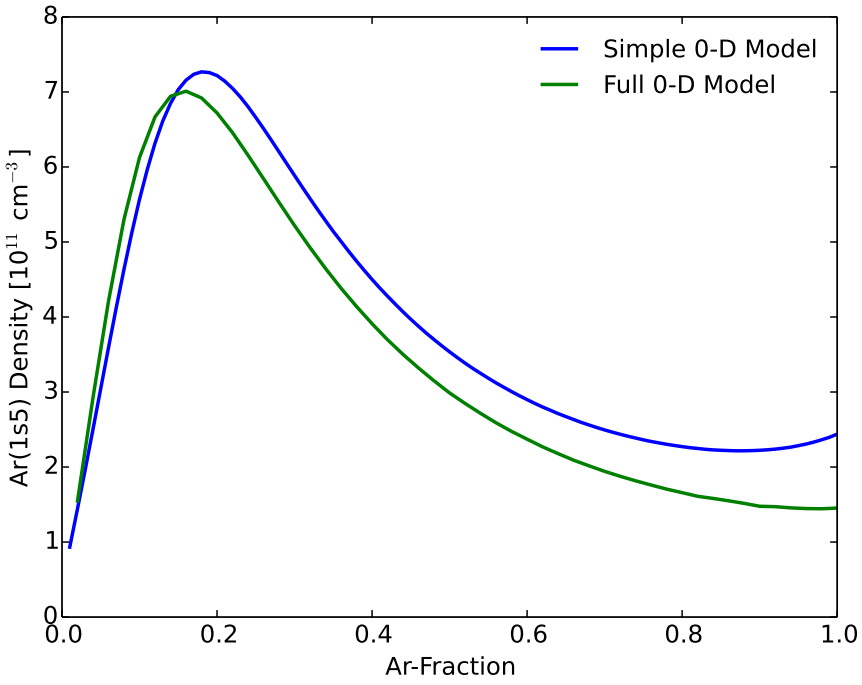

Figure 116. Metastable density as a function of Ar-fraction at a pressure of 200 Torr using both a full discharge model (ZDPlasKin) and the simplified RF-DBD model.

4.5 Conclusions

Simulations of an α-mode radio frequency dielectric barrier discharge are performed for a variety of Ar-He mixtures and gas pressures. Results from a one-dimensional fluid model are compared to a zero-dimensional effective DC model in the bulk plasma, showing general agreement over Ar-fractions ranging from 5 to 100% and pressures between 200 and 500 Torr. The agreement between the two models indicates that the zero-dimensional effective DC model provides a valid approach to modeling the bulk plasma of a high pressure RF-DBD.

Peak metastable densities at 300 Torr are observed near a 15% Ar in He mixture for the geometry of the discharge chamber used in the simulations, corresponding to the peak E/N for the varying mixtures. Electron temperature and electron density are observed to increase with increasing Ar-fraction. Metastable densities are shown to decrease with increasing pressure due to a reduction in E/N and a quadratic increase in metastable loss rates through excimer formation: $Ar(1s_5) + Ar + M \rightarrow Ar_2^* + M$. The decrease in bulk plasma E/N is primarily due to an increase in ionization through $Ar_2^* + e^- \rightarrow Ar_2^+ + 2e^-$, which requires significantly less energy than ionization through $Ar + e^- \rightarrow Ar^+ + 2e^-$.

Additionally, the peak $Ar(1s_5)$ density shifts from an Ar-fraction of approximately 15% at 200 Torr to 10% at 500 Torr. The increased excimer formation rate at elevated pressures raises Ar_2^* densities for He rich mixtures, causing the peak E/N to occur at lower Ar-fractions as the pressure is increased. This shift in E/N corresponds to a shift in the peak metastable densities, which occur at lower Ar-fractions as pressure is increased.

Calculations varying the applied voltage from 500 to 1750 V show an increase in $Ar(1s_5)$ density as the voltage is increased. Bulk plasma metastable densities above 10^{12} cm^{-3} are observed for applied voltages above 750 V, corresponding to average

applied powers greater than 25 W. While the increase in metastable density with increasing voltage is promising, gas heating must be taken into account as the voltage and current densities are increased to determine thresholds for thermal instabilities that collapse the discharge to a filamentary mode. An α to γ-mode transition is observed for an applied voltage of 1400 V using a 15% Ar-fraction at a pressure of 200 Torr with a secondary electron emission coefficient of 0.1. The spatially averaged electron density matches the critical electron density provided by Raizer et al. [1995]. For a secondary emission coefficient of 0.01, no α to γ-mode transition is observed in the range of applied voltages. No large increase in electron or metastable density is observed at the onset of the γ-mode, which is most likely due to the limitations of a one-dimensional fluid model and the subnormal current densities caused by the dielectric barriers.

Extending the zero-dimensional simulations to a ring electrode experiment provides a comparison of simulated and measured $Ar(1s_5)$ and $Ar(1s_4)$ densities as a function of pressure and Ar-fraction. Measured $Ar(1s_5)$ densities show a large decrease from 10 to 25% Ar-fraction, while the simulated peaks occur near 20% for pressures below 160 Torr. The simulated densities show reasonable agreement with the measured densities as a function of pressure, exhibiting a large decrease as the pressure is increased from 10 to 160 Torr. This reduction is mainly due to a decrease in the ambipolar diffusion loss rate which corresponds to a reduction in the bulk plasma E/N, demonstrating the effect of electron loss rates on metastable density.

Our simulations indicate that an OPRGL using an α-mode RF-DBD in the pressure range of 200-500 Torr will be provided the largest metastable density using a mixture of approximately 15% Ar in He at 200 Torr. While the metastable density decreases with increasing pressure, the gas pressure must also be taken into account when mapping to laser performance. Both the diode pump absorption linewidth and

spin orbit mixing rate via $Ar(2p_9) + M \rightarrow Ar(2p_{10}) + M$ increase with increasing pressure, requiring a laser kinetics model to analyze laser performance as a function of pressure and Ar-fraction for this discharge scenario.

A simplified zero-dimensional steady-state model of an RF-DBD is developed showing excellent agreement with the time-dependent simulations from ZDPlasKin. An analysis of the electron production and loss rates as a function of Ar-fraction and pressure indicates that the ionization contributions of $Ar + e^- \rightarrow Ar^+ + 2e^-$ relative to $Ar_2^* + e^- \rightarrow Ar_2^+ + 2e^-$ controls the steady-state E/N, which in turn controls metastable production rates. The metastable loss rates through $Ar(1s_5) + Ar + M \rightarrow Ar_2^* + M$ increase quadratically with pressure and are a factor of 2 larger for $M = Ar$ than for $M = He$. These combined effects cause the metastable density to decrease with increasing pressure and produce peak metastable densities near Ar-fractions of 15% at 200 Torr shifting to 10% at 500 Torr.

V. Optically Pumped Rare Gas Laser Simulations

An optically pumped rare gas laser with Ar as the rare gas uses a diode laser to pump metastable $Ar(1s_5)$ atoms to the $Ar(2p_9)$ energy level [Han et al., 2013]. Near-atmospheric pressures are required for rapid collisional relaxation from $Ar(2p_9)$ to $Ar(2p_{10})$ to create a population inversion and subsequent lasing between $Ar(2p_{10})$ and $Ar(1s_5)$, as displayed in Figure 1. Additionally, the high pressures broaden the absorption line width, enhancing pump laser absorption. Optical gain depends on the diode laser absorption, which depends on the $Ar(1s_5)$ density [Rawlins et al., 2015; Demyanov et al., 2013]. A gas discharge is employed to produce sufficient metastable densities to act as the ground state of the OPRGL system.

Several kinetic studies of OPRGLs have been performed recently [Demyanov et al., 2013; Yang et al., 2015; Rawlins et al., 2015; Han et al., 2014]. One study found that at atmospheric pressures, a mixture of approximately 1% Ar in He provides the largest efficiency, defined as the output power divided by sum of pump and discharge power [Demyanov et al., 2013]. A separate kinetic analysis determined the effect of metastable density on output laser powers, predicting output intensities above 1 kW/cm^2 for metastable densities on the order of 10^{13} cm^{-3} and pump laser intensities above 2 kW/cm^2 [Yang et al., 2015].

An experimental and computational analysis of an OPRGL using microwave resonator-driven microplasmas as the metastable source measured a laser output of 22 mW for an absorbed pump power of 40 mW and an estimated metastable density of 3×10^{12} cm^{-3} [Rawlins et al., 2015]. This measurement provides an optical efficiency of approximately 55%. The gain, G, was found to be linear with respect to metastable density, following $[Ar(1s_5)]/G = 4 \times 10^{12}$ cm^{-2}, measured at 760 Torr for a mixture of 2% Ar in He. Additionally, a computational analysis of the laser kinetics found a better fit to the data when an Arrhenius temperature scaling was applied to the

neutral collision transfer rates between the different excited Ar species.

While the rate coefficients for collisional de-excitation via $Ar(2p)+M \rightarrow Ar(1s)+M$ are well documented [Chang and Setser, 1978; Han and Heaven, 2014], the branching ratio to the specific $Ar(1s)$ levels ($1s_5$ to $1s_2$) are uncertain. Additionally, as discussed in Chang and Setser [1978], the rate coefficients depend strongly on diabatic coupling near crossings of the potential energy surfaces, not just the energy difference between states. Due to the uncertainty in the branching ratios, previous kinetic studies of optically pumped rare gas laser performance have assumed that all $Ar(2p)+M \rightarrow Ar(1s)+M$ collisions channel directly to $Ar(1s_5)$ bypassing the other $Ar(1s)$ levels [Demyanov et al., 2013; Yang et al., 2015; Rawlins et al., 2015; Han et al., 2014].

This chapter analyzes the effect of the $Ar(2p)+M \rightarrow Ar(1s)+M$ branching ratio on OPRGL performance with an RF-DBD as the source of metastable production. Absorbed pump laser intensities and output laser intensities are calculated as a function of Ar-fraction, pressure, and $Ar(2p)+M \rightarrow Ar(1s)+M$ branching ratio using a time-dependent zero-dimensional discharge model including laser kinetics. Due to the uncertainty in the branching ratio, a sensitivity study of the branching ratio effect on laser performance is performed. Additionally, a simplified laser kinetic model is developed and compared to the full discharge laser model.

The OPRGL analysis is based on metastable densities simulated for the RF-DBD scenario outlined in Section 4.2 with a peak applied voltage of 500 V. A lower voltage was selected to ensure an α-mode discharge over all pressures and mixtures, which corresponds to metastable densities on the order of 10^{11} cm^{-3}. The relatively low metastable densities for this discharge scenario are considerably suboptimal for laser performance, but instead allow for a study of laser intensity trends as a function of pressure, Ar-He mixture, and branching ratio. Alternative discharge scenarios may

yield higher metastable densities necessary for high power OPRGL laser performance.

5.1 Model

Gas discharge simulations are performed using the zero-dimensional effective DC model outlined in Section 4.1 with an RF-DBD as the source of metastable production. In addition to the reactions provided in Table 2, transfer rates due to pump laser absorption and circulating laser intensity are included [Yang et al., 2015; Zameroski et al., 2011; Hager and Perram, 2010; Beach et al., 2004]. The absorbed pump intensity, I_{abs}, and corresponding reaction rate from $Ar(1s_5)$ to $Ar(2p_9)$, W_{abs}, follow

$$I_{abs} = I_p \int \mathrm{d}\nu \, g_p(\nu) \{1 - \exp\left[-\left([Ar(1s_5)] - \frac{5}{7}[Ar(2p_9)]\right)\sigma_{pl}(\nu)\,\ell_{gain}\right]\} \quad (139)$$
$$\{1 + R_p \exp\left[-\left([Ar(1s_5)] - \frac{5}{7}[Ar(2p_9)]\right)\sigma_{pl}(\nu)\,\ell_{gain}\right]\},$$

$$W_{abs} = \frac{I_{abs}}{E_{pl}\ell_{gain}}, \quad (140)$$

where $I_p = 1$ kW/cm^2 is the incident pump laser intensity, $[Ar(1s_5)]$ is the $Ar(1s_5)$ density, $[Ar(2p_9)]$ is the $Ar(2p_9)$ density, $\ell_{gain} = 5.1$ cm is the length of gain medium, R_p is the pump laser reflectivity (assumed to be 1), and E_{pl} is the pump transition energy [Beach et al., 2004; Zameroski et al., 2011; Yang et al., 2015]. In this analysis, the pump delivery and mode overlap factors are ignored (assumed to be 1). The line shape of the pump laser, $g_p(\nu)$, is assumed to be a Gaussian distribution with a FWHM linewidth of 30 GHz [Beach et al., 2004]. The absorption cross section, $\sigma_{pl}(\nu)$, is assumed to have a Lorentzian line shape with a pressure broadening coefficient of $17\sqrt{T_{gas}/300}$ MHz/Torr, where T_{gas} is the neutral gas temperature in Kelvin [Rawlins et al., 2015]. This pressure broadening coefficient is assumed to be independent of Ar/He mixture. At 760 Torr and 300 K, the peak absorption cross section is calculated

to be $\sigma_{pl} \approx 4.3 \times 10^{-13}$ cm^2, which is close to the value of 4.5×10^{-13} cm^2 provided by Demyanov et al. [2013].

The average two-way circulating laser intensity, I_l, and corresponding reaction rate from $Ar(2p_{10})$ to $Ar(1s_5)$, W_l, follow

$$\frac{dI_l}{dt} = \frac{I_l c}{2\ell_{cavity}}\{R_l R_{oc} T_r^2 \exp\left[2\left([Ar(2p_{10})] - \frac{3}{5}[Ar(1s_5)]\right)\sigma_{ul}\ell_{gain}\right] - 1\}, \quad (141)$$

$$W_l = \sigma_{ul}\left([Ar(2p_{10})] - \frac{3}{5}[Ar(1s_5)]\right)\frac{I_l}{E_{ul}}, \quad (142)$$

where $[Ar(2p_{10})]$ is the $Ar(2p_{10})$ density, R_l is back mirror reflectivity (assumed to be 1), $R_{oc} = 0.95$ is the output coupler reflectivity, T_r is the one-way cavity transmission (assumed to be 1), ℓ_{cavity} is the cavity length (assumed to be equal to ℓ_{gain}), and E_{ul} is the output laser transition energy [Zameroski et al., 2011; Yang et al., 2015]. A threshold gain of approximately 0.02 cm^{-1} is calculated for this system. The gain cross section is calculated by $\sigma_{ul} = 5.0 \times 10^{-13}\,(N_{atm}/N)$ cm^2, where N_{atm} is the gas pressure at 760 Torr and 300 K and N is the gas density used in the simulations [Demyanov et al., 2013]. The output laser intensity, I_{out}, follows [Hager and Perram, 2010]

$$I_{out} = \frac{W_l E_{ul}\ell_{gain}\,(1 - R_{oc})\,T_r \exp\left[\left([Ar(2p_{10})] - \frac{3}{5}[Ar(1s_5)]\right)\sigma_{ul}\ell_{gain}\right]}{\{\exp\left[\left([Ar(2p_{10})] - \frac{3}{5}[Ar(1s_5)]\right)\sigma_{ul}\ell_{gain}\right] - 1\}\{1 + T_r^2 R_{oc}\exp\left[\left([Ar(2p_{10})] - \frac{3}{5}[Ar(1s_5)]\right)\sigma_{ul}\ell_{gain}\right]\}}. \quad (143)$$

For this study, the branching ratio is defined as the ratio of the rate coefficient for $Ar(2p) + M \rightarrow Ar(1s_5) + M$ relative to the total rate coefficient for $Ar(2p) + M \rightarrow Ar(1s) + M$ excluding quenching to the ground state. All $Ar(2p)$ species are assumed to have the same branching ratio to simplify the analysis. Since $Ar(1s_4)$ is the only other $Ar(1s)$ level maintained in this analysis, the branching ratio can be described

by

$$\text{branching ratio} = \frac{k_{Ar(1s_5)}}{k_{Ar(1s_5)} + k_{Ar(1s_4)}}. \tag{144}$$

Up to this point, a branching ratio of 50% has been assumed (Table 2) for our discharge simulations. However, previous OPRGL simulations have assumed a branching ratio of 100% [Demyanov et al., 2013; Yang et al., 2015; Rawlins et al., 2015; Han et al., 2014], highlighting the need for a sensitivity study.

Before the inclusion of the laser rates due to the introduction of the pump laser, zero-dimensional simulations of the RF-DBD are carried out to an initial steady-state, providing pre-laser densities and discharge conditions. Then, the laser rates are included and the simulations are executed to a new steady-state where the densities and laser intensities are constant in time.

5.2 Results

Pre-laser discharge simulations are performed for an RF-DBD with an applied voltage of 500 V peak for a variety of Ar in He mixtures and pressures ranging from 200-500 Torr. The pre-laser metastable densities in the bulk plasma show a peak of approximately 7.0×10^{11} cm^{-3} near 15% Ar in He at 200 Torr, as displayed in Figure 65 for a branching ratio of 50%. The metastable density is reduced as the pressure is increased, and the peak metastable density shifts to a lower Ar-fraction. At 500 Torr, the peak metastable density is reduced to $\sim 2.4 \times 10^{11}$ cm^{-3}, occurring at an Ar-fraction of approximately 10%. This decrease in metastable density with increasing pressure is due to elevated metastable loss rates, primarily through excimer formation via $Ar(1s_5) + Ar + M \rightarrow Ar_2^* + M$. For the discharge scenario modeled, the peak metastable densities for all pressures in the range of 200-500 Torr are on the order of 10^{11} cm^{-3}. A slight variation in pre-laser metastable density is observed with respect to the branching ratio, with an average relative difference under 5% for

all mixtures and pressures when compared to the branching ratio of 50%. Pre-laser metastable densities are not strongly dependent on the branching ratio due to the relatively low metastable production rates from collision relaxation of $Ar(2p)$.

After laser initiation, a drastic increase in $Ar(2p)$ densities is observed as a result of pump laser absorption. This increase in $Ar(2p)$ densities increases the $Ar(2p) + M \rightarrow Ar(1s) + M$ rates, forcing the post-laser kinetics to be strongly dependent on the branching ratio. As displayed in Figure 117, the intensity of pump laser absorption increases with an increasing branching ratio due mainly to a reduction in excited Ar species densities collected in $Ar(1s_4)$. The peak absorption over all pressures and mixtures increases from approximately 4.7 to 31.2 W/cm^2 as the branching ratio increases from 25 to 100%. Additionally, the peak absorption shifts to a higher pressure ranging from 400 to 440 Torr as the branching ratio increases.

The output laser intensity, as displayed in Figure 118, also shows an increase with increasing branching ratio. Similar to the pump laser absorption, the peak laser output occurs at a higher pressure for larger branching ratios (Table 9). As the pressure increases, the $Ar(2p) + M \rightarrow Ar(1s) + M$ rates also increase. For lower branching ratios, this rate increase is detrimental to laser performance due to a loss of excited species densities directly involved with laser performance: $Ar(1s_5)$, $Ar(2p_9)$, and $Ar(2p_{10})$. This loss is caused by quenching from $Ar(2p)$ to $Ar(1s_4)$ and subsequent pooling at $Ar(1s_4)$. As the branching ratio increases, the rate to $Ar(1s_4)$ decreases while the rate to $Ar(1s_5)$ increases, thereby decreasing the detrimental effect of the pressure increase. Additionally, the $Ar(2p_9) + M \rightarrow Ar(2p_{10}) + M$ relaxation rate and pump laser absorption linewidth both increase with increasing pressure, enhancing laser performance. The pre-laser metastable density trend is clearly visible in the laser intensity trend as a function of Ar-fraction and pressure, and no lasing occurs for Ar rich mixtures with reduced metastable densities at the lower branching

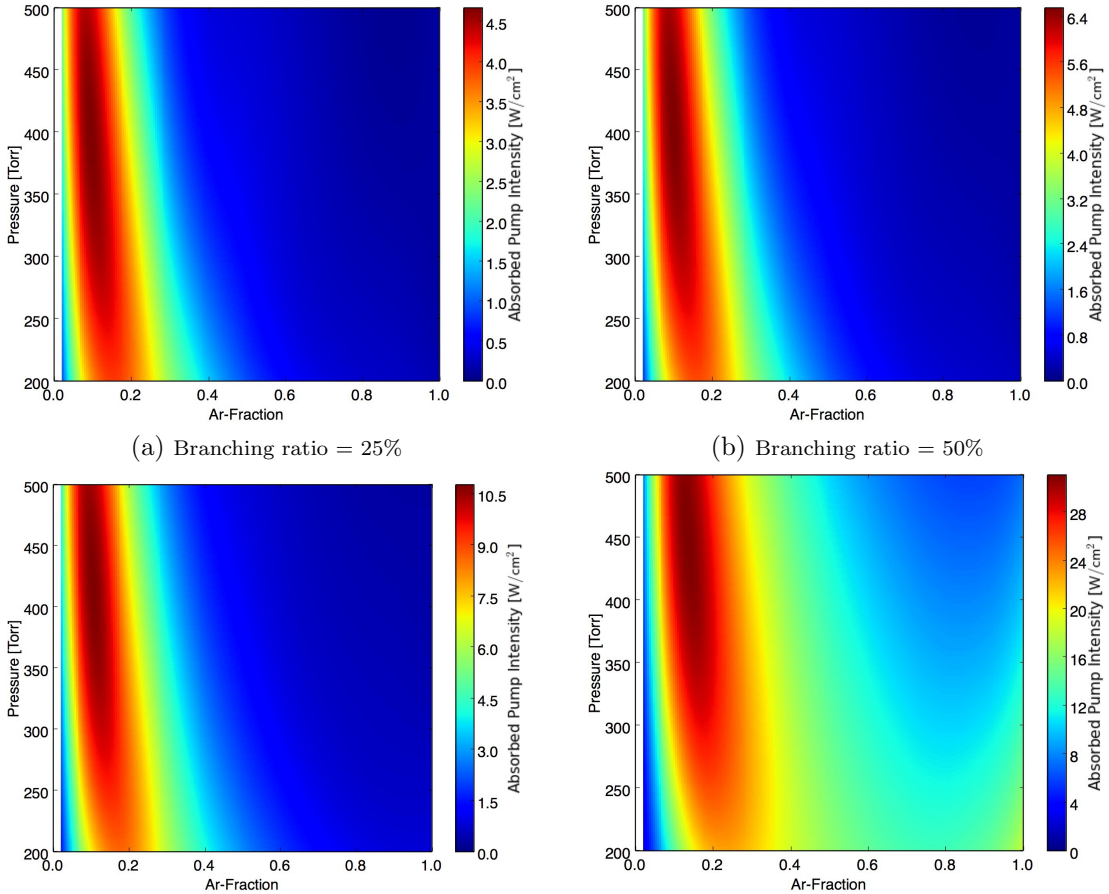

(a) Branching ratio = 25%

(b) Branching ratio = 50%

(c) Branching ratio = 75%

(d) Branching ratio = 100%

Figure 117. Absorbed pump laser intensity as a function of Ar-fraction and pressure for variable branching ratios. Note the change in scale for the different images.

ratios.

A peak output intensity of approximately 2.1 W/cm^2 is observed at 440 Torr for a branching ratio of 25%, while a peak of 14.2 W/cm^2 is predicted at 500 Torr for a branching ratio of 100% (Table 9). The peaks occur at an Ar-fraction of 12% for the 100% branching ratio and at 8% Ar-fraction for the other branching ratios. This nearly 7 fold increase in peak laser intensity highlights the importance of the branching ratio in OPRGL operation.

Table 9. Parameters associated with peak output laser intensities as a function of branching ratio.

Branching Ratio	Peak Laser Intensity [W/cm^2]	Pressure [Torr]	Ar-Fraction	Absorbed Pump Intensity [W/cm^2]
0.25	2.1	440	0.08	4.7
0.50	3.1	460	0.08	6.5
0.75	5.1	480	0.08	10.5
1.00	14.2	500	0.12	30.8

Analyzing the 460 Torr, 8% Ar-fraction scenario (corresponding to the peak laser intensity for a branching ratio of 50%) as a function of branching ratio shows a nearly 7 fold increase in laser output and pump laser absorption as the branching ratio is increased from 2 to 100% (Figure 119). The fraction of post-laser excited Ar species population collected in $Ar(1s_4)$ is defined by Ω:

$$\Omega = \frac{[Ar(1s_4)]_{post-laser}}{[Ar^*]_{post-laser}}, \tag{145}$$

where $[Ar^*] = [Ar(1s_5) + Ar(1s_4) + Ar(2p_{10}) + Ar(2p_9) + Ar(2p_8)]$. As the branching ratio increases, Ω is reduced due to a reduction in the $Ar(2p) + M \rightarrow Ar(1s_4) + M$ rates (Figure 120). For a branching ratio of 2%, nearly 90% of the Ar^* population is collected in $Ar(1s_4)$, which limits the population directly involved with laser kinetics. At a branching ratio of 100%, approximately 50% of the Ar^* population is collected

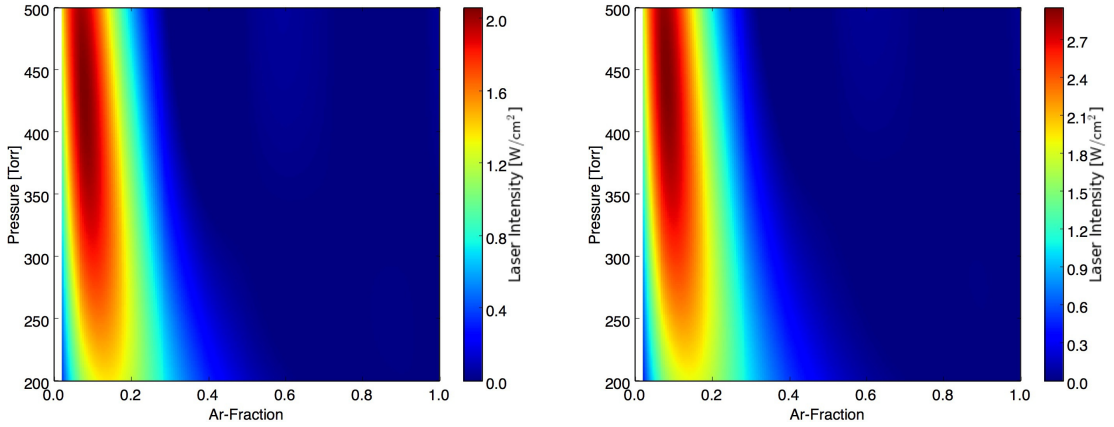

(a) Branching ratio = 25%

(b) Branching ratio = 50%

(c) Branching ratio = 75%

(d) Branching ratio = 100%

Figure 118. Output laser intensity as a function of Ar-fraction and pressure for variable branching ratios. Note the change in scale for the different images.

in $Ar(1s_4)$.

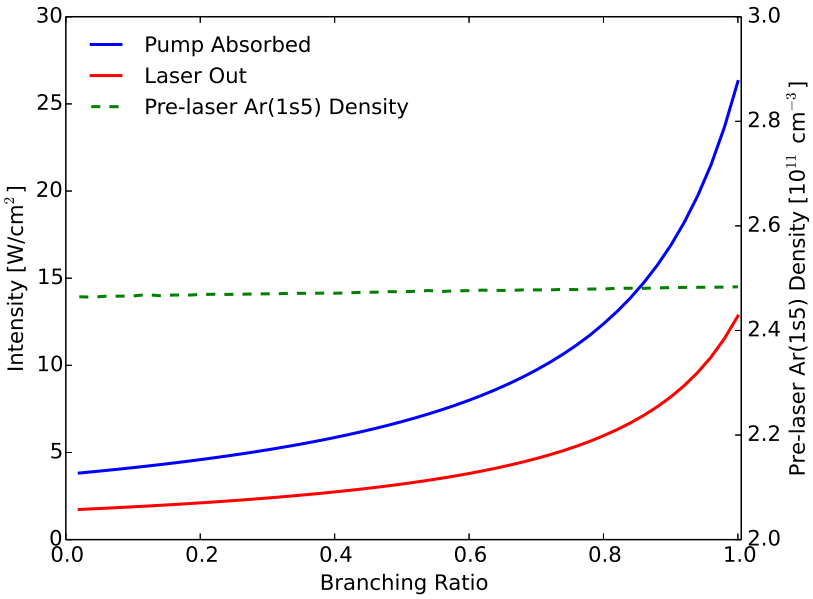

Figure 119. Absorbed pump laser intensity, output laser intensity, and pre-laser metastable density as a function of branching ratio at a pressure of 460 Torr and 8% Ar-fraction.

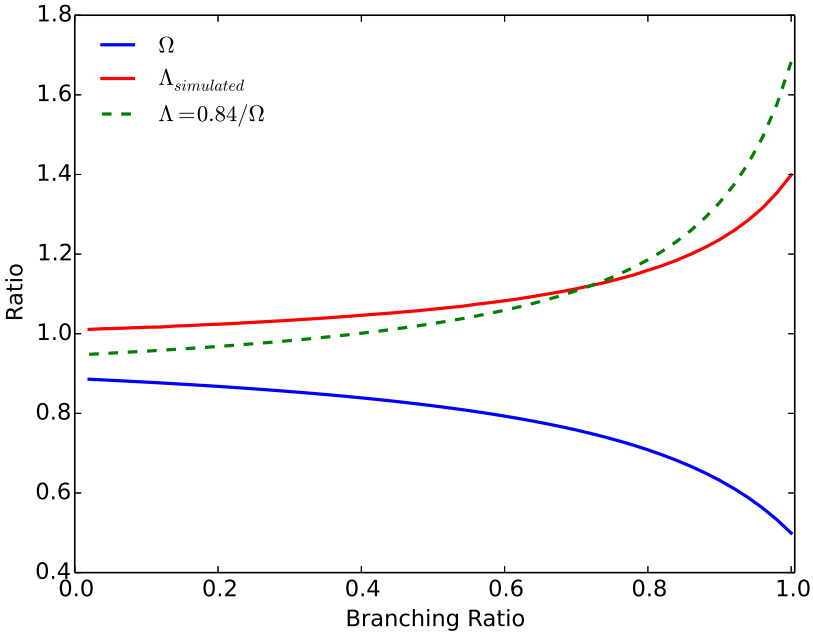

Figure 120. Fraction of Ar^* population collected in $Ar(1s_4)$, Ω, and ratio of Ar^* density after laser initiation to pre-laser density, Λ, as a function of branching ratio at a pressure of 460 Torr and 8% Ar-fraction.

The reduced electric field, E/N, is weakly affected by the laser ignition due to

the minor role of stepwise ionization. As a result, the electron impact excitation rates of ground state Ar are weakly affected by the laser kinetics. Loss rates diminishing the overall excited Ar species densities, $[Ar^*]$, through excimer formation or radiation/quenching to the ground state are dependent on the $Ar(1s_4)$ and $Ar(1s_5)$ densities. A list of the loss reactions for Ar^* is displayed in Table 10. With the assumption that the post-laser loss rates through $Ar(1s_5)$ are insignificant compared to loss rates through $Ar(1s_4)$ and that the excitation rates from the ground state are unchanged by laser kinetics, the pre-laser and post-laser loss rates are approximately equal:

$$\begin{aligned}
&[Ar(1s_5)]_{pre-laser}\left(k_1\left[He\right]+k_2\left[Ar\right]\left[Ar\right]+k_3\left[Ar\right]\left[He\right]\right)\\
&+\left[Ar(1s_4)\right]_{pre-laser}\left(k_4\left[Ar\right]\left[Ar\right]+k_5\left[Ar\right]\left[He\right]+k_6\right)\\
&\quad\approx\left[Ar(1s_4)\right]_{post-laser}\left(k_4\left[Ar\right]\left[Ar\right]+k_5\left[Ar\right]\left[He\right]+k_6\right). \qquad (146)
\end{aligned}$$

Before laser ignition, roughly 90% of the Ar^* density is collected in $Ar(1s_5)$, with the other 10% in $Ar(1s_4)$. Solving for the ratio of post-laser $Ar(1s_4)$ density to total pre-laser Ar^* density provides the ratio Γ:

$$\begin{aligned}
\Gamma &= \frac{\left[Ar(1s_4)\right]_{post-laser}}{\left[Ar^*\right]_{pre-laser}}\\
&\approx \frac{0.9\left(k_1\left[He\right]+k_2\left[Ar\right]\left[Ar\right]+k_3\left[Ar\right]\left[He\right]\right)+0.1\left(k_4\left[Ar\right]\left[Ar\right]+k_5\left[Ar\right]\left[He\right]+k_6\right)}{k_4\left[Ar\right]\left[Ar\right]+k_5\left[Ar\right]\left[He\right]+k_6}.
\end{aligned} \qquad (147)$$

This simplified form of Γ allows for an understanding of the kinetics controlling the simulated change in Ar^* density. From the definition of Ω in Equation 145, the

following relationship is obtained:

$$\Omega \left[Ar^*\right]_{post-laser} = \Gamma \left[Ar^*\right]_{pre-laser} \tag{148}$$

$$\implies \Lambda = \frac{\left[Ar^*\right]_{post-laser}}{\left[Ar^*\right]_{pre-laser}} = \frac{\Gamma}{\Omega}, \tag{149}$$

where Λ is the ratio of the Ar^* density post-laser to the Ar^* density pre-laser.

Table 10. A list of loss reactions for the excited Ar species, Ar^*.

Rate Coefficient Label	Reaction	Rate Coefficient [1/s, cm^3/s, or cm^6/s]	Ref.
k_1	$Ar(1s_5) + He \rightarrow Ar + He$	1.60×10^{-14}	Han and Heaven [2016][a]
k_2	$Ar(1s_5) + Ar + Ar \rightarrow Ar_2^* + Ar$	$3.60 \times 10^{-31} T_{gas}^{-0.6}$	Wieme and Lenaerts [1981]
k_3	$Ar(1s_5) + Ar + He \rightarrow Ar_2^* + He$	$1.80 \times 10^{-31} T_{gas}^{-0.6}$	Wieme and Lenaerts [1981][b]
k_4	$Ar(1s_4) + Ar + Ar \rightarrow Ar_2^* + Ar$	0.95×10^{-32}	Wieme and Lenaerts [1981]
k_5	$Ar(1s_4) + Ar + He \rightarrow Ar_2^* + He$	0.48×10^{-32}	Wieme and Lenaerts [1981][b]
k_6	$Ar(1s_4) \rightarrow Ar + \hbar\omega$	$1.20 \times 10^8/700$	Kramida et al. [2015][c]

[a] Reaction may be a proxy for quenching due to impurities Stefanović et al. [2014]
[b] Assuming three-body rate coefficients with He as the third body are 1/2 the rate coefficient for Ar as the third body
[c] Reduction by a factor of 700 due to radiation trapping [Holstein, 1947; Belostotskiy et al., 2011]

At a pressure of 460 Torr and a mixture of 8% Ar in He, Γ from Equation 147 is estimated to be 0.84. This estimate along with the simulated values of Ω and Λ directly from the zero-dimensional model are displayed in Figure 120. The two approaches provide a similar trend for Λ as a function of branching ratio. To reach a steady-state after laser ignition, an overall increase in Ar^* density is required to increase the post-laser loss rates through $Ar(1s_4)$ so that they are equal to the pre-laser loss rates. For a constant pressure and Ar-fraction Λ shows an increase from 1.0 to 1.4 as the branching ratio is increased from 2 to 100%.

The Ar^* loss rates are functions of pressure and Ar-fraction. Repeating the calculations for a pressure of 350 Torr and a mixture of 10% Ar in He provides the ratios displayed in Figure 121. At this pressure and Ar-fraction, Γ calculated from Equation 147 provides a value of 0.68. Unlike the 460 Torr scenario, which predicts an increase in Ar^* densities due to laser kinetics, the 350 Torr scenario shows a reduction in Ar^* densities caused by laser ignition for branching ratios below ap-

proximately 80%. At this lower pressure, the reduced pre-laser loss rates allows for a reduced post-laser $Ar(1s_4)$ density to match the pre-laser loss rates, which causes a reduction in the Ar^* densities after laser ignition.

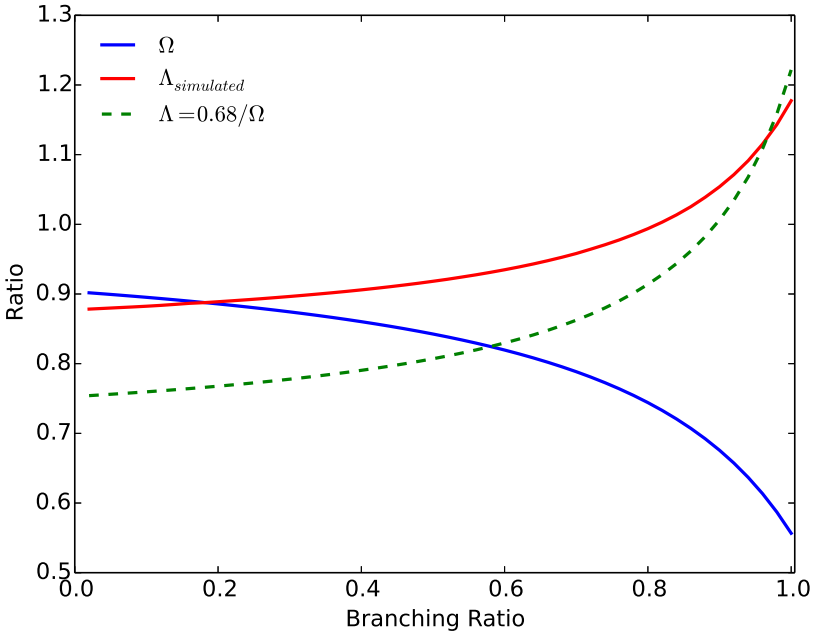

Figure 121. Fraction of Ar^* population collected in $Ar(1s_4)$, Ω, and ratio of Ar^* density after laser initiation to pre-laser density, Λ, as a function of branching ratio at a pressure of 350 Torr and 10% Ar-fraction.

The optical to optical conversion efficiency, defined as the ratio of the output laser intensity to the pump laser absorption, is weakly related to the branching ratio. For the 8% Ar-fraction at 460 Torr, a change of less than 4% is observed over the range of branching ratios, increasing from 45% to 49% as the branching ratio increases from 2 to 100%. Overall, the range of efficiencies is moderately less than the experimentally measured efficiency of 55% [Rawlins et al., 2015].

5.3 Simplified Model

Previous kinetic models of an OPRGL have used a steady-state approach, which estimates laser intensities and densities based on the assumption of a steady-state [Demyanov et al., 2013; Yang et al., 2015; Rawlins et al., 2015; Han et al., 2014]. In

this approach, discharge kinetics are assumed to be unchanged due to the introduction laser kinetics, and the overall Ar^* density is assumed to remain constant. To compare the results of this simplified kinetic approach to the results of the full discharge laser model outlined in Section 5.1, the simulations performed in Section 5.2 are repeated using a steady-state approach.

Model Description.

Following the procedure outlined in Section 4.4, a simplified model of the laser is developed. Instead of using a time-dependent method to calculate a steady-state after laser ignition, a steady-state is assumed and the corresponding densities and laser intensities are calculated directly. Initial excited Ar species densities are extracted from the results of Section 4.2 for a 500 V applied voltage in the pressure range of 200-500 Torr. Laser parameters are the same as in Section 5.1. Electron impact rates between excited species are ignored to fully simplify the model [Yang et al., 2015; Rawlins et al., 2015; Han et al., 2014]. Additionally, the Ar^* densities are assumed to be unchanged due to laser ignition, and the loss rates for excimer formation, radiation to the ground state, or quenching to the ground state are ignored. A list of the reactions included in the model is displayed in Table 11, which includes spontaneous emission and two-body neutral collisions between the different Ar^* species.

At steady-state, there is no variation in the species densities, providing the fol-

Table 11. A list of the reactions and rate coefficient labels used in the simple laser model. Only spontaneous emission and two-body neutral collisions are maintained to fully simplify the kinetic model.

Rate Coefficient Label	Reaction
k_1	$Ar(1s_5) + He \rightarrow Ar(1s_4) + He$
k_2	$Ar(1s_5) + Ar \rightarrow Ar(1s_4) + Ar$
k_3	$Ar(1s_4) + He \rightarrow Ar(1s_5) + He$
k_4	$Ar(1s_4) + Ar \rightarrow Ar(1s_5) + Ar$
k_5	$Ar(2p_{10}) + He \rightarrow Ar(1s_5) + He$
k_6	$Ar(2p_{10}) + Ar \rightarrow Ar(1s_5) + Ar$
k_7	$Ar(2p_9) + He \rightarrow Ar(1s_5) + He$
k_8	$Ar(2p_9) + Ar \rightarrow Ar(1s_5) + Ar$
k_9	$Ar(2p_8) + He \rightarrow Ar(1s_5) + He$
k_{10}	$Ar(2p_8) + Ar \rightarrow Ar(1s_5) + Ar$
k_{11}	$Ar(2p_9) \rightarrow Ar(1s_5) + \hbar\omega$
k_{12}	$Ar(2p_8) \rightarrow Ar(1s_5) + \hbar\omega$
k_{13}	$Ar(2p_{10}) + He \rightarrow Ar(1s_4) + He$
k_{14}	$Ar(2p_{10}) + Ar \rightarrow Ar(1s_4) + Ar$
k_{15}	$Ar(2p_9) + He \rightarrow Ar(1s_4) + He$
k_{16}	$Ar(2p_9) + Ar \rightarrow Ar(1s_4) + Ar$
k_{17}	$Ar(2p_8) + He \rightarrow Ar(1s_4) + He$
k_{18}	$Ar(2p_8) + Ar \rightarrow Ar(1s_4) + Ar$
k_{19}	$Ar(2p_{10}) \rightarrow Ar(1s_4) + \hbar\omega$
k_{20}	$Ar(2p_8) \rightarrow Ar(1s_4) + \hbar\omega$
k_{21}	$Ar(2p_{10}) + He \rightarrow Ar(2p_9) + He$
k_{22}	$Ar(2p_{10}) + Ar \rightarrow Ar(2p_9) + Ar$
k_{23}	$Ar(2p_{10}) + He \rightarrow Ar(2p_8) + He$
k_{24}	$Ar(2p_{10}) + Ar \rightarrow Ar(2p_8) + Ar$
k_{25}	$Ar(2p_9) + He \rightarrow Ar(2p_{10}) + He$
k_{26}	$Ar(2p_9) + Ar \rightarrow Ar(2p_{10}) + Ar$
k_{27}	$Ar(2p_8) + He \rightarrow Ar(2p_{10}) + He$
k_{28}	$Ar(2p_8) + Ar \rightarrow Ar(2p_{10}) + Ar$
k_{29}	$Ar(2p_9) + He \rightarrow Ar(2p_8) + He$
k_{30}	$Ar(2p_9) + Ar \rightarrow Ar(2p_8) + Ar$
k_{31}	$Ar(2p_8) + He \rightarrow Ar(2p_9) + He$
k_{32}	$Ar(2p_8) + Ar \rightarrow Ar(2p_9) + Ar$

lowing coupled non-linear equations:

$$
\begin{aligned}
[Ar(1s_5)]\left(k_1[He]+k_2[Ar]\right)+W_{abs} &= [Ar(1s_4)]\left(k_3[He]+k_4[Ar]\right)+[Ar(2p_{10})]\left(k_5[He]+k_6[Ar]\right)\\
&+[Ar(2p_9)]\left(k_7[He]+k_8[Ar]+k_{11}\right)+[Ar(2p_8)]\left(k_9[He]+k_{10}[Ar]+k_{12}\right)+W_l,\\
[Ar(1s_4)]\left(k_3[He]+k_4[Ar]\right) &= [Ar(1s_5)]\left(k_1[He]+k_2[Ar]\right)+[Ar(2p_{10})]\left(k_{13}[He]+k_{14}[Ar]+k_{19}\right)\\
&+[Ar(2p_9)]\left(k_{15}[He]+k_{16}[Ar]\right)+[Ar(2p_8)]\left(k_{17}[He]+k_{18}[Ar]+k_{20}\right),\\
[Ar(2p_{10})]\left(k_5[He]+k_6[Ar]+k_{13}[He]+k_{14}[Ar]+k_{21}[He]+k_{22}[Ar]+k_{23}[He]+k_{24}[Ar]+k_{19}\right)&\\
+W_l &= [Ar(2p_9)]\left(k_{25}[He]+k_{26}[Ar]\right)+[Ar(2p_8)]\left(k_{27}[He]+k_{28}[Ar]\right),\\
[Ar(2p_9)](k_7[He]+k_8[Ar]+k_{15}[He]+k_{16}[Ar]+k_{25}[He]+k_{26}[Ar]+k_{30}[He]+k_{11})&\\
=[Ar(2p_{10})]\left(k_{21}[He]+k_{22}[Ar]\right)+[Ar(2p_8)]\left(k_{31}[He]+k_{32}[Ar]\right)+W_{abs},&\\
[Ar(1s_5)]+[Ar(1s_4)]+[Ar(2p_{10})]+[Ar(2p_9)]+[Ar(2p_8)] &= [Ar^*],\\
R_lR_{oc}T_r^2\exp\{2\left([Ar(2p_{10})]-3[Ar(1s_5)]/5\right)\sigma_{ul}\ell_{gain}\} &= 1,
\end{aligned}
\tag{150}
$$

where W_{abs} is the rate due to pump laser absorption, W_l is the rate due to circulating laser intensity, $[Ar^*]$ is the total excited species density before laser ignition, and the final equation provides the threshold laser condition. The system of equations is solved using a root finding technique implemented through Mathematica.

Results.

To begin the analysis of laser performance over Ar-fraction and pressure, it is helpful to analyze laser performance for a constant metastable density over all pressures and Ar-fractions to provide insight into laser performance independent of metastable density. A similar analysis was performed by Demyanov et al. [2013] where the maximum excitation efficiency, defined as the fraction of energy spent exciting the $Ar(1s)$ manifold, was used for each Ar-fraction at atmospheric pressures. This excitation frequency does not correspond to a specific discharge, but provides the best case sce-

nario for OPRGL operation in terms of metastable production. Similarly, the use of a constant metastable density does not provide a realistic trend of laser intensities as a function of Ar-fraction and pressure, but instead yields insight into the behavior of an ideal OPRGL system independent of metastable density.

For this analysis, a metastable density of 4.5×10^{11} cm^{-3} is implemented for all Ar-fractions and pressures, corresponding to the metastable density for the 300 Torr, 10% Ar-fraction RF-DBD scenario. The absorbed pump laser intensities and output laser intensities are displayed in Figures 122 and 123 for a branching ratio of 50%. For this scenario, the peak absorption and output laser intensity occur at a 1% Ar-fraction and pressure of 500 Torr, indicating that the laser performance is enhanced at lower Ar-fractions and higher pressures. This matches the results of Demyanov et al. [2013], where the peak laser efficiency was found to occur for Ar-fractions near 1% at atmospheric pressures.

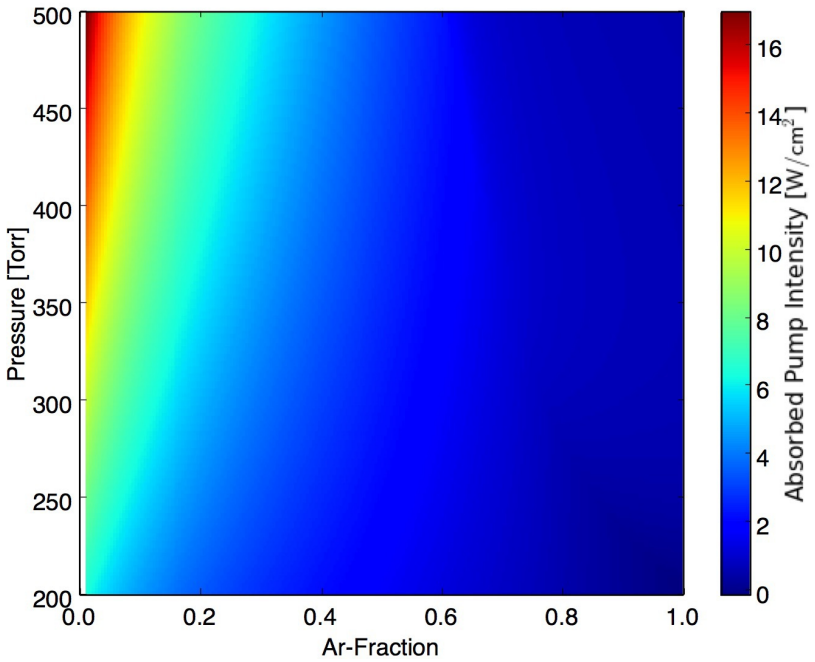

Figure 122. Absorbed pump laser intensities as a function of Ar-fraction and pressure using a constant metastable density for all Ar-fractions and pressures and a branching ratio of 50%.

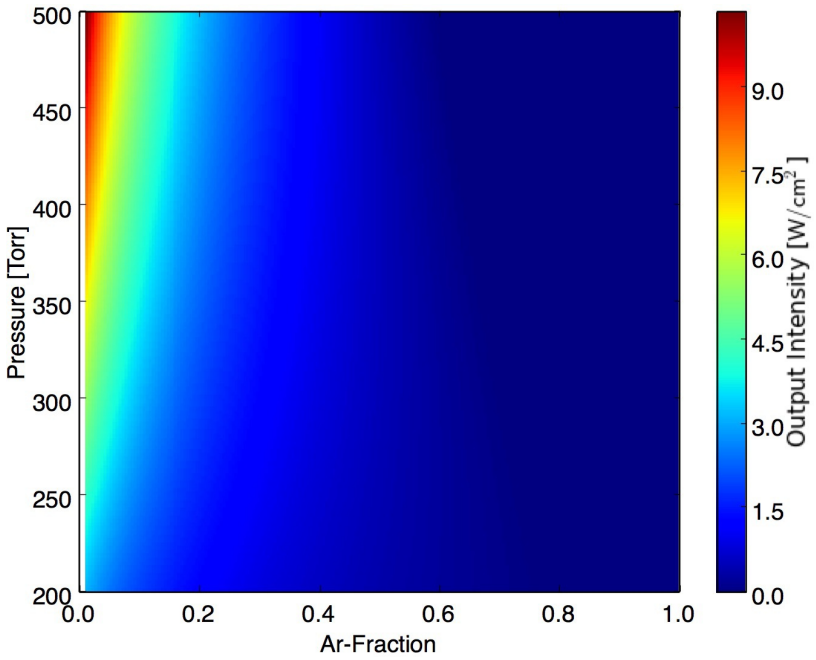

Figure 123. Output laser intensities as a function of Ar-fraction and pressure using a constant metastable density for all Ar-fractions and pressures and a branching ratio of 50%.

As pressure is increased, the spin-orbit mixing rate of $Ar(2p_9) + M \rightarrow Ar(2p_{10}) + M$ is increased, thus increasing laser performance. Collisional relaxation rates via $Ar(1s_4) + M \rightarrow Ar(1s_5) + M$ at a gas temperature of 440 K are an order of magnitude larger for He than for Ar, with the rate coefficient for $M = He$ at 3.7×10^{-13} cm^3/s and the rate coefficient for $M = Ar$ equal to 2.6×10^{-14} cm^3/s. Additionally, the quenching rate coefficients of $Ar(2p) + M \rightarrow Ar(1s) + M$ are at least an order of magnitude larger for Ar than for He. Combining these effects, for a constant metastable density, the laser performs more efficiently at low Ar-fractions and high pressures.

For a realistic calculation of the laser intensities taking into account the change in metastable density as a function of Ar-fraction and pressure due to discharge kinetics, the analysis above is repeated using the variable metastable density calculated for an RF-DBD (Figure 65). The difference between this steady-state approach and the full discharge laser model outlined in Section 5.1 is the assumption of a constant

Ar^* after laser ignition and the removal of discharge and electron impact kinetics. A steady-state approach ignores the discharge kinetics and uses a provided set of initial densities to calculate steady-state densities and laser intensities while maintaining a constant Ar^*. The full discharge laser model calculates discharge kinetics in addition to laser kinetics over time until a steady-state is reached.

Absorbed pump intensities and output laser intensities calculated using the steady-state approach with a variable metastable density are displayed in Figures 124 and 125. Similar to the results from the full discharge laser model (Figures 117 and 118), the metastable density trend is clearly visible in the laser intensity profiles. Additionally, the pressure associated with the peak absorption and output laser intensities increases as the branching ratio is increased.

Due to a reduction in the Ar^* density collected in $Ar(1s_4)$, the laser intensities increase as the branching ratio is increased (Table 12). Overall, the laser intensity trends match the trends calculated by the full discharge laser model (Table 9). However, the pressures associated with the peak output laser power are nearly 100 Torr less than the peak pressures predicted by the full discharge laser model, and the laser intensities for the 100% branching ratio scenario are approximately 50% less. This difference is the result of a change in Ar^* densities observed in the full discharge laser model after laser ignition. At elevated pressures, the Ar^* densities were shown to increase due to the laser kinetics (Figure 120), and the larger branching ratios correspond to a larger increase in density than the lower branching ratios. This increase in Ar^* densities causes an increase in the population of species directly involved with laser performance, thus increasing the laser intensities. The simplified model does not account for this change in density, which causes the peak intensities to occur at lower pressures.

A comparison of the absorbed pump laser intensity and output laser intensity

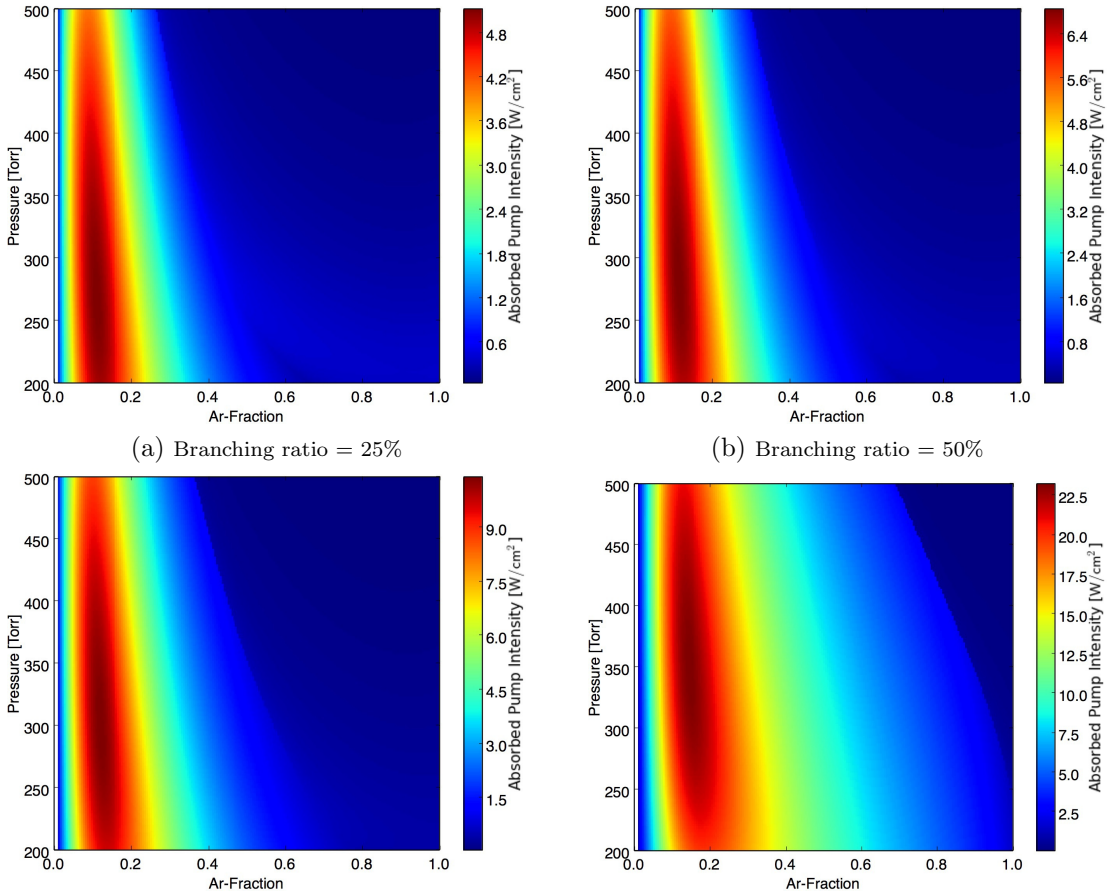

(a) Branching ratio = 25%

(b) Branching ratio = 50%

(c) Branching ratio = 75%

(d) Branching ratio = 100%

Figure 124. Absorbed pump laser intensity as a function of Ar-fraction and pressure for variable branching ratios using the simplified laser model. Note the change in scale for the different images.

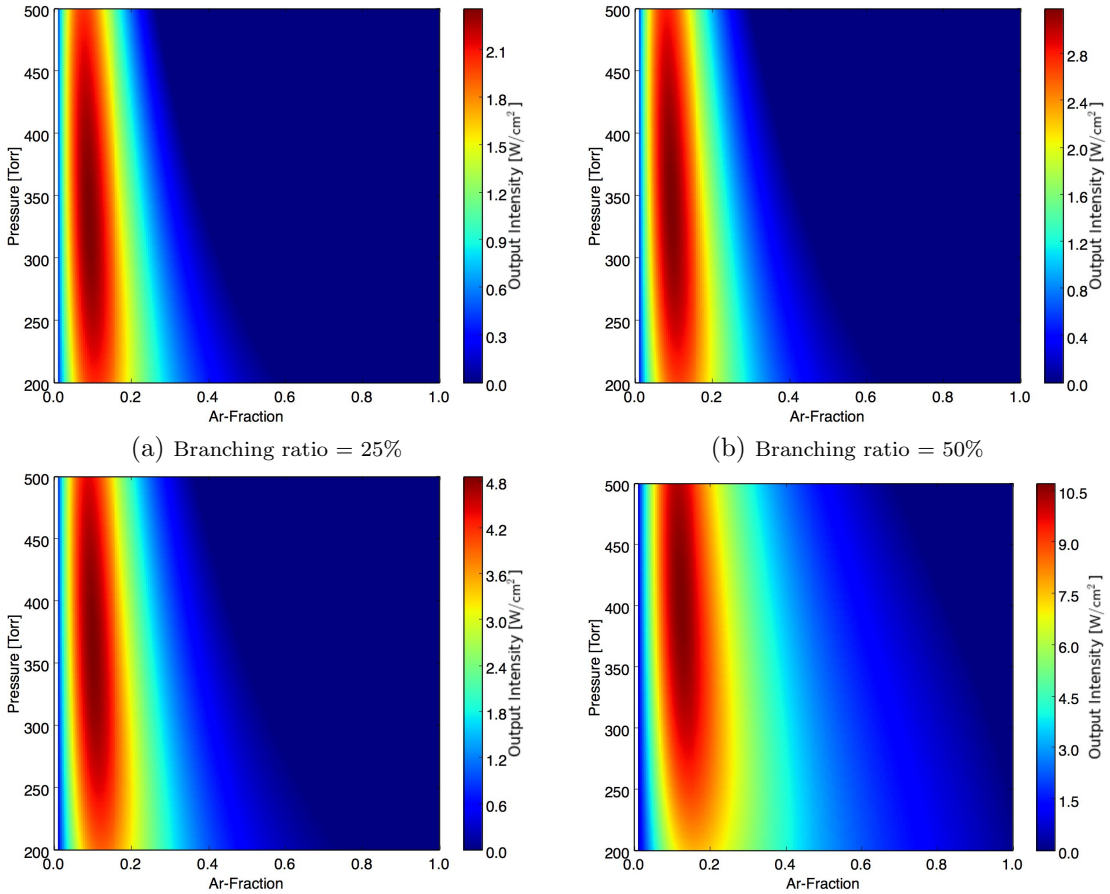

(a) Branching ratio = 25%

(b) Branching ratio = 50%

(c) Branching ratio = 75%

(d) Branching ratio = 100%

Figure 125. Output laser intensity as a function of Ar-fraction and pressure for variable branching ratios using the simplified laser model. Note the change in scale for the different images.

Table 12. Parameters associated with peak output laser intensities as a function of branching ratio using the simplified laser model.

Branching Ratio	Peak Laser Intensity [W/cm^2]	Pressure [Torr]	Ar-Fraction	Absorbed Pump Intensity [W/cm^2]
0.25	2.4	330	0.09	5.0
0.50	3.2	350	0.09	6.6
0.75	4.9	360	0.10	10.2
1.00	10.7	410	0.12	22.6

for the simplified and full discharge laser model as a function of branching ratio at a pressure of 460 Torr and 8% Ar-fraction is displayed in Figure 126. Overall, the two models are in agreement. As the branching ratio approaches 100%, the intensities from the simple model are underestimated due to a constant Ar^* density. The steady-state model provides a simple, fast method of calculating laser intensities and is capable of providing insight into the dominant kinetics controlling laser behavior. However, the full discharge laser model also provides insight into the change in discharge kinetics due to the introduction of the laser rates, which is important to understanding the complete behavior of an OPRGL system.

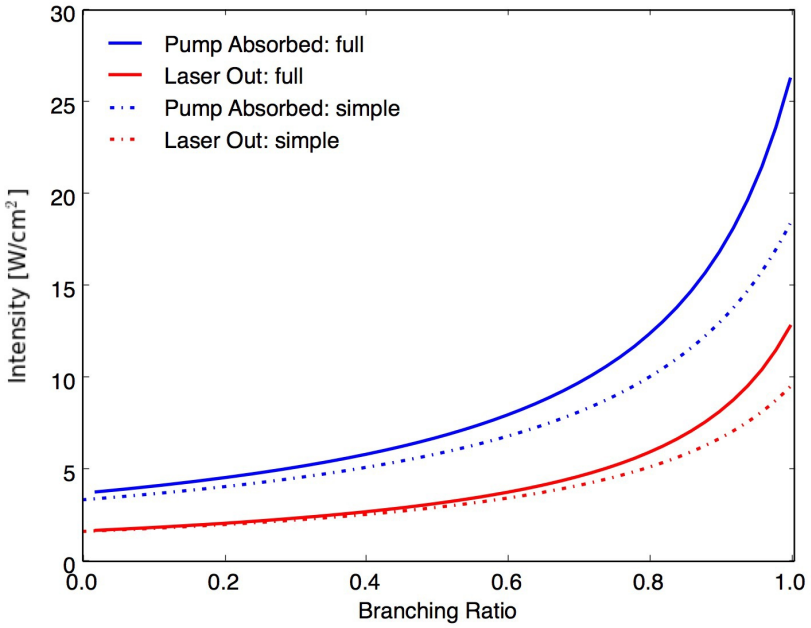

Figure 126. A comparison of the absorbed pump laser intensity and output laser intensity as a function of branching ratio for the simplified and full discharge laser models at a pressure of 460 Torr and 8% Ar-fraction.

5.4 Conclusions

Simulations of an optically pumped rare gas laser are performed as a function of the $Ar(2p) + M \rightarrow Ar(1s) + M$ branching ratio using a radio frequency dielectric barrier discharge as the source of metastable production. A time dependent zero-dimensional discharge model including laser kinetics is used to calculate pump laser absorption and output laser intensities over a range of Ar-He mixtures from 200-500 Torr. While the pre-laser metastable densities show a decrease with increasing pressure, the peak output laser intensities occur at higher pressures due to the increased $Ar(2p_9) + M \rightarrow Ar(2p_{10}) + M$ relaxation rates and increased pump laser absorption linewidths. Additionally, the peak output intensity shifts to higher pressures as the branching ratio is increased caused by a decrease in the detrimental $Ar(2p) + M \rightarrow Ar(1s_4) + M$ rates. A large increase in pump laser absorption and output laser intensity are observed as the branching ratio to $Ar(1s_5)$ is increased,

resulting in a factor of 7 increase in the peak output intensity as the branching ratio is increased from 25 to 100%.

The $Ar(1s_4)$ species plays a key role in laser kinetics. As the branching ratio increases, the fraction of Ar^* populations collected in $Ar(1s_4)$ decreases, which increases the densities of the species directly involved with laser performance: $Ar(1s_5)$, $Ar(2p_9)$, and $Ar(2p_{10})$. Additionally, the electron excitation rates of ground state Ar are weakly affected by the introduction of the laser kinetics. As a result, the total post-laser Ar^* density evolves to match the pre-laser loss rates due to a redistribution of the Ar^* densities. The laser ignition can cause an increase or decrease in the Ar^* density, depending on the Ar-fraction, pressure, and branching ratio.

A simplified model of the laser kinetics is developed, showing reasonable agreement with the full discharge laser model. However, the peak laser intensities occur at lower pressures for the simplified model due to a constant Ar^* density. The full discharge laser model allows for a change in Ar^* density as a result of laser kinetics, which shows an increase in density as the pressure is increased. This increase in density corresponds to an increase in laser intensities, and provides a measure of the laser's influence on the plasma which cannot be captured by the simplified model.

An analysis of the laser performance for a constant initial metastable density over all Ar-fractions and pressures indicates that laser efficiency is increased as pressure is increased and Ar-fraction is decreased, matching the results from Demyanov et al. [2013]. A peak output laser intensity is observed at 500 Torr (the maximum pressure of this analysis) for a 1% Ar-fraction (the minimum Ar-fraction). As the pressure is increased, the $Ar(2p_9) + M \rightarrow Ar(2p_{10}) + M$ mixing rates are elevated, increasing laser intensities. Additionally, He rich mixtures account for larger $Ar(1s_4) + M \rightarrow Ar(1s_5) + M$ rates and lower $Ar(2p) + M \rightarrow Ar(1s) + M$ rates, which also improve laser performance.

While the $Ar(2p) + M \rightarrow Ar(1s) + M$ branching ratios are not well known, the effect on laser intensities is strong. Additional kinetic measurements of the branching ratio would be beneficial to fully understand optically pumped rare gas laser performance.

VI. Conclusions

Two discharge scenarios are analyzed to understand the discharge conditions and chemical kinetics conducive to continuous, large volume production of $Ar(1s_5)$ metastable densities on the order of 10^{13} cm^{-3} required for high-power optically pumped rare gas laser operation. Elevated pressures increase the likelihood of thermal instabilities, placing limitations on the types of non-thermal gas discharges capable of stable operation at near atmospheric pressures. This analysis focuses on pulsed direct current discharges and radio frequency dielectric barrier discharges, which are both known to maintain stability at elevated pressures. After discharge simulations are performed for the two scenarios, laser performance is analyzed as a function of pressure, Ar-He mixture, and $Ar(2p) + M \rightarrow Ar(1s) + M$ branching ratio, using a zero-dimensional discharge model including laser kinetics.

For the pulsed circuit discharge, simulations of a 7% Ar in He pulsed DC discharge at a pressure of 270 Torr are performed for 1000 V pulses with temporal widths of 1, 20, and 35 μs using a zero-dimensional kinetic model. Species relevant to the operation of an optically pumped rare-gas laser are analyzed over a single pulse duration to identify key kinetic pathways. Comparisons to the experimental voltage, current, fluorescence, and absorption measurements by Han et al. [2016] show temporal agreement. The inclusion of radiation trapping for the $Ar(1s_4) \rightarrow Ar + \hbar\omega$ transition decreases post-pulse metastable decay rates, matching the measured trends.

One-dimensional fluid simulations are also performed for the 20 μs, 1000 V scenario, providing spatial density profiles. Comparisons of the zero and one-dimensional models show agreement in the positive column, where the zero-dimensional model is appropriate. Both models predict a spike in excitation and ionization rates during breakdown due to elevated voltage, E/N magnitude, and T_e during pulse initiation. After breakdown, the combination of a reduced electrode voltage and cathode fall for-

mation results in a factor of 5 decrease in the positive column E/N. This reduction in E/N drastically decreases Ar excitation and ionization via electron impact, with an order of magnitude reduction in excitation rates and a two order of magnitude reduction in ionization rate within 2 μs after breakdown.

Electron densities steadily approach a constant value while the dominant ion shifts from Ar^+ to Ar_2^+ over the pulse duration due to three-body collisions. For the geometry and simulated discharge conditions, dissociative recombination is found to be the dominant electron loss mechanism. Metastable loss rates rapidly increase post-breakdown, resulting in peak metastable densities near 4×10^{12} cm^{-3}, decreasing by a factor of 3 over the pulse duration. Radiation trapping plays a key role in metastable decay rates through the reaction sequence $Ar(1s_5) + e^- \rightarrow Ar(1s_4) + e^-$ followed by $Ar(1s_4) \rightarrow Ar + \hbar\omega$. The $Ar(2p)$ species display initial spikes followed by an immediate reduction in density after breakdown due to the reduced electron excitation rates from ground state at the post-breakdown E/N. Collisions with He are observed to be responsible for $Ar(2p_9)$ loss, with an almost equal transfer to the $Ar(2p_{10})$ and $Ar(2p_8)$ levels. As expected, excited species densities are largest near the cathode layer, with a two order of magnitude difference between the peak and positive column densities.

A sensitivity analysis of the reaction rate package is also performed, pinpointing the dominant pathways for each species. The number of reactions are reduced by placing a threshold on pathway contributions to the total rate for each species during breakdown and after breakdown. Reducing the number of reactions from 175 to 31 produces a minor change in the simulation results. Further reducing the number of reactions to 20 creates a noticeable difference in the simulations with a factor of 1.5 difference in the metastable densities during the pulse, compared to the full rate package. This sensitivity analysis is performed at a pressure of 270 Torr for a 7% Ar

in He mixture, and cannot be extended to all Ar-He discharge scenarios.

An analysis of the one-dimensional fluid model dependence on EEDF calculations is also performed, showing a slight difference between the two methods of calculating the EEDFs. The first method relies on EEDFs calculated from the positive column densities predicted by ZDPlasKin, which is run prior to the fluid model to provide a lookup table of rate coefficients based on the local T_e. The second method calculates a set of EEDFs for the fluid model densities predicted in the negative glow and a separate set of EEDFs for the positive column densities. These two sets of EEDFs are then interpolated to provide an EEDF based on the metastable density at each position. The positive column electron temperatures, electron densities, and metastable densities are nearly equal for the two approaches, verifying the use of pre-calculated EEDFs for simulations of the positive column.

Extending the analysis to an α-mode radio frequency dielectric barrier discharge, simulations of a clam shell electrode experiment are performed for a variety of Ar-He mixtures and gas pressures. Results from a one-dimensional fluid model are compared to a zero-dimensional effective DC model in the bulk plasma, showing general agreement over Ar-fractions ranging from 5 to 100% and pressures between 200 and 500 Torr. The agreement between the two models indicates that the zero-dimensional effective DC model provides a valid approach to modeling the bulk plasma of a high pressure RF-DBD.

Peak metastable densities at 300 Torr are observed near a 15% Ar in He mixture for the geometry of the discharge chamber used in the simulations, corresponding to the peak E/N for the varying mixtures. Electron temperature and electron density are observed to increase with increasing Ar-fraction. Metastable densities are shown to decrease with increasing pressure due to a reduction in E/N and a quadratic increase in metastable loss rates through excimer formation: $Ar(1s_5) + Ar + M \rightarrow Ar_2^* + M$.

The decrease in bulk plasma E/N is primarily due to an increase in ionization through $Ar_2^* + e^- \rightarrow Ar_2^+ + 2e^-$, which requires significantly less energy than ionization through $Ar + e^- \rightarrow Ar^+ + 2e^-$.

Additionally, the peak $Ar(1s_5)$ density shifts from an Ar-fraction of approximately 15% at 200 Torr to 10% at 500 Torr. The increased excimer formation rate at elevated pressures raises Ar_2^* densities for He rich mixtures, causing the peak E/N to occur at lower Ar-fractions as the pressure is increased. This shift in E/N corresponds to a shift in the peak metastable densities, which occur at lower Ar-fractions as pressure is increased.

Calculations varying the applied voltage from 500 to 1750 V show an increase in $Ar(1s_5)$ density as the voltage is increased. Bulk plasma metastable densities above 10^{12} cm^{-3} are observed for applied voltages above 750 V, corresponding to average applied powers greater than 25 W. While the increase in metastable density with increasing voltage is promising, gas heating must be taken into account as the voltage and current densities are increased to determine thresholds for thermal instabilities that collapse the discharge to a filamentary mode. An α to γ-mode transition is observed for an applied voltage of 1400 V using a 15% Ar-fraction at a pressure of 200 Torr with a secondary electron emission coefficient of 0.1. The spatially averaged electron density matches the critical electron density provided by Raizer et al. [1995]. For a secondary emission coefficient of 0.01, no α to γ-mode transition is observed in the range of applied voltages. No large increase in electron or metastable density is observed at the onset of the γ-mode, which is most likely due to the limitations of a one-dimensional fluid model and the subnormal current densities caused by the dielectric barriers.

Extending the zero-dimensional simulations to a ring electrode experiment provides a comparison of simulated and measured $Ar(1s_5)$ and $Ar(1s_4)$ densities as a

function of pressure and Ar-fraction. Measured $Ar(1s_5)$ densities show a large decrease from 10 to 25% Ar-fraction, while the simulated peaks occur near 20% for pressures below 160 Torr. The simulated densities show reasonable agreement with the measured densities as a function of pressure, exhibiting a large decrease as the pressure is increased from 10 to 160 Torr. This reduction is mainly due to a decrease in the ambipolar diffusion loss rate which corresponds to a reduction in the bulk plasma E/N, demonstrating the effect of electron loss rates on metastable density.

Our simulations indicate that an OPRGL using an α-mode RF-DBD in the pressure range of 200-500 Torr will be provided the largest metastable density using a mixture of approximately 15% Ar in He at 200 Torr. While the metastable density decreases with increasing pressure, the gas pressure must also be taken into account when mapping to laser performance. Both the diode pump absorption linewidth and spin orbit mixing rate via $Ar(2p_9) + M \rightarrow Ar(2p_{10}) + M$ increase with increasing pressure, requiring a laser kinetics model to analyze laser performance as a function of pressure and Ar-fraction for this discharge scenario.

A simplified zero-dimensional steady-state model of an RF-DBD is developed showing excellent agreement with the time-dependent simulations from ZDPlasKin. An analysis of the electron production and loss rates as a function of Ar-fraction and pressure indicates that the ionization contributions of $Ar + e^- \rightarrow Ar^+ + 2e^-$ relative to $Ar_2^* + e^- \rightarrow Ar_2^+ + 2e^-$ controls the steady-state E/N, which in turn controls metastable production rates. The metastable loss rates through $Ar(1s_5) + Ar + M \rightarrow Ar_2^* + M$ increase quadratically with pressure and are a factor of 2 larger for $M = Ar$ than for $M = He$. These combined effects cause the metastable density to decrease with increasing pressure and produce peak metastable densities near Ar-fractions of 15% at 200 Torr shifting to 10% at 500 Torr.

Finally, coupling laser kinetics to the discharge kinetics for a radio frequency

dielectric barrier discharge, simulations of an optically pumped rare gas laser are performed as a function of the $Ar(2p) + M \rightarrow Ar(1s) + M$ branching ratio. A time dependent zero-dimensional discharge model including laser kinetics is used to calculate pump laser absorption and output laser intensities over a range of Ar-He mixtures from 200-500 Torr. While the pre-laser metastable densities show a decrease with increasing pressure, the peak output laser intensities occur at higher pressures due to the increased $Ar(2p_9) + M \rightarrow Ar(2p_{10}) + M$ relaxation rates and increased pump laser absorption linewidths. Additionally, the peak output intensity shifts to higher pressures as the branching ratio is increased caused by a decrease in the detrimental $Ar(2p) + M \rightarrow Ar(1s_4) + M$ rates. A large increase in pump laser absorption and output laser intensity are observed as the branching ratio to $Ar(1s_5)$ is increased, resulting in a factor of 7 increase in the peak output intensity as the branching ratio is increased from 25 to 100%.

The $Ar(1s_4)$ species plays a key role in laser kinetics. As the branching ratio increases, the fraction of Ar^* populations collected in $Ar(1s_4)$ decreases, which increases the densities of the species directly involved with laser performance: $Ar(1s_5)$, $Ar(2p_9)$, and $Ar(2p_{10})$. Additionally, the electron excitation rates of ground state Ar are weakly affected by the introduction of the laser kinetics. As a result, the total post-laser Ar^* density evolves to match the pre-laser loss rates due to a redistribution of the Ar^* densities. The laser ignition can cause an increase or decrease in the Ar^* density, depending on the Ar-fraction, pressure, and branching ratio.

Similar to the simplified RF-DBD model, a simplified model of the laser kinetics is developed showing reasonable agreement with the full discharge laser model. However, the peak laser intensities occur at lower pressures for the simplified model due to a constant Ar^* density. The full discharge laser model allows for a change in Ar^* density as a result of laser kinetics, which shows an increase in density as the pressure is

increased. This increase in density corresponds to an increase in laser intensities, and provides a measure of the laser's influence on the plasma which cannot be captured by the simplified model.

An analysis of the laser performance for a constant initial metastable density over all Ar-fractions and pressures indicates that laser efficiency is increased as pressure is increased and Ar-fraction is decreased, matching the results from Demyanov et al. [2013]. A peak output laser intensity is observed at 500 Torr (the maximum pressure of this analysis) for a 1% Ar-fraction (the minimum Ar-fraction). As the pressure is increased, the $Ar(2p_9) + M \rightarrow Ar(2p_{10}) + M$ mixing rates are elevated, increasing laser intensities. Additionally, He rich mixtures account for larger $Ar(1s_4) + M \rightarrow Ar(1s_5) + M$ rates and lower $Ar(2p) + M \rightarrow Ar(1s) + M$ rates, which also improve laser performance.

While the $Ar(2p) + M \rightarrow Ar(1s) + M$ branching ratios are not well known, the effect on laser intensities is strong. Additional kinetic measurements of the branching ratio would be beneficial to fully understand optically pumped rare gas laser performance.

Metastable $Ar(1s_5)$ densities on the order of 10^{12} cm^{-3} are estimated for the positive column of a pulsed direct current discharge and the bulk plasma of a radio frequency dielectric barrier discharge for pressures in the range of 200-300 Torr and applied voltages near 1000 V. While the $Ar(1s_5)$ density is found to increase as the applied voltage increases, further calculations are required to analyze thermal instabilities at high voltages. In regions of elevated E/N, as observed in the sheaths, metastable densities are above the 10^{13} cm^{-3} desired for use in an optically pumped rare gas laser. In the bulk plasma, the E/N magnitudes are reduced, which limits the metastable densities due to decreased electron impact excitation rates. Pulsed direct current discharges are capable of producing elevated E/N magnitudes in the

bulk plasma for short time durations during the pulse onsets. For a steady-state discharge, elevating electron loss rates in the bulk plasma may provide a mechanism for increasing E/N magnitudes. However, excimer formation is problematic to producing large metastable densities at atmospheric pressures.

While the metastable density is vital to laser operation, the gas pressure, temperature, and Ar-He mixture are also important. As demonstrated in this analysis, peak output laser intensities are estimated for elevated pressures and He rich mixtures even though the metastable density is reduced at elevated pressures. The decrease in metastable density observed with increasing pressure requires a trade-off between metastable density and pressure to maximize laser performance.

Bibliography

Ashida, S., Lee, C., and Lieberman, M. (1995). Spatially averaged (global) model of time modulated high density argon plasmas. *Journal of Vacuum Science & Technology A*, 13(5):2498–2507.

Balcon, N., Aanesland, A., and Boswell, R. (2007). Pulsed rf discharges, glow and filamentary mode at atmospheric pressure in argon. *Plasma Sources Science and Technology*, 16(2):217.

Balcon, N., Hagelaar, G., and Boeuf, J. (2008). Numerical model of an argon atmospheric pressure rf discharge. *IEEE Transactions on Plasma Science*, 36(5):2782–2787.

Beach, R. J., Krupke, W. F., Kanz, V. K., Payne, S. A., Dubinskii, M. A., and Merkle, L. D. (2004). End-pumped continuous-wave alkali vapor lasers: experiment, model, and power scaling. *JOSA B*, 21(12):2151–2163.

Bekefi, G. (1976). Principles of laser plasmas. *New York, Wiley-Interscience, 1976. 712 p*, 1.

Belostotskiy, S. G., Ouk, T., Donnelly, V. M., Economou, D. J., and Sadeghi, N. (2011). Time-and space-resolved measurements of ar($1s_5$) metastable density in a microplasma using diode laser absorption spectroscopy. *Journal of Physics D: Applied Physics*, 44(14):145202.

Biagi, S. F. (2011). Program magboltz, version 8.97. nl.lxcat.net.

Bin, L., Qiang, C., Zhong-Wei, L., and Zheng-Duo, W. (2011). A large gap of atmospheric pressure rf-dbd glow discharges in ar and mixed gases. *Chinese Physics Letters*, 28(1):015201.

Biondi, M. A. and Chanin, L. M. (1961). Blanc's law: ion mobilities in helium-neon mixtures. *Physical Review*, 122(3):843.

Blanc, A. (1908). Recherches sur les mobilités des ions dans les gaz. *J. Phys. Theor. Appl.*, 7(1):825–839.

Boeuf, J. and Pitchford, L. (1995). Two-dimensional model of a capacitively coupled rf discharge and comparisons with experiments in the gaseous electronics conference reference reactor. *Physical Review E*, 51(2):1376.

Boeuf, J.-P. and Pitchford, L. (2004). Modeling high pressure micro hollow cathode discharges. Technical report, DTIC Document.

Brown, P. N., Byrne, G. D., and Hindmarsh, A. C. (1989). Vode: A variable-coefficient ode solver. *SIAM journal on scientific and statistical computing*, 10(5):1038–1051.

Bultel, A., van Ootegem, B., Bourdon, A., and Vervisch, P. (2002). Influence of ar 2+ in an argon collisional-radiative model. *Physical review E*, 65(4):046406.

Chang, R. and Setser, D. (1978). Radiative lifetimes and two-body deactivation rate constants for ar ($3p^5$,4p) and ar ($3p^5$,4p') states. *The Journal of Chemical Physics*, 69(9):3885–3897.

Cherrington, B. E. (2014). *Gaseous electronics and gas lasers*, volume 94. Elsevier.

COMSOL (2016). *Plasma Module User's Guide*. COMSOL Multiphysics^{TM} v. 5.2a, Stockholm, Sweden.

Crompton, R., Elford, M., and Jory, R. (1967). The momentum transfer cross section for electrons in helium. *Australian Journal of Physics*, 20(4):369–400.

Dabrowski, I., Herzberg, G., and Yoshino, K. (1981). The spectrum of hear^{+}. *Journal of Molecular Spectroscopy*, 89(2):491–510.

Deloche, R., Monchicourt, P., Cheret, M., and Lambert, F. (1976). High-pressure helium afterglow at room temperature. *Physical Review A*, 13(3):1140.

Demyanov, A., Kochetov, I., and Mikheyev, P. (2013). Kinetic study of a cw optically pumped laser with metastable rare gas atoms produced in an electric discharge. *Journal of Physics D: Applied Physics*, 46(37):375202.

Derzsi, A., Hartmann, P., Korolov, I., Karacsony, J., Bánó, G., and Donkó, Z. (2009). On the accuracy and limitations of fluid models of the cathode region of dc glow discharges. *Journal of Physics D: Applied Physics*, 42(22):225204.

Eismann, B. (2011). *Etude numérique et théorique des phénomènes liés aux hautes pressions dans les microdécharges*. PhD thesis, Université de Toulouse, Université Toulouse III-Paul Sabatier.

Emmert, F., Angermann, H., Dux, R., and Langhoff, H. (1988). Reaction kinetics of the he(2p) and the he_2^*(a,v) states in high-density helium. *Journal of Physics D: Applied Physics*, 21(5):667.

Eshel, B., Rice, C. A., and Perram, G. P. (2016). Pressure broadening and shift rates for ar (s–p) transitions observed in an ar–he discharge. *Journal of Quantitative Spectroscopy and Radiative Transfer*, 179:40–50.

Farouk, T., Farouk, B., Staack, D., Gutsol, A., and Fridman, A. (2006). Simulation of dc atmospheric pressure argon micro glow-discharge. *Plasma Sources Science and Technology*, 15(4):676.

Fiala, A., Pitchford, L., and Boeuf, J. (1994). Two-dimensional, hybrid model of low-pressure glow discharges. *Physical Review E*, 49(6):5607.

Frensley, W. R. (2004). Scharfetter-gummel discretization scheme for drift-diffusion equations. Technical report, Technical report, University of Texas at Dallas-Engineering and Computer Science.

Fridman, A., Chirokov, A., and Gutsol, A. (2005). Non-thermal atmospheric pressure discharges. *Journal of Physics D: Applied Physics*, 38(2):R1.

Garscadden, A., Kushner, M. J., and Eden, J. G. (1991). Plasma physics issues in gas discharge laser development. *IEEE transactions on plasma science*, 19(6):1013–1031.

Gogolides, E. and Sawin, H. H. (1992). Continuum modeling of radio-frequency glow discharges. i. theory and results for electropositive and electronegative gases. *Journal of applied physics*, 72(9):3971–3987.

Gregório, J., Leprince, P., Boisse-Laporte, C., and Alves, L. (2012). Self-consistent modelling of atmospheric micro-plasmas produced by a microwave source. *Plasma Sources Science and Technology*, 21(1):015013.

Haas, R. A. (1973). Plasma stability of electric discharges in molecular gases. *Physical Review A*, 8(2):1017.

Hagelaar, G., De Hoog, F., and Kroesen, G. (2000). Boundary conditions in fluid models of gas discharges. *Physical Review E*, 62(1):1452.

Hagelaar, G. and Pitchford, L. (2005). Solving the boltzmann equation to obtain electron transport coefficients and rate coefficients for fluid models. *Plasma Sources Science and Technology*, 14(4):722.

Hager, G. D. and Perram, G. (2010). A three-level analytic model for alkali metal vapor lasers: part i. narrowband optical pumping. *Applied Physics B: Lasers and Optics*, 101(1):45–56.

Han, J., Glebov, L., Venus, G., and Heaven, M. C. (2013). Demonstration of a diode-pumped metastable ar laser. *Optics letters*, 38(24):5458–5461.

Han, J. and Heaven, M. (2012). Gain and lasing of optically pumped metastable rare gas atoms. *Optics letters*, 37(11):2157.

Han, J. and Heaven, M. (2016). Personal Communication.

Han, J. and Heaven, M. C. (2014). Kinetics of optically pumped ar metastables. *Optics Letters*, 39(22):6541–6544.

Han, J., Heaven, M. C., Emmons, D., Perram, G. P., Weeks, D. E., and Bailey, W. F. (2016). Pulsed discharge production ar* metastables. In *SPIE LASE*, pages 97290D–97290D. International Society for Optics and Photonics.

Han, J., Heaven, M. C., Hager, G. D., Venus, G. B., and Glebov, L. B. (2014). Kinetics of an optically pumped metastable ar laser. In *SPIE LASE*, pages 896202–896202. International Society for Optics and Photonics.

Holstein, T. (1947). Imprisonment of resonance radiation in gases. *Physical Review*, 72(12):1212.

Holstein, T. (1951). Imprisonment of resonance radiation in gases. ii. *Physical Review*, 83(6):1159.

Hoskinson, A. R., Gregorío, J., Hopwood, J., Galbally-Kinney, K., Davis, S. J., and Rawlins, W. T. (2016). Argon metastable production in argon-helium microplasmas. *Journal of Applied Physics*, 119(23):233301.

Johnsen, R., Leu, M., and Biondi, M. A. (1973). Studies of nonresonant charge transfer between atomic ions and atoms. *Physical Review A*, 8(4):1808.

Jones, J., Lister, D., Wareing, D., and Twiddy, N. (1980). The temperature dependence of the three-body reaction rate coefficient for some rare-gas atomic ion-atom reactions in the range 100-300k. *Journal of Physics B: Atomic and Molecular Physics*, 13(16):3247.

Jonkers, J., van de Sande, M., Sola, A., Gamero, A., Rodero, A., and van der Mullen, J. (2003). The role of molecular rare gas ions in plasmas operated at atmospheric pressure. *Plasma Sources Science and Technology*, 12(3):464.

Kannari, F., Obara, M., and Fujioka, T. (1985). An advanced kinetic model of electron-beam-excited krf lasers including the vibrational relaxation in krf*(b) and collisional mixing of krf*(b, c). *Journal of applied physics*, 57(9):4309–4322.

Kramida, A., Ralchenko, Y., Reader, J., and NIST ASD Team (2015). Nist atomic spectra database (ver. 5.3). http://physics.nist.gov/asd.

Krupke, W. F., Beach, R. J., Kanz, V. K., and Payne, S. A. (2003). Resonance transition 795-nm rubidium laser. *Optics letters*, 28(23):2336–2338.

Kushner, M. J. (2005). Modelling of microdischarge devices: plasma and gas dynamics. *Journal of Physics D: Applied Physics*, 38(11):1633.

Łach, G., Jeziorski, B., and Szalewicz, K. (2004). Radiative corrections to the polarizability of helium. *Physical review letters*, 92(23):233001.

Lee, F., Collins, C., and Waller, R. (1976). Measurement of the rate coefficients for the bimolecular and termolecular charge transfer reactions of he_2^+ with ne, ar, n_2, co, co_2, and ch_4. *The Journal of Chemical Physics*, 65(5):1605–1615.

Lehmann, R. (2004). An algorithm for the determination of all significant pathways in chemical reaction systems. *Journal of atmospheric chemistry*, 47(1):45–78.

Lieberman, M. A. and Lichtenberg, A. J. (2005). *Principles of plasma discharges and materials processing*. Wiley, Hoboken, New Jersey, second edition.

Lindinger, W. and Albritton, D. (1975). Mobilities of various mass-identified positive ions in helium and argon. *The Journal of Chemical Physics*, 62(9):3517–3522.

Lindinger, W., Schmeltekopf, A., and Fehsenfeld, F. (1974). Temperature dependence of de-excitation rate constants of he(2^3s) by ne, ar, xe, h_2, n_2, o_2, nh_3, and co_2. *The Journal of Chemical Physics*, 61(7):2890–2895.

Lymberopoulos, D. P. and Economou, D. J. (1993). Fluid simulations of glow discharges: Effect of metastable atoms in argon. *Journal of applied physics*, 73(8):3668–3679.

Lymberopoulos, D. P. and Economou, D. J. (1995). Spatiotemporal electron dynamics in radio-frequency glow discharges: fluid versus dynamic monte carlo simulations. *Journal of Physics D: Applied Physics*, 28(4):727.

Madson, J. and Oskam, H. (1967). Mobility of argon ions in argon. *Physics Letters A*, 25(5):407–408.

Maier-Leibnitz, H. (1935). Ausbeutemessungen beim stoß langsamer elektronen mit edelgasatomen. *Zeitschrift für Physik*, 95(7-8):499–523.

Markosyan, A. H., Luque, A., Gordillo-Vázquez, F. J., and Ebert, U. (2014). Pumpkin: A tool to find principal pathways in plasma chemical models. *Computer Physics Communications*, 185(10):2697–2702.

McCann, K., Flannery, M., and Hazi, A. (1979). Theoretical cross sections for ionization of metastable excimers ne_2^* and ar_2^* by electron impact. *Applied Physics Letters*, 34(9):543–545.

Mehr, F. and Biondi, M. A. (1968). Electron-temperature dependence of electron-ion recombination in argon. *Physical Review*, 176(1):322.

Mesyats, G. A. (2006). Similarity laws for pulsed gas discharges. *Physics-Uspekhi*, 49(10):1045.

Miura, N. and Hopwood, J. (2011). Spatially resolved argon microplasma diagnostics by diode laser absorption. *Journal of Applied Physics*, 109(1):013304.

Napartovich, A. (2001). Overview of atmospheric pressure discharges producing nonthermal plasma. *Plasmas and Polymers*, 6(1):1–14.

Neeser, S., Kunz, T., and Langhoff, H. (1997). A kinetic model for the formation of excimers. *Journal of Physics D: Applied Physics*, 30(10):1489.

Oskam, H. and Mittelstadt, V. (1963). Ion mobilities in helium, neon, and argon. *Physical Review*, 132(4):1435.

Pancheshnyi, S., Eismann, B., Hagelaar, G., and Pitchford, L. (2008). *Computer code ZDPlasKin, University of Toulouse, LAPLACE*. CNRS–UPS–INP, Toulouse, France, http://www.zdplaskin.laplace.univ-tlse.fr.

Passchier, J. and Goedheer, W. (1993). A two-dimensional fluid model for an argon rf discharge. *Journal of applied physics*, 74(6):3744–3751.

Phelps, A. (2008). Phelps database. http://jilawww.colorado.edu/∼avp/.

Pitchford, L., Alves, L., Bartschat, K., Biagi, S., Bordage, M., Phelps, A., Ferreira, C., Hagelaar, G., Morgan, W., Pancheshnyi, S., et al. (2013). Comparisons of sets of electron–neutral scattering cross sections and swarm parameters in noble gases: I. argon. *Journal of Physics D: Applied Physics*, 46(33):334001.

Pitz, G. A., Fox, C. D., and Perram, G. P. (2011). Transfer between the cesium $6^2p_{1/2}$ and $6^2p_{3/2}$ levels induced by collisions with h_2, hd, d_2, ch_4, c_2h_6, cf_4, and c_2f_6. *Physical Review A*, 84(3):032708.

Raizer, Y. P. (1997). *Gas discharge physics*, volume 2. Springer Berlin.

Raizer, Y. P., Shneider, M. N., and Yatsenko, N. A. (1995). *Radio-frequency capacitive discharges*. CRC Press.

Rapp, D. and Englander-Golden, P. (1965). Total cross sections for ionization and attachment in gases by electron impact. i. positive ionization. *The Journal of Chemical Physics*, 43(5):1464–1479.

Rauf, S. and Kushner, M. J. (1999). Dynamics of a coplanar-electrode plasma display panel cell. i. basic operation. *Journal of applied physics*, 85(7):3460–3469.

Rawlins, W., Galbally-Kinney, K., Davis, S., Hoskinson, A., Hopwood, J., and Heaven, M. (2015). Optically pumped microplasma rare gas laser. *Optics express*, 23(4):4804–4813.

Rolin, M., Shabunya, S., Rostaing, J., and Perrin, J. (2007). Self-consistent modelling of a microwave discharge in neon and argon at atmospheric pressure. *Plasma Sources Science and Technology*, 16(3):480.

Roos, B. O., Lindh, R., Malmqvist, P.-Å., Veryazov, V., and Widmark, P.-O. (2004). Main group atoms and dimers studied with a new relativistic ano basis set. *The Journal of Physical Chemistry A*, 108(15):2851–2858.

Scharfetter, D. L. and Gummel, H. K. (1969). Large-signal analysis of a silicon read diode oscillator. *Electron Devices, IEEE Transactions on*, 16(1):64–77.

Shon, J. W. (1993). *Modeling of High-Pressure Rare Gas Lasers: Kinetics and Plasma Chemistry*. PhD thesis, University of Illinois at Urbana-Champaign.

Shon, J. W. and Kushner, M. J. (1994). Excitation mechanisms and gain modeling of the high-pressure atomic ar laser in he/ar mixtures. *Journal of applied physics*, 75(4):1883–1890.

Smirnov, B. (1981). Physics of weakly ionized gases.

Stauffer, A. (2014). Ngfsrdw database, york university. nl.lxcat.net.

Stefanović, I., Kuschel, T., Schröter, S., and Böke, M. (2014). Argon metastable dynamics and lifetimes in a direct current microdischarge. *Journal of Applied Physics*, 116(11):113302.

Steinfeld, J. I., Francisco, J. S., and Hase, W. L. (1999). *Chemical kinetics and dynamics*. Prentice Hall.

Tachibana, K. (1986). Excitation of the $1s_5$, $1s_4$, $1s_3$, and $1s_2$ levels of argon by low-energy electrons. *Physical Review A*, 34(2):1007.

Von Engel, A. (1965). *Ionized Gases*. Oxford.

Ward, A. (1962). Calculations of cathode-fall characteristics. *Journal of Applied Physics*, 33(9):2789–2794.

Wieme, W. and Lenaerts, J. (1981). Excimer formation in argon, krypton, and xenon discharge afterglows between 200 and 400 k. *The Journal of Chemical Physics*, 74(1):483–493.

Yamabe, C., Buckman, S., and Phelps, A. (1983). Measurement of free-free emission from low-energy-electron collisions with ar. *Physical Review A*, 27(3):1345.

Yang, Z., Yu, G., Wang, H., Lu, Q., and Xu, X. (2015). Modeling of diode pumped metastable rare gas lasers. *Optics express*, 23(11):13823–13832.

YATSENKO, N. (1992). Slot gas lasers. *Bulletin of the Russian Academy of Sciences*, 56(12):1901–1907.

Zameroski, N. D., Hager, G. D., Rudolph, W., and Hostutler, D. A. (2011). Experimental and numerical modeling studies of a pulsed rubidium optically pumped alkali metal vapor laser. *JOSA B*, 28(5):1088–1099.

Zhu, X.-M. and Pu, Y.-K. (2010). A simple collisional–radiative model for low-temperature argon discharges with pressure ranging from 1 pa to atmospheric pressure: kinetics of paschen 1s and 2p levels. *Journal of Physics D: Applied Physics*, 43(1):015204.

REPORT DOCUMENTATION PAGE

Form Approved
OMB No. 0704–0188

1. REPORT DATE *(DD–MM–YYYY)*	2. REPORT TYPE	3. DATES COVERED *(From — To)*
14-09-2017	Doctoral Dissertation	Sep 2014 — Sep 2017

4. TITLE AND SUBTITLE

Analysis of Ar(1s5) Metastable Populations in High Pressure Argon-Helium Gas Discharges

5a. CONTRACT NUMBER

5b. GRANT NUMBER

5c. PROGRAM ELEMENT NUMBER

6. AUTHOR(S)

Emmons II, Daniel J., Maj, USAF

5d. PROJECT NUMBER

5e. TASK NUMBER

5f. WORK UNIT NUMBER

7. PERFORMING ORGANIZATION NAME(S) AND ADDRESS(ES)

Air Force Institute of Technology
Graduate School of Engineering and Management (AFIT/EN)
2950 Hobson Way
WPAFB OH 45433-7765

8. PERFORMING ORGANIZATION REPORT NUMBER

AFIT-ENP-DS-17-S-025

9. SPONSORING / MONITORING AGENCY NAME(S) AND ADDRESS(ES)

High Energy Laser Joint Technology Office
901 University Blvd. SE, Suite 100
Albuquerque NM 87106
505-248-8208, harro.ackermann@jto.hpc.mil
ATTN: Dr. Harro Ackermann

10. SPONSOR/MONITOR'S ACRONYM(S)

HEL JTO

11. SPONSOR/MONITOR'S REPORT NUMBER(S)

12. DISTRIBUTION / AVAILABILITY STATEMENT

Distribution Statement A:
Approved for Public Release; Distribution Unlimited

13. SUPPLEMENTARY NOTES

This work is declared a work of the U.S. Government and is not subject to copyright protection in the United States.

14. ABSTRACT

Simulations of an argon-helium plasma are performed for two high pressure discharge scenarios to find a uniform, large-volume plasma with Ar(1s5) metastable densities on the order of 10^{13} cm^{-3} for use as the ground state in an optically pumped rare gas laser. An analysis of a pulsed direct current discharge is performed for a 7% argon in helium mixture at a pressure of 270 Torr using both zero and one-dimensional models. Kinetics of species relevant to the operation of an optically pumped rare gas laser are analyzed throughout the pulse duration to identify key reaction pathways. Simulations are extended to an α-mode radio frequency dielectric barrier discharge with varying mixtures of argon and helium at pressures ranging from 200-500 Torr. Metastable densities are analyzed as a function of argon fraction and pressure to determine the optimal conditions maximizing metastable density. Finally, optically pumped rare gas laser performance is analyzed as a function of the Ar(2p)+M→Ar(1s)+M branching ratio. A sensitivity study is performed due to the uncertainty in the branching ratio.

15. SUBJECT TERMS

High Pressure Argon-Helium Gas Discharge, Optically Pumped Rare Gas Laser, Ar(1s5) Metastable Density Kinetics

16. SECURITY CLASSIFICATION OF:			17. LIMITATION OF ABSTRACT	18. NUMBER OF PAGES	19a. NAME OF RESPONSIBLE PERSON
a. REPORT	b. ABSTRACT	c. THIS PAGE			Dr. David E. Weeks, AFIT/ENP
U	U	U	UU	206	19b. TELEPHONE NUMBER *(include area code)* (937) 255-3636, x4561; david.weeks@afit.edu